Università degli Studi di Napoli Federico II

Department of Structures for Engineering and Architecture

Ph.D. in Structural Engineering, Geotechnical and Seismic

XXIX cycle

Ph.D. Dissertation

A NEW RIGID BLOCK MODEL FOR MASONRY STRUCTURES

Antonino Iannuzzo

Ph.D. Coordinator
Prof. Eng. Luciano Rosati

Thesis Supervisors
Prof. Eng. Antonio Gesualdo
Prof. Archt. Maurizio Angelillo

A NEW RIGID BLOCK MODEL FOR MASONRY STRUCTURES

by

Antonino Iannuzzo

Abstract. This dissertation presents a new rigid block model for the analysis of masonry elements and structures. In this work a masonry structure is modelled as a continuum composed by Normal Rigid No-Tension (NRNT) material. The NRNT represents an extension of the model material of Heyman to 2d/3d continua. The material is rigid in compression, but extensional deformations, allowed at zero energy price, can be either regular or singular; then extensional deformation can appear as either diffuse (smeared cracks) or concentrated (macroscopic cracks), and there is not any reason to prefer one upon another, on an energy ground.

The fact that rigid block deformation seems to be the preferred failure mode for real masonry structures stems from mechanical characteristics, such as toughness, interlocking, finite friction and cohesion, that are not inherent to the simplified NRNT continuum model. So, it is interesting to see if rigid block mechanisms can arise naturally in solving the equilibrium problem, and if there is any legitimate way to force rigid block mechanisms over diffuse cracking.

The boundary value problem for a continuum composed of NRNT material is formulated as an energy minimum search, and two numerical methods for approximating the solution are proposed. With the PR method the energy is minimized in the set of piecewise-rigid (PR) displacements. With the C^0 method the possibility to restrict the search of the minimum to continuous (C^0) displacement fields, by adopting some classical Finite Element (FE) approximation, is explored. The C^0 solution, though more cumbersome from the numerical point of view, appears as more adaptable than the rigid block approximation, in approximating fracture lines that are slanted, that is far from being located on the skeleton of a mesh. This sluggishness of the rigid block approximation in reproducing "slanted" cracks (that is cracks not developing along the boundary of the rigid elements), is one of the main critical issues inherent to the piecewise rigid (PR) approximation. Then there is another reason to adopt the C^0 approximation, namely for seeing if the C^0 approximation can be used, in combination with the PR approximation, as a preliminary analysis for suggesting the optimal rigid block partition.

After the two methods are introduced, some benchmark problems are analysed to illustrate the numerical performances of the two approaches and the "pro et contra" of these two opposed strategies.

The effectiveness of the rigid block approach combined with energy minimization, is also tested on some benchmark problems, such as the problem of the arch subject to given settlements, the Couplet's problem, and the determination of the collapse load multiplier of horizontal forces.

A number of case studies concerning real masonry structures is also presented to illustrate the effectiveness of the proposed method.

Keywords. New Rigid Block model, PR method, C^0 method, masonry structures, unilateral materials, NRNT, smeared and concentrated cracks, limit analysis, settlements, horizontal actions.

Thesis supervisors
Prof. Archt. Maurizio Angelillo
Prof. Eng. Antonio Gesualdo

Acknowledgements

First of all, I would like to thank my two advisors, Prof. Antonio Gesualdo and Prof. Maurizio Angelillo, for guiding my research and for their precious suggestions in writing this dissertation.

I have had a consolidated relationship with Prof. Gesualdo for a long time, since he has been my tutor in my two previous thesis. It is thanks to him that I started this adventure: he has pushed me to face this pathway, giving me his continuous support, the right advices at the right time and ideas on the issues to be explored, without any preconceptions. All this has always been important and fundamental for me: I owe to him my scientific as well as cultural and even human growth.

During my research pathway, I was so lucky to meet Prof. Angelillo with whom I have started a close cooperation. He has contributed a lot to my research work and my further scientific growth, allowing me to approach the specific issue with a new vision, which now is also mine. The continuous exchange of opinions, suggestions and advices, and not least its help and care of details in the thesis review, have made this work better, so I hope it will be a source of inspiration for others.

The group of Prof. Gesualdo, Prof Angelillo and Fabiana de Serio has been for me a small scientific family.

My warm thanks to Prof. Katalin Bagi who, during my short but intense period of research study abroad at the Budapest University of Technology and Economics, has led me towards new issues, widening my ideas on the topic. Thanks also to Tamás Forgács and, especially to Nicko Kassotakis: I had the luck to know him there and now I'm bound by a true friendship.

I thank my readers, Profs. Santiago Huerta and Elio Sacco, and my Ph.D. coordinator Prof. Luciano Rosati for their constructive feedbacks.

Finally, last but not least, special thanks to Prof. Renato Fiorenza, who has deeply affected my training and for whom I feel a deep and sincere esteem.

The realization of this dissertation and the related studies have required commitment and also implied limitations I have never felt the weight of, both because the topic has intrigued and fascinated me a lot, and because I have always had the support of my "Famiglia", Lidia and my "Amici" (a special thank goes to Pasquale Colarusso ☺JM).

Ai miei genitori,

Pino e Pupetta

TABLE OF CONTENTS

PART I

INTRODUCTION

Chapter 1

INTRODUCTION

Prologue. In this dissertation, considering plane masonry structures in equilibrium under the action of known loads, we propose a method for predicting the effect, in terms of displacements and fractures, of given settlements and load conditions.

Fractures and cracks in masonry are physiological, and rather than the result of over-loading, are most likely the direct product of small changes of the boundary conditions. However, geometry and loads play a role in the specific fracture pattern that actually nucleates into the structure. In other words, the specific way in which a certain fracture pattern opens up and evolves, even if usually not directly due to an excess of loading (and more likely the direct effect of settlements of the foundation or of internal distortions), is in a strong relation with the geometry of the structure and of the loads themselves.

A simple mathematical model allowing for the prediction of this peculiar behaviour is the unilateral masonry-like material of Heyman (1966), a very crude but genial model for masonry, for which the two theorems of Limit Analysis, created for analysing ductile structures, are still valid.

We refer to the works by Kooharian (1952), Livesley (1978), Como (1992), Angelillo (2014b), Brandonisio et al [(2015),(2017)], Gesualdo et al (2016a), Angelillo et al (2014), Fortunato et al (2016), Huerta [(2002),(2006),(2008)], Block et al (2006), Block (2009), Marmo and Rosati (2017), Bagi (2014) for the discussion and the application of limit analysis to masonry-like structures.

■ 1.1 THE UNILATERAL MODEL FOR MASONRY

It is a fact that the key issue in the peculiar response of masonry structures, is represented by their essentially unilateral behaviour. While a standard structure

under bilateral constraints, will usually respond to comparatively small settlements and eigenstrains with elastic deformations, and then with a substantial modification of the internal forces, a unilateral structure, even if heavily over-constrained, can exhibit zero energy modes, and then may compensate the effect of comparatively large settlements without any increase of the internal forces, through mechanisms requiring essentially vanishing energy dissipation.

We call the search for a kinematically admissible displacement, that is for the solution of the boundary value problem (bvp) for the displacement $\boldsymbol{u}$ under Heyman's restrictions: *kinematical problem*, as opposed to the *equilibrium problem*, that is the search of a statically admissible stress field under Heyman's restrictions. For masonry-like materials these two problems are essentially independent, and can be dealt with separately.

When trying to solve the boundary value problem with a kinematic approach, the problem arises of selecting, among the possibly many kinematically admissible displacement fields responding to the given kinematical data (settlements and eigenstrains), the ones that guarantee also the equilibrium of the loads imposed on the structure.

For elastic, and even for some elastic-brittle materials, these states, that we call *"solutions of the boundary value problem"*, can be found by searching for the minimum of some, suitably defined, form of energy. For elastic-brittle materials this energy is the sum of the potential energy of the loads, of the elastic energy and of the interface energy necessary to activate a crack on an internal surface, see (Angelillo et al, 2012) and (Gesualdo et al, 2015). For elastic materials is the sum of the potential energy of the loads and of the elastic energy. For Heyman's materials is just the potential energy of the loads.

Then we may search a displacement field which is the solution of the boundary value problem, by minimizing the potential energy $\wp$ of the loads over a convenient function set $\mathcal{K}$ for the displacements. Here we consider two numerical approximations of the minimum problem, based on a finite element subdivision of the structure into parts. With the first (PR) method, we consider that the structure is an assembly of a finite number of rigid elements, with potential strong discontinuities along the common interfaces (i.e. the common boundaries among the blocks). This approach is usually called in the recent literature Discrete Element Method (DEM). In the plane case, these interfaces must be made of straight pieces. With the second method, we consider classical C^0 finite elements (FEM). Indeed, a possible simple choice for approximating this set $\mathcal{K}$ for a continuum made of Heyman's material is to consider that the strain is zero a.e. inside the domain, namely $\mathcal{K}$ is the set of piecewise rigid displacements. This is actually the case if the structure

is composed of monolithic blocks which are not likely to break at their inside (De Serio et al, 2016)

We must point out that piecewise rigid displacements, which are the most frequent and evident manifestation of masonry deformation in real masonry constructions, are not at all simple displacement fields for a continuum, and are usually ruled out in the standard numerical codes for fluids and solids which are employed to handle the complex boundary value problems of continuum mechanics. A usual setting for problems in which finite jumps of the displacement are admitted is the space SBV (Ambrosio et al, 2000). The main difficulty with displacements that belongs to the space SBV, (besides, for deformable materials, the managing of the singularity of strain at the tip of the crack) is the fact that the location of the support of the singularity (that is of the jump set) is not known in advance, and that the shape and the topology of the parts over which the displacement is regular, can be, in principle, rather wild.

Actually, a recent piecewise rigidity result by Chambolle et al (2007) generalizing the classical Liouville result for smooth functions now states that an SBV function y satisfying the constraint $\nabla y \in SO(2)$ a.e. ($SO(2)$ being the group of rotation tensors in 2d), is a collection of an at most countable family of rigid deformations, i.e. the body may be divided into different components each of which is subject to a different rigid motion.

Some issues connected with the managing of rigid deformation with unknown interfaces is discussed, with the aid of some simple examples, in the forthcoming paper of Cennamo et al (2017), from which we make the following citation:

> *"...then we may search a displacement field* $\mathbf{u}$ *which is the solution of the boundary value problem (i.e. the kinematical and the equilibrium problem for masonry-like structures), by minimizing the potential energy* $\wp$ *of the loads. ... Actually, the functional* $\wp$ *is linear in* $\mathbf{u}$*; then, if the set of kinematically admissible displacements is discretized by fixing a given partition of the domain into rigid parts* Ω_i *(that is the supports of the possible strain singularities -i.e. the fractures- are fixed in advance), the minimization of* $\wp$ *reduces to the minimization of a linear functional under linear unilateral and bilateral constraints (i.e. the constraints expressing the unilateral contact with no-sliding among blocks). Such a problem is, at least in principle, an easy problem of convex analysis that can be solved, for example, with the simplex method. The case of movable interfaces, that is the case in which the partition into blocks is not fixed in advance, is a completely different story. The functional* $\wp$*, though still a linear function of* $\mathbf{u}$*, becomes a strongly nonlinear function of the position of the interfaces, and its*

minimization under the given constraints, requires a much bigger effort."

Summing up, in the present work to obtain an approximation of the minimizer (that is of the displacement minimizing the energy) with the two methods, we proceed as described below.

PR. With the first method, fractures will appear concentrated. We fix a mesh geometry and iterate the minimization with respect to the rigid body displacements of the elements, by refining the mesh until a satisfying picture of the fractures is obtained. This way produces a sequence of linear programming problems.

$\boldsymbol{C^0}$. With the second method, fractures will appear as smeared. We fix a FE mesh and find the minimizer. The minimal solution may return diffuse cracking with large peaks in the vicinity of lines and then, essentially, a partition of the domain into rigid blocks. This second method, computationally more time-consuming, allows to detect the exact position and inclination of the fractures by approximating them with narrow bands. Then, the second (C^0) method can be used also to select an optimal partition into rigid blocks to be fed into the first method (PR).

The description of fractures and rigid block mechanisms is inherent to the unilateral model, but masonry sometimes presents also other kinds of local and global failure modes that we describe and analyse in the following sections.

■ 1.2 MODEL FOR MASONRY: NO-TENSION ASSUMPTION

A common architectural definition of masonry says: *masonry is the building of structures from individual units, which are often laid in and bound together by mortar*.

The common materials of masonry construction are various: generally, bricks and building stones such as marble, granite, limestone, tuff and concrete blocks. The materials used, the quality of the mortar and workmanship, and the pattern in which the units are assembled can significantly affect the performance and the durability of the overall masonry construction. Generally, well executed masonry assemblies are a highly durable form of construction. Indeed, in particular in Europe, masonry constructions are the great majority of the buildings and the most important

monuments of its architectural heritage. Despite the continuous growth of demand for masonry safety assessments, nevertheless, as Como noted, *"there is a lack of a widely accepted approach to studying the statics of masonry structures"* (Como, 2013, p. VII).

The main question in masonry modelling is: *it is possible to group a large variety of masonry structures into a single material class in order to apply a unified and general approach?*

If the answer be negative, any particular structure would be approached with an "ad hoc" model. Probably a definite answer to this question does not exist, and in this sense the way used for the analysis of a masonry structure could be justified in case by case fashion; in a certain sense these two approaches could be viewed as complementary.

In the current scientific context, there are essentially two ways of approaching the modelling of masonry: the first aims at the modelling of large classes of masonry buildings (e.g. old masonry structures). The second one is more pragmatic and restricts to the mechanical description of very specific types of masonry (masonry structures of regularly arranged blocks, e.g. brickworks of known geometry, see De Buhan and De Felice (1997), Sacco [(2009),(2014)], Milani (2011), Lourenço et al (2014) and Lebon (2014).

In the present work, we follow the first approach and develop numerical models, which can be applied to solve equilibrium problems for a large class of masonry structures. It is to be pointed out that while the second approach adopts sophisticated material models, requiring a high degree of knowledge about the behaviour of masonry material, the first approach requires only minimal (and mainly qualitative) information on the material. Indeed, one of the reasons to prefer, at least at the macro-scale, the first approach over the second is the fact that often the parameters required by the second approach (e.g. the microscopic geometry, the specific material behaviour and the construction details) are either not known or are affected by an elevated randomness and uncertainty.

The basic idea behind the first approach is centred on the assumption that the material is unilateral, that is tensile strength can be neglected and only compressive stresses can be considered: this is the so called **No-Tension assumption**. Making this assumption, it is possible to take into account and predict one of the main characteristic aspects of masonry behaviour, namely the fractures. Indeed, fracturing, as noted by Heyman, is *"the way in which the masonry buildings relieve and can survive also to radical and, sometimes, dramatic changes of the environment)"* (Angelillo, 2014a, p. 2). Here we describe briefly three models, which we call simplified models, and that are based on the No-Tension assumption.

■ 1.3 MASONRY MECHANICAL BEHAVIOUR

As previously defined, masonry is a heterogeneous assemblage of units and joints. Units can be such as bricks, blocks, ashlars, adobes, irregular stones and others. Mortar is a workable paste used to bind masonry blocks together filling the gaps between them. Modern mortars can be typically clay, bitumen, chalk, lime/cement based mortar or other. The large possibilities of combination of such elements, either from a mechanical point of view or from a geometrical one (assemblage), leads to a wide variety of "masonry" cells. Thus, we can easily imagine that the accurate knowledge and mechanical characterization of a particular masonry is strictly connected to the in situ material proprieties. In what follows we treat, briefly, some mechanical macroscopic aspects, referring to a macroscopic portion of a masonry wall composed of many individual blocks as an elementary representative element, neglecting the specific behaviour either of mortar or of the block components.

Masonry Type	$f_c\left(\frac{daN}{cm^2}\right)$	$f_t\left(\frac{daN}{cm^2}\right)$	$E\left(\frac{daN}{cm^2}\right)$	$\rho\left(\frac{kg}{m^3}\right)$
Disarranged masonry of cobbles/boulders	10-18	0.40-0.64	6900-10500	1900
Masonry of roughhewed stones	20-30	0.70-1.00	10200-14400	2000
Masonry of cut stones	26-38	1.12-0.74	15000-19800	2100
Masonry of soft stones	14-24	0.56-0.84	9000-12600	1600
Masonry of squared stone blocks	60-80	1.80-2.40	24000-32000	2200
Brickwork of solid blocks and lime mortar	24-40	1.20-1.84	12000-18000	1800
Brickwork of semisolid blocks and cem. mortar	50-80	4.80-6.40	35000-56000	1500
Brickwork of air bricks (45%)	40-60	6.00-8.00	36000-54000	1200
Brickwork of air bricks (< 45%)	30-40	2.00-2.60	27000-36000	1100
Masonry of concrete air-blocks (45-65 %)	30-44	3.60-4.80	24000-35200	1400
Masonry of concrete air-blocks (< 45 %)	15-20	1.90-2.50	12000-16000	1200

Tab. 1.1 - Compressive strength f_c, tensile strength f_t, elastic modulus E and mass density ρ of different types of coarse masonry with poor mortar are reported (source: Italian Code for Constructions, DM 14.1.2008).

It has to be pointed out that the size of the representative element of masonry is at least one order of magnitude bigger than any representative volume element of other materials such as steel and concrete; for example, a polycrystal has grains of size of the order of 10^{-5}-10^{-4}m, concrete aggregates have a size of 10^{-3}-10^{-2}m and bricks of 10^{-1}m. The main feature of masonry is that its tensile strength is much lower than the compressive one, their ratio being lower than 0.1 and often around 0.01. This feature can be noticed from **Tab. 1.1**, where the main mechanical parameters of different types of coarse masonry with poor mortar are reported. In **Fig. 1.1a** and **Fig. 1.1b** two qualitative stress-displacement diagrams for a masonry wall are reported. The symbols f_c and f_t indicate the compressive and tensile strength of the

wall. Obviously, the strength of the wall depends on the mixing of the strengths of its components (blocks and mortar) and their assemblage: many empiric relations between the strength of the basic components and the global strength of a masonry wall are available in the literature and reported in construction codes.

In **Fig. 1.1** G_c and G_t represent respectively the compressive and tensile fracture energy. In particular, G_t, also known as *toughness*, is the surface energy per unit area required to open a crack in elongation. Instead, G_c represent the surface energy per unit area connected with the fracture pattern forming during the crushing of the wall. There exist some empirical formulas which allow to evaluate G_c as a function of the compressive strength f_c, some other relations expressing G_t as a function of f_c.

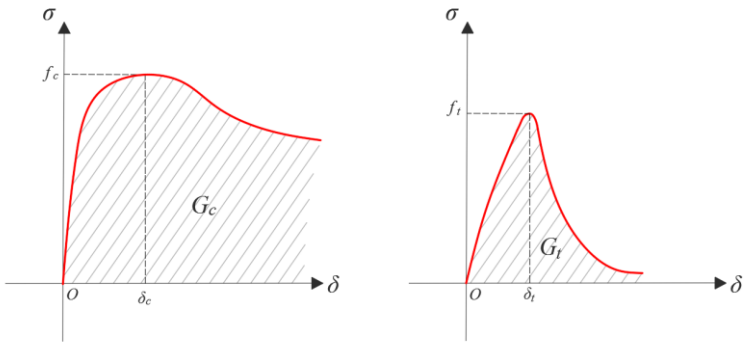

Fig. 1.1 - Two qualitative stress-displacement diagrams, in compression (a) and in tension (b), for a masonry wall are reported. The symbols f_c and f_t denote the compressive and tensile strength of the wall, whilst G_c a G_t represent the compressive and tensile fracture energy (toughness).

Remark 1|1. Since the tensile strength is much lower than the compressive one, the energy G_t required to open a crack, as can be easily deducted from **Fig. 1.1b**, is negligibly small with respect to the energy required to crush the material; therefore neglecting the tensile strenght and the corresponding toughness is justified on an energetical ground. ■

■ 1.4 MASONRY STRUCTURES: FAILURE MODES

In this section, we present some typical failure modes showing images selected from (Faccio, a.a. 2014-15), (De Maria), (Giuffrè, 1991), (Calderoni, 2015) and (Papa et al, 2001).

1.4.1 Local failure modes

Masonry structures exhibit essentially three main local failure modes. The first is associated with the low tensile strength of masonry and manifests itself through a clear and definite detachment between two adjacent and intact parts (see **Fig. 1.2**). Usually these detachments, called fractures, can involve or not the bricks (see **Fig. 1.3**), depending on the mutual strength of mortar and brick. Usually this kind of failures are the less alarming, since through them masonry structures can accommodate the possible change in boundary conditions (e.g. settlements).

Fig. 1.2 - Some typical failure modes of the first type: detachments.

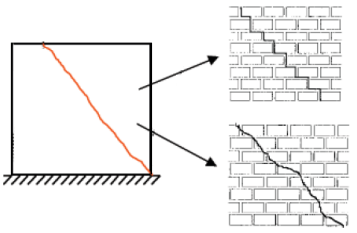

Fig. 1.3 - Detachments can involve or not the brick: a scheme.

The second one involves both fractures of detachment and sliding, and is typical of in-plane shear mechanisms **Fig. 1.4**): this failure mode appears when masonry is subjected to high compressive loads and shears.

Fig. 1.4 - Some typical failure modes of the second type: detachments and sliding. These fractures occur when the structure is close to collapse (e.g. under seismic action).

The third one is the crushing of the material due to compression and occurs when the compressive stress is close to the compressive strength of the material (**Fig. 1.5** and **Fig. 1.6**). Generally, since masonry structures are designed to work under low compressive stresses (usually a mean background stress level of 10% with respect to the compressive strength is present), this failure mode is far less frequent.

Fig. 1.5 - Some typical failure modes of the third type: crushing of the material occurring when the compressive stress is close to the compressive strength of the material.

Citing from Angelillo: *"The first type of fractures is the most frequent and usually irrelevant. The second and third modes often occur when the load is critical or close to become a collapse load. The third one is the most dangerous since failure under compression is usually sudden"* (Angelillo, 2014, p. 3).

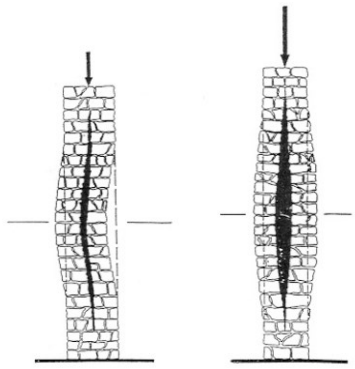

Fig. 1.6 - Drawing from (Mastrodicasa, 1988): a typical crushing failure of a masonry pillar.

1.4.2 Global failure modes: mechanisms

Here we present the main typical collapse mechanisms. Besides the failure modes due to poor quality of masonry (**Fig. 1.7**), the typical mechanisms are classifiable into two main categories: out of plane failure and in-plane failure.

Fig. 1.7 - Examples of poor quality masonry (Onna).

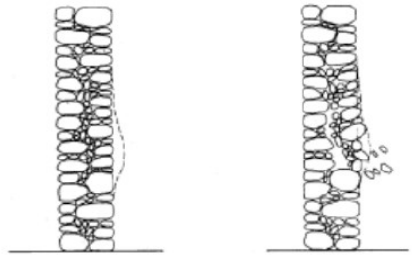

Fig. 1.8 – A schematic representation of a failure of a poor quality masonry.

The first ones (**Fig. 1.9**) are the most frequent and visible collapse modes for masonry structures. They essentially depend either on the poor clamping between the wall and the remaining part of the structure or on the pushing of the roofs, slabs and other transverse walls. The mitigation of this kind of failures is obtained by adopting some geometrical and mechanical prescriptions.

Fig. 1.9 - Some typical out of plane mechanisms.

The second ones (**Fig. 1.10** and **Fig. 1.11**) concern well-designed masonry structures failing globally. Indeed, a good design practice should avoid the first mechanism and allow only global mechanisms. Generally, this second mode displays itself through detachments and sliding (see **Fig. 1.4**) involving the formations of such internal resistant structures (see **Fig. 1.12** and **Fig. 1.13**).

Fig. 1.10 - Some typical in-plane mechanisms.

Fig. 1.11 - Some typical in-plane mechanisms for arches and vaults.

The aim of this work is the development of a model and of the related numerical code for the analysis of in-plane mechanisms and of the effects of settlements. In particular, it should be noted that often, with reference to these two cases, the approach used in the literature to analyse a masonry structure is to guess a typical mechanism (or select it among a given set of typical ones) and making on it the related assessments of safety (see **Fig. 1.12**, **Fig. 1.13** and **Fig. 1.14**).

Instead, our methods aims at determining automatically the mechanism, on which all the required analyses could be applied.

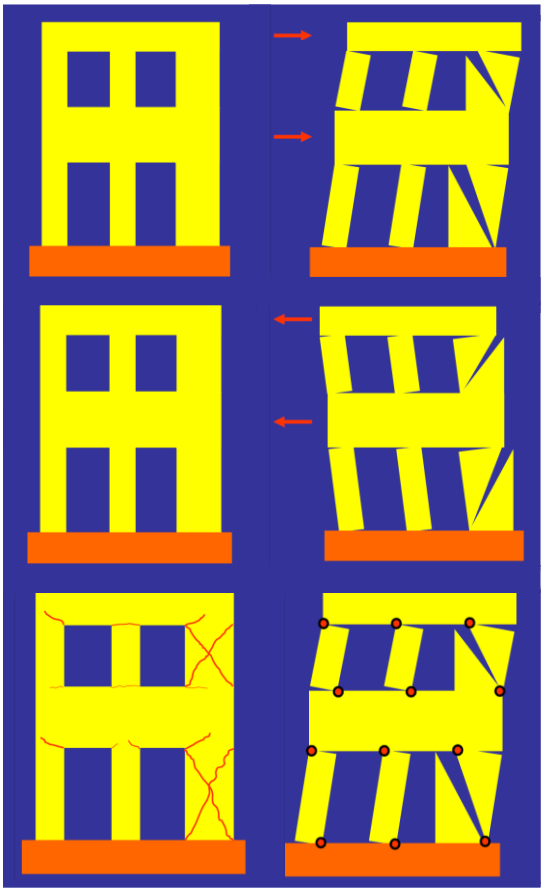

Fig. 1.12 - Drawings from (Faccio, a.a. 2014-15): the effects of earthquake and the related internal resistant structures are shown.

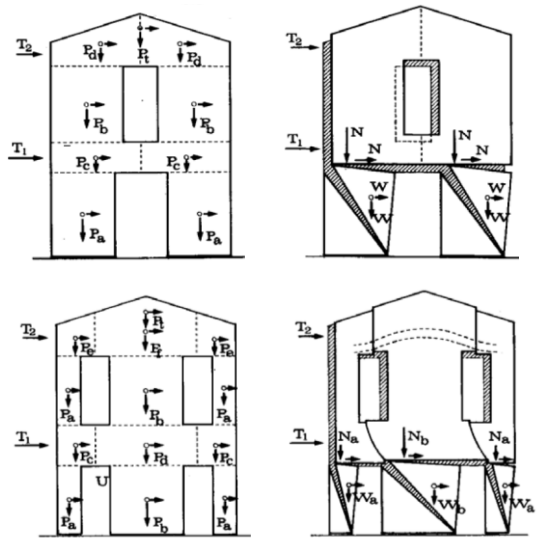

Fig. 1.13 - Two typical mechanisms hypothesized for the analysis of a masonry structure under horizontal actions, source: (AA.VV, 1999).

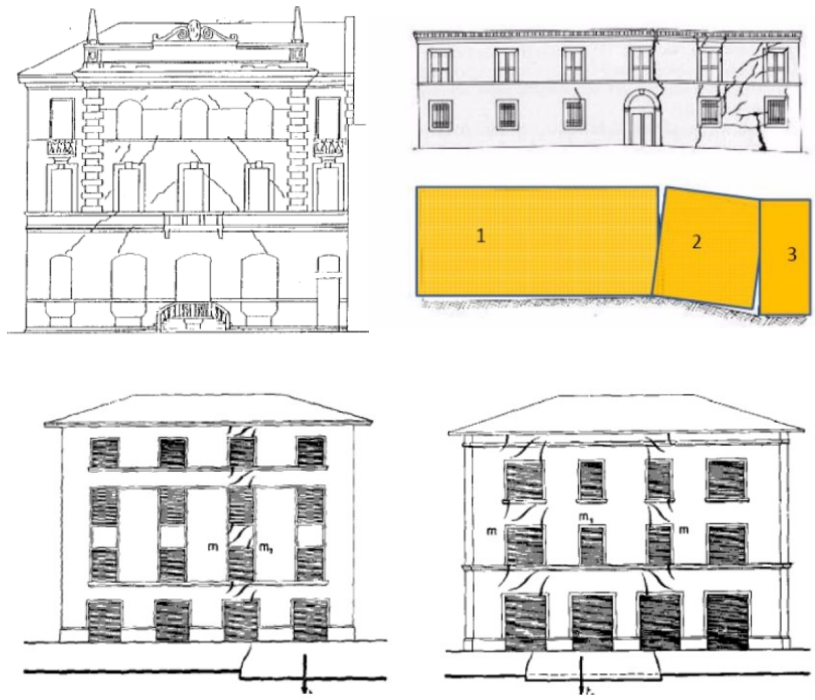

Fig. 1.14 - Some drawings reporting the effects of settlements on masonry structures. Masonry structures accommodate the settlements through the formation of rigid blocks (real examples redrawn from the website of "Vigili del Fuoco" Bergamo, courtesy of Paolo Faccio).

■ 1.5 SIMPLIFIED MODELS

In order to model and characterize the behaviour of masonry-like materials in 1d, we adopt the same classification of (Angelillo, 2014b) sorting these models with an increasing number coinciding with the number of parameters required for their definition. The models adopted are three, namely: "model zero", "model one" and "model two" and then the number of independent parameters required is respectively zero, one and two.

Remark 2|1. Before discussing these models, it would be useful to fix a preliminary and basic concept: by using the term *"elasticity"* in what follows, we refer to its primitive definition, namely: *stress* $\boldsymbol{T}$ *uniquely determined by strain* $\boldsymbol{E}$*, namely*

$$\boldsymbol{T} = f(\boldsymbol{E}) \; . \blacksquare \tag{1.1}$$

1.5.1 Model Zero (NRNT)

The most essential and restrictive idealization is "model zero", that is the **Normal Rigid No-Tension** (NRNT) model. No mechanical parameter is required to define this model.

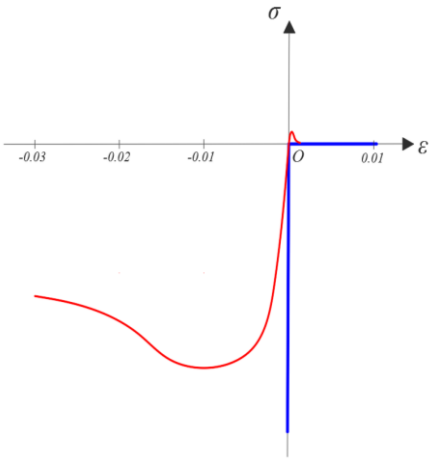

Fig. 1.15 – Uniaxial behaviour (blue line) defining model zero compared to a typical stress-stain plot for masonry (red line). Both stiffness and strength are assumed to be infinite. Since for $\varepsilon > 0$ the stress is completely determined by the strain, the behaviour is elastic for any positive deformation, while the stress is non-constitutive for $\varepsilon = 0$.

The $\sigma - \varepsilon$ plot of **Fig. 1.15** illustrates the idealized behaviour of such a material compared to a typical stress-strain plot. The material is rigid in compression and completely compliant in extension, that is strength and stiffness are assumed to be infinite in compression and zero in tension, so such a material can exhibit an arbitrary stretching at zero energy dissipation price.

It is to be noticed that a positive deformation, coupled with the absence of stress, could be interpreted as a fracture deformation (smeared or concentrated) for which the energy required for crack opening is neglected. The stress due to a positive deformation is zero, and according to the previous definition of elasticity the stress is completely determined by the actual strain. This implies that the behavior in elongation is elastic and perfectly reversible.

On the other hand, the behaviour in compression is non-elastic being modelled as infinitely stiff and strong. This hypothesis of rigidity in compression can be seen as an internal constraint on the strain and consequently the stress required to realize it is non-constitutive (non-elastic). The fact that neither the behaviour in compression nor in tension does require any constitutive parameter is the key factor in giving an essentially geometric strength to ideal masonry structures made of this material. This model is widely diffused since it was first successfully introduced by Heyman (1966) and subsequently taken up and extended in Italy by Di Pasquale (1984) and developed by other members of Italian school of Structural Mechanics.

1.5.2 Model One (NENT)

A further step to refine model zero, is to add a mechanical parameter to it, that is to define an ideal uniaxial behaviour using only one parameter. Potentially two different options, both regarding the behaviour in compression, can be made:

- consider a finite stiffness, still assuming an infinite strength (**Fig. 1.16a**);
- limit the strength, still assuming infinite stiffness (**Fig. 1.16b**).

The first way, as depicted in **Fig. 1.16a**, produce an elastic response (see **Remark 2|1**), whilst the second choice (**Fig. 1.16b**), which adds a limited strength in compression would require a history dependent behaviour. Since, generally, model one is oriented to study a masonry structure under working condition, the first model is commonly preferred to the second and is more diffused. This model is called **Normal Elastic No-Tension** (NENT) and was introduced and widely studied by the Italian school of structural mechanics, see Romano and Romano (1979), Baratta and Toscano (1982), Como and Grimaldi (1985), Romano and Sacco (1985), Castellano (1988), Del Piero (1989), Angelillo (1993).

With model one the strain could be either positive or negative, and the behaviour is elastic: then compressive stress is also constitutive. The material is actually hyperelastic and it is possible to consider a stored elastic energy density: the NENT material is hyperelastic. In 1d, the parameter required to define the model is the elastic modulus E.

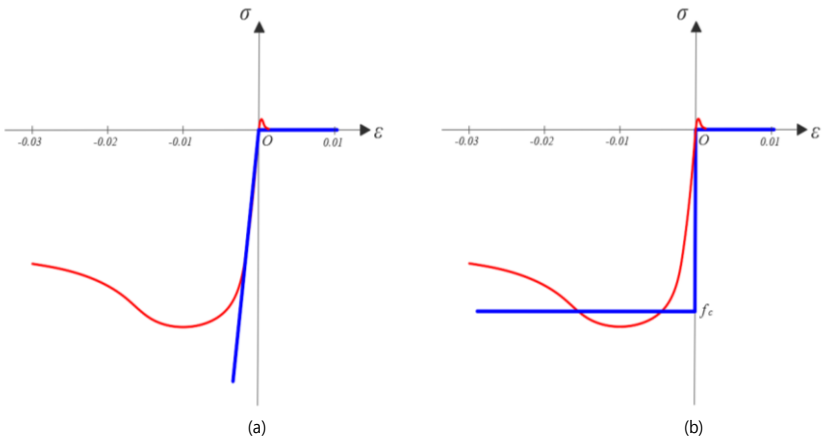

Fig. 1.16 - Two possible 1d models obtained by adding one material parameter. In (a) a finite stiffness is fixed while the strength is still assumed to be infinite. In (b) the strength has a finite value and the stiffness remains infinite.

1.5.3 Model Two (ML)

An additional step, to refine model one (**Fig. 1.16a**), is to add a limit stress in compression. The additional parameter is the compressive strength f_c (**Fig. 1.17**). Model two can be viewed as the ultimate step of refinement for a macroscopic simplified model; for this reason, this model is sometimes referred to as the **Masonry-Like** (ML) model.

The uniaxial behaviour in elongation remains still elastic (reversible), and the strain represents again fracture. The behaviour in compression, instead, is now elastic-perfectly plastic and then the compressive response is still constitutive but incremental and, in this sense, path dependent. Stress is determined by the global strain history. The plastic deformation developed in compression are, obviously, irreversible due to crushing. This evident difference between the behaviour in elongation (reversible) and compression (irreversible) causes the impossibility to cancel the plastic deformations (i.e. crushing) simply reversing the strain. The two

mechanical parameters required to define model 2 are the elastic modulus E and the strength in compression f_c.

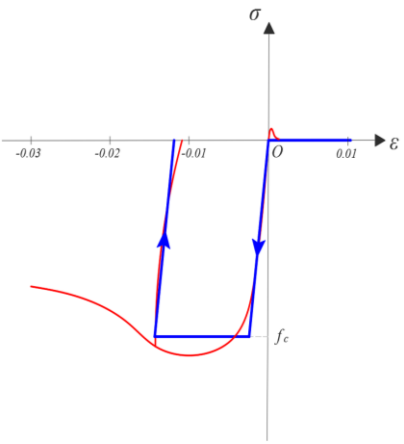

Fig. 1.17 - Typical uniaxial behaviour of model two (blue line). The behaviour for positive strains remains elastic, whilst the behaviour for negative strains becomes elastic-perfectly plastic, and then incremental and path dependent.

■ 1.6 EXTENSION TO CONTINUUM MODELS

The uniaxial behaviour can be extended to continuum models. The No-Tension hypothesis is naturally extended restricting the stress tensor $\boldsymbol{T}$ to belong to the convex cone of the semidefinite negative symmetric tensors Sym^-, namely:

$$\boldsymbol{T} \in Sym^- . \tag{1.2}$$

Concerning the latent strain, that is strain needed to support the unilateral condition on stress, it is necessary to extend the corresponding restrictions case by case. In particular, the assumptions that we will do on the strain is a law of normality on the latent strain with respect to Sym^-. This law of normality allows to apply **Limit Analysis** and its basic tools: the **Safe Theorem** and the **Kinematic Theorem**. For model zero the normality assumption entails the condition that on fracture lines sliding cannot occur. The fulfilling of normality, that can be formulated for the total strain, is equivalent to the two following restrictions: the stress does not work for the anelastic strain $\boldsymbol{E}$ (i.e. the fracture strain), namely:

$$\boldsymbol{T} \cdot \boldsymbol{E} = 0 , \tag{1.3}$$

and the strain $\boldsymbol{E}$ has to belong to the semidefinite positive convex cone Sym^+:

$$\boldsymbol{E} \in Sym^{+} . \tag{1.4}$$

These three-basic assumptions are the minimal ingredients needed to apply Limit Analysis. Also model one and two can be extended to a continuum model. Since, in both cases, the stress fields have to belong to a convex set, the main difference between them stays in the fact that whilst model one (and model zero) is governed by a law of elastic type (non-incremental), instead model two is governed by an evolutionary equation. Model one is commonly extended assuming the behaviour in compression as isotropic and defining a further mechanical parameter: the Poisson ratio ν. The behaviour of the material remains hyperelastic and so path independent. The extension of model two is more involved, requiring to define a limit surface in compression and to introduce a flow rule for the compressive plastic strain rate (modelling crushing). The flow rule could be associated or, taking into account sliding, non-associated (Romano and Sacco, 1985). Whatever be the choice, the response of the material becomes incremental and path dependent.

Remark 2|1. With regards to the continuum extension, the restrictions on $\boldsymbol{T}$, that must belong to the convex cone of the semidefinite negative symmetric tensors Sym^{-} is the basic assumption for all the simplified models. In the first two models, since there is not any limit in compression, the stress tensor $\boldsymbol{T}$ can belong to the whole cone Sym^{-}. In model two, a limit surface is fixed, and the stress tensor $\boldsymbol{T}$ can belong only to a finite subset of Sym^{-}. In **Fig. 1.18** the biaxial failure domain of concrete (Kupfer, 1973) and the convex cone Sym^{-} are depicted for the plane case in the 2d space of the principal stresses. ■

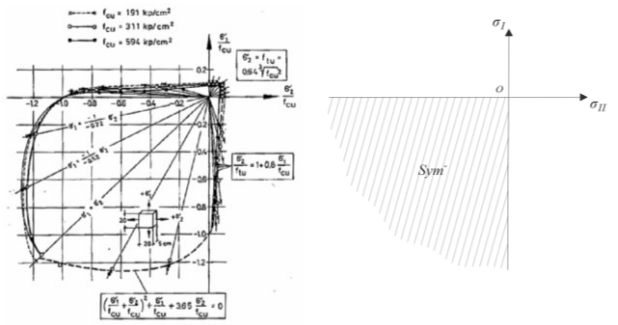

Fig. 1.18 - Two feasible stress domains: in (a) biaxial failure domain of concrete (Kupfer, 1973), in (b) the convex cone Sym^{-}.

■ 1.7 OUTLINE OF CHAPTERS

This dissertation presents a new rigid block model to solve the bvp for NRNT material. The main motivation that substantiates this work consists in the observation that real masonry structures exhibit such rigid block mechanisms when subject to severe settlements or when shaken by serious earthquakes.

An energy criterion, thought of as selection criterion, to search a displacement field which is the solution of the boundary value problem is considered and two numerical methods to approximate the sought solution of the boundary value problem are proposed. With the PR method we search the solution of the bvp in the set of piecewise rigid displacements: the strain coincides with its singular part and is represented by line Dirac deltas: the crack pattern is concentrated along lines. The C^0 method, instead, consists in the approximation of the solution in the set of continuous displacements: the strain admits only of a regular part.

The main result obtained by using the C^0 method is that, even if continuous functions are considered, the solution will often returns an approximate partition of the whole structure into essentially rigid blocks: this results confirms the observation of rigid block mechanisms in real masonry structures.

The dissertation is divided into five parts. In **Part I** (**Chapter 1**, **2**, **3**), the motivation and goals of the research are given. In **Chapter 2** the definition of Normal Linear Elastic material and, as a particular case, the definition of the Normal Elastic No-Tension material, are introduced.

Chapter 3 reviews the main ingredients of the theory of Normal Rigid No-Tension (NRNT) materials: the simplest model that can be used to study masonry structures. The NRNT material represents the natural way to extend the Heyman's theory to masonry structures treated as continua. The main result of this chapter is that the NRNT model allows for the application of the theorems of Limit Analysis and then the safe and kinematic theorems for normal-unilateral materials are briefly recalled, and the compatibility of loads and distortions is discussed.

Part II (**Chapter 4**, **5**) presents the rigid block model, which are proposed. In **Chapter 4**, an energy criterion to select the solution of the boundary value problem, dealt with a displacement approach, is considered and two numerical methods are proposed to approximate the search for the minimal solution, namely the PR method, based on rigid blocks (modelling the cracks as concentrated), and the C^0 method, based on continuous functions (modelling the cracks as smeared).

In **Chapter 5**, some basic applications to trivial benchmark problems of the two numerical methods are proposed. It will be seen that with the application of the C^0 method, the solution will often returns a hint on a partition into rigid blocks. In particular, in the cases in which the fracture lines are difficult to be detected (due to their location or slope), the subdivision suggested by the C^0 approach could be used to start another analysis with the PR method, based on rigid blocks.

Part III (**Chapter 6**, **7**, **8**) presents some applications and results of rigid block model using both approximation methods. In **Chapter 6**, in order to understand the peculiar behavior of old masonry structures, we analyze the masonry arch handling it with the PR method (i.e. rigid blocks). The goal of this Chapter is two-fold: revisiting the old theory of the arch and demonstrating, on a simple and fundamental application, the effectiveness of our method in tackling the structural analysis of masonry. With reference to the last goal we use firstly some well-known results as benchmarks for our PR method and secondly we test our model comparing our results with other ones obtained analytically and reported in the **Appendices** (**D** and **E**).

In **Chapter 7** some applications concerning simple portals and wall with openings analysed using the two numerical methods described in **Chapter 4**, are proposed. In the final part, we present three case studies, developed with the PR method, in order to illustrate the way in which a particular fracture pattern can be identified.

In **Chapter 8**, some applications concerning the analysis of simple masonry structures under horizontal actions are considered. We illustrate how the use of the C^0 method, based on continuous functions, could simplify the problem providing an indication of the structure partition into rigid blocks. Finally as a case study, an arch under horizontal shaking action is considered. We find the static collapse multiplier and then, by using the partition obtained through the PR method, we develop an example of dynamic analysis based on the model of rocking of a rigid block.

In **Part IV**, **Chapter 9** provides general conclusions.

Finally in **Part V**, some appendices are reported. In particular, in **Appendix D** and **E** analytical results concerning the Couplet's problem and the assessment of the horizontal static multiplier (e.g. circular arch with a variable springing angle) are shown.

Chapter 2

CONSTITUTIVE EQUATIONS FOR NENT MATERIAL

Prologue. In this Chapter, we introduce the material restrictions characterizing the Normal Linear Elastic materials and, as a particular case, the constitutive equations of Normal Elastic No-Tension materials , showing that this kind of unilateral material, though unilateral, is elastic and even hyperelastic. Our analysis follows closely the developments given by Del Piero (1989) and Šilhavý (2014). Some peculiarities of NENT materials, related to the stress diffusion are also discussed. Limit analysis for masonry-like materials is presented in **Chapter 3**.

■ 2.1 CONSTITUTIVE EQUATION FOR NORMAL LINEAR ELASTIC MATERIAL

Limit Analysis finds its mathematical fundament on two basic theorems (the **Safe** and the **Kinematic Theorems**) demonstrated by Drucker et al in (1952). Firstly Kooharian (1952), with reference to a concrete arch, and successively Heyman (1966), with regards to a generic masonry structure composed by rigid blocks, used these two theorems with a new twist, by applying them to No-Tension materials. Only some years later, it was demonstrated that these materials can be described by a constitutive equation of elastic type, generated by a variational inequality [(Romano and Romano, 1979), (Del Piero, 1989)], and only recently Del Piero, in two works (1996) and (1998), demonstrates rigorously the applicability of the two fundamental theorems of limit analysis to NENT materials. In this section, after recalling some concepts of constrained elasticity, we discuss Normal Elastic No-Tension materials.

In **Chapter 3** the reader will find the main results related to Limit Analysis for NRNT materials.

The basic general principles, see (Truesdell and Noll, 1965), assumed as postulates governing the mechanical behaviour of materials, are:

- **principle of material frame indifference**: the response of material is independent from the observers;
- **principle of determinism**: the actual stress is determined only by the history of the motion;
- **principle of local action**: which asserts that the actual stress in a point depends only by history of the motion of a *"small neighbourhood"* of the considered particle.

Starting only from these three basic principles and adding only the definition of *internal constraint* (both for stress and deformation), *"a natural way"* to define a *normal elastic material* can be introduced.

Generally, an internal constraint could be thought of as a vector-valued function of a tensor variable. In particular, with reference to a kinematical internal constraint, according to (Truesdell and Noll, 1965) the tensor variable coincides with the history of the deformation gradient $\boldsymbol{F}$ which prescribes the local motion of particles. Obviously, these restrictions have to be constitutive and usually expressed as:

$$\boldsymbol{\gamma}(\boldsymbol{F}) = \boldsymbol{0}\,, \tag{2.1}$$

but in some case these can be written also by a set of scalar inequalities. Below we refer to a scalar-valued function γ of a tensor variable. For a body subjected to internal constraints is necessary to review the principle of determinism. One notices that *"the description of a constraint in mechanics requires fundamentally more information that merely defining a set of permitted configurations"* (Moreau, 1974), indeed a kinematical constraint is always coupled with forces.

Then, the basic question is how to restrict the set of these generalized forces in order to define a constitutive equation for a constrained material. In (Truesdell and Noll, 1965) one extends the virtual work principle from unconstrained material to constrained one by assuming that forces maintaining the constraints are that which do not work for the admissible displacements. This assumption allows to use kinematical internal constraint as constitutive equation and to rearrange the principle of determinism for simple materials: *"in a simple material subject to internal constraints the stress is determined by the history of the deformation gradient only within a stress $\boldsymbol{N}_a$ that does no work in any motion satisfying the constraints"*.

Then, following this reasoning, the stress tensor $\boldsymbol{T}$ can be split into an elastic part $\boldsymbol{T}_e$, determined by the actual value of $\boldsymbol{F}$, and an anelastic one $\boldsymbol{N}_a$, undetermined, which does not work for any virtual motion satisfying the kinematical constraints, namely:

$$\boldsymbol{T} = \boldsymbol{T}_e + \boldsymbol{N}_a \,, \tag{2.2}$$

with

$$\boldsymbol{T}_e = \boldsymbol{T}_e(\boldsymbol{F}) \,, \tag{2.3}$$
$$\boldsymbol{N}_a \cdot (\boldsymbol{F}^* - \boldsymbol{F}) = 0 \,, \tag{2.4}$$

where $(\boldsymbol{F}^* - \boldsymbol{F})$ is a variation of the gradient displacement field compatible with the restriction $\gamma(\boldsymbol{F}) = 0$. Differentiating the equation (2.4), one obtains:

$$\nabla\gamma(\boldsymbol{F}) \cdot (\boldsymbol{F}^* - \boldsymbol{F}) = 0 \,. \tag{2.5}$$

Confronting (2.4) e (2.5), one deduces that $\boldsymbol{N}_a$ is collinear with the $\nabla\gamma(\boldsymbol{F})$. With only these basic hypotheses the principle of determinism, opportune rearranged for simple constrained material, result in an assumption of normality for the undetermined part of stress $\boldsymbol{N}_a$. Moreover, if the restriction is given by an inequality:

$$\gamma(\boldsymbol{F}) \leq 0 \,, \tag{2.6}$$

the condition (2.4), in order to be constitutive, has to be written in the following form:

$$\boldsymbol{N}_a \cdot (\boldsymbol{F}^* - \boldsymbol{F}) \leq 0 \,. \tag{2.7}$$

This constitutes the main characterization of the undetermined part of the stress due to the kinematical restriction (Prager, 1957).

Remark 1|2. The relation (2.7) implies that $\boldsymbol{N}_a$ has to be $\boldsymbol{0}$ in the region:

$$\Omega = \{\boldsymbol{p} \mid \gamma(\boldsymbol{F})|_P < 0\} \,, \tag{2.8}$$

and could be different from zero only on the level set $\partial\Omega$ defined by $\gamma(\boldsymbol{F}) = 0$. Furthermore, considering a point $P \in \partial\Omega$ where $\boldsymbol{N}_a|_P \neq \boldsymbol{0}$, from (2.7) it follows that $\boldsymbol{N}_a$ is normal in P to $\partial\Omega$ and, in particular, it points out. ■

On the other hand, a specular ("dual") reasoning in presence of a unilateral constraint on the stress can be formulated. Likewise, a constraint on the stress is coupled with a restriction on the displacements, or better it causes a restriction of the set of all admissible deformations. Introducing, as made below, a unilateral constraint on stress, it is possible to describe completely and rigorously a particular class of

materials: the normal linear elastic material. By virtue of our needs, below we refer only to small displacements and to small deformations. A scalar unilateral restriction on the Cauchy stress tensor can be expressed by the following scalar-valued function of a tensor variable $\boldsymbol{T}$, namely:

$$\delta(\boldsymbol{T}) \leq 0\,. \tag{2.9}$$

Since it is possible to split the deformation gradient $\boldsymbol{E}$ into an elastic part $\boldsymbol{E}^e$ and an anelastic one $\boldsymbol{\lambda}$:

$$\boldsymbol{E} = \boldsymbol{E}^e + \boldsymbol{\lambda}\,, \tag{2.10}$$

and noting that the actual stress is completely determined only by elastic part $\boldsymbol{E}^e$:

$$\boldsymbol{T} = f(\boldsymbol{E}^e)\,, \tag{2.11}$$

it follows that is possible to characterize the anelastic part $\boldsymbol{\lambda}$ through a specular "normal" relation founded on the assumption that *"the complementary power of is non -positive for any variation of the stress which is compatible with the constraint"* (Del Piero, 1989), namely:

$$\boldsymbol{\lambda} \cdot (\boldsymbol{T}^* - \boldsymbol{T}) \leq 0\,. \tag{2.12}$$

Let $\mathcal{K}$ be the subset of all second-order tensors compatible with the unilateral constraint (2.9), namely:

$$\mathcal{K} = \{\boldsymbol{T}^* \in Lin \mid \delta(\boldsymbol{T}^*) \leq 0\}\,. \tag{2.13}$$

By introducing the well-known fourth-order elasticity tensor:

$$\mathbb{C}\colon Sym \to Sym\,, \tag{2.14}$$

which relates the Cauchy stress tensor only with the elastic part of deformation:

$$\boldsymbol{T} = \mathbb{C}\,\boldsymbol{E}^e. \tag{2.15}$$

It is possible to write the anelastic part of the deformation as:

$$\boldsymbol{\lambda} = \boldsymbol{E} - \mathbb{C}^{-1}\,\boldsymbol{T}\,. \tag{2.16}$$

Thus, the normality assumption can be expressed as:

$$(\boldsymbol{E} - \mathbb{C}^{-1}\boldsymbol{T}) \cdot (\boldsymbol{T}^* - \boldsymbol{T}) \leq 0\,. \tag{2.17}$$

This is a linear variational inequality and the problem can be posed as follows:

"given $\boldsymbol{E} \in Sym$*, find a* $\boldsymbol{T} \in \mathcal{K}$ *satisfied the inequality* (2.17) *for any* $\boldsymbol{T}^* \in \mathcal{K}$*."*

The problem is well-posed since Moreau (1974) demonstrates that:

Theorem 1|2. For any $\boldsymbol{E} \in Sym$, the problem (2.17) admits a unique solution if and only if $\mathcal{K}$ is a convex region and $\mathbb{C}$ is definite positive.

Thus, one defines the *response function* or the *stress function* $\widehat{\boldsymbol{T}}$

$$\widehat{\boldsymbol{T}}: \boldsymbol{E} \in Sym \to \widehat{\boldsymbol{T}}(\boldsymbol{E}) \in Sym\,, \tag{2.18}$$

such that to any $\boldsymbol{E} \in Sym$ associate the unique solution $\widehat{\boldsymbol{T}}(\boldsymbol{E}) \in \mathcal{K}$ of the linear variation inequality (2.17).

The definition of a Normal Linear Elastic Material, now, can be introduced:

Definition 1|2. A **Normal Linear Elastic Material** is a constrained material characterized by the linear variational inequality

$$(\boldsymbol{E} - \mathbb{C}^{-1}\,\boldsymbol{E}^e) \cdot (\boldsymbol{T}^* - \boldsymbol{T}) \leq 0 \quad \forall\, \boldsymbol{T}^* \in \mathcal{K}\,, \tag{2.19}$$

where $\mathcal{K}$ is a closed convex region of Sym and $\mathbb{C}$ is a positive definite fourth order tensor.

Remark 2|2. The term *"Normal"* in the previous definition is due to the normal assumption $\boldsymbol{\lambda} \cdot (\boldsymbol{T}^* - \boldsymbol{T}) \leq 0$ whilst *"Linear"* derives from the linearity of the variational inequality and, in this sense, it does not depend of the response function. ■

■ 2.2 CONSTITUTIVE EQUATIONS FOR NORMAL ELASTIC NO-TENSION MATERIAL

In this section, one introduces the model commonly adopted for masonry-like material (i.e. NENT model) as a particularization of a Linear Normal Elastic Material. What we would like to do is to catch a twofold behaviour of the material: the absence of any tensile strength and the subsequent possibility to exhibit some fracture strain: then, before defining the NENT class, the main objects needed to formulate a precise characterization should be introduced, namely:

1. the stress tensor $\boldsymbol{T}$ and consequently the set $\mathcal{K}$ of the admissible stresses;
2. the infinitesimal strain tensor $\boldsymbol{E}$;
3. a linear map between $\boldsymbol{T}$ and $\boldsymbol{E}$;
4. a normality rule.

* * *

1. First of all, since we consider a material which does not support tensile stresses, the Cauchy stress tensor $\boldsymbol{T}$ has to be semidefinite (see **Section 1.6**), namely:

$$\boldsymbol{T} \in Sym^{-} , \tag{2.20}$$

and this implies that all the eigenvalues are non-positive:

$$\boldsymbol{T} = \sigma_1 \boldsymbol{n_1} \otimes \boldsymbol{n_1} + \sigma_2 \boldsymbol{n_2} \otimes \boldsymbol{n_2} + \sigma_3 \boldsymbol{n_3} \otimes \boldsymbol{n_3} \quad , \quad \sigma_1, \sigma_2, \sigma_3 \in \mathbb{R}_0^{-}. \tag{2.21}$$

This result suggests to define the set $\mathcal{K}$ as:

$$\mathcal{K} = Sym^{-} , \tag{2.22}$$

and the internal constraint, introduced before through the generalized scalar relation $\delta(\boldsymbol{T}^*) \leq 0$ (2.9), here could be considered as a function of the principal stresses. It is easy to see that $\mathcal{K} = Sym^{-}$ is a closed convex cone.

* * *

2. Regarding the infinitesimal strain tensor $\boldsymbol{E} \in Sym$, one supposes to split it into two parts: an elastic part $\boldsymbol{E}^e$ and an anelastic one $\boldsymbol{E}^a$:

$$\boldsymbol{E} = \boldsymbol{E}^e + \boldsymbol{E}^a , \tag{2.23}$$

where the anelastic part could be thought of as the fracture part (also called "latent strain", i.e. the strain needed to sustain the constraint on stresses). It is noticed that the elastic part defines completely the actual stress $\boldsymbol{T}$ as pointed out better below.

* * *

3. One supposes that there is a linear relationship between the stress tensor $\boldsymbol{T}$ and the elastic deformation $\boldsymbol{E}^e$:

$$\widehat{\boldsymbol{T}}: \boldsymbol{E}^e \in Sym \to \mathbb{C}\, \boldsymbol{E}^e \in Sym^{-}\,, \tag{2.24}$$

where $\mathbb{C}: Sym \to Sym$ is the well known fourth-order tensor of elastic constants, which is also a positive definite symmetric tensor characterized by the following proprieties:

$$\boldsymbol{A} \cdot \mathbb{C}\, \boldsymbol{A} \geq 0 \quad \forall\, \boldsymbol{A} \in Sym\,, \tag{2.25}$$

$$\boldsymbol{A} \cdot \mathbb{C}\, \boldsymbol{A} = 0 \Leftrightarrow \boldsymbol{A} = \boldsymbol{0}\,, \tag{2.26}$$

$$\boldsymbol{A}_1 \cdot \mathbb{C}\, \boldsymbol{A}_2 = \boldsymbol{A}_2 \cdot \mathbb{C}\, \boldsymbol{A}_1 \quad \forall\, \boldsymbol{A}_1, \boldsymbol{A}_2 \in Sym\,. \tag{2.27}$$

By using the elasticity tensor $\mathbb{C}$, it is possible to introduce the elastic energetic scalar product $\langle \cdot\,, \cdot \rangle_E$ and the energetic norm $|\cdot|$ defined as:

$$\langle\, \boldsymbol{A}_1\,, \boldsymbol{A}_2\, \rangle_E = \boldsymbol{A}_1 \cdot \mathbb{C}\, \boldsymbol{A}_2\,, \tag{2.28}$$

$$|\boldsymbol{A}| = \sqrt{\langle\, \boldsymbol{A}\,, \boldsymbol{A}\, \rangle_E} = \sqrt{\boldsymbol{A} \cdot \mathbb{C}\boldsymbol{A}}\,, \tag{2.29}$$

for all $\boldsymbol{A}, \boldsymbol{A}_1, \boldsymbol{A}_2 \in Sym$, and where one puts in evidence the dependence of the energetic and scalar norm from elastic part.

* * *

4. Finally, it remains to define a rule which allows to characterize the anelastic part of the deformation $\boldsymbol{E}^a$. In particular, one supposes that $\boldsymbol{E}^a$ verifies the following hypotheses of normality:

$$(\boldsymbol{T} - \boldsymbol{T}^*) \cdot \boldsymbol{E}^a \geq 0 \qquad \forall\, \boldsymbol{T}^* \in \mathcal{K}\,. \tag{2.30}$$

Considering the previous three step-points, relation (2.30) can be rewritten as:

$$(\boldsymbol{T} - \boldsymbol{T}^*) \cdot (\boldsymbol{E} - \boldsymbol{E}^e) \geq 0 \qquad \forall\, \boldsymbol{T}^* \in \mathcal{K}\,, \tag{2.31}$$

or

$$(\boldsymbol{T} - \boldsymbol{T}^*) \cdot (\boldsymbol{E} - \mathbb{C}^{-1}\boldsymbol{T}) \geq 0 \qquad \forall\, \boldsymbol{T}^* \in \mathcal{K}\,. \tag{2.32}$$

* * *

Finally, the previous four main points can be symbolically collected into the following system:

$$(\mathrm{A}):\begin{cases} \boldsymbol{T} \in Sym^{-} \\ \boldsymbol{E} = \boldsymbol{E}^{e} + \boldsymbol{E}^{a} \\ \boldsymbol{T} = \mathbb{C}\,\boldsymbol{E}^{e} \\ (\boldsymbol{T} - \boldsymbol{T}^{*}) \cdot \boldsymbol{E}^{a} \geq 0 \quad \forall\, \boldsymbol{T}^{*} \in Sym^{-} \end{cases}. \tag{2.33}$$

The problem is well-posed since the following theorem holds:

Theorem 2|2. If $\boldsymbol{E} \in Sym$, there exists a unique triplet $(\boldsymbol{T}, \boldsymbol{E}^{e}, \boldsymbol{E}^{a})$ solution of the problem (A). ■

Now it is possible to introduce a rigorous definition of the Normal Elastic No-Tension Material.

Definition 2|2. A **Normal Elastic No-Tension** (**NENT**) **Material** is a constrained material characterized by the normality assumption:

$$(\boldsymbol{T} - \boldsymbol{T}^{*}) \cdot (\boldsymbol{E} - \boldsymbol{E}^{e}) \geq \boldsymbol{0} \qquad \forall\, \boldsymbol{T}^{*} \in \mathcal{K}\,, \tag{2.34}$$

where $\mathcal{K} = Sym^{-}$ is a closed convex. ■

This is an essential and rigorous way to introduce this concept, but there are other alternatives to do it. Indeed, it is possible to demonstrate that if and only if the set of admissible stresses $\mathcal{K}$ is equal to Sym^{-} then the two following relations:

$$(\boldsymbol{T} - \boldsymbol{T}^{*}) \cdot \boldsymbol{\lambda} \geq \boldsymbol{0} \;\; \forall\, \boldsymbol{T}^{*} \in Sym^{-} \;\; \Leftrightarrow \;\; \boldsymbol{\lambda} \in Sym^{+} \;\; and \;\; \boldsymbol{T} \cdot \boldsymbol{\lambda} = 0\,, \tag{2.35}$$

are equivalent. Then, a NENT can be also characterized by the following system of relations:

$$(\mathrm{B}):\begin{cases} \boldsymbol{T} \in Sym^{-}, \boldsymbol{\lambda} \in Sym^{+} \\ \boldsymbol{E} = \boldsymbol{E}^{e} + \boldsymbol{\lambda} \\ \boldsymbol{T} = \mathbb{C}\,\boldsymbol{E}^{e} \\ \boldsymbol{T} \cdot \boldsymbol{\lambda} = 0 \end{cases}. \tag{2.36}$$

Furthermore, there exists another equivalent geometrical characterization, according to which a NENT material is defined starting only from these three relations:

$$(\mathrm{C}):\begin{cases} \boldsymbol{E} = \boldsymbol{E}^{e} + \boldsymbol{\lambda} \\ \boldsymbol{T} = \mathbb{C}\,\boldsymbol{E}^{e} \\ \boldsymbol{E}^{e} = P(\boldsymbol{E}) \end{cases}, \tag{2.37}$$

where

$$P: \boldsymbol{E} \in Sym \rightarrow P(\boldsymbol{E}) \in \mathbb{C}^{-1}(Sym^{-}) \,, \tag{2.38}$$

is the projection from Sym onto $\mathbb{C}^{-1}(Sym^{-})$ with respect to the energetic scalar product $\langle \cdot \,, \cdot \rangle_E$. This is a very interesting characterization, because, on one hand, it condenses analytically in a single relation both the condition $\boldsymbol{T} \cdot \boldsymbol{\lambda} = 0$ and the two restrictions, one on the stress, $\boldsymbol{T} \in Sym^{-}$, and the other one on the anelastic part of deformation, namely $\boldsymbol{\lambda} \in Sym^{+}$, but on the other hand it characterizes in a new geometrical way, the behaviour of such a material. Can be useful to demonstrate the equivalence between relations (A) and (C).

Proof. Assuming that characterization (C) holds, we want demonstrate that (C) ⇒ (A). In particular, being (A.2) and (A.3) equal to (C.1) and (C.2), it remains to demonstrate that (C.3) implies, at the same time, both (A.1) and (A.4). Since $\boldsymbol{E}^e \in \mathbb{C}^{-1}(Sym^{-})$ is the projection of $\boldsymbol{E} \in Sym$ onto the space $\mathbb{C}^{-1}(Sym^{-})$ with respect to the energetic scalar product $\langle \cdot \,, \cdot \rangle_E$, recalling $\boldsymbol{T} = \mathbb{C}\, \boldsymbol{E}^e$, one obtains that $\boldsymbol{T} \in Sym^{-}$ (A.1.1). It is to be noted that, being Sym^{-} a closed convex cone, even $\mathbb{C}^{-1}(Sym^{-})$ is a closed convex cone. Thus, being $\boldsymbol{E}^e$the projection of $\boldsymbol{E}$ onto the closed convex cone $\mathbb{C}^{-1}(Sym^{-})$, it results:

$$\langle \boldsymbol{E} - \boldsymbol{E}^e \,, \boldsymbol{A} \rangle_E \leq 0 \quad \forall \boldsymbol{A} \in \mathbb{C}^{-1} Sym^{-} \,, \tag{2.39}$$

$$\langle \boldsymbol{E} - \boldsymbol{E}^e \,, \boldsymbol{E}^e \rangle_E = 0 \,. \tag{2.40}$$

Using the map $\mathbb{C}^{-1}: Sym \rightarrow Sym$, it is possible to identify an element $\boldsymbol{A}$ of the $\mathbb{C}^{-1} Sym^{-}$ cone with a generic element $\boldsymbol{T}^*$ belong to the Sym^{-} cone through the relation $\boldsymbol{A} = \mathbb{C}^{-1} \boldsymbol{T}^*$; then (2.39) and (2.40) can be rewritten as follows:

$$\langle \boldsymbol{E} - \boldsymbol{E}^e \,, \mathbb{C}^{-1} \boldsymbol{T}^* \rangle_E \leq 0 \quad \forall\, \boldsymbol{T}^* \in Sym^{-} \,, \tag{2.41}$$

$$\langle \boldsymbol{E} - \boldsymbol{E}^e \,, \boldsymbol{E}^e \rangle_E = 0 \,. \tag{2.42}$$

From (2.41) we obtain:

$$(\boldsymbol{E} - \boldsymbol{E}^e) \cdot \boldsymbol{T}^* \leq 0 \quad \forall\, \boldsymbol{T}^* \in Sym^{-} \,, \tag{2.43}$$

and taking into account that $\boldsymbol{E} = \boldsymbol{E}^e + \boldsymbol{\lambda}$, it follows:

$$\boldsymbol{\lambda} \cdot \boldsymbol{T}^* \leq 0 \quad \forall\, \boldsymbol{T}^* \in Sym^{-} \,, \tag{2.44}$$

which implies that $\boldsymbol{\lambda} \in Sym^{+}$ (A.1.2). From the second one, similarly, one obtains $\boldsymbol{\lambda} \cdot \boldsymbol{E}^e = 0$, and considering that $\boldsymbol{E}^e = \mathbb{C}^{-1} \boldsymbol{T}$ since $\boldsymbol{T} \in Sym^{-}$ it reuslts $\boldsymbol{\lambda} \cdot \boldsymbol{T} = 0$ and then also (A.4) is proved. ■

Remark 3|2. Since the existence and uniqueness of the projection of a point onto a convex cone is a proved mathematical result, $\boldsymbol{E}^e$ exists and is unique, then even the uniqueness and of $\boldsymbol{\lambda}$ and $\boldsymbol{T}$ follows from (A.2) and (A.3): the existence and uniqueness of the triplet $(\boldsymbol{T}, \boldsymbol{E}^e, \boldsymbol{\lambda})$, which completely characterized the behavior of NENT, then follows. ■

Remark 4|2. According to the characterization (C), using the energetic scalar product $\langle \cdot , \cdot \rangle_E$ above defined, it results:

$$(\boldsymbol{T} - \boldsymbol{T}^*) \cdot \boldsymbol{\lambda} \geq 0 \quad \forall\, \boldsymbol{T}^* \in Sym^- \;\Leftrightarrow\; \langle \boldsymbol{E}^e - \boldsymbol{E}^* , \boldsymbol{\lambda} \rangle_E \geq 0 \quad \forall\, \boldsymbol{E}^* \in \mathbb{C}^{-1} Sym^- , \tag{2.45}$$

and recalling that $\boldsymbol{\lambda} = (\boldsymbol{E} - \boldsymbol{E}^e)$, it follows:

$$(\boldsymbol{E} - \boldsymbol{E}^e) \in Norm(\mathbb{C}^{-1} Sym^-, \boldsymbol{E}^e) , \tag{2.46}$$

that is the fracture part $\boldsymbol{\lambda}$ belongs to the normal cone to $\mathbb{C}^{-1} Sym^-$ at $\boldsymbol{E}^e$. ■

Remark 5|2. The anelastic part of the deformation $\boldsymbol{\lambda}$ is also called "the fracture tensor": this term derives from the fact that it is directly connected to the fractures appearing in a body in those zones where the unilateral constraint on stress is verified with the equality sign. ■

Remark 6|2. For NENT, the response function $\widehat{\boldsymbol{T}}$ is the map

$$\widehat{\boldsymbol{T}} : \boldsymbol{E} \in Sym \rightarrow \widehat{\boldsymbol{T}}(\boldsymbol{E}) \in Sym , \tag{2.47}$$

which to any $\boldsymbol{E} \in Sym$ associates the unique solution $\widehat{\boldsymbol{T}}(\boldsymbol{E}) \in Sym$ of this linear variation inequality

$$(\boldsymbol{T} - \boldsymbol{T}^*) \cdot (\boldsymbol{E} - \mathbb{C}\, \boldsymbol{E}^e) \geq \boldsymbol{0} \qquad \forall\, \boldsymbol{T}^* \in Sym^- . \tag{2.48}$$

In particular, it results $\widehat{\boldsymbol{T}}(\boldsymbol{E}) = \mathbb{C}(\boldsymbol{\lambda} - \boldsymbol{E}) = \mathbb{C}\, \boldsymbol{E}^e$. Furthermore, $\widehat{\boldsymbol{T}}$ is homogeneous of degree one, monotone and Lipschitz continuous. ■

Remark 7|2. Since $\boldsymbol{T} \in Sym^-$ and $\boldsymbol{T} \cdot \boldsymbol{\lambda} = 0$, it results $\boldsymbol{\lambda} \cdot \boldsymbol{T} = 0$ also: then $\boldsymbol{\lambda}$ and $\boldsymbol{T}$ commute and then they are also coaxial. This is a geometrical result, independent of the particular elastic behaviour. Furthermore, it can be proved that if the tensor $\mathbb{C}$ is isotropic all these three tensors are coaxial: $\boldsymbol{T}$, $\boldsymbol{E}$ and $\boldsymbol{\lambda}$. Indeed, for an isotropic material, $\mathbb{C}$ has the following form

$$\mathbb{C}\boldsymbol{E}^e = \boldsymbol{2}\lambda tr(\boldsymbol{E}^e)\boldsymbol{1} + 2\mu \boldsymbol{E}^e, \tag{2.49}$$

where $\boldsymbol{1} \in Lin$ is the second order identity tensor, and λ and μ are the Lame moduli satisfying $\mu > 0$ and $\lambda + \mu > 0$: using this expression, through some algebraic passages, the coaxiality between $\boldsymbol{T}$, $\boldsymbol{E}$ and $\boldsymbol{\lambda}$ can be easily achieved. ■

Remark 8|2. Using the response function $\widehat{\boldsymbol{T}} : \boldsymbol{E} \in Sym \rightarrow \widehat{\boldsymbol{T}}(\boldsymbol{E}) \in Sym$, a scalar-valued tensor function can be defined:

$$\widehat{w}: \boldsymbol{E} \in Sym \to \frac{1}{2}\,\widehat{\boldsymbol{T}}(\boldsymbol{E}) \cdot \boldsymbol{E}^e \in \mathbb{R}\,, \tag{2.50}$$

$\widehat{w}$ is known as the stored energy. Recalling $\widehat{\boldsymbol{T}}(\boldsymbol{E}) \cdot \boldsymbol{E}^e = \langle \boldsymbol{E}^e\,, \boldsymbol{E}^e \rangle_E \geq 0$ and

$$P: \boldsymbol{E} \in Sym \to P(\boldsymbol{E}) \in \mathbb{C}^{-\mathbf{1}}(Sym^-)\,, \tag{2.51}$$

is the projection from Sym onto $\mathbb{C}^{-\mathbf{1}}(Sym^-)$ with respect to the energetic scalar product $\langle \cdot\,,\ \cdot \rangle_E$. ■

Remark 9|2. Besides the compatibility of loads, which we will discuss in the **Chapter 3**, it is worth noting that one of the main consequences of the no-tension assumption is the incompatibility of masonry with the phenomenon of load scattering. This is depicted in **Fig. 2.1**, where a body, occupying a domain Ω, is subjected, only on the boundary, to two loads. The stress vanishes outside any cylinder $\overline{\Omega}$ whose bases contain the loaded portions.

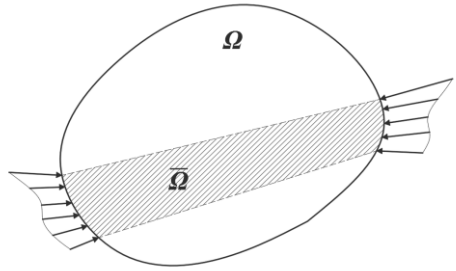

Fig. 2.1 - The no-tension assumption causes the lack of the diffusion of internal stresses. The stress vanishes in the region $\Omega \backslash \overline{\Omega}$. The Saint Venant's postulates does not hold for a NENT material.

Consequently, the Saint Venant's postulate does not hold, and then the lack of the diffusion of internal stresses makes the internal resistant structure depending only on the geometry. In **Fig. 2.2** a comparison, using transmission photoelasticity, between the stress diffusion in an elastic body and in a NENT material is depicted. It is to be noted that a highly localized stress percolation is visible in the masonry model.

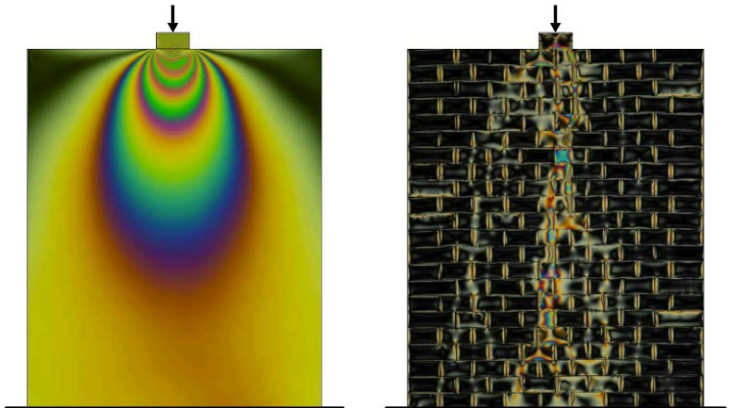

Fig. 2.2 - A comparison, using transmission photoelasticity, between the stress diffusion in an elastic body (a) and in a model (NENT) of masonry (b) in which a highly localized stress percolation is visible. Drawing from website of University of Trento, Italy Department of Civil, Environmental and Mechanical Engineering.

As early as the 19th century, Viollet–Le Duc in the XIX grasped this behaviour: *"The loads determine the resistant masonry structure within the actual masonry body: if the loads change, the resistant masonry structure will consequently change"* (Viollet-le-Duc, 1858–1868). Four examples of the internal resistant structure in a masonry wall subjected to different type of load conditions are reported in **Fig. 2.3**. ■

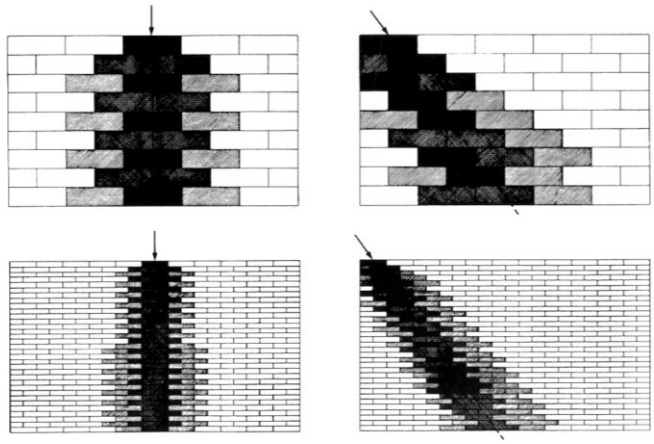

Fig. 2.3 - Drawings from Giuffrè (1993): four examples of the internal resistant structure in a masonry wall subjected to different types of loads are depicted.

Chapter 3

THE NRNT MODEL: LIMIT ANALYSIS

Prologue. In this Chapter, we introduce the main ingredients of the theory of Normal Rigid No-Tension (NRNT) materials: the simplest model that can be used to study masonry structures. As remarked in **Chapter 1**, this model represents a way for extending Heyman's theory to masonry structures treated as continua. After introducing the restrictions defining the NRNT model, the definitions of statically admissible and kinematically admissible fields are given. The NRNT model allows for the application of the theorems of Limit Analysis. Notice that these theorems are valid as long as normality of the anelastic strain (or of the anelastic strain rate) to the limit surface is enforced, then, in particular, they are also valid for NENT materials. The safe and kinematic theorems for normal-unilateral materials are briefly recalled, and the compatibility of loads and distortions is discussed.

■ 3.1 NRNT MASONRY-LIKE MATERIAL

A 2d masonry structure S is modelled as a continuum occupying a domain Ω of the 2d Euclidean space $\mathcal{E}^2$. The stress inside Ω is denoted $\boldsymbol{T}$ and the displacement of material points $\boldsymbol{x}$ belonging to Ω is denoted $\boldsymbol{u}$. We restrict to the case of small strains and displacements and adopt the infinitesimal strain $\boldsymbol{E}$ as the strain measure.

We call masonry-like material a continuum that is **Normal Rigid No-Tension** (Angelillo, 2014b) in the sense defined by the following restrictions

$$\boldsymbol{T} \in Sym^{-} \ , \ \boldsymbol{E} \in Sym^{+} \ , \ \boldsymbol{T} \cdot \boldsymbol{E} = 0 \ , \tag{3.1}$$

Sym^-, Sym^+ being the convex cones of negative semidefinite and positive semidefinite symmetric tensors.

Under these restrictions, the material satisfies a law of normality with respect to the cone Sym^- of the feasible stresses, in the sense that restrictions (3.1) are equivalent to:

$$\boldsymbol{T} \in Sym^- \ , \ (\boldsymbol{T} - \boldsymbol{T}^*) \cdot \boldsymbol{E} \geq 0 \ , \ \forall \boldsymbol{T}^* \in Sym^- \ , \tag{3.2}$$

and, dually,

$$\boldsymbol{E} \in \boldsymbol{Sym}^+ \ , \ (\boldsymbol{E} - \boldsymbol{E}^*) \cdot \boldsymbol{T} \geq \boldsymbol{0} \ , \ \forall \boldsymbol{E}^* \in \boldsymbol{Sym}^+ \ . \tag{3.3}$$

In particular, the previous assumptions represent the essential ingredients for proving the validity of the theorems of Limit Analysis, see also (Angelillo et al, 2014), (Fortunato et al, 2014) and (Fortunato et al, 2016).

Remark 1|3. The theorems of Limit Analysis are valid if a normality law of the anelastic strain (or strain rate) to the limit surface is enforced. So they are equally valid for NENT and ML materials. ■

We observe that the restrictions (3.1) essentially translate into mathematical terms and extrapolate to 2d-3d continua the Heyman's assumptions on masonry behaviour (Heyman, 1966), namely:

(i) Stone has no tensile strength;
(ii) The compressive strength of stone is effectively infinite;
(iii) Sliding of one stone upon another cannot occur.

Remark 2|3. Though Heyman analysis is not concerned with a continuum, condition (3.1)[1] appears as a natural extension of assumptions (i), (ii). The presence of elastic deformations in compression, even if is not explicitly excluded, is never considered by Heyman. For what concerns the law of normality, Heyman formulates it for characteristics rather than for stresses. Consequently, the role of and the restrictions on the latent strain, that is the deformation associated to the unilateral constraint on stress, are not defined. In the context of the continuum model, assumption (iii), that is the no-sliding assumption, is implied by normality, but the no-sliding assumption, by itself, is not sufficient to prove normality in this broader context. ■

■ 3.2 DISPLACEMENT AND STRAIN FIELDS

The displacement field $\boldsymbol{u}$ is compatible if, in addition to being regular enough for the corresponding strain $\boldsymbol{E}(\boldsymbol{u})$ to exist, satisfies the boundary conditions on the constrained part $\partial\Omega_D$ of the boundary, namely:

$$\boldsymbol{u} = \bar{\boldsymbol{u}} \text{ on } \partial\Omega_D \,. \tag{3.4}$$

Adopting a variational formulation, for linearly elastic bodies the basic request is that $\boldsymbol{E}$ be square summable, namely:

$$\sqrt{\int_\Omega \boldsymbol{E}\cdot\boldsymbol{E}da} < \infty \,. \tag{3.5}$$

Indeed, for some rigid, perfectly plastic (or rigid unilateral) materials, it is sufficient to assume that $\boldsymbol{E}$ be summable:

$$\int_\Omega \sqrt{\boldsymbol{E}\cdot\boldsymbol{E}}da < \infty \,. \tag{3.6}$$

Thus, the set of competing functions has to be enlarged to bounded measures, that is to summable distributions $\widetilde{\boldsymbol{E}}$; then the displacement $\boldsymbol{u}$ can admit finite discontinuities, i.e. $\boldsymbol{u}$ can be a function with bounded variation. The summability of $\nabla\boldsymbol{u}$ would imply that $\boldsymbol{u} \in BV(\Omega)$ exactly. But $\boldsymbol{E}$ is only the symmetric part of $\nabla\boldsymbol{u}$, then $\boldsymbol{u}$ has to belong to a larger space: $BD(\Omega)$. The strain corresponding to $\boldsymbol{u}$ is again a bounded measure

$$\int_\Omega \left|\widetilde{\boldsymbol{E}}\right| da < \infty \,. \tag{3.7}$$

which, in general, can be decomposed uniquely into the sum of two parts, namely:

$$\widetilde{\boldsymbol{E}} = \widetilde{\boldsymbol{E}}^r + \widetilde{\boldsymbol{E}}^s \,, \tag{3.8}$$

where $\widetilde{\boldsymbol{E}}^r$ is absolutely continuous with respect to the area measure (that is $\widetilde{\boldsymbol{E}}^r$ is a density per unit area) and $\widetilde{\boldsymbol{E}}^s$ is the singular part. $\widetilde{\boldsymbol{E}}^s$ has support on the union of a set of linear 1d measure (the jump set of $\boldsymbol{u}$) and a set of fractional measure. In what follows, we restrict to deformations $\widetilde{\boldsymbol{E}}$ whose singular part is concentrated on a finite number of regular arcs, that is bounded measures admitting on such curves a density $\widetilde{\boldsymbol{E}}^s$ with respect to the length measure (that is special bounded measures with empty Cantor part).

Remark 3|3. From (Angelillo, 2014b). If $\boldsymbol{u} \in BD(\Omega)$, that is $\boldsymbol{u}$ can be discontinuous, the boundary condition $\boldsymbol{u} = \bar{\boldsymbol{u}}$ on $\partial\Omega_D$ makes no sense. A way to keep alive the boundary condition of Dirichlet type is to identify the masonry body rather than with the domain Ω (an open set) with the set $\Omega \cup \partial\Omega$ and to assume that $\boldsymbol{u}$ must comply with the constraint $\boldsymbol{u} = \bar{\boldsymbol{u}}$ on the skin $\partial\Omega_D$, admitting possible singularities of the strain at the constrained boundary. Then, from here on, we shall deviate from standard notation referring to Ω as to the set $\Omega \cup \partial\Omega$. Given the displacement field $\boldsymbol{u}$ of $\boldsymbol{x}$, by taking the gradient of $\boldsymbol{u}$, in a classical sense if $\boldsymbol{u}$ is regular, and in a generalized sense if $\boldsymbol{u}$ is singular, the strain $\boldsymbol{E}(\boldsymbol{u})$ is derived. Vice versa, if $\boldsymbol{E}$ of $\boldsymbol{x}$ is given, the possibility of integrating the components $E_{\alpha\beta}$ to get the (possibly discontinuous) components u_α of $\boldsymbol{u}$, is submitted to the necessary compatibility conditions (also sufficient if Ω is simply connected):

$$\boldsymbol{E}_{11,22} + \boldsymbol{E}_{22,11} - 2\boldsymbol{E}_{12,12} = 0\,, \tag{3.9}$$

where a comma followed by an index, say α, means differentiation with respect to x_α. The reader will see in what follows, that, on admitting discontinuous displacements, this condition can be reinterpreted in a generalized sense and applied (with some care), also to discontinuous, and even singular, strains. ■

3.2.1 Latent Strain

For masonry-like (NRNT) materials the only possible strain is the anelastic strain. In particular, the material is rigid in compression, that is cannot exhibit any shortening in any direction since from (3.1)^2 it descends

$$\boldsymbol{E} \cdot \boldsymbol{n} \otimes \boldsymbol{n} \;\geq 0\;,\quad \forall \boldsymbol{n} \in \mathcal{E}^2\,. \tag{3.10}$$

The strain $\boldsymbol{E}$ is a positive semi-definite tensor field doing no work for the corresponding stress, and representing detachment fractures. As exposed in **Chapter 2**, $\boldsymbol{E}$ could be viewed as a sort of "reaction" deformation associated to the constraint on stress $\boldsymbol{T} \in Sym^-$, and, therefore, is also called latent strain.

Since we consider displacement fields $\boldsymbol{u}$ having finite discontinuities on a finite number of regular arcs Γ, the strain $\boldsymbol{E}(\boldsymbol{u})$ consists of a regular part $\boldsymbol{E}^r$, that is a diffuse deformation over $\Omega - \Gamma$, and a singular part $\boldsymbol{E}^s$ in the form of a line Dirac delta, concentrated on Γ, then either smeared cracks ($\boldsymbol{E}^r$) or concentrated ones ($\boldsymbol{E}^s$) are allowed. Displacement fields, admitting finite jumps, have to belong to the set of functions of Bounded Variation ($BV(\Omega)$); the gradient of a BV function, and then the

strain $\boldsymbol{E}$, is a bounded measure. In general, bounded measures can be decomposed into the sum of two parts

$$\boldsymbol{E} = \boldsymbol{E}^r + \boldsymbol{E}^s \ , \tag{3.11}$$

where $\boldsymbol{E}^r$ is absolutely continuous with respect to the area measure (that is $\boldsymbol{E}^r$is a density per unit area) and $\boldsymbol{E}^s$ is the singular part. For simplicity only bounded measures whose singular part is concentrated on a finite number of regular arcs, that is bounded measures admitting on such curves a density $\boldsymbol{E}^s$ with respect to the length measure, are usually considered.

3.2.2 Concentrated Strain

If the displacements exhibit a jump discontinuity on a regular curve Γ, on such a curve the strain is concentrated, i.e. it is a line Dirac delta whose intensity is the jump of $\boldsymbol{u}$ across Γ. By denoting $\boldsymbol{t}, \boldsymbol{n}$ the unit tangent and the unit normal to Γ, and calling, Ω^-, Ω^+ the two parts on the two sides of Γ, Ω^+ being the part toward which $\boldsymbol{n}$ points, the jump of $\boldsymbol{u}$ on Γ can be written as

$$[\boldsymbol{u}] = \boldsymbol{u}^+ - \boldsymbol{u}^- \ , \tag{3.12}$$

and decomposed into normal and tangential components:

$$[\boldsymbol{u}] = w\,\boldsymbol{t} + v\,\boldsymbol{n} \ , \ w = [\boldsymbol{u}]\cdot\boldsymbol{t} \ , \ v = [\boldsymbol{u}]\cdot\boldsymbol{n} \ . \tag{3.13}$$

Calling $\delta(\Gamma)$ the unit line Dirac delta with support on Γ, the strain along Γ can be written as

$$\boldsymbol{E} = v\,\delta(\Gamma)\,\boldsymbol{n}\otimes\boldsymbol{n} + \tfrac{1}{2}w\,\delta(\Gamma)\,(\boldsymbol{t}\otimes\boldsymbol{n} + \boldsymbol{n}\otimes\boldsymbol{t}) \ . \tag{3.14}$$

For masonry-like (NRNT) materials the strain must be positive semidefinite, then, in the plane case, it must be:

$$tr\boldsymbol{E} \geq 0 \ , \ det\boldsymbol{E} \geq 0 \ , \tag{3.15}$$

from which

$$v \geq 0 \ , \ \ -\tfrac{1}{4}w^2 \geq 0 \ , \tag{3.16}$$

that is the two parts Ω^-, Ω^+ can separate but not compenetrate and the sliding w must vanish. So, for NRNT materials, on a fracture line Γ, it must be

$$\boldsymbol{E} = v\,\delta(\Gamma)\,\boldsymbol{n}\otimes\boldsymbol{n}\ ,\quad v \geq 0\ , \tag{3.17}$$

and then we may see that Heyman's assumption (iii) follows from (3.1)[2].

■ 3.3 STRESS FIELDS

It is assumed that the body, occupying the domain Ω of $\mathbb{R}^2$, is loaded by given tractions $\overline{\boldsymbol{s}}$ on the complementary part $\partial\Omega_N = \partial\Omega - \partial\Omega_D$ of the boundary. A stress field $\boldsymbol{T}$ is said to be equilibrated with the given actions $(\overline{\boldsymbol{s}}, \boldsymbol{b})$, if it satisfies the equilibrium equations:

$$div\boldsymbol{T} + \boldsymbol{b} = \boldsymbol{0} \tag{3.18}$$

and the traction boundary conditions

$$\boldsymbol{T}\boldsymbol{m} = \overline{\boldsymbol{s}}\ \ on\ \partial\Omega_N\ , \tag{3.19}$$

where $\boldsymbol{m}$ denotes the unit outward normal to $\partial\Omega$. $\boldsymbol{T}$ is a tensor valued function of $\boldsymbol{x} \in \Omega$, for which some kind of regularity must be assumed. If the differential equations of equilibrium are considered in a strong sense, the stress field $\boldsymbol{T}$ must be differentiable and its divergence must be continuous. On adopting a variational formulation, if the material is linearly elastic, the minimal request for $\boldsymbol{T}$ is to be square summable, that is

$$\sqrt{\int_\Omega \boldsymbol{T}\cdot\boldsymbol{T}da} < \infty\ . \tag{3.20}$$

For some rigid perfectly plastic materials (such as rigid unilateral materials), less regular and even singular stresses may be admitted. The minimal request for such materials is that $\boldsymbol{T}$ be summable

$$\int_\Omega \sqrt{\boldsymbol{T}\cdot\boldsymbol{T}}da < \infty\ . \tag{3.21}$$

If one admits stress fields that are only summable, the set of competing functions enlarges to bounded measures, that is to summable distributions)

$$\int_\Omega \left|\widetilde{\boldsymbol{T}}\right|da < \infty\ , \tag{3.22}$$

which, in general, can be decomposed into the sum of two parts

$$\widetilde{\boldsymbol{T}} = \widetilde{\boldsymbol{T}}^r + \widetilde{\boldsymbol{T}}^s \,, \tag{3.23}$$

where $\widetilde{\boldsymbol{T}}^r$ is absolutely continuous with respect to the area measure (that is $\widetilde{\boldsymbol{T}}^r$ is a density per unit area) and $\widetilde{\boldsymbol{T}}^s$ is the singular part. In the examples considered in this work, the analysis will be restricted to bounded measures $\widetilde{\boldsymbol{T}}$ whose singular part is concentrated on a finite number of regular arcs, that is bounded measures admitting on such curves a density $\widetilde{\boldsymbol{T}}^s$ with respect to the length measure, that is special bounded measures with empty Cantor part; for reference to these function spaces see (Ambrosio et al, 2000).

Remark 4|3. If the stress field is summable (and also if it is square summable), it is not differentiable in strong sense, and the equilibrium equations have to be reformulated in variational form (e.g. through the Virtual Work equation). Singular stresses require also special modifications of the boundary conditions; the trace of the stress $\boldsymbol{T}$ on the loaded part of the boundary is not given by $\boldsymbol{Tm}$ if $\boldsymbol{T}$ is singular (see also **Remark 5|3**). ■

3.3.1 Concentrated Stress

A typical application of the safe theorem to masonry structures composed of Heyman's material concerns the equilibrium of a voussoir arch. Based on the safe theorem, the arch cannot collapse if any line of thrust Γ in equilibrium with the given loads, can be constructed inside the masonry. In a continuum context, such line of thrust Γ can be interpreted as a 1d structure carrying the load by means of an internal axial contact force. The load can be transmitted to the structure from the body and from the boundary, by regular stresses having an unbalanced jump across Γ. In mathematical terms Γ is the support of a singular stress, that is a line Dirac delta applied along Γ having the form

$$\boldsymbol{T} = P\,\delta(\Gamma)\,\boldsymbol{t} \otimes \boldsymbol{t} \,. \tag{3.24}$$

The first to adopt singular stresses for the approximation of the equilibrium of a 2d continuum were Fraternali et al (2002). For masonry-like materials the first to introduce and adopt singular stresses for the application of the safe theorem to masonry structures were Lucchesi et al in (2013).

Adopting this view, the stress $\boldsymbol{T}$, is a bounded measure. As we observed in the case of strain, bounded measures can be decomposed into the sum of two parts

$$\boldsymbol{T} = \boldsymbol{T}^r + \boldsymbol{T}^s \,, \tag{3.25}$$

where $\boldsymbol{T}^r$ is absolutely continuous with respect to the area measure (that is $\boldsymbol{T}^r$is a density per unit area) and $\boldsymbol{T}^s$ is the singular part.

Let Γ be a regular curve on which the stress field exhibits a jump discontinuity. We denote with $\boldsymbol{t}, \boldsymbol{n}$ the unit tangent and the unit normal to Γ, and call Ω^-, Ω^+ the two parts on the two sides of Γ, Ω^+ being the part toward which $\boldsymbol{n}$ points. The stress vector $\boldsymbol{s}$ is associated to the regular part $\boldsymbol{T}^r$ of $\boldsymbol{T}$. The jump of $\boldsymbol{s}$ on Γ, that is the unbalanced emerging stress can be written as

$$[\boldsymbol{s}] = \boldsymbol{s}^+ - \boldsymbol{s}^- = \left(\boldsymbol{T}^{r+} - \boldsymbol{T}^{r-}\right)\mathbf{n}\,, \tag{3.26}$$

where with $\boldsymbol{T}^{r+}$ and $\boldsymbol{T}^{r-}$ we denote the regular part of the stress on the two sides, Ω^+ and Ω^-, of Γ.

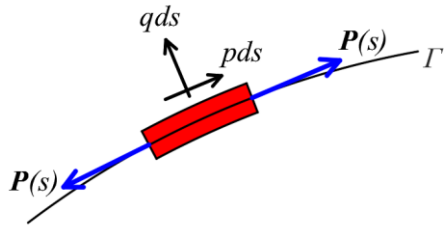

Fig. 3.1 - Equilibrium of the emerging stress at a singular interface. The regular stress $\boldsymbol{T}^r$ has an unbalanced jump across Γ: the equilibrium is satisfied by the singular part $\boldsymbol{T}^s$ of the stress field with support on Γ.

The jump of the stress vector, can be decomposed into normal and tangential components:

$$[\boldsymbol{s}] = p\,\boldsymbol{t} + q\,\boldsymbol{n}\ ,\ p = [\boldsymbol{s}]\cdot\boldsymbol{t}\ ,\ q = [\boldsymbol{s}]\cdot\boldsymbol{n}\,. \tag{3.27}$$

The unbalanced emerging stress is in equilibrium if it is balanced by the singular stress $\boldsymbol{T}^s$ concentrated on Γ. Indeed, denoting $\delta(\Gamma)$ the unit line Dirac delta with support on Γ, the singular part of stress along Γ can be written as

$$\boldsymbol{T}^s = P\,\delta(\Gamma)\,\boldsymbol{t}\otimes\boldsymbol{t}\,, \tag{3.28}$$

and for equilibrium (see **Fig. 3.1**) it must be:

$$P' + p = 0\ ,\ P\rho + q = 0\,, \tag{3.29}$$

where ρ denotes the curvature of the line Γ.

For masonry-like (NRNT) materials, the stress $\boldsymbol{T}$ must be negative semidefinite, therefore, in the plane case, it must be

$$tr\boldsymbol{T} \leq 0 \ , \ det\boldsymbol{T} \geq 0 \ , \tag{3.30}$$

from which

$$P \leq 0 \ , \tag{3.31}$$

that is the axial contact force P must be compressive. For simplicity, also for stress, only bounded measures whose singular part is concentrated on a finite number of regular arcs, that is bounded measures admitting on such curves a density $\boldsymbol{T}^s$ with respect to the length measure, are here considered.

■ 3.4 THE BOUNDARY VALUE PROBLEM FOR MASONRY-LIKE MATERIALS

We consider a masonry structure Ω, composed of masonry-like material in equilibrium under the action of body loads, and given surface loads and surface settlements prescribed on a fixed partition of its boundary $\partial\Omega_N \cup \partial\Omega_D = \partial\Omega$ (**Fig. 3.2**).

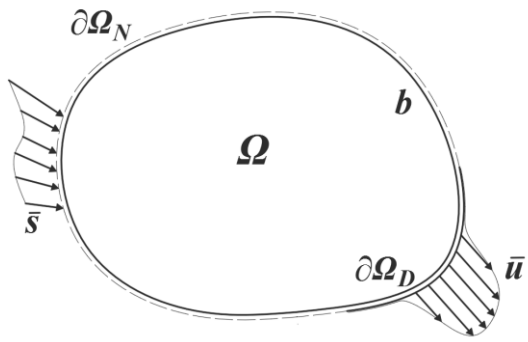

Fig. 3.2 - Loads and distortions applied to a continuum occupying a domain Ω.

The boundary value problem (bvp) for such a structure can be formulated as follows:

"Find a displacement field $\boldsymbol{u}$ *and the allied strain* $\boldsymbol{E}$*, and a stress field* $\boldsymbol{T}$ *such that*

$$\boldsymbol{E} = \frac{1}{2}(\nabla\boldsymbol{u} + \nabla\boldsymbol{u}^T) \ , \ \boldsymbol{E} \in Sym^+ \ , \ \boldsymbol{u} = \bar{\boldsymbol{u}} \ on \ \partial\Omega_D \ , \tag{3.32}$$

$$div\boldsymbol{T} + \boldsymbol{b} = 0 \ , \ \boldsymbol{T} \in Sym^- \ , \ \boldsymbol{T}\boldsymbol{m} = \bar{\boldsymbol{s}} \ \ on \ \partial\Omega_N \ , \tag{3.33}$$

$$\boldsymbol{T} \cdot \boldsymbol{E} = 0 \ ," \tag{3.34}$$

$\boldsymbol{m}$ being the unit outward normal to $\partial\Omega$.

Remark 5|3. On admitting discontinuous displacements and singular stresses, the differential equations in (3.32), (3.33) must be interpreted in a weak sense. Besides, the boundary condition in (3.33) makes sense only if we consider that the domain is closed on $\partial\Omega_D$, that is, that the displacement must actually take the given value on this part of the boundary, and considering the possible mismatch of the displacement between the outside and the inside of the domain as a concentrated strain along the boundary. Finally, in the boundary condition in (3.33), the trace of $\boldsymbol{T}$ at the boundary, that is the emerging stress vector $\boldsymbol{s}(\boldsymbol{T})$ on $\partial\Omega_N$, is not of the Cauchy form $\boldsymbol{s}(\boldsymbol{T}) = \boldsymbol{T}\boldsymbol{m}$, unless $\boldsymbol{T}$ is regular. If $\boldsymbol{T}$ is a line Dirac delta of the form $\boldsymbol{T} = P\,\delta(\Gamma)\,\boldsymbol{t}\otimes\boldsymbol{t}$ and Γ crosses the boundary at a point $X \in \Gamma$ at an angle, that is $\cdot\, \boldsymbol{m} \neq 0$, then $\boldsymbol{s}(\boldsymbol{T}) = P\,\delta(\Gamma)\,\boldsymbol{t}$. The special case in which the line Γ is tangent to $\partial\Omega_N$, deserves a special attention. In such a case, there is not any stress vector $\boldsymbol{s}(\boldsymbol{T})$ emerging at the boundary due to the singular stress, but still the boundary condition $\boldsymbol{T}\boldsymbol{m} = \bar{\boldsymbol{s}}$ must be modified, since the given tractions $\bar{\boldsymbol{s}}$ can be balanced, wholly or in part, by the singular stress concentrated on Γ. Therefore, there is not any local restriction on the sign of the normal component of the tractions given along the boundary: purely tangential tractions and even tensile loads may be applied if the boundary is locally concave. In the particular case in which the interface is straight, equilibrium and material restrictions can be enforced if and only if $\bar{\boldsymbol{s}}\cdot\boldsymbol{m} \leq 0$, but still there is no restriction on $\bar{\boldsymbol{s}}\cdot\boldsymbol{k}$, $\boldsymbol{k}$ being the unit tangent vector to $\partial\Omega$. ■

■ 3.5 Two Trivial Examples of Solutions of BVP's Using Singular Stress and Strain

In this section, we present two examples of bvp regarding an NRNT material, exploiting for the solution both singular stress and strain. We consider purely singular strains: the deformation is concentred along a finite number of lines. As for the stress field, we consider both a regular part and a singular part.

The first example is concerned with a wall of NRNT material, loaded at the top edge by a uniformly distributed load. The left and right edges are subjected to a prescribed outward settlement (see **Fig. 3.3**).

In **Fig. 3.4** a solution of the problem using singular stresses and strains is represented. Since the closed domain includes its boundary (see **Remark 3|3**), the panel shows three fractures. With the crosshatch in red lines the singular deformations $\boldsymbol{E}^s$ along the fracture lines is represented. The dash-dotted blue line represents, instead, the support of a singular stress field $\boldsymbol{T}^s$ in equilibrium with the given loads: this could be thought of as a thrust line. The regular part of the stress is

a uniaxial vertical stress field discontinuous across the line of thrust. The solution is compatible and verifies the relation $\boldsymbol{T}^S \cdot \boldsymbol{E}^S = 0$.

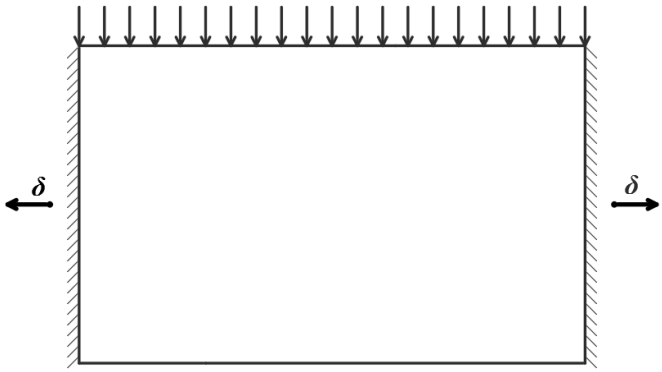

Fig. 3.3 - A panel of NRNT material subjected to two symmetric outward horizontal settlements. The only load considered is a uniform load acting along the top edge.

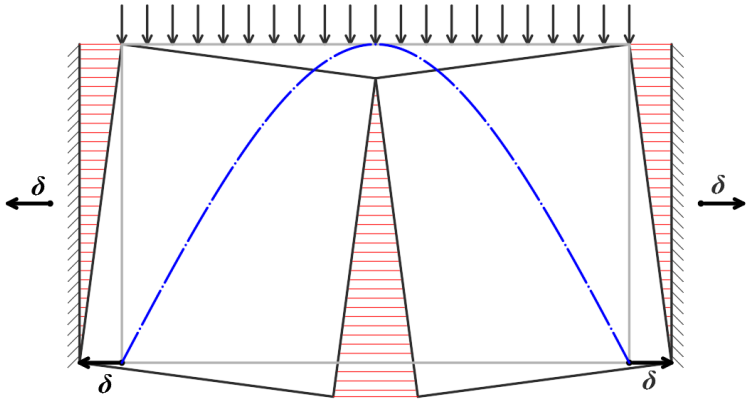

Fig. 3.4 - A possible solution of the bvp depicted in **Fig. 3.3** consisting of singular stress and strain fields. The crosshatch in red represents the singular deformations $\boldsymbol{E}^S$ along the fracture lines; the dash-dotted blue line represents the support of a singular stress field $\boldsymbol{T}^S$ in equilibrium with the given loads. The solution verifies the relation $\boldsymbol{T}^S \cdot \boldsymbol{E}^S = 0$.

The second example (**Fig. 3.5**, see also (Heyman, 1995)) concerns the problem of a round arch loaded only by the self-weight and subjected to given outward settlements at the bases.

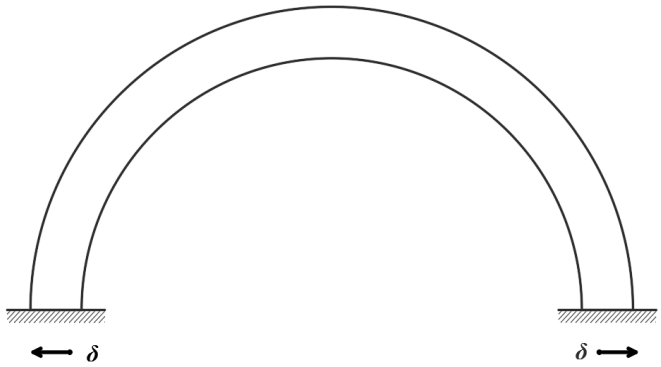

Fig. 3.5 - An arch of NRNT material, loaded only by the self-weight, subjected to given outward settlements at the bases.

A possible solution, consisting of singular strain and stress fields, is depicted in **Fig. 3.6**. In this case, three hinges form and the red crosshatch represents the singular deformations $\boldsymbol{E}^s$ along the hinges. The dash-dotted blue line represents, instead, the line of thrust, that is the support of an admissible singular stress field $\boldsymbol{T}^s$ in equilibrium with the given loads. The solution is compatible and verifies the relation $\boldsymbol{T}^s \cdot \boldsymbol{E}^s = 0$.

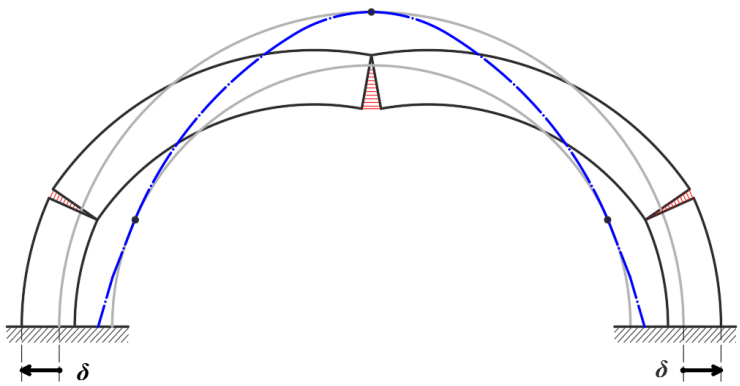

Fig. 3.6 - A possible solution of the bvp depicted in **Fig. 3.5** consisting of singular stress and strain fields. Three hinges form and the arch becomes a statically determined structure. The red crosshatch represents the singular deformations $\boldsymbol{E}^s$ along the hinges. The blue dash-dotted line is the curve Γ, that is the support of the singular stress field $\boldsymbol{T}^s = P\,\delta(\Gamma)\,\boldsymbol{t} \otimes \boldsymbol{t}$, representing the thrust line: a statically admissible singular stress field in equilibrium with the given load and verifying the condition $\boldsymbol{T}^s \cdot \boldsymbol{E}^s = 0$.

■ 3.6 STATICALLY AND KINEMATICALLY ADMISSIBLE FIELDS

We introduce the sets of kinematically admissible displacements $\mathcal{K}$, and of statically admissible stresses $\mathcal{H}$, defined as follows:

$$\mathcal{K} = \left\{ \boldsymbol{u} \in S \ / \ \boldsymbol{E} = \frac{1}{2}(\nabla \boldsymbol{u} + \nabla \boldsymbol{u}^T) \in Sym^+ \ \& \ \ \boldsymbol{u} = \bar{\boldsymbol{u}} \ on \ \partial\Omega_D \right\} , \tag{3.35}$$

$$\mathcal{H} = \{ \boldsymbol{T} \in S' \ / \ div\boldsymbol{T} + \boldsymbol{b} = \boldsymbol{0} \ \ , \ \ \boldsymbol{T} \in Sym^- \ \ , \ \boldsymbol{Tm} = \bar{\boldsymbol{s}} \ on \ \partial\Omega_N \} , \tag{3.36}$$

S, S' being two suitable function spaces. As observed in **Sections 3.2** and **3.3**, a sensible choice for these spaces is $S \equiv SBV$ and $S' \equiv SBM$, that is the spaces of Special Bounded Variation and of Special Bounded Measures.

Remark 6|3. Taking into account the previous definitions, a solution of the bvp for masonry-like structures is a triplet $(\boldsymbol{u}, \boldsymbol{E}(\boldsymbol{u}), \boldsymbol{T})$ such that $\boldsymbol{u} \in \mathcal{K}$, $\boldsymbol{T} \in \mathcal{H}$, and $\boldsymbol{T} \cdot \boldsymbol{E}(\boldsymbol{u}) = 0$. ■

Remark 7|3. With regard to a statically admissible stress field $\boldsymbol{T} \in \mathcal{H}$, the domain Ω can be decomposed into three parts:

$$\Omega_1 = \{ \boldsymbol{x} \in \Omega \ / \ tr\boldsymbol{T} \ \leq 0 \ \ , \ \ det\boldsymbol{T} > 0 \} , \tag{3.37}$$

$$\Omega_2 = \{ \boldsymbol{x} \in \Omega \ / \ tr\boldsymbol{T} \ \leq 0 \ \ , \ \ det\boldsymbol{T} = 0 \} , \tag{3.38}$$

$$\Omega_3 = \{ \boldsymbol{x} \in \Omega \ / \ \boldsymbol{T} = \boldsymbol{0} \} , \tag{3.39}$$

whose two by two intersections are empty: this constitutes a partition of the whole domain Ω. In particular, Ω_1 is characterized by a biaxial compression, Ω_2 by a uniaxial compression whilst Ω_3 is inert. ■

3.6.1 Compatibility of loads and distortions

The data of a general bvp for a NRNT body can be split into two parts

$$\ell \leftrightarrow \ (\bar{\boldsymbol{s}}, \boldsymbol{b}) \ \approx \ loads , \tag{3.40}$$

$$\ell^* \leftrightarrow \ (\bar{\boldsymbol{u}}, \bar{\boldsymbol{E}}) \ \approx \ distorsions . \tag{3.41}$$

For NRNT materials, the search of an admissible stress field (**Equilibrium Problem**) or of an admissible displacement field (**Kinematical Problem**) under given data are essentially independent, in the sense that they are uncoupled but for condition $\boldsymbol{T} \cdot \boldsymbol{E} = 0$.

The kinematical problem is defined as the search of kinematical admissible fields under given distortions. The distortions are compatible if and only if the set $\mathcal{K}$ is not empty. A similar definition can be introduced for the Equilibrium Problem (for a thorough study of compatibility conditions on the loads see (Del Piero, 1989) and (Angelillo and Rosso, 1995)). The following two statements hold:

$$\ell \; is \; compatible \quad \Leftrightarrow \quad \mathcal{H} \neq \emptyset \; , \tag{3.42}$$

$$\ell^* \; is \; compatible \quad \Leftrightarrow \quad \mathcal{K} \neq \emptyset \; . \tag{3.43}$$

The existence of a solution of the bvp for a NRNT material requires, as necessary condition, the compatibility both of loads and distortions, that is that $\mathcal{H}$, $\mathcal{K}$ must be not empty. Such a condition is not sufficient, since it has to be verified also the condition:

$$\boldsymbol{T} \cdot \boldsymbol{E} = 0 \; . \tag{3.44}$$

The formulation of incompatibility criteria either for distortions or for loads requires the definition of two further sets, namely:

$$\mathcal{K}^0 = \left\{ \boldsymbol{u}^0 \in S \; / \; \boldsymbol{E} = \frac{1}{2}\left(\nabla \boldsymbol{u}^0 + \nabla \boldsymbol{u}^{0^T}\right) \in Sym^+ \; \& \;\; \boldsymbol{u}^0 = \boldsymbol{0} \; on \; \partial\Omega_D \right\} \; , \tag{3.45}$$

$$\mathcal{H}^0 = \{ \boldsymbol{T}^0 \in S' \; / \; div\boldsymbol{T}^0 = 0 \;\; , \;\; \boldsymbol{T}^0 \in Sym^- \;\; , \; \boldsymbol{T}^0\boldsymbol{m} = 0 \; on \; \partial\Omega_N \} \; , \tag{3.46}$$

$\mathcal{K}^0$ represents the set of kinematically admissible displacements verifying homogeneous conditions at the constrained boundary $\partial\Omega_D$, whilst $\mathcal{H}^0$ represents a self-equilibrated statically admissible stress fields.

The incompatibility criterions can be formulated as follows:

$$\ell \; incompatible \quad \Leftrightarrow \quad \exists \, \boldsymbol{u}^0 \in \mathcal{K}^0 \; such \; that \; \langle \ell, \boldsymbol{u}^0 \rangle > 0 \, , \tag{3.47}$$

$$\ell^* \; incompatible \quad \Leftrightarrow \quad \exists \, \boldsymbol{T}^0 \in \mathcal{H}^0 \; such \; that \; \langle \boldsymbol{T}^0, \ell^* \rangle > 0 \, , \tag{3.48}$$

where $\langle \ell, \boldsymbol{u}^0 \rangle$ and $\langle \boldsymbol{T}^0, \ell^* \rangle$ represent the work of the loads ℓ and distorsions ℓ^* for $\boldsymbol{u}^0$ and $\boldsymbol{T}^0$ respectively.

Remark 8|3. If $\mathcal{H}$ is empty the load $(\bar{\boldsymbol{s}}, \boldsymbol{b})$ is incompatible, in the sense that no possibility of equilibrium with purely compressive stresses exists. The incompatibility of a given set of loads means that equilibrium is not possible and that acceleration of the structure takes place driven by the given loads. The incompatibility of a given set of distortions means that the given kinematical data cannot be accommodated with a zero energy mechanism and demand for more complex, deformable, material models. ■

■ 3.7 THE KINEMATICAL PROBLEM, THE EQUILIBRIUM PROBLEM AND THE COUPLING OF STRESS AND STRAIN

We call the search for a kinematically admissible displacement, that is the solution for the displacement $\boldsymbol{u}$ of the boundary value problem (bvp) under Heyman's restrictions: *kinematical problem*, as opposed to the *equilibrium problem*, that is the search of a statically admissible stress field under Heyman's restrictions.

Definitely the bvp for masonry-like materials can be split into two parts: the search of a displacement field belonging to $\mathcal{K}$, and the search for a stress field belonging to $\mathcal{H}$. The first problem is called **"the Kinematical Problem (KP) for NRNT structures"**, and the second problem **"the Equilibrium Problem (EP) for NRNT structures"**. These two problems are essentially uncoupled but for condition (3.1)[3], and can be undertaken separately.

First of all, we observe that either of the two problems can be incompatible, in the sense that the sets $\mathcal{K}$, $\mathcal{H}$ can both be empty. In particular, the compatibility of the *EP* is the key issue of the two theorems of Limit Analysis, which deal with the possibility of collapse of the structure.

In what follows we will assume that both $\mathcal{K}$, $\mathcal{H}$ are not empty, that is that the kinematical and the equilibrium problem are both compatible (that is, in particular, there is no possibility of collapse) and study the case in which both $\mathcal{K}$ and $\mathcal{H}$ have infinitely many elements.

When trying to solve the kinematical problem, the problem arises of selecting, among the possibly many kinematically admissible displacement fields responding to the given kinematical data (settlements and eigenstrains), the ones that guarantee also the equilibrium of the internal stress with the loads imposed on the structure.

Remark 9|3. A trivial case of compatibility occurs if the data are homogeneous. If the displacement data are zero, the KP is homogeneous and admits as solution $\boldsymbol{u} = \boldsymbol{0}$. If the load data are zero, the *EP* is homogeneous and admits the solution $\boldsymbol{T} = \boldsymbol{0}$. ■

In what follows we will study thoroughly the KP in the case in which the displacement data (the settlements) are not zero, and also the load applied on Ω are not zero.

■ 3.8 DISPLACEMENT APPROACH

As said before, the solution of the bvp for masonry-like structures is a triplet:

$$(\boldsymbol{u}, \boldsymbol{E}(\boldsymbol{u}), \boldsymbol{T}) \text{ such that } \boldsymbol{u} \in \mathcal{K}, \boldsymbol{T} \in \mathcal{H}, \text{ and } \boldsymbol{T} \cdot \boldsymbol{E}(\boldsymbol{u}) = 0\,. \tag{3.49}$$

In this work, we use a displacement approach, that is for a given structure under given loads ℓ and distortions ℓ^*, we look for a displacement field $\boldsymbol{u} \in \mathcal{K}$ such that there exists a stress field $\boldsymbol{T} \in \mathcal{H}$ such that $\boldsymbol{T} \cdot \boldsymbol{E}(\boldsymbol{u}) = 0$.

To solve the bvp with the displacement approach we use the energetic criterion described in the **Chapter 4**.

■ 3.9 LIMIT ANALYSIS

We have seen in the preceding sections that, for RNT bodies, both force and displacement data are subject to compatibility conditions, that is the existence of a statically admissible stress field and the existence of a kinematically admissible displacement field, are subordinated to some necessary or sufficient conditions on the given data. Recalling the material restrictions defining NRNT materials, we can observe that restrictions (3.1) are equivalent to a rule of normality of the total strain to the cone of admissible stress states, and normality is the essential ingredient allowing for the application of the two theorems of Limit Analysis (Del Piero, 1998).

Limit Analysis, with its two main theorems, answers to the question if a fixed structure under give loads ℓ (and distortions ℓ^*) is in a safe condition. Since the distortions ℓ^* play no role in the assessment of collapse, the question focuses only on the loads ℓ. The safe theorem and the kinematic theorem can be reformulated with reference to this two sets:

$$\mathcal{H} = \{\boldsymbol{T} \in S' / \, div\boldsymbol{T} + \boldsymbol{b} = \boldsymbol{0} \;\; , \;\; \boldsymbol{T} \in Sym^{-} \;\; , \;\; \boldsymbol{T}\boldsymbol{m} = \bar{\boldsymbol{s}} \; on \; \partial\Omega_N \}\,, \tag{3.50}$$

$$\mathcal{K}^0 = \left\{\boldsymbol{u}^0 \in S \;/\; \boldsymbol{E} = \tfrac{1}{2}\left(\nabla\boldsymbol{u}^0 + \nabla\boldsymbol{u}^{0T}\right) \in Sym^{+} \;\&\; \boldsymbol{u}^0 = \boldsymbol{0} \; on \; \partial\Omega_D \right\}, \tag{3.51}$$

$\mathcal{K}^0$ being the set of displacement fields verifying homogeneous conditions on the constrained boundary $\partial\Omega_D$, whilst $\mathcal{H}$ is the set of statically admissible stresses. In particular, each of these two sets contains the test functions to be used for the formalization of the statements of the two theorems. Limit Analysis deals with the assessment of collapse, collapse being an unbounded acceleration of the structure driven by the given loads. The two theorems can be formulated as follows:

Safe Theorem. Collapse does not occur if $\mathcal{H}$ is not empty. ■

Kinematic Theorem. Collapse occurs if there exists any displacement field $\boldsymbol{u}^0 \in \mathcal{K}^0$ such that $\langle \ell, \boldsymbol{u}^0 \rangle > 0$. ■

The safe theorem expresses a sufficient condition for the absence of collapse, whilst the kinematic theorem represents a sufficient condition for collapse to take place.

Remark 10|3. A well-known application of the safe theorem with regard to the arch structures, is contained in the following statement: *"an arch is safe under fixed loadings if and only if there exists a line of thrust lying wholly within the geometry of the arch".* The line of thrust could be thought of as the the support of a concentrated statically admissible stress field $\mathbf{T} \in \mathcal{H}$, that is a singular tensor stress field, in equilibrium with the given loads, represented in the form:

$$\boldsymbol{T}^s = P\,\delta(\Gamma)\,\boldsymbol{t} \otimes \boldsymbol{t} \quad , \quad P < 0 \ , \tag{3.52}$$

where Γ is the geometric image of the thrust line, $\delta(\Gamma)$ is the unit line Dirac delta with support on Γ and P is the intensity of the Dirac delta. Finding a statically admissible compressive singular stress field, i.e. a line of thrust in equilibrium with the given loads and wholly within the arch geometry, is a sufficient condition for the stability of an arch: this result does not depend on the fact that this specific line of thrust be the actual stress state of the arch, it is only sufficient that at least one thrust line verifying these conditions exists. ■

PART II

RIGID BLOCK MODEL

Chapter 4

AN ENERGY CRITERION

Prologue. In this Chapter, using a displacement approach, we propose an energy criterion (see **Section 4.1** below) to solve the bvp for NRNT materials (see **Chapter 3**). Two numerical methods are proposed to approximate the search for the minimal solution. With the PR method we search the solution of the bvp in the set of piecewise rigid displacements. The strain coincides with its singular part and is represented by line Dirac deltas: the crack pattern is concentrated along lines. The C^0 method, instead, consists in the approximation of the solution in the set of continuous displacements: the strain admits only of a regular part.

The main motivation for using the PR approximation derives from the observation that real masonry structures exhibit such rigid block mechanisms, when subject to severe settlements (see **Fig. 4.1**) or when shaken by serious earthquakes.

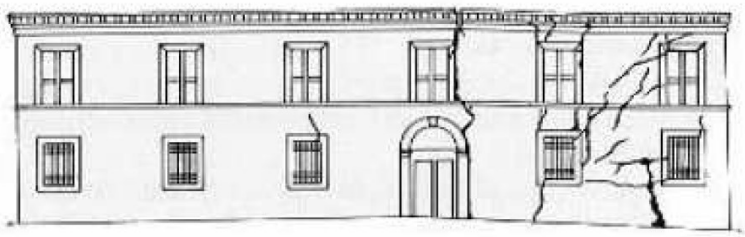

Fig. 4.1 - The effect of soil settlements on a XVII century building in Bergamo. Courtesy of Paolo Faccio, IUAV Venezia.

Besides, rigid block approximations are rather popular when solving manually simple plasticity problems, and implementing this kind of strategy on a computer is quite interesting "per se".

Actually with the NRNT model the material is rigid in compression, but extensional deformations, allowed at zero energy price, can be either regular or singular; then extensional deformation can appear as either diffuse (smeared cracks) or concentrated (macroscopic cracks), and there is not any reason to prefer one upon another, on an energy ground.

The fact that rigid block deformation seems to be the preferred failure mode for real masonry structures stems from mechanical characteristics, such as toughness and cohesion, which are not inherent to the simplified NRNT continuum model. So, it is interesting to see if rigid block mechanisms can arise naturally in solving the minimum problem (4.1), and if there is any legitimate way to force rigid block mechanisms over diffuse cracking.

Then, with the C^0 method we explore the possibility to tackle problem (4.1) by restricting the search to continuous (C^0) displacement fields, namely by using some classical Finite Element (FE) approximation. The C^0 displacement approximations for unilateral materials were already proposed and adopted with success in the paper by Angelillo et al (2010), in the case of Normal Elastic No-Tension (NENT) materials. What can be seen from this work by looking at some benchmark examples, is that, when the solution presents strain concentrations on some internal lines, the numerical solution exhibits large gradients (tending to become infinite for finer mesh sizes), on narrow bands approximating the fracture lines. The C^0 solution, though more cumbersome from the numerical point of view, appears as more adaptable than the rigid block approximation, in approximating fracture lines that are far from being located on the skeleton of the mesh.

This sluggishness of the rigid block approximation in reproducing "slanted" cracks (that is cracks not developing along the boundary of the rigid elements), is one of the main critical issues inherent to the piecewise rigid (PR) approximation. Then there is another reason to adopt the C^0 approximation, namely for seeing if the C^0 approximation can be used, in combination with the PR approximation, as a preliminary analysis for suggesting the optimal rigid block partition.

After the two methods are introduced, some benchmark problems are analysed to illustrate the numerical performances of the two approaches and the "pro et contra" of these two opposed strategies.

■ 4.1 THE KP: AN ENERGY CRITERION

The solution of the bvp for masonry-like structures is represented by a triplet $(\boldsymbol{u}, \boldsymbol{E}(\boldsymbol{u}), \boldsymbol{T})$ such that $\boldsymbol{u} \in \mathcal{K}$, $\boldsymbol{T} \in \mathcal{H}$, and $\boldsymbol{T} \cdot \boldsymbol{E}(\boldsymbol{u}) = 0$. With respect to a given structure under given loads ℓ and distortions ℓ^*, the use of a displacement approach consists in the search of a displacement field $\boldsymbol{u} \in \mathcal{K}$ for which there exist a stress field $\boldsymbol{T} \in \mathcal{H}$ such that $\boldsymbol{T} \cdot \boldsymbol{E}(\boldsymbol{u}) = 0$. In order to solve the bvp using a displacement approach we can use an energetic criterion.

Several problems in physics and Engineering can be formulated as a minimum search: a functional describing the energy of the system and depending on an unknown function has to be minimized over the set of all admissible functions. When trying to solve the kinematical problem, that is the boundary value problem for the displacement $\boldsymbol{u}$ under Heyman's restrictions, the problem arises of selecting, among the possibly many kinematically admissible displacement fields, the ones that guarantee also the equilibrium of the loads imposed on the structure.

For elastic, and even for some elastic-brittle materials, these states, that we can call solutions of the boundary value problem, can be found by searching for the minimum of some, suitably defined, form of energy. For Heyman's materials it is just the potential energy of the loads.

Then the idea is to search a displacement field which is the solution of the boundary value problem, by minimizing the potential energy $\wp$ of the loads. Such minimum problem is formulated as follows:

"Find a displacement field $\boldsymbol{u}^\circ \in \mathcal{K}$*, such that*

$$\wp(\boldsymbol{u}^\circ) = \min_{\boldsymbol{u}\in\mathcal{K}} \wp(\boldsymbol{u}) \ ," \tag{4.1}$$

where

$$\wp(\boldsymbol{u}) = -\int_{\partial\Omega_N} \bar{\boldsymbol{s}} \cdot \boldsymbol{u}\, ds - \int_{\Omega} \boldsymbol{b} \cdot \boldsymbol{u}\, da \ , \tag{4.2}$$

is the potential energy of the given loads and $\mathcal{K}$ is the set of kinematically admissible displacements, defined in **Chapter 3**.

■ 4.2 MINIMUM OF $\wp$ AND EQUILIBRIUM

The proof of the existence of the minimizer $\boldsymbol{u}^\circ$ of $\wp(\boldsymbol{u})$ for $\boldsymbol{u} \in \mathcal{K}$, is a complex mathematical question and is beyond the scopes of the present text. On assuming that the KP is compatible (that is $\mathcal{K} \neq \emptyset$), what we can easily show is that:

Theorem a. If the load is compatible (that is $\mathcal{H} \neq \emptyset$) the linear functional $\wp(\boldsymbol{u})$ is bounded from below. ■

Theorem b. If the triplet $(\boldsymbol{u}^\circ, \boldsymbol{E}(\boldsymbol{u}^\circ), \boldsymbol{T}^\circ)$ is a solution of the bvp, it corresponds to a weak minimum of the functional $\wp(\boldsymbol{u})$. ■

The proofs of this two theorems are reported below.

Proof. a. If the load is compatible then there exists a stress field $\boldsymbol{T} \in \mathcal{H}$, through which the functional $\wp(\boldsymbol{u})$ defined on $\mathcal{K}$, for any $\boldsymbol{u} \in \mathcal{K}$, can be rewritten as follows

$$\wp(\boldsymbol{u}) = -\int_{\partial\Omega_N} \bar{\boldsymbol{s}} \cdot \boldsymbol{u}\, ds - \int_{\Omega} \boldsymbol{b} \cdot \boldsymbol{u}\, da = \int_{\partial\Omega_D} \boldsymbol{s}(\boldsymbol{T}) \cdot \bar{\boldsymbol{u}}\, ds - \int_{\Omega} \boldsymbol{T} \cdot \boldsymbol{E}(\boldsymbol{u}) da\,, \qquad (4.3)$$

$\boldsymbol{s}(\boldsymbol{T})$ being the trace of $\boldsymbol{T}$ at the boundary (see **Remark 5|3**). Assuming that the displacement data are sufficiently regular (say continuous), being $\boldsymbol{s}(\boldsymbol{T})$ a bounded measure (see **Remark 5|3**), the integral $\int_{\partial\Omega_D} \boldsymbol{s}(\boldsymbol{T})\ \bar{\boldsymbol{u}}\, d\sigma$ is finite; then, since $\boldsymbol{T} \in Sym^-$ and $\boldsymbol{E} \in Sym^+$, the volume integral is non negative, and $\wp(\boldsymbol{u})$ is bounded from below. ■

Proof b. If $(\boldsymbol{u}^\circ, \boldsymbol{E}(\boldsymbol{u}^\circ), \boldsymbol{T}^\circ)$ is a solution of the bvp, then, for any $\boldsymbol{u} \in \mathcal{K}$, we can write

$$\wp(\boldsymbol{u}) - \wp(\boldsymbol{u}^\circ) = -\int_{\partial\Omega_N} \bar{\boldsymbol{s}} \cdot (\boldsymbol{u} - \boldsymbol{u}^\circ) ds - \int_{\Omega} \boldsymbol{b} \cdot (\boldsymbol{u} - \boldsymbol{u}^\circ) da = -\int_{\Omega} \boldsymbol{T}^\circ \cdot \big(\boldsymbol{E}(\boldsymbol{u}) - \boldsymbol{E}(\boldsymbol{u}^\circ)\big)\, da. \quad (4.4)$$

The result $\wp(\boldsymbol{u}) - \wp(\boldsymbol{u}^\circ) \geq 0\ ,\ \forall \boldsymbol{u} \in \mathcal{K}$, follows form normality (3.3). ■

The physical interpretation of the above result is the following. Since the displacement field solving the bvp corresponds to a state of weak minimum for the energy, then it is a neutrally stable equilibrium state, in the sense that the transition to a different state requires a non negative supply of energy.

Remark 1|4. Based on the minimum principle, if the EP is compatible and the KP is homogeneous, $\boldsymbol{u} = \boldsymbol{0}$ is a minimum solution. Indeed, in such a case

$$\wp(\boldsymbol{u}) = -\int_{\partial\Omega_N} \bar{\boldsymbol{s}} \cdot \boldsymbol{u}\, ds - \int_{\Omega} \boldsymbol{b} \cdot \boldsymbol{u}\, da = -\int_{\Omega} \boldsymbol{T} \cdot \boldsymbol{E}(\boldsymbol{u}) da\,, \qquad (4.5)$$

$\boldsymbol{T}$ being any element of $\mathcal{H}$. Since the right hand side of (4.2) is non negative, $\wp(\boldsymbol{0}) = 0$ is the minimum of $\wp$ and $\boldsymbol{u} = \boldsymbol{0}$ is a minimizer of the potential energy. Notice that, in this case, any $\boldsymbol{T} \in \mathcal{H}$ is a possible solution in terms of stress, since $\boldsymbol{T} \cdot \boldsymbol{E}(\boldsymbol{0}) = 0$ for any $\boldsymbol{T}$. ■

■ 4.3 PR METHOD, PIECEWISE RIGID DISPLACEMENTS: RIGID BLOCKS

4.3.1 PR Method: theory

We consider the approximate solution of the minimum problem (4.1) obtained by restricting the search of the minimum in the restricted class $\mathcal{K}_{pr}$ of piecewise rigid displacements. This infinite dimensional space is discretized by considering a finite partition

$$(\Omega_i)_{i\in\{1,2,..,M\}} \ , \tag{4.6}$$

of Ω into a number M of rigid pieces, such that

$$\sum_{i=1}^{M} P(\Omega_i) < \infty \ , \tag{4.7}$$

$P(\Omega_i)$ being the perimeter of Ω_i. In particular, restricting to convex polygonal elements, the boundary $\partial\Omega_i$ of the n-polygon Ω_i, is composed of n segments Γ, of length ℓ, whose extremities are denoted generically 0,1. We call *interfaces* the segments Γ that are, either the common boundaries between adjacent elements, or part of the constrained boundary (that is those Γ representing interfaces with the soil). We call $\mathcal{K}_{pr}^{M}$ the finite dimensional approximation of $\mathcal{K}_{pr}$ generated by this partition. The minimum problem becomes:

$$\wp(\widehat{\boldsymbol{u}}) = \min_{\boldsymbol{u}\in\mathcal{K}_{pr}^{M}} \wp(\boldsymbol{u}) \ . \tag{4.8}$$

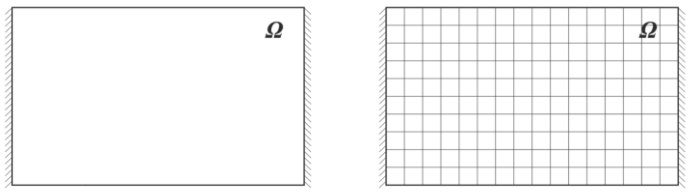

Fig. 4.2 - The infinite dimensional space $\mathcal{K}_{pr}$ of piecewise rigid displacement with support in Ω (a) is discretized considering a partition of the whole domain into convex polygonal elements: in (b) an example of the partition of the domain Ω with a grid of M squares is shown. The finite dimensional approximation generated by the fixed partition is called $\mathcal{K}_{pr}^{M}$.

To represent a generic piecewise rigid displacement $\boldsymbol{u} \in \mathcal{K}_{pr}^{M}$ we may use the vector $\boldsymbol{U}$ of $3M$ components represented by the $3M$ rigid body parameters of translation and rotation of the elements. These parameters are restricted by the assumption that the strain must be positive semidefinite. For piecewise rigid displacements, the strain coincides with its singular part (see **Section 3.2**), namely:

$$\boldsymbol{E} = \boldsymbol{E}^{s} = v\,\delta(\Gamma)\,\boldsymbol{n} \otimes \boldsymbol{n} + \frac{1}{2} w\,\delta(\Gamma)\,(\boldsymbol{t} \otimes \boldsymbol{n} + \boldsymbol{n} \otimes \boldsymbol{t})\,, \tag{4.9}$$

and it is concentrated along the interfaces among blocks, that is, in the present case, along the segments Γ. Since the sliding is not allowed, only detachments are possible, then:

$$v = [\boldsymbol{u}] \cdot \boldsymbol{n} \;\geq 0\,, \tag{4.10}$$
$$w = [\boldsymbol{u}] \cdot \boldsymbol{t} = 0\;, \tag{4.11}$$

and the strain takes the form:

$$\boldsymbol{E} = v\,\delta(\Gamma)\,\boldsymbol{n} \otimes \boldsymbol{n}\,. \tag{4.12}$$

Notice that conditions (4.10), (4.11), derived from the assumption of normality, represent a condition of unilateral contact with no-sliding among blocks.

The static counterpart of these constraints concerns the stress vector $\boldsymbol{s}$ applied along Γ. Such a stress vector represents, along the interfaces (that is the internal interfaces and the external interfaces with the soil), the reaction associated to the constraints (4.10), (4.11). The stress vector $\boldsymbol{s}$ coincides with the given applied tractions $\bar{\boldsymbol{s}}$ where the boundary of the blocks becomes the loaded part of the boundary. By calling

$$\sigma = \boldsymbol{s} \cdot \boldsymbol{n}\;,\; \tau = \boldsymbol{s} \cdot \boldsymbol{t}\;, \tag{4.13}$$

the normal and tangential stress along Γ, the condition on $\boldsymbol{s}$ is

$$\sigma \leq 0\,. \tag{4.14}$$

Notice that the tangential component of $\boldsymbol{s}$ is not constrained and can be applied along the straight interface Γ, even if $\sigma = 0$ (see **Remark 5|3**).

By calling N the number of the interfaces Γ, and $v(0), v(1), w(0), w(1)$ the normal and tangential components of the relative displacements of the ends 0, 1 of the segment Γ, restrictions (4.10), (4.11) are equivalent to the $2N$ inequalities

$$v(0) \geq 0\,,\; v(1) \geq 0\;, \tag{4.15}$$

and the $2N$ equalities

$$w(0) = 0\,,\ w(1) = 0\ . \tag{4.16}$$

The restrictions (4.15), (4.16) can be easily expressed in terms of $\widehat{\boldsymbol{U}}$, rewriting them in the matrix forms:

$$\boldsymbol{A}\,\widehat{\boldsymbol{U}} \geq \boldsymbol{0}\ , \tag{4.17}$$
$$\boldsymbol{B}\,\widehat{\boldsymbol{U}} = \boldsymbol{0}\ . \tag{4.18}$$

Finally, the minimum problem (4.8) which approximates the minimum problem (4.1) can be transformed into:

$$\wp\left(\widehat{\boldsymbol{U}}^0\right) = \min_{\widehat{\boldsymbol{U}}\in\mathbb{K}^M} \wp\left(\widehat{\boldsymbol{U}}\right)\ , \tag{4.19}$$

$\mathbb{K}^M$ being the set:

$$\mathbb{K}^M = \{\widehat{\boldsymbol{U}} \in \mathbb{R}^{3M} \,/\, \boldsymbol{A}\,\widehat{\boldsymbol{U}} \geq \boldsymbol{0}\ ,\ \boldsymbol{B}\,\widehat{\boldsymbol{U}} = \boldsymbol{0}\}\ . \tag{4.20}$$

Remark 2|4. The minimization problem (4.19) that we propose for approximating the minimization problem (4.1), transforms the original minimization problem for a continuum, into a minimization problem for a structure composed of rigid parts, acted on by given loads and given settlements and subject to unilateral contact conditions along the interfaces. Problem (4.19) is a standard linear finite dimensional minimization problem, since the function $\wp\left(\widehat{\boldsymbol{U}}\right)$ is a linear function of the $3M$-vector $\widehat{\boldsymbol{U}}$ and the constraints are linear. The existence of the solution of this approximate problem is trivially guaranteed if the original problem is bounded from below. For a small number of variables it can be solved exactly with the simplex method (Dantzig et al, 1955), and for large problems there exist a number of well-known, and efficient, approximate alternatives [see (Mehrotra, 1992), (Vanderbei, 2015) and (Dantzig et al, 2016)]. ■

4.3.2 PR Method: numerical strategy

The examples presented in this work are developed with the program Mathematica® (Wolfram, 2003). Generally, the application of the method proceeds into the following steps:

1. definition of the structural geometry and of its discretization;
2. discretization of the displacement field as piecewise rigid displacement;

3. definition of the potential energy as a linear functional of the rigid displacement parameters;
4. definition of the internal and external boundary conditions;
5. numerical solution of the problem with a linear programming routine;
6. post-processing (evaluation of the displacement corresponding to the solution).

* * *

1. Let us denote Ω_* the domain representing the structural geometry in $\mathcal{E}^2$; consider the minimum rectangular domain Ω^* containing Ω_*. The whole domain Ω^* is partitioned into N rectangular basic units Ω_i, we call them subdomains. The set $\pi^* = (\Omega_i)_{i\in\{1,\dots,N\}}$ constitutes a partition of Ω^*, that is:

$$\bigcup_{i=1}^{N} \Omega_i = \Omega^* \quad \& \quad \Omega_i \cap \Omega_j = \emptyset \ , \ \forall i,j \in \{1,\dots,N\} \ / \ i \neq j \ . \tag{4.21}$$

To take into account the presence of voids in the domain Ω_* is necessary to perform an appropriate elimination of some elements belonging to π^*. To this purpose, we consider the set

$$\pi_M = \{\Omega_i \in \pi^* \ / \ \Omega_i \cap \Omega_* \neq \emptyset\} \, , \tag{4.22}$$

where M is the cardinality of π_M. Defining $\Omega = \cup_{\Omega_j \in \pi_M} \Omega_j$ from (4.22) it follows:

$$\Omega \supseteq \Omega_* \, . \tag{4.23}$$

Therefore π_M is a particular cover of the real structural domain Ω_*: it is the minimum cover of Ω_* (with respect to the cardinality) and at the same time it constitutes a finite partition of Ω, which becomes *our structural model domain*. Finally, it is to be noticed that π_M is a countable set of subdomains having finite perimeter, therefore, is a Caccioppoli partition of Ω in the sense of Chambolle et al (2007).

* * *

2. The displacement field $\boldsymbol{u} = \boldsymbol{u}(\boldsymbol{x})$**,** defined in Ω, is approximated as piecewise rigid. We use π_M to introduce this approximation, namely:

$$\boldsymbol{u}: \boldsymbol{x} \in \Omega \rightarrow \begin{cases} \boldsymbol{u}_1 \ , \ if \ \boldsymbol{x} \in \Omega_1 \, , \\ \vdots \\ \boldsymbol{u}_j \ , \ if \ \boldsymbol{x} \in \Omega_j \ , \\ \vdots \\ \boldsymbol{u}_M \ , \ \text{if} \ \boldsymbol{x} \in \Omega_M \, , \end{cases} \tag{4.24}$$

where $\boldsymbol{u}_j = \boldsymbol{u}|_{\Omega_j}\ \forall\, j \in \{1, \dots, M\}$ is an infinitesimal rigid displacement. In 2d problems, $\boldsymbol{u}_j$ is a function of three Lagrangian parameters assumed as the two translations of the centroid G_j of Ω_j and the rotation about G_j. In vector form:

$$\boldsymbol{u}_j = \boldsymbol{v}_j + \boldsymbol{\Phi}_j\left(\boldsymbol{x} - \boldsymbol{x}_j^0\right), \tag{4.25}$$

where $\boldsymbol{x}_j^0$ is the position vector of G_j, and

$$\boldsymbol{\Phi}_j \in Skw\,, \tag{4.26}$$

and then

$$\mathrm{Sym}\nabla\boldsymbol{u}_j = \boldsymbol{0}\,. \tag{4.27}$$

In (4.25) $\boldsymbol{v}_j = \left(U_j, V_j\right)$ is the translation vector, whose components are the two translation parameters in a fixed global Cartesian reference, and:

$$\boldsymbol{\Phi}_j = \begin{pmatrix} 0 & -\Phi_j \\ \Phi_j & 0 \end{pmatrix} \tag{4.28}$$

is the infinitesimal rotation matrix in the same reference. Therefore, the displacement field $\boldsymbol{u} = \boldsymbol{u}(\boldsymbol{x})$ depends on $3M$ unknown Lagrangian parameters:

$$\left(U_j, V_j, \Phi_j\right)_{j\in\{1,..,M\}}\,. \tag{4.29}$$

The $3M$ independent parameters can be collected in the single vector:

$$\widehat{\boldsymbol{U}} = \left(U_1, V_1, \Phi_1, .., U_j, V_j, \Phi_j, .., U_M, V_M, \Phi_M\right)\,,\quad \widehat{\boldsymbol{U}} \in \mathbb{R}^{3M}\,. \tag{4.30}$$

* * *

3. Since in our theory, both fracture energy and elastic energy are neglected, the potential energy $\wp$ coincides with the potential energy of the external forces only, and can be expressed in terms of the components of $\widehat{\boldsymbol{U}}$. $\wp$ is the opposite of the scalar product of the applied forces times the displacements of their points of application, and is a linear function of $3M$ unknown Lagrangian parameters, that can be symbolically expressed as follows:

$$\wp = \wp\left(\widehat{\boldsymbol{U}}\right)\,,\ \widehat{\boldsymbol{U}} \in \mathbb{R}^{3M}\,. \tag{4.31}$$

The problem can be formulated, as already described in (4.19), as a linear programming one, in the form:

$$\min_{\widehat{\boldsymbol{U}}\in\mathbb{K}^M} \wp\left(\widehat{\boldsymbol{U}}\right), \tag{4.32}$$

$\mathbb{K}^M$ being the subset of $\mathbb{R}^{3M}$ defined by the unilateral and bilateral constraints associated to the contact and fixing conditions. It remains to define explicitly the subset $\mathbb{K}^M \subseteq \mathbb{R}^{3M}$ from Heyman's restrictions defining the NRNT materials. The kinematical consequence of Heyman's assumptions (i.e. (i), (ii) and (iii)) are summarized in **Section 3.2** and condensed in the conditions (3.15), (3.16). In the subsequent point such restrictions are rewritten as contact conditions along the element interfaces, in terms of relative displacements, taking into account the analysis presented in **Section 4.3.1** (see conditions (4.10), (4.11) and (4.15), (4.16)).

* * *

4. To fix ideas, let Ω_i and Ω_j be two contiguous subdomains, with the $l(A,B)$ side in common (see **Fig. 4.3**). Let $\boldsymbol{n}$ and $\boldsymbol{t}$ be the normal and tangential unit vectors to $l(A,B)$ (see **Fig. 4.3b),** and $\boldsymbol{u}_j(A)$ the nodal displacement of the material point A belonging to the Ω_j subdomain.

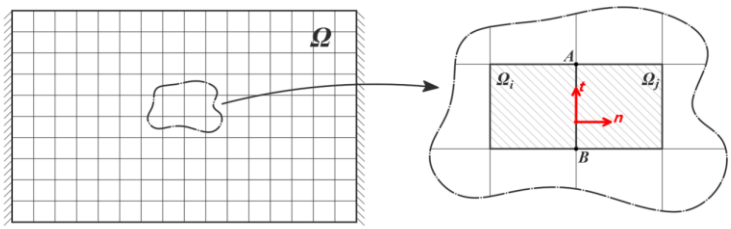

Fig. 4.3 - Example of the partition of the domain with a grid of squares (a). Close up of two adjacent elements Ω_i and Ω_j and showing the common interface $l(A,B)$ (b).

The kinematical conditions between Ω_i and Ω_j along $l(A,B)$ can be expressed (recalling (4.10), (4.11)) as follows:

$$\left(\boldsymbol{u}_j(P)-\boldsymbol{u}_i(P)\right)\cdot\boldsymbol{n}\geq 0 \quad \forall\, P\in l(A,B)\,, \tag{4.33}$$

$$\left(\boldsymbol{u}_j(P)-\boldsymbol{u}_i(P)\right)\cdot\boldsymbol{t}= 0 \quad \forall\, P\in l(A,B)\,, \tag{4.34}$$

Ω_j being the subdomain toward which the unit normal $\boldsymbol{n}$ points. Taking into account the linearity of $\boldsymbol{u}_k \;\; \forall\, k\in\{1,\dots,M\}$, the first of the previous conditions is equivalent to two inequalities (see (4.15)):

$$\left(\boldsymbol{u}_j(A)-\boldsymbol{u}_i(A)\right)\cdot\boldsymbol{n}\geq 0\,, \tag{4.35}$$

$$\left(\boldsymbol{u}_j(B)-\boldsymbol{u}_i(B)\right)\cdot\boldsymbol{n}\geq 0\,. \tag{4.36}$$

Similarly, the no-sliding condition can be expressed (in a redundant way) through the two equations (see (4.16)):

$$\Big(\boldsymbol{u}_j(A) - \boldsymbol{u}_i(A)\Big) \cdot \boldsymbol{t} = 0\,, \tag{4.37}$$

$$\Big(\boldsymbol{u}_j(B) - \boldsymbol{u}_i(B)\Big) \cdot \boldsymbol{t} = 0\,, \tag{4.38}$$

that, due to the rigidity, can be rewritten into one of the two equivalent forms:

$$\Big(\boldsymbol{u}_j(A) - \boldsymbol{u}_i(B)\Big) \cdot \boldsymbol{t} = 0 \;\Leftrightarrow\; \Big(\boldsymbol{u}_j(B) - \boldsymbol{u}_i(A)\Big) \cdot \boldsymbol{t} = 0\,. \tag{4.39}$$

Finally, the Heyman conditions (3.15) and (3.16) relative to $l(A,B)$ are synthesized into three relations:

$$\Big(\boldsymbol{u}_j(A) - \boldsymbol{u}_i(A)\Big) \cdot \boldsymbol{n} \geq 0\;, \tag{4.40}$$

$$\Big(\boldsymbol{u}_j(B) - \boldsymbol{u}_i(B)\Big) \cdot \boldsymbol{n} \geq 0\;, \tag{4.41}$$

$$\Big(\boldsymbol{u}_j(A) - \boldsymbol{u}_i(B)\Big) \cdot \boldsymbol{t} = 0\;, \tag{4.42}$$

which can be easily expressed in terms of the 6 Lagrangian parameters $(U_k, V_k, \Phi_k)_{k\in\{i,j\}}$.

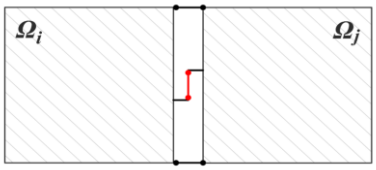

Fig. 4.4 - The three conditions (4.40-42) between two adjacent domains Ω_i and Ω_j could be represented by three internal constraints: two unilateral (horizontal black connections in the Figure) and a bilateral (vertical red connection in the Figure).

If n denotes the number of internal interfaces, the internal boundary conditions consist of $2n$ linear inequalities and n linear equalities; with some easy transformations, the external boundary conditions can be implemented as fictitious internal contact conditions. If the constraints are perfect, then the corresponding equalities and inequalities are homogeneous. The given settlements (or eigenstrains) are the known terms of the non-homogeneous conditions. All together the constraints define a domain $\mathbb{K}^M \subseteq \mathbb{R}^{3M}$, in which the optimal solution has to be found; such domain is a convex polytope of the $\mathbb{R}^{3M}$ space.

* * *

5. With the above approximation the structural problem is formulated as a minimum problem: "*find a piecewise rigid displacement* $\widehat{\boldsymbol{U}}^0$ *which minimizes the potential energy* $\wp$ *in* $\mathbb{K}^M$*:*

$$\min_{\widehat{\boldsymbol{U}}\in\mathbb{K}^M} \wp\left(\widehat{\boldsymbol{U}}\right) \text{ ."} \tag{4.43}$$

This linear programming problem is solved with the simplex method, or with the interior point method if the number of unknowns and conditions is large.

* * *

6. Once the minimizer $\widehat{\boldsymbol{U}}^0$ has been obtained it is an easy task to construct the deformed shape of the structure. The moving part of the structure represents a one degree of freedom mechanism controlled by the form of the given settlements, i.e. it is statically determined. The relative displacements among the blocks play the role of fractures, and hopefully give an approximation of the real fracture pattern produced by known settlements.

Remark 3|4. Usually, the kinematical problem to be solved for real structures presents itself in a different way, since cracks are detectable and the settlements producing them are usually unknown. Therefore, to adopt our scheme in practical applications, a sort of inverse identification procedure must be implemented. ■

■ 4.4 C^0 METHOD, CONTINUOUS DISPLACEMENTS: SMEARED CRACKS

4.4.1 C^0 Method: theory

In the previous sections, we formulated an approximate solution of the minimum problem (4.1) by restricting the search of the minimum in the class $\mathcal{K}_{pr}$ of piecewise rigid displacements. $\mathcal{K}_{pr}$ is a particular subspace of SBV functions which allows us to simulate the cracks forming in the structure through gap "openings" between adjacent rigid blocks, that is concentrated strains in the form of line Dirac delta functions defined over the skeleton of the mesh.

In the present section, we consider a completely different approximation strategy based on continuous (C^0) displacement fields, namely we consider a classical approximation based on a Finite Element (FE) mesh. It is to be pointed out, that whilst the use of piecewise rigid displacements belongs the class of so-called discrete element methods [see (Cundall, 1971) and (Sarhosis et al, 2016) and for applications (Tóth et al, 2009), (Simon and Bagi, 2016) and (Forgács et al, 2017)], the approximation of the minimum problem (4.1) through C^0 functions yields a FEM-like formulation. The formulation of the C^0 method proceeds as follows. The first simplification made is to considerer only the infinite dimensional set of $\mathcal{K}$ constituted by continuous functions. The second approximation is to restrict to a finite subset of it, by discretizing the domain Ω into a number M of elements with the finite partition

$$(\Omega_i)_{i\in\{1,2,..,M\}} \ , \tag{4.44}$$

such that

$$\sum_{i=1}^{M} P(\Omega_i) < \infty \ , \tag{4.45}$$

$P(\Omega_i)$ being the perimeter of Ω_i. In particular, in what follows, we refer to polygonal elements, such that the boundary $\partial\Omega_i$ of the n-polygon Ω_i, is composed of n segments Γ linking n points.

Remark 4|4. We remark that, whilst with the PR method, the interfaces between blocks plaid a crucial role being potential fracture lines, in the second formulation two nodes belonging to two different elements must have the same displacements, and so the interfaces play a secondary role. ■

Assuming the continuity of the displacement field at the nodes, the NRT material restrictions have to be enforced inside the elements. In particular, recalling definition (3.1), the Normal Rigid No-Tension material is completely defined by the restrictions:

$$\boldsymbol{T} \in Sym^{-} \ , \ \boldsymbol{E} \in Sym^{+} \ , \ \boldsymbol{T} \cdot \boldsymbol{E} = 0 \ . \tag{4.46}$$

On approaching the problem as an energy minimization of the type (4.1), the latent strain $\boldsymbol{E}$ has to belong to the positive semidefinite cone:

$$\boldsymbol{E} \in Sym^{+} \ . \tag{4.47}$$

This restriction, for 2d problems, is equivalent to the two following inequalities:

$$tr\boldsymbol{E} \geq 0 \ , \ det\boldsymbol{E} \geq 0 \ . \tag{4.48}$$

In the 2d Euclidean space, a generic tensor, such as the latent strain $\boldsymbol{E}$, can be represented, in a fixed Cartesian reference, by a 2x2 matrix:

$$\boldsymbol{E} = \begin{bmatrix} \varepsilon_{11} & \varepsilon_{12} \\ \varepsilon_{21} & \varepsilon_{22} \end{bmatrix} . \tag{4.49}$$

Geometrically, the condition $det\boldsymbol{E} \geq 0$ defines a double cone in the space Sym, and the additional condition $tr\boldsymbol{E} \geq 0$ selects one of the two parts of the cone, namely the semidefinite positive space which is a convex cone. In particular, analytically, with reference to the three dimensional space Sym spanned by the dyadic orthonormal base $(\boldsymbol{e}_1 \otimes \boldsymbol{e}_1 \, , \boldsymbol{e}_2 \otimes \boldsymbol{e}_2 \, , \sqrt{2}(\boldsymbol{e}_1 \otimes \boldsymbol{e}_2 + \boldsymbol{e}_2 \otimes \boldsymbol{e}_1))$, conditions (4.48) or equivalently (3.15) can be written in terms of Cartesian components, as:

$$\varepsilon_{11}\varepsilon_{22} - {\varepsilon_{12}}^2 \geq 0 \ , \ \ \varepsilon_{11} + \varepsilon_{22} \geq 0 \, , \tag{4.50}$$

which is actually a condition on the displacement field $\boldsymbol{u}$ since $\boldsymbol{E} = \mathrm{Sym}\nabla\boldsymbol{u}$. We choose to implement numerically conditions (4.50) in an approximate way in order not to loose the linearity of the problem. The idea is to approximate the cone Sym^{+} by a plane envelope.

The partition $(\Omega_i)_{i\in\{1,2,..,M\}}$ constitutes a discretization of the geometrical domain, the displacement field $\boldsymbol{u}$ is a function of the nodal displacements. In particular, let $\widehat{\boldsymbol{U}} \in \mathcal{R}^{2N}$ be the vector which collects the displacement components of the $2N$ nodes, the displacement field can be expressed as a functions of the node displacement:

$$\boldsymbol{u} = \boldsymbol{u}\big(\widehat{\boldsymbol{U}}\big) \, , \tag{4.51}$$

where $\widehat{\boldsymbol{U}} = (U_1, V_1, .., U_i, V_i, .., U_N, V_N)$ and (U_i, V_i) denotes the displacement of the node i. If $\mathcal{K}_c^N$ denotes the finite subspace of SBV defined by the continuous functions

associated with the finite element chosen, the minimum problem can be written as follows:

$$\wp(\widehat{\boldsymbol{u}}) = \min_{\boldsymbol{u}\in\mathcal{K}_c^N} \wp(\boldsymbol{u}) \,, \tag{4.52}$$

in which the continuous displacement $\boldsymbol{u} \in \mathcal{K}_c^N$ is expressed by $2N$ scalar parameters, that are the components of the displacements of the N nodes of the given mesh.

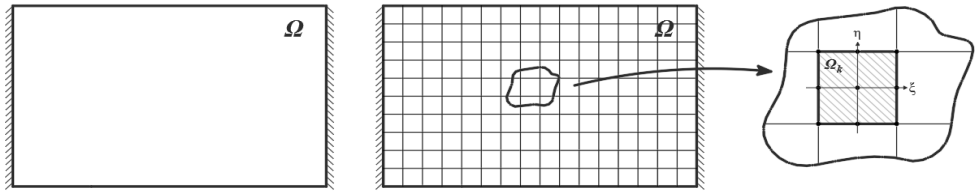

Fig. 4.5 - The infinite dimensional space $\mathcal{K}_c$ of continuous displacements with support in Ω (a) is discretized considering a partition $(\Omega_i)_{i\in\{1,2,..,M\}}$ of the whole domain into e.g. quadrangular elements (b): the finite dimensional approximation generated by the fixed partition is called $\mathcal{K}_c^N$, where N is the number of nodes. In (c) a subdomain Ω_k and the second order Lagrangian element with 9 nodes is shown.

These parameters are restricted by the assumption that the strain must belong to the linearized envelope of the cone Sym^+. Thus, whilst for piecewise rigid displacements the strain is concentrated along the interfaces among blocks, in this case the latent strain is diffused inside the elements (smeared cracks). In some cases, the latent strain could coagulate in narrow bands which could be viewed as an approximation of fracture lines. We recall that the condition

$$\boldsymbol{E} \in Sym^+ \,, \tag{4.53}$$

is enforced in an approximated way by restricting $\boldsymbol{E}$ to belong to a tangent plane envelope. Therefore the only internal restrictions that we have in this case are linear inequalities, which can be expressed in terms of the unknown nodal displacements in the matrix form:

$$\boldsymbol{A}\,\widehat{\boldsymbol{U}} \geq 0 \,. \tag{4.54}$$

Finally, with the proposed FE approximations, the minimum problem (4.8) which approximates the minimum problem (4.1) can be transformed into

$$\wp\left(\widehat{\boldsymbol{U}}^{\boldsymbol{0}}\right) = \min_{\widehat{\boldsymbol{U}}\in\mathbb{K}^N} \wp\left(\widehat{\boldsymbol{U}}\right) \,, \tag{4.55}$$

$\mathbb{K}^N$ being the set

$$\mathbb{K}^N = \{\widehat{\boldsymbol{U}} \in \mathbb{R}^{2N} \,/\, \boldsymbol{A}\,\widehat{\boldsymbol{U}} \geq 0\}\ . \tag{4.56}$$

4.4.2 C^0 Method: numerical strategy

Also in this case the solution of the specific problems here analysed is obtained by implementing the method with the program Mathematica ® (Wolfram, 2003). The analysis proceeds into the following steps:

1. definition of the structural geometry and of its discretization;
2. discretization of the displacement field;
3. definition of the potential energy as a linear functional of the nodal displacement parameters;
4. definition of the side conditions;
5. definition of the external boundary conditions;
6. numerical solution of the problem with a linear programming routine;
7. post-processing (evaluation of the displacement and of the strain corresponding to the approximate solution).

* * *

1. Let us denote Ω_* the domain representing the structural geometry in $\mathcal{E}^2$; consider the minimum rectangular domain Ω^* containing Ω_*. The whole domain Ω^* is partitioned into *N* basic units (i.e. rectangular, triangular units) Ω_i, we call them subdomains. The set $\pi^* = (\Omega_i)_{i\in\{1,\dots,N\}}$ constitutes a partition of Ω^*, that is:

$$\bigcup_{i=1}^{N} \Omega_i = \Omega^* \quad \& \quad \Omega_i \cap \Omega_j = \emptyset\ ,\ \ \forall i,j \in \{1,\dots,N\}\ \ /\ \ i \neq j\ . \tag{4.57}$$

To take into account the presence of voids in the domain Ω_* is necessary to perform an appropriate elimination of some elements belonging to π^*. To this purpose, we consider the set

$$\pi_M = \{\Omega_i \in\ \pi^* \,/\, \Omega_i \cap\, \Omega_* \neq \emptyset\}\,, \tag{4.58}$$

where *M* is the cardinality of π_M. Defining $\Omega\ = \mathrm{U}_{\Omega_j\in\pi_M}\,\Omega_j$ from (4.58) it follows:

$$\Omega\ \supseteq\ \Omega_*\ . \tag{4.59}$$

Therefore π_M is a particular cover of the real structural domain Ω_*: it is the minimum cover of Ω_* (with respect to the cardinality) and at the same time it constitutes a finite partition of Ω, which becomes *our structural model domain*. Finally, it is to be noticed

that π_M is a countable set of subdomains having finite perimeter, therefore, is a Caccioppoli partition of Ω in the sense of Chambolle et al (2007).

* * *

2. The displacement field $\boldsymbol{u} = \boldsymbol{u}(\boldsymbol{x})$, defined in Ω, is approximated through C^0 functions belonging to a subset of C^0 depending strictly to the finite element considered (Bathe and Wilson, 1976). In our analysis, we try to adopt various finite element, but the best choice, balancing accuracy and simplicity, turned out to be a second order Lagrangian quadrangular element (**Fig. 4.6**). In what follows, we refer to this special kind of element and to its shape functions.

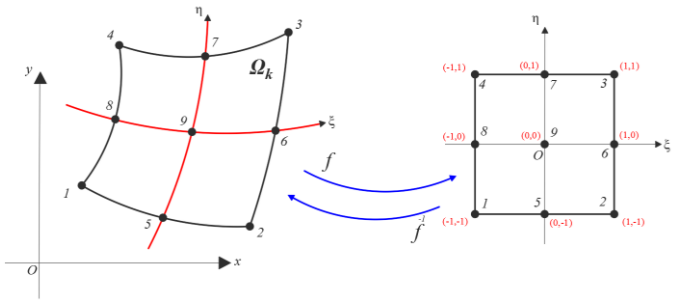

Fig. 4.6 - The generic domain Ω_k and the second order Lagrangian element with 9 nodes is shown. The functions f represents the diffeomorphism from these two domains.

With reference to **Fig 4.7**, in the plane (ξ, η) the shape function $N_{ij} = N_{ij}(\xi, \eta)$ with $(i, j) \in \{1,2,3\} \times \{1,2,3\}$ is referred to the point of coordinates (ξ_i, η_j). In particular, has to result $N_{ij}(\xi_i, \eta_j) = 1$ and $N_{ij}(\xi_k, \eta_l) = 0$ for all $(k, l) \in \{1,2,3\} \times \{1,2,3\} \backslash (i, j)$.

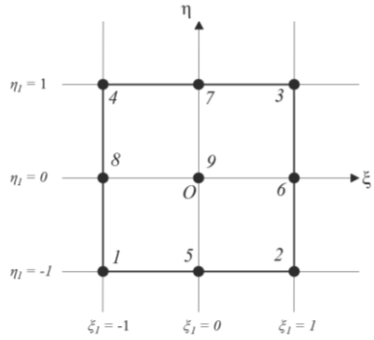

Fig. 4.7 - The generic subdomain Ω_k and the second order Lagrangian element with 9 nodes is shown.

The generic shape function could be obtained as the product of two one-dimensional second order Lagrangian shape functions, e.g. the shape function N_{23} is:

$$N_{23} = \frac{(\xi-\xi_1)(\xi-\xi_3)}{(\xi_2-\xi_1)(\xi_2-\xi_3)} \cdot \frac{(\eta-\eta_1)(\eta-\eta_2)}{(\eta_3-\eta_1)(\eta_3-\eta_2)} \tag{4.60}$$

and, obviously, results $N_{23}(\xi_2,\eta_3) = 1$ and $N_{23}(\xi_i,\eta_j) = 0$ for all $(i,j) \in \{1,2,3\} \times \{1,2,3\}\backslash(2,3)$. It is well-known that the maximum one-dimensional polynomial degree is of the second order (i.e. $\propto \xi^2, \eta^2$) whilst the maximum polynomial term is of the fourth order (i.e. $\propto \xi^2\eta^2$).

Remark 5|4. In the elastic case, Lagrangian shape functions needing the definition of many internal nodes, are not convenient since the process of global assembly gets rid of superfluous internal stiffness contributions. Anyhow, in our analysis, since the stiffness plays no role, the internal nodes are more useful because they allow a better description of displacement fields with sharp gradients inside the domain. ■

Using the diffeomorphism *f*, namely:

$$f\colon (x,y) \in \Omega_{\mathrm{k}} \to \big(\xi(x,y), \eta(x,y)\big)\,, \tag{4.61}$$

it is possible to associate to each node belonging to the domain Ω_k in the plane (x,y) the relative shape function $N_{ij}^f(x,y)$ defined as:

$$N_{ij}^f\colon (x,y) \in \Omega_{\mathrm{k}} \to N_{ij} \circ f(x,y)\,. \tag{4.62}$$

In the global reference (O,x,y), denoting with $l \in \{1,..,9\}$ the generic node of the finite element Ω_{k}, the displacement $\boldsymbol{u}_k$ can be expressed as:

$$\boldsymbol{u}_k\colon (x,y) \in \Omega_{\mathrm{k}} \to \sum_{l=1}^{9} N_l^f(x,y) \cdot (U_l, V_l)\,, \tag{4.63}$$

where (U_l, V_l) is the vector collecting the two unknown scalar translations of the nodes l. The global displacement is written as:

$$\boldsymbol{u}\colon \boldsymbol{x} \in \Omega \to \begin{cases} \boldsymbol{u}_1\ ,\ if\ \boldsymbol{x} \in \Omega_1\ , \\ \vdots \\ \boldsymbol{u}_j\ ,\ if\ \boldsymbol{x} \in \Omega_j\ , \\ \vdots \\ \boldsymbol{u}_M\ ,\ \mathrm{if}\ \boldsymbol{x} \in \Omega_M\ , \end{cases} \tag{4.64}$$

where $\boldsymbol{u}_k = \boldsymbol{u}|_{\Omega_k}\ \forall\, k \in \{1, \dots, M\}$. In particular, the continuity on the boundary is ensured by the finite element chosen ad its relative shape function. Furthermore, it is to be notice that the global displacement field $\boldsymbol{u}$ depends on $2N$ scalar translational parameters:

$$(U_l, V_l,)_{l\in\{1,..,N\}}\ . \tag{4.65}$$

These $2N$ independent parameters can be collected in the single vector:

$$\widehat{\boldsymbol{U}} = \left(U_1, V_1, .., U_j, V_j, .., U_N, V_N\right)\ ,\quad \widehat{\boldsymbol{U}} \in \mathbb{R}^{2N}\ . \tag{4.66}$$

* * *

3. The potential energy $\wp$, coincident with the potential energy of the external forces only, can be expressed again in terms of the components of $\widehat{\boldsymbol{U}}$, $\wp$ being the opposite of the scalar product of the applied forces times the displacements of their points of application, that is a linear function of $2N$ unknown Lagrangian parameters, that can be symbolically expressed as follows:

$$\wp = \wp\left(\widehat{\boldsymbol{U}}\right)\ ,\ \widehat{\boldsymbol{U}} \in \mathbb{R}^{2N}\ . \tag{4.67}$$

The problem can be formulated, as already described in (4.55), as a linear programming one, in the form:

$$\min_{\widehat{\boldsymbol{U}}\in\mathbb{K}^N} \wp\left(\widehat{\boldsymbol{U}}\right), \tag{4.68}$$

$\mathbb{K}^N$ being the subset of $\mathbb{R}^{2N}$ defined by the unilateral constraints enveloping the convex cone Sym^+ to which the latent strain $\boldsymbol{E}$ must belong. It remains to define explicitly the subset $\mathbb{K}^N \subseteq \mathbb{R}^{2N}$.

* * *

4. Since the subset $\mathbb{K}^N$ is substantially identified by a number of inequalities on the latent strain $\mathbf{E}$, in what follows we summarize how to write such unilateral restrictions in terms of the displacements of the nodes of the element Ω_k. Recalling that the displacement field in each finite element Ω_k can be expressed as follows:

$$\boldsymbol{u}_k = \boldsymbol{u}|_{\Omega_k} = \sum_{l=1}^{9} N_l^f(x, y) \cdot (U_l, V_l)\ , \tag{4.69}$$

the latent strain, obtained as the symmetric part of the gradient of $\boldsymbol{u}_k$, is:

$$\mathbf{E}_k = \boldsymbol{E}|_{\Omega_k} = \mathrm{Sym}\nabla \boldsymbol{u}_k \ . \tag{4.70}$$

The latent strain has to belong to the semidefinite positive space Sym^+. This condition, in the space $(\varepsilon_{11}, \varepsilon_{22}, \sqrt{2}\varepsilon_{12})$, is represented geometrically in **Fig. 4.8** where he intersection between the cone $C: det\boldsymbol{E} \geq 0$ and the half-space $tr\boldsymbol{E} \geq 0$ is depicted.

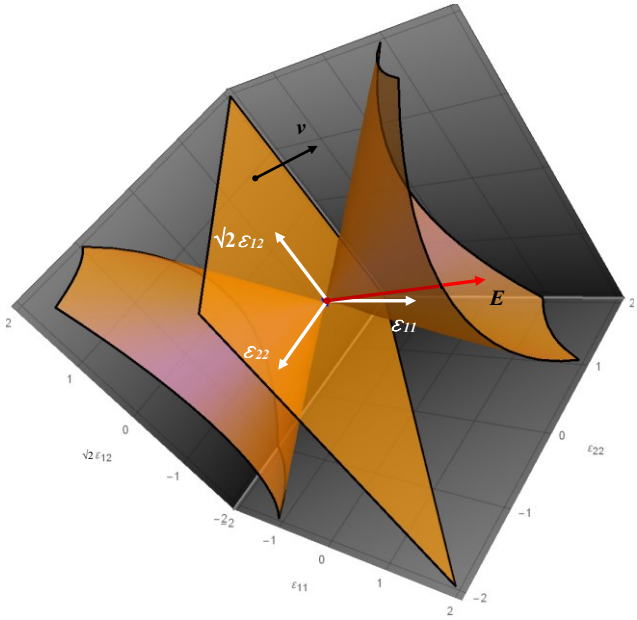

Fig. 4.8 - Three-dimensional representation, in the space $(\varepsilon_{11}, \sqrt{2}\varepsilon_{12}, \varepsilon_{22})$, of the cone $C: det\boldsymbol{E} \geq 0$ and of the plane $\pi: tr\boldsymbol{E} = 0$. The vector $\boldsymbol{v}$ is orthogonal to the π plane and points to the half-space $tr\boldsymbol{E} \geq 0$. The intersection between the half-space and the cone individuates the semidefinite positive convex cone Sym^+. A compatible vector $\boldsymbol{E}$ belonging to Sym^+ is depicted in red.

As already said, the condition on $\boldsymbol{E}$ is non-linear. Anyhow it is possible to approximate it with a finite set of linear relations, in order to reduce the non-linear problem to a linear one.

The idea at the base of this transformation is to linearly approximate the convex cone through a certain number of tangent planes. The construction can be based on a set of points, equally spaced along a cross-section of the cone. For each point of this set we define a tangent plane. The set of all tangent planes constitutes an envelope of the cone. Increasing the number of points the envelope tends to give a better fit of the non-linear surface as depicted in **Fig 4.9**.

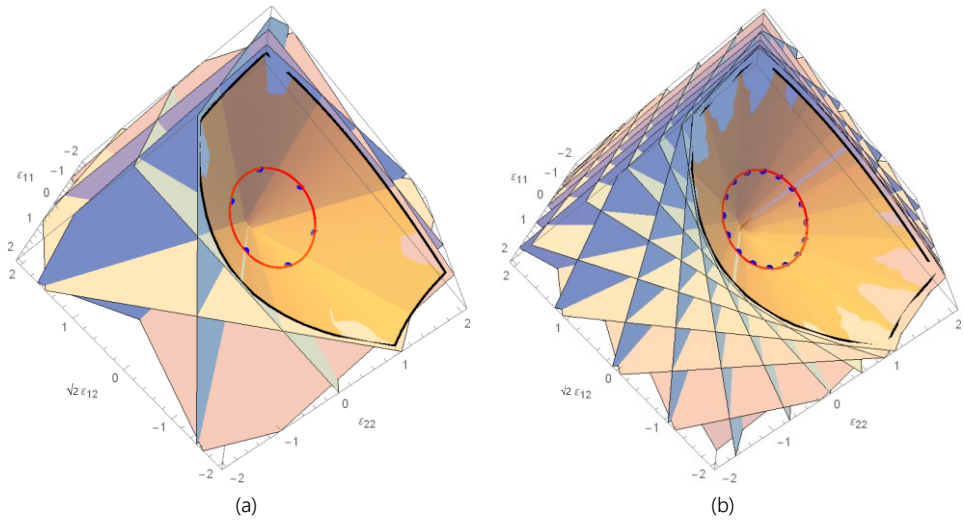

Fig. 4.9 - Two envelopes are presented in a comparative way. In (a) envelope formed by 6 tangent planes and in (b) by 16 planes. The cross-section between the cone and a plane, orthogonal to the axis of the cone, is represented by the red curve. The blue dots, belonging to the curve, are the "generators" of the plane envelope.

Thus, being $(\tilde{x}, \tilde{y})$ the coordinates of the node l belonging to the domain Ω_k, the condition $\boldsymbol{E} \in Sym^+$, can be written punctually as:

$$\mathbf{E}_k(\tilde{x}, \tilde{y}) \in Sym^+ , \tag{4.71}$$

and it is transformed, using n tangent planes, to the following inequalities:

$$\mathbf{A}_k(\tilde{x}, \tilde{y})\, \hat{\boldsymbol{U}}_k \geq \mathbf{0} , \tag{4.72}$$

where $\mathbf{A}_k(\tilde{x}, \tilde{y})$ is a matrix collecting the components of normal vectors (see **Fig. 4.10**) to the tangent planes and $\hat{\boldsymbol{U}}_k$ is the vector of the nodal translational parameters relative to the element k.

These unilateral relations have to be written for all nodes of the element Ω_k and for all elements of the global domain Ω. Collecting all these relations in matrix form, we have a set of unilateral constraints, of the type:

$$\boldsymbol{A}\, \hat{\boldsymbol{U}} \geq \mathbf{0} . \tag{4.73}$$

These relations can be viewed as restriction on the vector $\hat{\boldsymbol{U}} = (U_k, V_k)_{k\in\{1,..,N\}} \in \mathbb{R}^{2N}$, defining the set

$$\mathbb{K}^N = \{\hat{\boldsymbol{U}} \in \mathbb{R}^{2N} \,/\, \boldsymbol{A}\, \hat{\boldsymbol{U}} \geq \mathbf{0}\} . \tag{4.74}$$

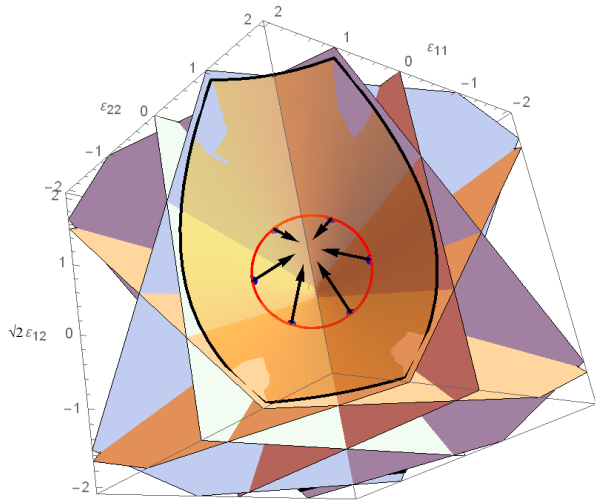

Fig. 4.10 - The envelope of the cone with 6 tangent planes and the surface gradients at the generating points are shown. The condition $\mathbf{E}_k(\tilde{x},\tilde{y}) \in Sym^+$ can be discretized by using the gradient vectors through inequalities expressed symbolically in the form $\mathbf{A}_k(\tilde{x},\tilde{y})\,\widehat{\boldsymbol{U}}_k \geq \mathbf{0}$.

Finally to this set must be added the external boundary conditions, written as for the PR method, and concerning the given settlements (or eigenstrains) and the fixing conditions. All together the constraints define a domain $\mathbb{K}^N \subseteq \mathbb{R}^{2N}$, in which the optimal solution has to be found; such domain is a convex polytope of the $\mathbb{R}^{2N}$ space.

* * *

5. With the above approximation the structural problem is formulated as a minimum problem: "*find a piecewise rigid displacement* $\widehat{\boldsymbol{U}}^0$ *which minimizes the potential energy* $\wp$ *in* $\mathbb{K}^N$*:*

$$\min_{\widehat{\boldsymbol{U}}\in\mathbb{K}^N} \wp\left(\widehat{\boldsymbol{U}}\right) \text{ ."} \tag{4.75}$$

This linear programming problem is solved with the simplex method, or with the interior point method if the number of unknowns is large.

* * *

6. Once the minimizer $\widehat{\boldsymbol{U}}^0$ has been obtained it is an easy task to construct the deformed shape of the structure, and graphically represent the corresponding rotation and strain.

Remark 6|4. We have to point out that the appearance of piece-wise rigid mechanisms (producing concentrated fractures) rather than continuous mechanisms (entailing diffuse fractures), is often due, in real structures, to mechanical characteristics, such as cohesion, toughness and finite friction, which are not accounted for by the NRNT model.

Indeed for NRNT materials, on an energetical ground, in general, it is not possible to prefer one way of deformation over the other. On formulating the bvp for NRNT materials as a minmum search, this peculiar behaviour is essentially ascribable to the absence of any growth property of the energy with respect to unbounded fracture strains. A growth property of the energy for displacement fields in $BD(\Omega)$ is restored by introducing the so-called "**Safe Load Condition**", a condition which is necessary, with the known theorems, to prove the existence of a displacement solution for the parent equilibrium problem concerning NENT materials, see (Giaquinta and Giusti, 1985), (Anzellotti ,1985).

There is then a legitimate way to encourage rigid block mechanisms over diffuse deformations. It consists in adding, all over the loaded boundary, an evanescent uniform pressure (say of the order of a small fraction of the atmospheic pressure). This trick is sufficient to provide the bvp with the "**Safe Load Condition**", and to make concentrated fractures, and then rigid block deformations, as the favorite minimizing mechanisms.

Chapter 5

SOME TRIVIAL EXAMPLES

Prologue. In this Chapter, we present some basic applications to trivial benchmark problems of our two numerical methods, namely the PR method based on rigid blocks (modelling the cracks as concentrated), and the C^0 method based on continuous functions (modelling the cracks as smeared). It will be seen that with the C^0 method the solution will often returns a hint on a partition into rigid blocks. In particular, in the cases in which the fractures lines are difficult to be detected (due to their location or slope), the subdivision suggested by the continuous approach could be used to start another analysis with the PR method.

■ 5.1 EXAMPLE 1: A TRIVIAL BENCHMARK CASE

As a first paradigmatic example we consider the first benchmark problem, illustrated in **Section 3.5** (see also **Fig. 3.3** and **Fig. 3.4**).

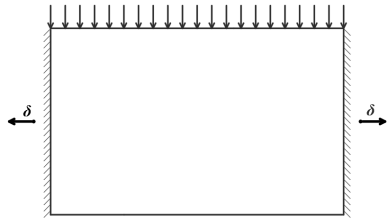

Fig. 5.1 - A panel of NRNT material, loaded on the top edge by a uniformly distributed load and subjected along the left and right sides to given outward settlements.

The example concerns a wall of NRNT material, loaded on the top edge by a uniformly distributed load and subjected along the left and right constrained sides to given outward settlements (see **Fig. 5.1**). The base is unconstrained and loaded by zero tractions.

5.1.1 Analytical solution

A possible analytical solution of the problem shown in **Fig. 5.1**, obtained considering singular stress and strain fields, is represented in **Fig. 5.2** (see **Section 3.5**).

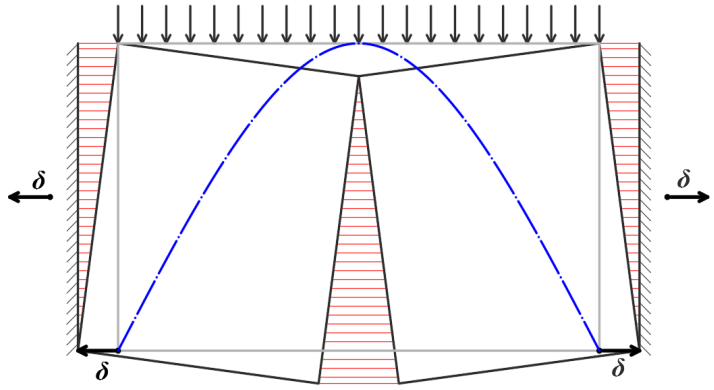

Fig. 5.2 - A solution of the bvp using singular stress and strain fields. The crosshatch in red represents the singular deformations $\boldsymbol{E}^s$ along the fracture lines whilst the dash-dotted blue line represents the support of the singular part $\boldsymbol{T}^s$ of the stress field, in equilibrium with the given loads.

5.1.2 Numerical analysis with the PR method (quadrilateral elements)

The NRNT panel is discretized with rigid blocks using 160 square elements. The load is applied on the top edge (yellow stripe). The left and right edge are subjected to a given outward settlement δ as shown below (**Fig. 5.3**). The boundary constraints, expressing the settlements, can be written in terms of the displacements of the nodes belonging to the interfaces lying on the constrained boundary. In particular, let $\boldsymbol{n}$ and $\boldsymbol{t}$ be the outward normal and tangential unit vectors to $l(A,B)$ side (see **Fig. 5.3**), $\boldsymbol{u}$ the piecewise rigid displacement of the whole structure and P a generic node belonging to $l(A,B)$.

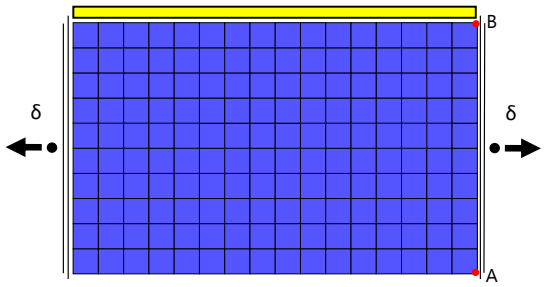

Fig. 5.3 - A panel of NRNT material loaded on the top edge by a uniformly distributed load (represented by the yellow strip) and subjected, on the left and right edges, to given outward settlements is discretized with 160 square elements.

The boundary relations for the right side $l(A,B)$ can be expressed as:

$$\begin{aligned} \boldsymbol{u}(P)\cdot\boldsymbol{t} &= 0 \qquad \forall\, \mathrm{P} \in l(A,B)\,, \\ \boldsymbol{u}(P)\cdot\boldsymbol{n} &\le \delta \qquad \forall\, \mathrm{P} \in l(A,B)\,. \end{aligned}$$

Similar relations have to be written for the left constrained side. These boundary relations combined with the internal ones (relative to the interfaces between the blocks) will define the subset $\mathbb{K}^M$ in which the optimal solution has to be found. Since the number of elements is 160, the total unknowns are 480 (i.e. the dimension of $\widehat{\boldsymbol{U}}$). The number of internal relations, both equalities and inequalities, defining the subset of $\mathbb{K}^M \subseteq \mathcal{R}^{480}$ is 1920 (to which the external boundary conditions have to be added). The solution $\widehat{\boldsymbol{U}}^0$ of the minimum problem:

$$\min_{\widehat{\boldsymbol{U}}\in\mathbb{K}^M} \wp\left(\widehat{\boldsymbol{U}}\right),$$

reached through the simplex method in 0.09s (with an Intel® Core™ i7-6700HQ), is shown in **Fig. 5.4**.

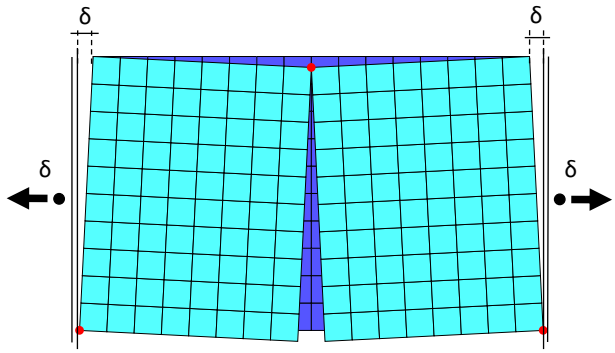

Fig. 5.4 - A graphical representation of the solution $\widehat{\boldsymbol{U}}^0$ of the minimum problem obtained with the PR method: the panel forms an isostatic substructure (three-pin arch).

From **Fig. 5.4**, it should be noted that three hinges formed. Initially the panel was hyperstatic with many redundancies, but the formation of these three hinges turns it into an isostatic substructure. By adopting a thrust line solution for the stress, the position of the hinges determines three conditions, which are sufficient to determine a unique pressure line, as shown in **Fig. 5.5**.

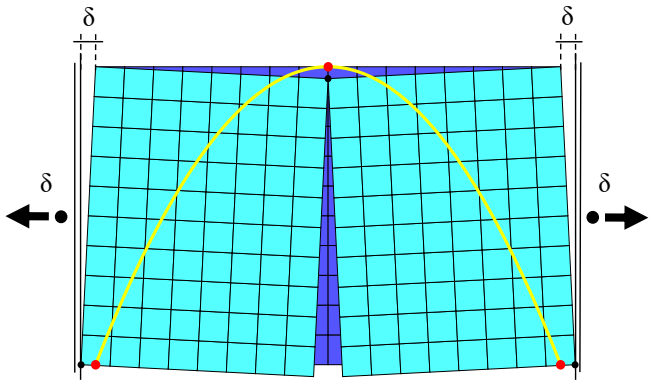

Fig. 5.5 - Hinges and corresponding thrust line.

Remark 1|5. It should be noted that the solution $\widehat{\boldsymbol{U}}^0$ of the minimum problem returns, as we expect, a partition of the whole domain into two rigid blocks. Accordingly, in this case, a discretization with a large number of elements is not necessary. ■

5.1.3 Numerical analysis with the PR method (triangular elements)

In order to test the PR method on different discretizations, we use here a structured triangular mesh. This choice would allow the panel to show also diagonal cracks. The NRNT panel is discretized with rigid blocks using 640 triangular elements. The load is applied as before and a given outward settlement δ is considered (see **Fig. 5.6**). The boundary constraints are expressed essentially in the same way. Since the number of elements is 640, the unknowns are 1920 (that is the dimension of $\widehat{\boldsymbol{U}}$). The number of internal relations, both equalities and inequalities, defining the subset of $\mathbb{K}^M \subseteq \mathcal{R}^{1920}$ is 5760 (to which the external boundary relations have to be added).

The solution $\widehat{\boldsymbol{U}}^0$ of the minimum problem is reached through the simplex method in 0.70s with an Intel® Core™ i7-6700HQ (see **Fig. 5.7**). The solution is the same as before: three hinges form then the panel becomes isostatic and the exact line of thrust can be determined (**Fig. 5.8**).

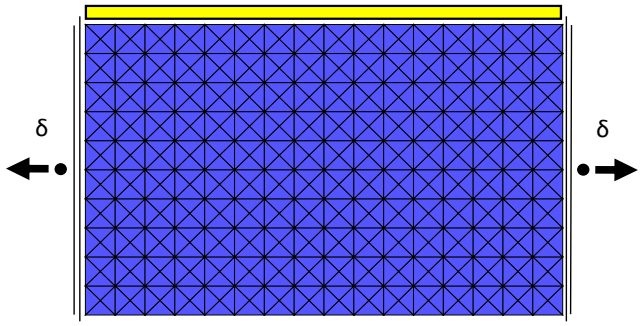

Fig. 5.6 - The same panel of NRNT material is discretized with triangular element. The load is uniform and acts on the top edge (yellow strip). The left and right edges are subjected to given outward settlements.

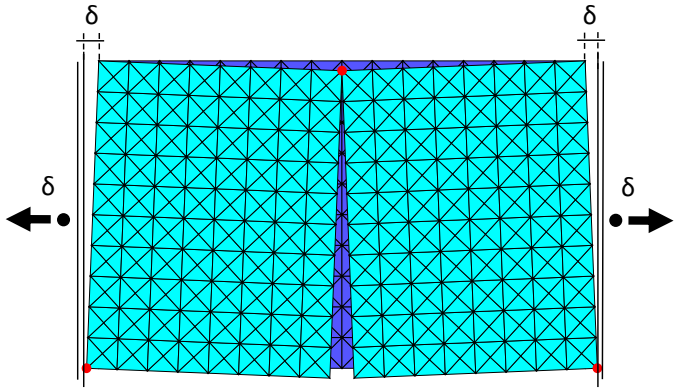

Fig. 5.7 - Solution $\widehat{U}^0$ of the minimum problem obtained with the PR method.

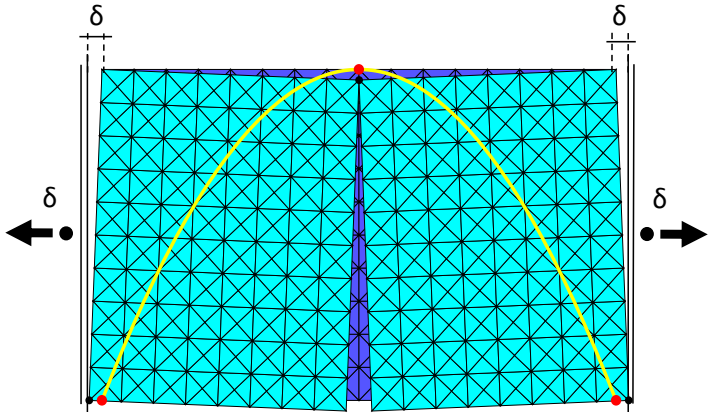

Fig. 5.8 - The hinges formed and the relative thrust line are represented.

5.1.4 Numerical analysis with the C^0 method (square FE mesh)

Here we analyse the problem of **Fig. 5.1** with the C^0 method, based on an approximation with continuous functions. The panel of NRNT material of **Fig. 5.1** is discretized using 40 9-nodes square elements (a second order Lagrangian quadrangular element). We consider only the load due to the self-weight applied to the Gaussian points of each element. The left and right edge are subjected to given outward settlements δ as shown in **Fig. 5.9**.

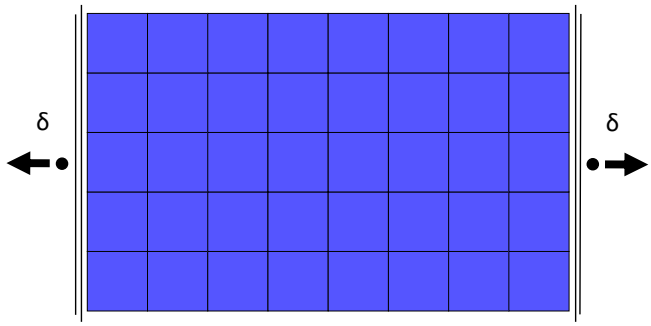

Fig. 5.9 - A panel of NRNT material discretized with 40 square elements. The load due to the self-weight is applied at the Gauss points of each element. The left and right edges are subjected to given outward settlements δ.

The solution $\widehat{\boldsymbol{U}}^0$ of the minimum problem is reached through the minimization of the energy into the finite element space defined previously (see Section 4.4). The solution obtained with the interior point method in 25s (with an Intel® Core™ i7-6700HQ) is shown graphically in **Fig. 5.10**.

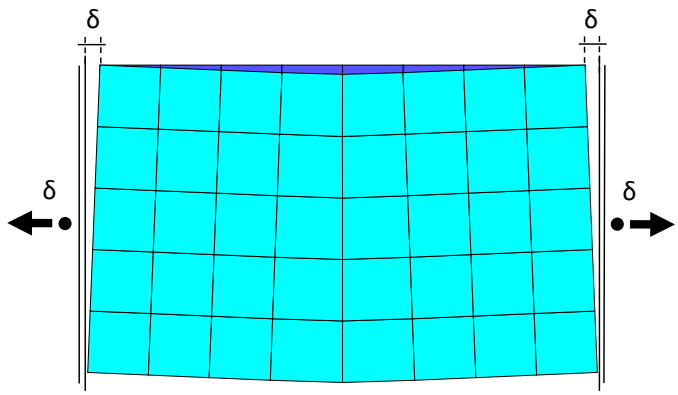

Fig. 5.10 - Solution $\widehat{\boldsymbol{U}}^0$ of the minimum problem defined in **Fig. 5.9**.

Below a stream plot of the displacement field is reported in **Fig. 5.11**. This graph indicates clearly two centres of rotation.

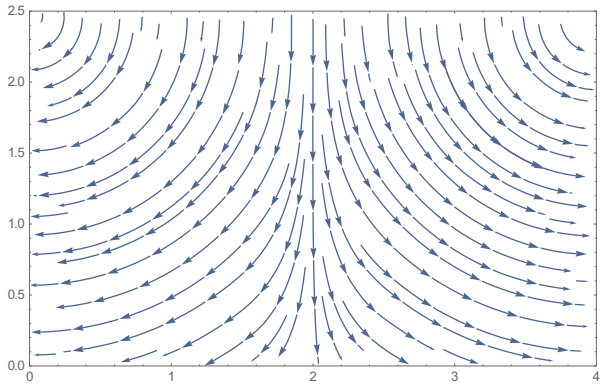

Fig. 5.11 - The stream plot of the displacement field is reported: two centres of rotation are clearly shown.

To represent the strain field $\boldsymbol{E}$, in **Fig. 5.12** we report a measure of the deformation, namely $|\boldsymbol{E}|^2 = tr(\boldsymbol{E}\boldsymbol{E}^T)$. From **Fig. 5.12** we see that the gradient of deformation is concentrated on the central strip of elements, whilst the other elements are characterized by strains whose norm is close to zero.

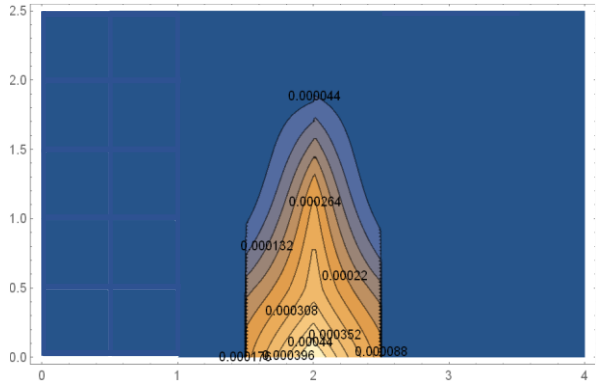

Fig. 5.12 - The field $|\boldsymbol{E}|^2 = tr(\boldsymbol{E}\boldsymbol{E}^T)$ is reported.

The skew-symmetric part of the displacement field, representing the local rotation field, is depicted in **Fig. 5.13**. It should be noticed that the gradient of rotation is essentially concentrated along the middle vertical line (**Fig. 5.13**).

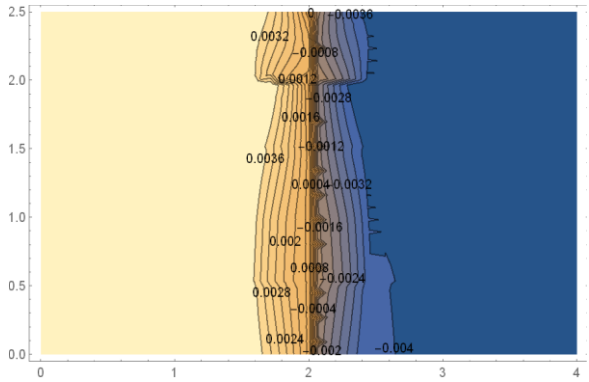

Fig. 5.13 - Rotation field over the whole domain.

By depicting the positive rotations in red and the negative ones in blue (**Fig. 5.14**), we obtain a neat subdivision of the domain into two blocks. Such blocks deform essentially as rigid bodies since the rotation is piece-wise constant and the deformation is practically constant (see **Fig. 5.14**). Notice that the strain, though we are using continuous functions, is practically all concentrated on a line, whose size would reduce if use a finer mesh were used.

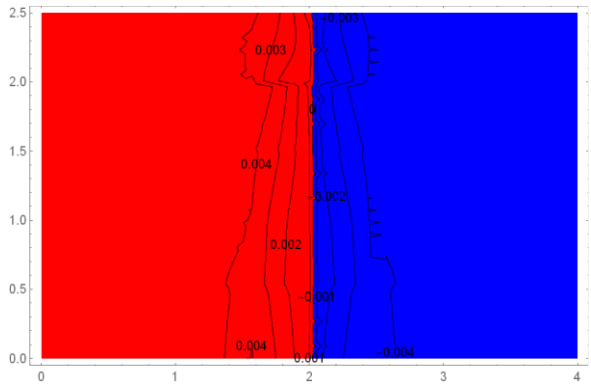

Fig. 5.14 - By depicting the positive rotations in red and the negative ones in blue, a neat partition of the whole domain into two rigid blocks can be seen.

Remark 2|5. By comparing the solution obtained with the C^0 method (see **Figs. 5.10-14**) with that obtained with the PR method (see e.g. **Fig. 5.4** or **Fig. 5.7**), the solution obtained with the C^0 method suggest the possibility of using them in combination: first run the solution with the C^0 method obtaining the optimal partition, then run another numerical solution, based on this optimal partition, by using the PR method.

5.1.5 Example 1 modified: numerical analysis with the C^0 method (square FE mesh)

Here we show an application of the C^0 method for the same kind of problem analysed in the previous section but considering a panel with a different discretization and aspect ratio (i.e. the hypothetical crack here should cross the internal part of the Lagrangian elements). The panel of NRNT material of **Fig. 5.1** is discretized using 45 9-nodes square elements (a second order Lagrangian quadrangular element). Even in this case the self-weight is applied to the Gaussian points of each elements and the left and right edge are subjected to given outward settlements δ as shown in **Fig. 5.15a**.

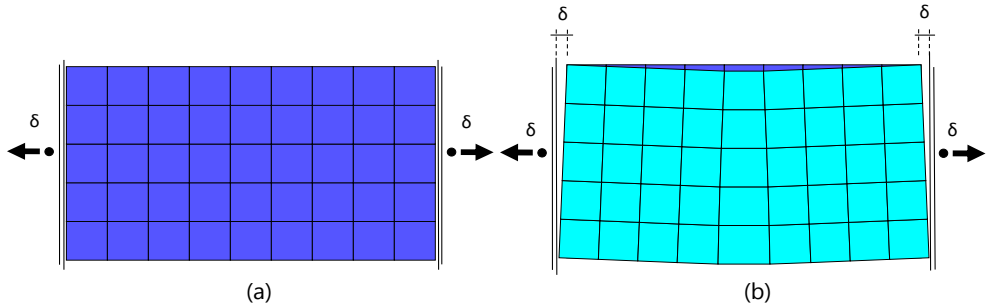

Fig. 5.15 - A panel of NRNT material discretized with 45 square elements (a): the self-weight is applied at the Gauss points of each element, and the left and right edges are subjected to given outward settlements δ. In (b) the displacement field corresponding to the solution $\widehat{\boldsymbol{U}}^0$ of the minimum problem is depicted.

The solution $\widehat{\boldsymbol{U}}^0$ of the minimum problem is reached through the minimization of the energy into the finite element space defined previously (see **Section 4.4**). The solution obtained with the interior point method in 30s (with an Intel® Core™ i7-6700HQ) is shown graphically in **Fig. 5.15b**.

The stream plot of the displacement field, showing clearly two centres of rotation, is reported in **Fig. 5.16a**. The measure of the deformation $|\boldsymbol{E}|^2 = tr(\boldsymbol{E}\boldsymbol{E}^T)$ is depicted in **Fig. 5.16b** and shows that the gradient of deformation is concentrated, even in this case, on the central strip of the elements (cutting them in their centreline), whilst other elements are characterized by strains whose norm is close to zero. The skew-symmetric part of the displacement field (i.e. the local rotation field) is reported in **Fig. 5.16c**: the gradient of rotation is essentially concentrated along the middle vertical line. In **Fig. 5.16d** a neat partition of the domain into two blocks is highlighted. Notice that from **Fig. 5.16b** and **Fig. 5.16c** such blocks behave as rigid bodies since both the deformation and the rotation fields are constant.

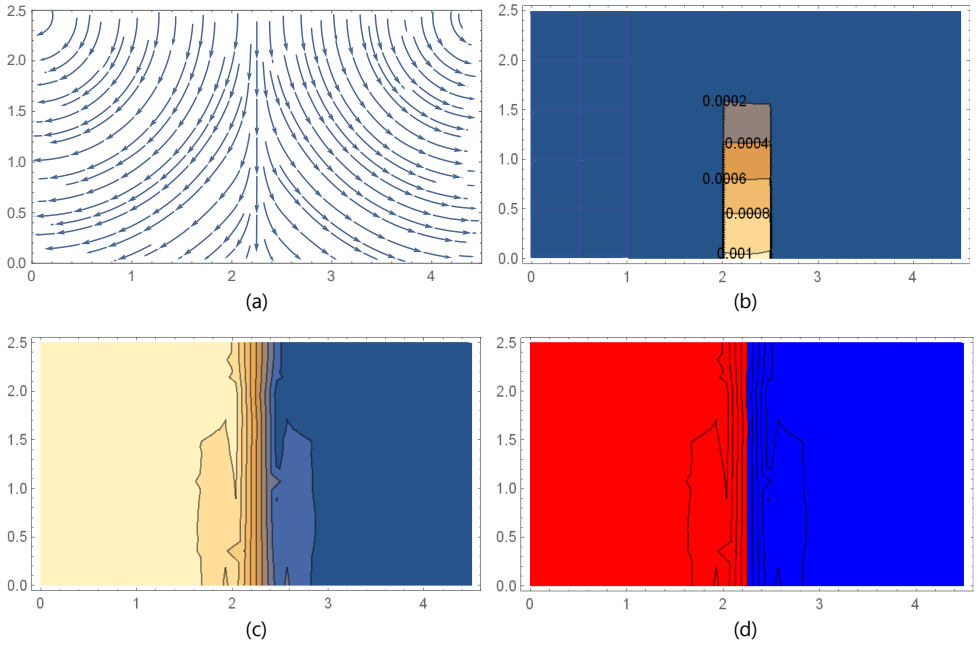

Fig. 5.16 - The stream plot of the displacement field (a), the field $|\boldsymbol{E}|^2 = tr(\boldsymbol{E}\boldsymbol{E}^T)$ (b) and the rotation field (c) over the whole domain are reported. By depicting the positive rotations in red and the negative ones in blue, in (d) a neat partition of the whole domain into two rigid blocks can be seen.

■ 5.2 EXAMPLE 2: DETECTING A VERTICAL CRACK

Let us consider the case of a panel of NRNT material, loaded by its own weight and constrained as shown in **Fig. 5.17a**. This is a so called *mixed problem*, since part of the boundary is loaded and the remaining part is constrained. Part of the bottom constraint is subjected to a given linear settlement distribution as shown in **Fig. 5.17a**. A vertical crack is expected as shown with a red line in **Fig. 5.17b**.

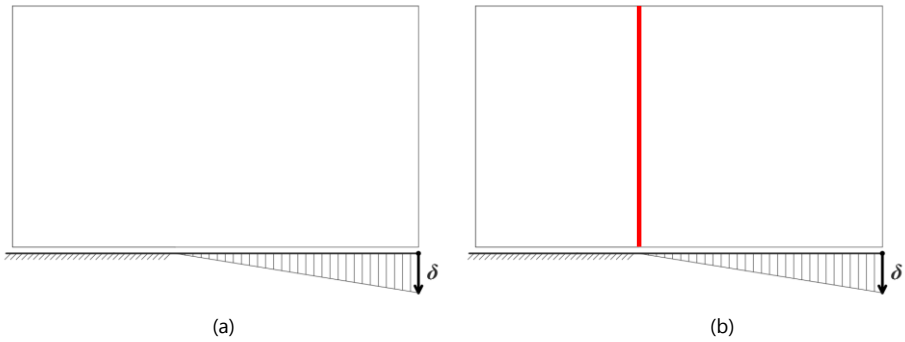

Fig. 5.17 - Mixed bvp for a panel of NRNT material (loaded by its own weight and constrained as shown) subjected to a given linear settlement distribution (a). A vertical crack is expected (b)

5.2.1 Analytical solution

Using singular strain and stress fields, a possible analytical solution of the mixed bvp (shown in **Fig. 5.17a**) is represented in **Fig. 5.18**.

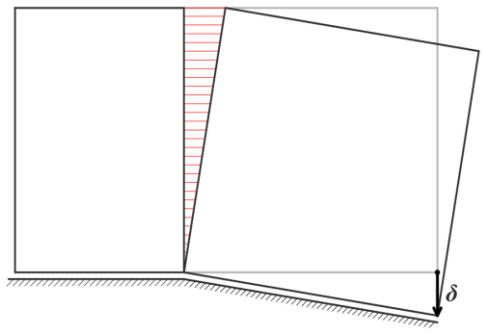

Fig. 5.18 - A possible analytical solution of the bvp depicted in **Fig. 5.17a**, using singular stress and strain fields, is reported. A hinge forms and the crosshatch in red represents the singular deformations $\boldsymbol{E}^s$ along the fracture line.

5.2.2 Numerical analysis with the PR method (quadrangular elements)

The NRNT panel is discretized with rigid blocks using 60 square elements. The load considered is the self-weight applied at the centres of gravity of each block. Part of the boundary is constrained (see **Fig. 5.19**) whilst a part of the bottom edged is subjected to a given linear settlement.

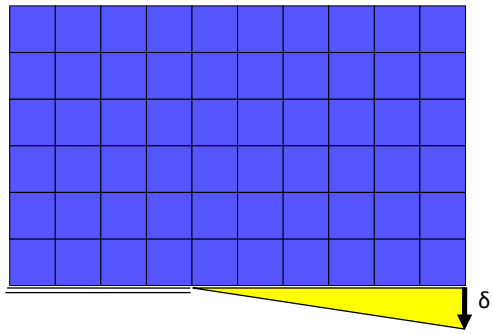

Fig. 5.19 - The NRNT panel of **Fig. 5.17a** is discretized with 60 rigid blocks. Part of the bottom edge is subjected to a given linear settlement δ.

The solution $\widehat{\boldsymbol{U}}^0$ of the minimum problem is reached through the minimization of the energy into the finite space of piecewise rigid displacements (see Section 6.3). The solution obtained with the interior point method in 0.03s (with an Intel® Core™ i7-6700HQ) is shown graphically in **Fig. 5.20**: the PR method returns a vertical crack.

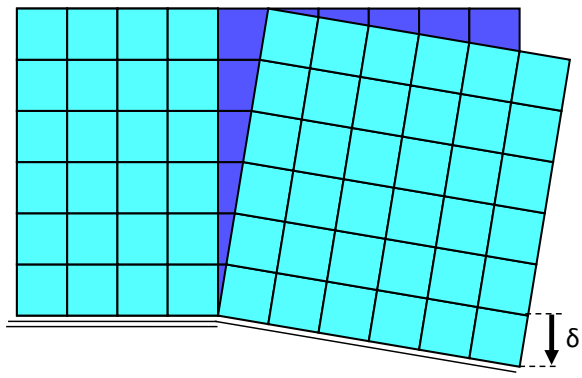

Fig. 5.20 - The solution $\widehat{\boldsymbol{U}}^0$ of the minimum problem is reported.

5.2.3 Numerical analysis with the PR method (triangular elements)

The NRNT panel is discretized with rigid blocks using 240 rigid triangular elements. The load considered is the self-weight applied at the centres of gravity of each triangle. Part of the boundary is constrained (see **Fig. 5.21**) whilst a part of the bottom edged is subjected to a given linear settlement.

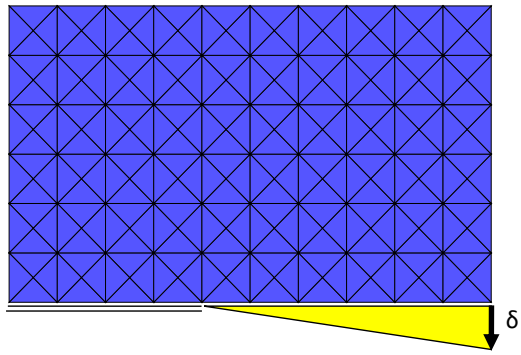

Fig. 5.21 - The NRNT panel of **Fig. 5.17a** is discretized with 240 rigid triangular blocks. Part of the bottom edge is subjected to a given linear settlement δ.

The solution $\widehat{\boldsymbol{U}}^0$ of the minimum problem is reached through the minimization of the energy into the finite space of piecewise rigid displacements (see Section 6.3). The solution obtained with the interior point method in 0.03s (with an Intel® Core™ i7-6700HQ) is shown graphically in **Fig. 5.22**: the PR method returns even in this case a vertical crack.

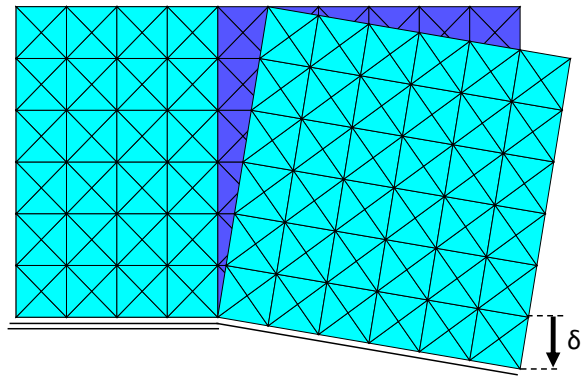

Fig. 5.22 - The solution $\widehat{\boldsymbol{U}}^0$ of the minimum problem is reported.

5.2.4 Numerical analysis with the C^0 method (square FE mesh)

A panel of NRNT material is discretized with 60 9-nodes square elements (a second order Lagrangian quadrangular element). We consider only the load due to the self-weight applied to the Gaussian points of each element. Part of the bottom edge is subjected to a given linear settlement δ as shown in **Fig. 5.23**.

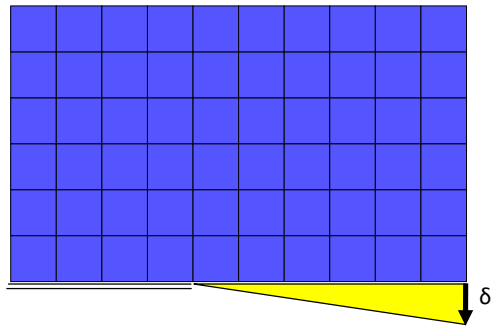

Fig. 5.23 - A panel of NRNT material is discretized by 60 square elements. The load due to the self-weight is applied at the Gaussian points of each element. Part of the bottom edge is subjected to a given linear settlement δ.

The solution $\widehat{\boldsymbol{U}}^0$ of the minimum problem is reached through the minimization of the energy into the finite element space defined previously (see Section 4.4). The solution obtained with the interior point method in 47s (with an Intel® Core™ i7-6700HQ) is shown graphically in **Fig. 5.24**.

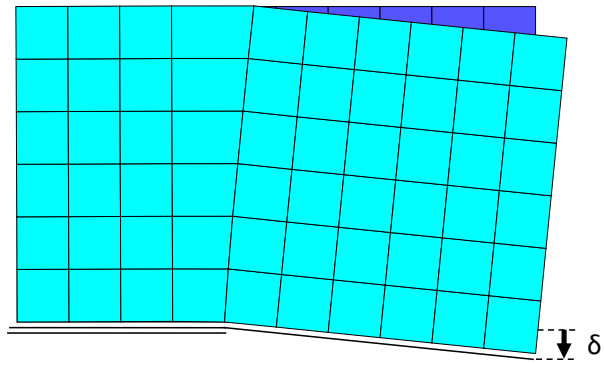

Fig. 5.24 - Solution $\widehat{\boldsymbol{U}}^0$ of the minimum problem defined in **Fig. 5.23**.

In **Fig. 5.25** a stream plot of the displacement field is reported: the graph indicates clearly the centre of rotation.

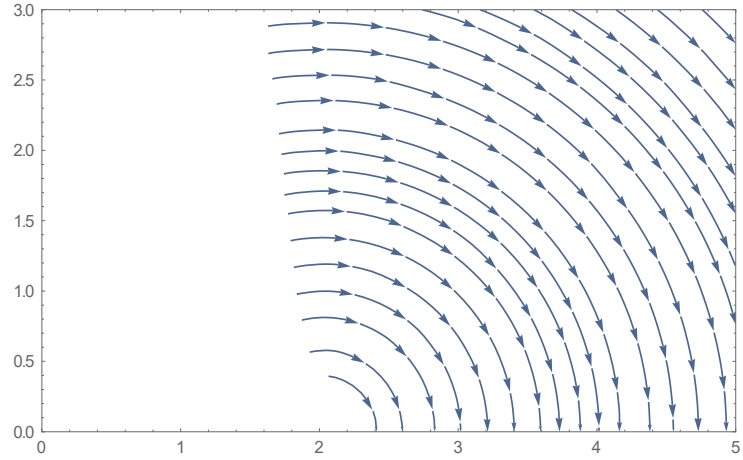

Fig. 5.25 - The stream plot of the displacement field is reported

To represent the strain field $\boldsymbol{E}$, in **Fig. 5.26** we report a measure of the deformation, namely $|\boldsymbol{E}|^2 = tr(\boldsymbol{E}\boldsymbol{E}^T)$. From **Fig. 5.26** we see that the gradient of deformation is concentrated on the central strip of elements, whilst the other elements are characterized by strains whose norm is close to zero.

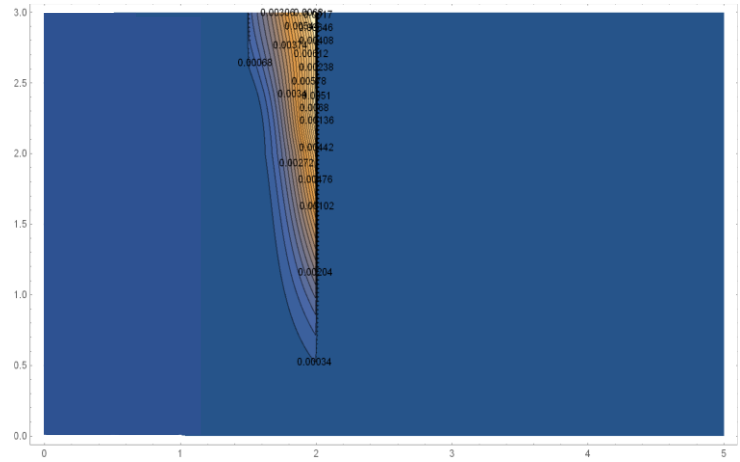

Fig. 5.26 - The field $|\boldsymbol{E}|^2 = tr(\boldsymbol{E}\boldsymbol{E}^T)$ is reported.

The skew-symmetric part of the displacement field, representing the local rotation field, is depicted in **Fig. 5.27**. It should be noticed that the gradient of rotation is essentially concentrated along a vertical line (**Fig. 5.27**).

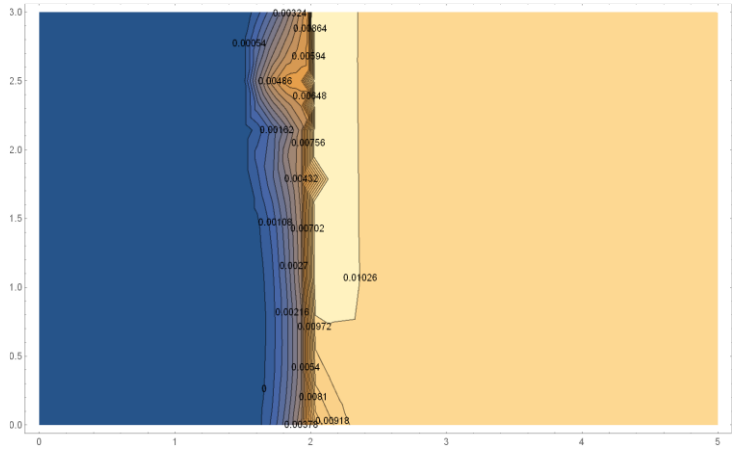

Fig. 5.27 - Rotation field over the whole domain.

By depicting the positive rotations in red and the negative ones in blue (**Fig. 5.28**), even in this case we obtain a neat subdivision of the domain into two blocks deforming as rigid bodies.

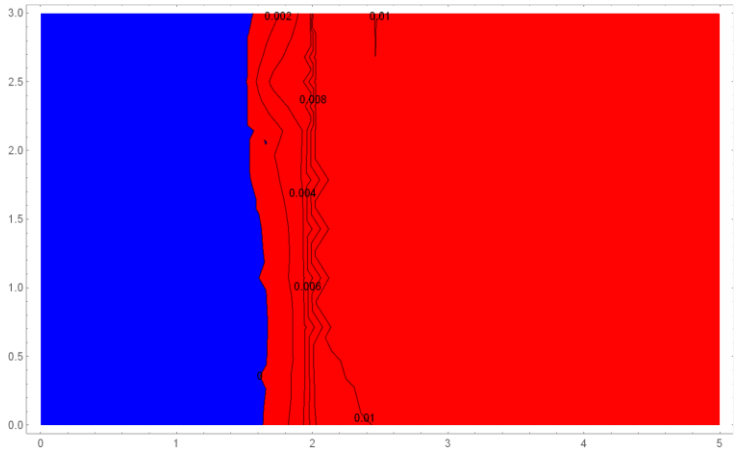

Fig. 5.28 - By depicting the positive rotations in red and the negative ones in blue, a neat partition of the whole domain into two rigid blocks can be seen.

■ 5.3 EXAMPLE 3: DETECTING A DIAGONAL CRACK

Let us consider the case of a panel of NRNT material, loaded by its own weight and constrained as shown in **Fig. 5.29a**. This is a so called *mixed problem*, since part of the boundary is loaded and the remaining part is constrained. Part of the bottom constraint is subjected to a given linear settlement as shown in **Fig. 5.29a**. A diagonal crack is expected as shown with a red line in **Fig. 5.29b**.

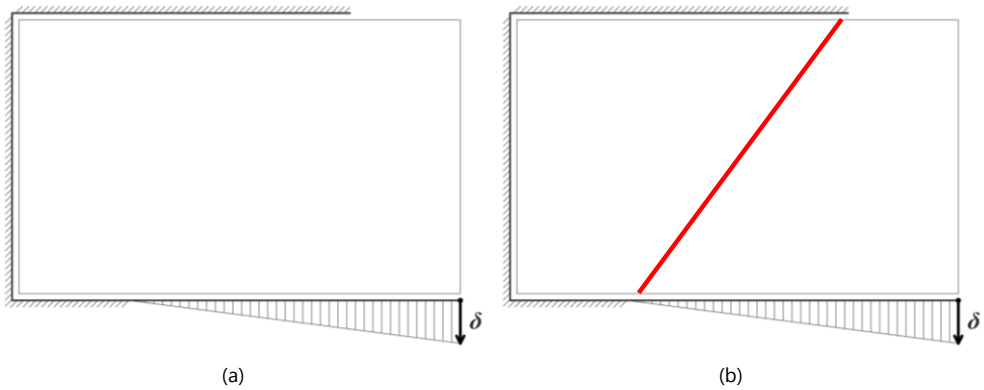

Fig. 5.29 - Mixed bvp for a panel of NRNT material (loaded by its own weight and constrained as shown) subjected to a given linear settlement (a). A diagonal crack is expected (b).

5.3.1 Analytical solution

Using singular strain and stress fields, a possible analytical solution of the mixed bvp (shown in **Fig. 5.29a**) is represented in **Fig. 5.30**.

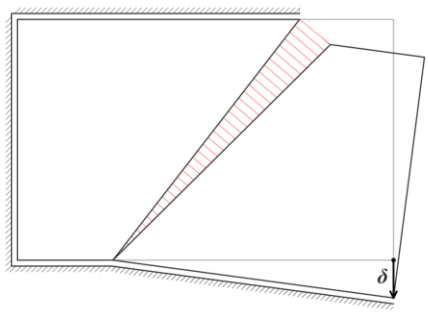

Fig. 5.30 - A possible analytical solution of the bvp depicted in **Fig. 5.29a**, using singular stress and strain fields, is reported. A hinge forms and the crosshatch in red represents the singular deformations $\boldsymbol{E}^s$ along the fracture line.

5.3.2 Numerical analysis with the PR method (quadrangular elements)

The NRNT panel is discretized with rigid blocks using 160 square elements. The load considered is the self-weight applied at the centres of gravity of each block. Part of the boundary is constrained (see **Fig. 5.31**) whilst a part of the bottom edged is subjected to a given linear settlement.

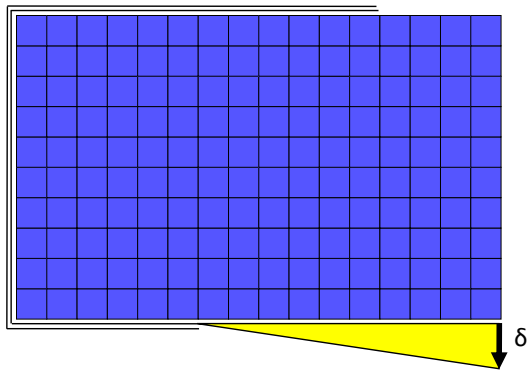

Fig. 5.31 - The panel of NRNT material of **Fig. 5.29** is discretized with 160 rigid blocks.

Though a diagonal crack is expected, the solution $\widehat{\boldsymbol{U}}^0$ of the minimum problem with the PR method returns a vertical crack (**Fig. 5.32**).

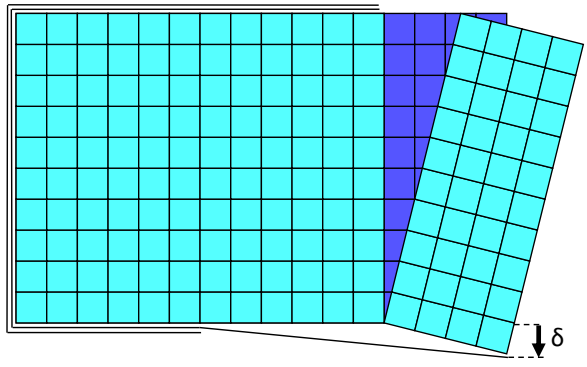

Fig. 5.32 - The solution $\widehat{\boldsymbol{U}}^0$ of the minimum problem is reported.

5.3.3 Numerical analysis with the PR method (triangular elements)

The mixed problem relative to the NRNT panel (**Fig. 5.29a**) and analysed previously (see **Fig. 5.31**) is here discretized with a mesh of 640 triangular elements as shown in (**Fig. 5.33**). The load considered is again the self-weight applied to the centres of gravity of each block and the boundary conditions are the same as those shown in **Fig. 5.29a**.

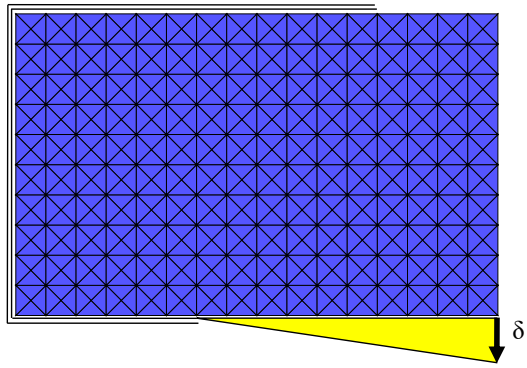

Fig. 5.33 - The NRNT panel is discretized with 640 triangular rigid blocks. Part of the boundary is constrained whilst part is subjected to a given linear settlement as shown.

The numerical solution $\hat{\boldsymbol{U}}^0$ of the minimum problem, with the PR method, now returns the crack pattern shown in **Fig. 5.34**.

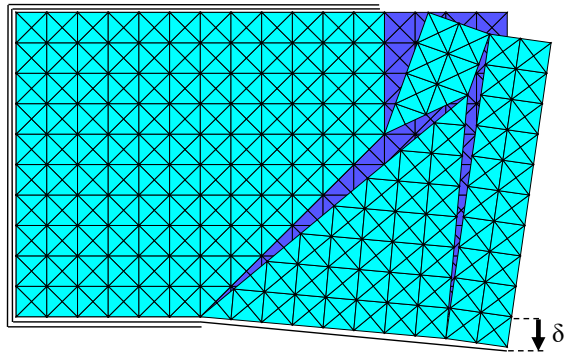

Fig. 5.34 - The solution $\hat{\boldsymbol{U}}^0$ of the minimum problem is reported.

The method cannot identify the expected crack since the given interfaces do no run along the expected direction of the crack.

Remark 3|5. The previous example points out a shortcoming of the PR method: the solution is unable to converge to a concentrated crack whose

support is not parallel to the skeleton of the mesh. The C^0 method does not suffer to this defect, and through more cumbersome from the numerical point of view, can converge to cracks whose support is not parallel to the interfaces of the elements.

Remark 4|5. The inability to catch the diagonal crack inherent to the PR method, can be explained as follows. Let us consider the same problem of **Fig. 5.29** and the coarse mesh of **Fig. 5.35a**.

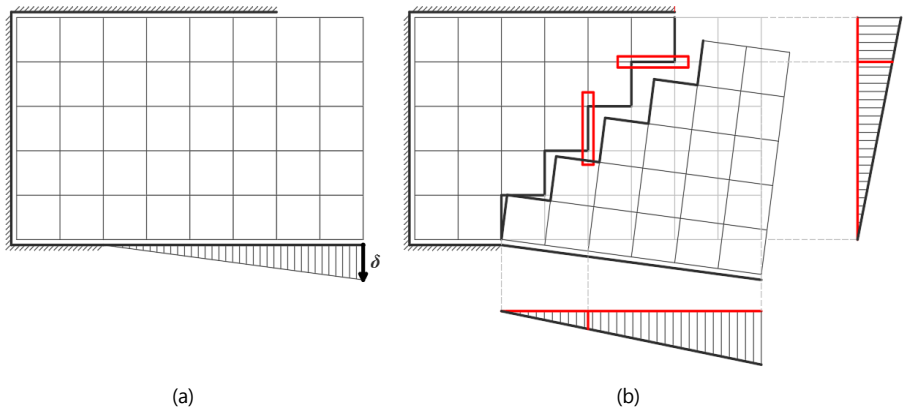

Fig. 5.35 - The NRNT panel of **Fig. 5.29a** discretized with 40 square elements (a). The approximation of a diagonal crack using square elements (b): two adjacent blocks lying along the opening exhibit relative sliding (e.g. for the two highlighted with the red rectangle).

The mechanism associated with an hypothetical diagonal crack is shown in **Fig. 5.35b**. It should be noted that such a diagonal crack using square elements would produce relative sliding among elements lying along a zig-zag line approximating the crack. Heyman's model is based on the assumption that two adjacent elements cannot slide one upon another, then such PR displacement fields, discontinuous along zig-zag lines, are not kinematically admissible. ■

5.3.4 Example 3 modified: numerical analysis with the PR method (triangular elements)

The NRNT panel is discretized with rigid blocks using 384 triangular elements (see **Fig. 5.36**). The load considered is again the self-weight applied to the centres of gravity of each block and the problem is of the same kind of that shown in **Fig. 5.29a**, only the aspect ratio is different.

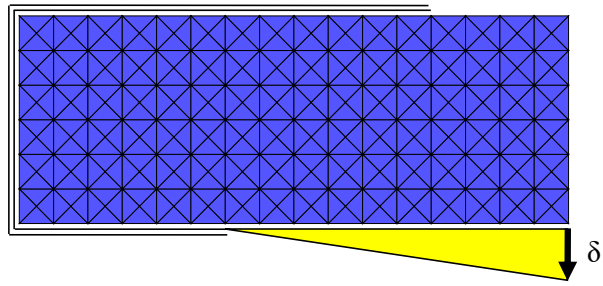

Fig. 5.36 - A panel of NRNT material is discretized with 384 triangular rigid elements. Notice that the interfaces of the elements now run along the expected crack.

The solution $\widehat{\boldsymbol{U}}^0$ of the minimum problem with the PR method now returns the expected diagonal crack (**Fig. 5.37**).

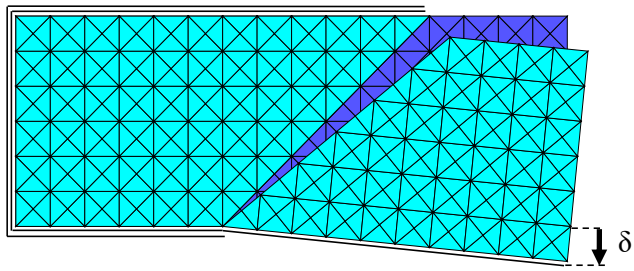

Fig. 5.37 - The solution $\widehat{\boldsymbol{U}}^0$ of the minimum problem shown in **Fig. 5.36** is reported.

Remark 5|5. As consequence of the **Remark 2|5**, here is clear that the possibility of obtain the expected solution is due to the right guessing of the orientation of the crack. ■

5.3.5 Numerical analysis with the C^0 method (square FE mesh)

A NRNT panel under the bvp described in **Fig. 5.29a** is discretized with 240 square finite elements using a second order 9-nodes Lagrangian elements (**Fig. 5.38**). We consider only the load due to the self-weight applied at the Gauss points of each element.

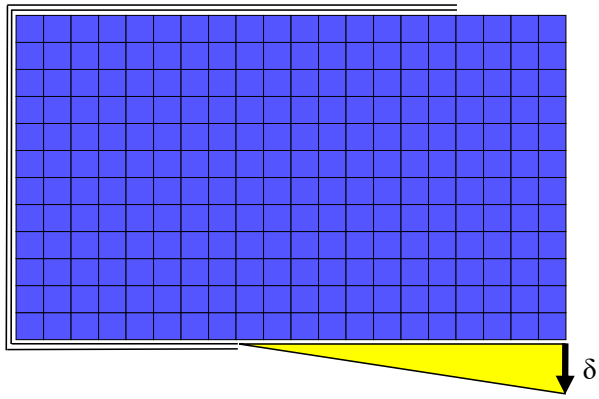

Fig. 5.38 - A panel of NRNT material is discretized by 240 square finite elements. The load due to the self-weight is applied at the Gaussian points of each element. Part of the constrained boundary is subjected to a given linear settlement as shown.

The solution $\widehat{\boldsymbol{U}}^0$ of the minimum problem is obtained through the interior point method in 600s (with an Intel® Core™ i7-6700HQ). The corresponding displacement is depicted in **Fig. 5.39**.

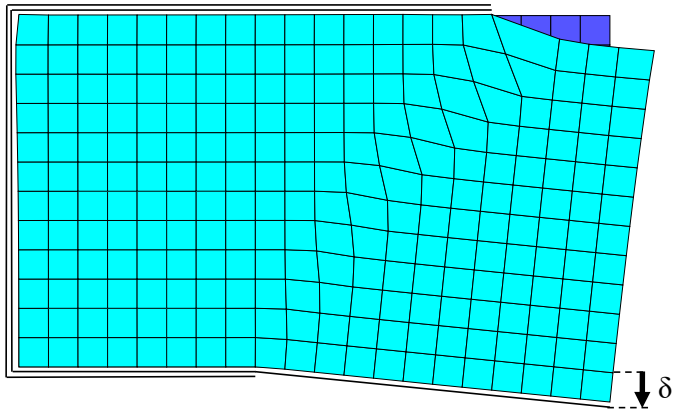

Fig. 5.39 - Displacement field corresponding to the solution $\widehat{\boldsymbol{U}}^0$ of the problem.

The streamlines of the displacement field are reported in **Fig. 5.40** where a centre of rotation can be clearly identified.

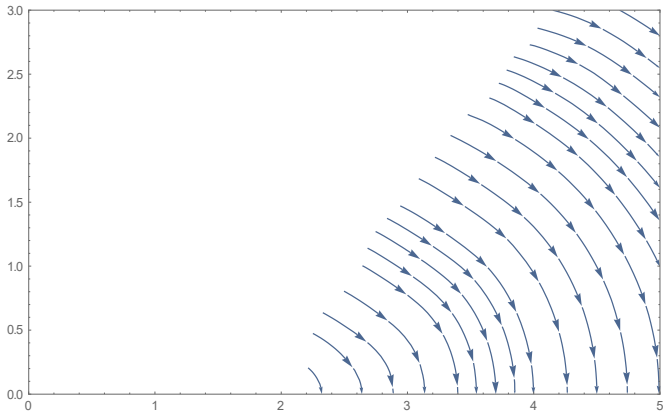

Fig. 5.40 - The stream plot of the displacement field is reported.

To represent the strain field $\boldsymbol{E}$, in **Fig. 5.41** we report a measure of the deformation, namely $|\boldsymbol{E}|^2 = tr(\boldsymbol{E}\boldsymbol{E}^T)$. From **Fig. 5.41**, we see that the gradient of deformation is concentrated along an oblique line, whilst the other elements are characterized by strains whose norm is close to zero.

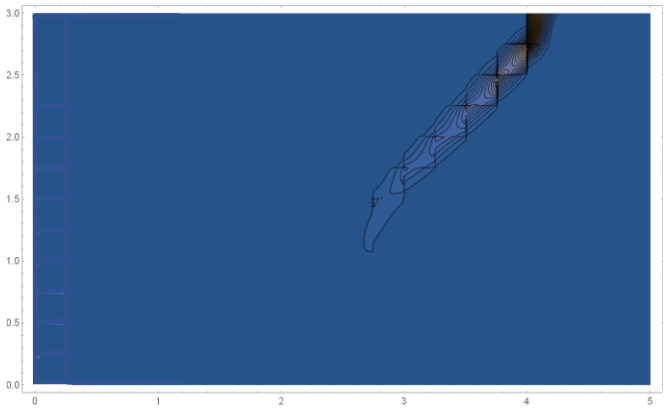

Fig. 5.41 - The field $|\boldsymbol{E}|^2 = tr(\boldsymbol{E}\boldsymbol{E}^T)$ is reported.

The skew-symmetric part of the displacement field, representing the local rotation field, is depicted in **Fig. 5.42**. It should be noticed that the gradient of rotation is essentially concentrated along a diagonal line (**Fig. 5.42**).

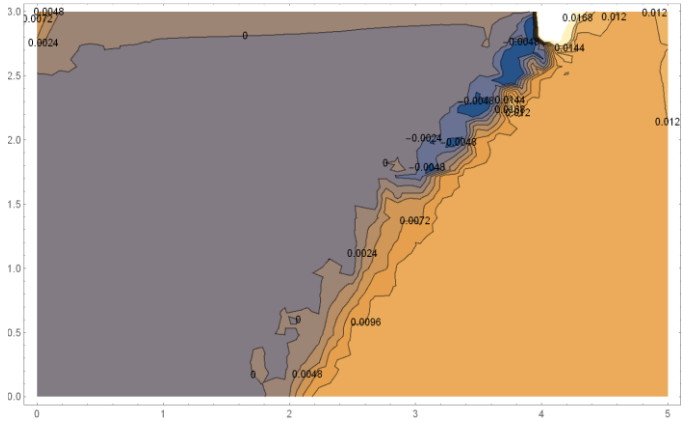

Fig. 5.42 - Rotation field over the whole domain.

By depicting the positive rotations in red and the negative ones in blue (**Fig. 5.43**), even in this case we obtain a neat subdivision of the domain into two blocks deforming as rigid bodies.

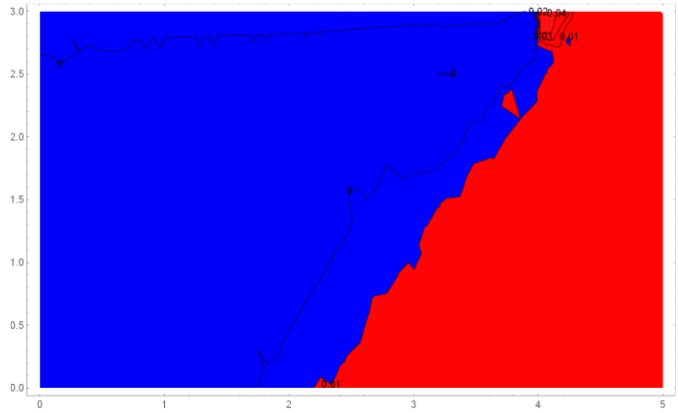

Fig. 5.43 - By depicting the positive rotations in red and the negative ones in blue, a neat partition of the whole domain into two rigid blocks can be seen.

PART III

APPLICATIONS AND RESULTS

Chapter 6

THE MASONRY ARCH

Prologue. In this Chapter, we analyze the masonry arch handling it with the PR method discussed in **Section 4.3**. The comprehension and the study of the masonry arch is a necessary element to understand the peculiar behavior of old masonry structures. The scope of the present Chapter is two-fold: revisiting the old theory of the arch and demonstrating, on a simple and fundamental application, the effectiveness of our method in tackling the structural analysis of masonry. With this aim, we make a brief introduction about the historical development of the architecture of the arch and subsequently an historical review about the mechanics of the arches (see also (Heyman, 1998)).

In the last part, we show some applications on masonry arches, carried out by applying the energy criterion with the proposed PR method.

Generally, the application of the kinematic theorem is made fixing a finite number of mechanism and finding between them the mechanism associated with the minimum multiplier of the loads. The application of the energy criterion (**Chapter 4**) allows us to find directly the mechanism solution of the kinematical problem considering either given loads and settlements. With this in mind, we use firstly some well-known results as benchmarks for PR method and secondly we test our model comparing our results with other our ones obtained analytically and reported in the **Appendix D** and **E**.

■ 6.1 THE MASONRY ARCH: HISTORICAL NOTES

A common definition of an arch says: "*an arch is a curved structure that spans a space and may or may not support weight above it".* The masonry arch is the most important and one of the most ancient masonry elements expressing in itself the most significant peculiarities, both conceptual and geometrical, of other more

complex masonry structures. The realization of the arch is one of the most revolutionary ideas in the history of constructions contributing significantly to the development of structures and to the human progress. Starting from the arch structure there was, during the history, the development of masonry vaults, which may be defined as a continuous arch forming a roof. Arches appeared as early as the 2nd millennium BC in the Mesopotamian brick architecture, and their systematic use started with the Ancient Romans who were the first to apply this technique to a wide range of structures. In a certain way, it is a primitive element whose structural analysis could conduct us to know better and to understand the intimate behavior of old masonry structures. With this aim, in this section, a brief analysis, both historical and structural, about masonry arch is presented.

Since the arch finds its function on the need to span on opening, probably its form derives from an evolution of some other primitive systems used for the same purpose. In **Fig. 6.1**, a schematic evolution which conducts to the arch passing through the post and lintel system and the corbelled arch is shown.

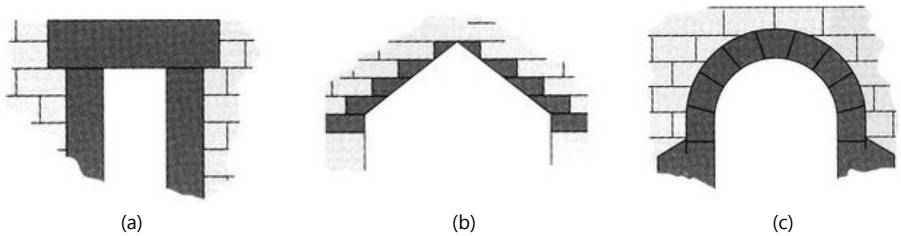

Fig. 6.1- Three methods of spanning a passageway: (a) post and lintel (b) corbelled arch (c) arch.

Post and lintel system (**Fig. 6.1a**), or a trabeated system, is a building system where strong horizontal elements are held up by vertical elements with spaces between them. The horizontal elements are called by a variety of names like lintel, header or architrave, whilst the supporting vertical elements may be called posts, columns or pillars.

Often, in many architectural traditions, to help the posts spreading the load transmitted by the lintel, wider elements (called *capitals*) at the top of the post were used. This structural system is a fundamental principle of Neolithic architecture and Ancient Indian, Greek and Egyptian architecture also; moreover, it was diffused in North and Central America by Mayan and in South America by Inca architecture also. Some typical examples of post and lintel ancient structures are shown in **Fig. 6.2**. In particular, with regard to the Lion Gate of Mycenae shown in **Fig. 6.2c**, it is possible to see an additional architectural innovation: the relieving triangle. It is designed to

reduce the weight putted on the lintel: the curved piece exhibiting the famous lions is composed of a stone lighter in weight than the surrounding blocks.

(a) (b)

(c) (d)

Fig. 6.2 - Some typical historical post and lintel systems: Stonehenge (a), Machu Picchu (b), The Lion Gate at Mycenae (c), Karnak (d).

The post and lintel system, by a structural point of view, whilst the two posts are under compression, the lintel is subjected to flexural compressive and tensile stresses due to the self-weight and the loads above it: this represents the biggest disadvantage to a post and lintel construction both for the limited weight that can be sustained and for the small distance that can be spanned.

* * *

At least from a geometrical aspect the **corbelled arch** (**Fig. 6.1b**) is a sort of intermediate step between a post-lintel structure and the proper arch. It could be imagined as a first step to achieve the structural behavior of the proper arch, but contrary to what one might guess, their similarity is only geometrical because the structural behavior is different. Corbelled arches were commonly used by ancient

civilization around 2000 BC, but first examples of this kind of constructions go back around 3000 BC like tholos tomb on the Iberian Peninsula and elsewhere around the Mediterranean. In many parts of the world it is possible to see constructions related, more or less directly, to the corbelled arch: Ancient Egyptian pyramids from around the time of Sneferu, Ebla in Syria, Ugarit, Nuraghe constructions in ancient Sardinia, Hittites constructions in ancient Anatolia, certain pre-Columbian Mesoamerican constructions, and many others in India and Cambodia. In **Fig. 6.3** some of these examples are shown.

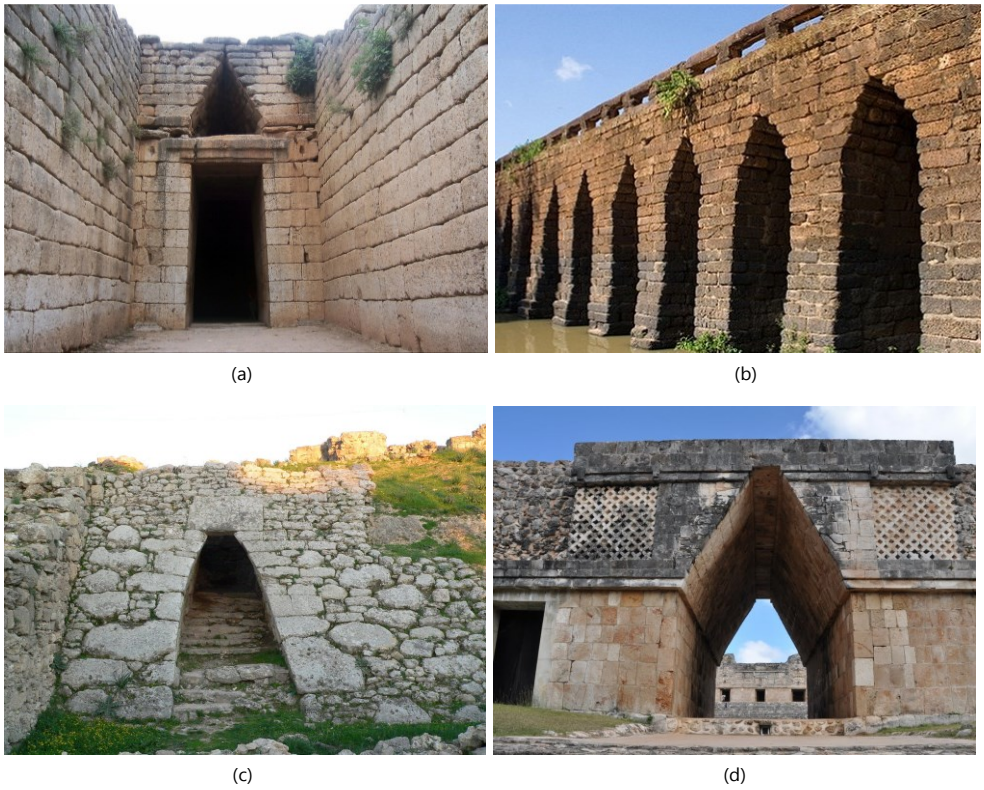

(a) (b)

(c) (d)

Fig. 6.3 - Some historical examples of a corbelled arch: Treasury of Atreus or Tomb of Agamemnon at Mycenae (a), Kompong Kdei Bridge of Cambodia (b), Entrance of Royal Palace of Ugarit (c),False arch at "Cuadrángulo de las monjas" at Uxmal in Yucatán - Maya architecture (d).

This structure takes its name from the **corbel**: a structural piece of stone jutting from a wall to carry a superincumbent weight, a type of bracket, nay a solid piece of material in the wall (see **Fig. 6.4a**). Corbel structures were often used in gothic architecture finding a combination between structural and ornamental functions (see **Fig. 6.4**).

A corbel arch is constructed by offsetting successive courses of stone at the springline of the walls so that they project towards the archway's center from each supporting side, until the courses meet at the apex of the archway (often, the last gap is bridged with a flat stone): so, each halve of arch is built with cantilever blocks. Although an improvement in load-bearing efficiency over the post and lintel design, corbeled arches are not entirely self-supporting structures, and the corbeled arch is sometimes termed a "**false arch**" for this reason. This conducts to an important difference from "proper" arches: not all of the structure's tensile stresses caused by the weight of the superstructure are transformed into compressive stresses.

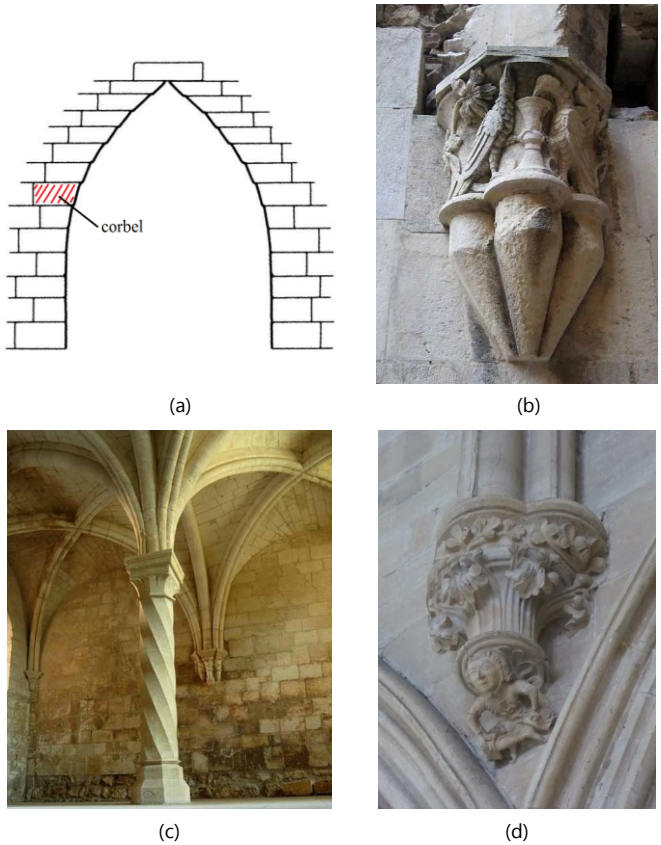

Fig. 6.4 - The corbel element of a false arch (a), corbel outside the Lisbon Cathedral (b), triple corbels in the Silvacane Abbey – Provence (c), corbel of Southwell Minster - Nottinghamshire (d).

Corbel arches require significantly thickened walls and an abutment of other stone or fill to counteract the effects of gravity, which otherwise would tend to collapse each side of the archway inwards. One should evaluate, before masonry starts to tilt, where the centre of gravity is of the arch being built. It should not go beyond the

limit of stability, which is the inner side of the pier. Then, for building such an arch, it is essential to pay attention to the balance of the masonry when courses rise (**Fig. 6.5**). In particular, the stability of a false arch depends first strictly on positioning the vertical joints in order to prevent the overturning of the blocks. If the arch is unloaded, each half-arch could be imaged as global freestanding corbel and the set of two halves oppose each other. Since the capacity of the blocks at the "key" position to transfer thrust is due to the super imposed load, the stability of an unloaded arch is ensured by the friction between stones and by the global stability with respect to the overturning of each haves.

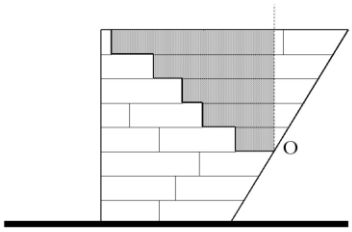

Fig. 6.5 – Drawing from (Como, 2013): "The safety of a false arch depends on positioning the vertical joints in such a way as to prevent the overturning of any of the blocks, which are set and therefore act in groups" (Como, 2013, p. 130).

Then, if a geometric similarity between corbelled arch and **proper arch** can be found, their structural behaviors are very different. Another important difference between these two kinds of structures, which probably caused the late spreading of the proper arch, stays in the ease of construction of the corbel arch: without support or centering, whilst the other need a more delicate and engineering building process. Though the passing from the structural scheme of a corbelled arch to the proper one would have needed only the rotation of the joints between stone blocks in a radial position, the historical development from one to the other required many centuries.

In what follows when we use the term "arch" we will refer exclusively to the proper arch.

* * *

The arch (**Fig. 6.1c**), from a structural point of view, is a pure curved compression form, which could span a large area by resolving forces into compressive stresses eliminating tensile stresses.

Even if some ancient Sumerian buildings contain examples of simple small arches and brick masonry arches were found in the ruins of Ur in Mesopotamia (1400 BC), the development and the wide spreading of the arch structure happened later. If the Etruscans were the first to make a systematic use of the masonry arches (see **Fig.**

6.6a), the Romans employed extensively this structure (in particular the round arch) diffusing this kind of structure in Europe by constructing many relevant masonry arch structures such as aqueducts (**Fig. 6.6d**), bridges, and finally the most famous ancient building constructed with arches: The Colosseum (see **Fig. 6.6b**).

Fig. 6.6 - Some historical arch structures: Etruscan arch in Volterra (a), Colosseum (b), Arch of Triumph (destroyed) in Syria's Palmyra ruins (c), aqueduct in the Old Town of Segovia (d).

The arch is not the first curved masonry structure in human history: as observed in (Como, 2013) it was preceded by corbeled vault. Nevertheless, the arch is the essential core and the elementary structural model whose knowledge is necessary to understand intimately the behavior of old masonry structure. With this aim, in the following pages, we review the historical essential steps conducting to the modern

scientific comprehension of the arch. Before discussing it, it is worthwhile to recall some definitions and nomenclatures concerning arch terminology (see **Fig. 6.7**):

- **voussoirs**: stones that make the arch (usually brick or wedge-shaped);
- **keystone**: the central stone of an arch;
- **impost**: the part of the arch's wall on which the arch rests;

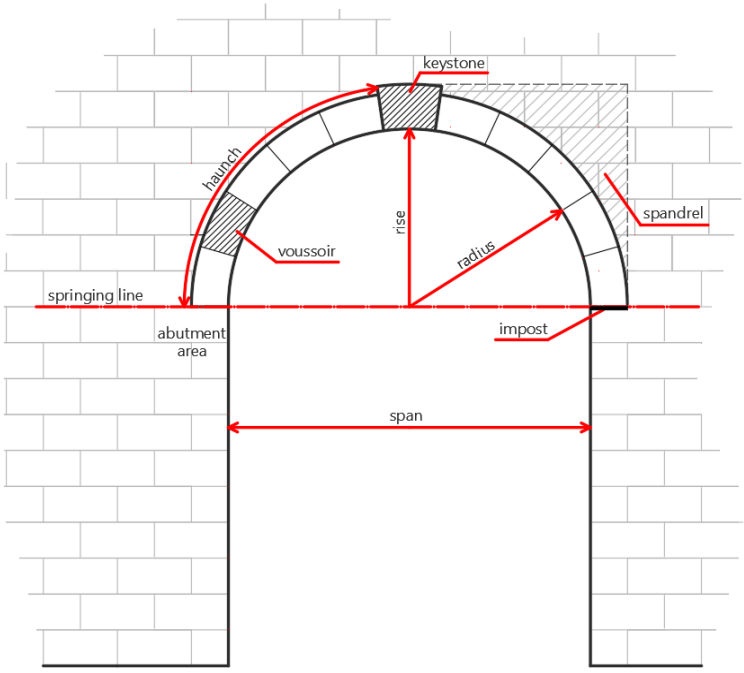

Fig. 6.7 - Arch terminology.

- **thrust**: the force which the arch makes;
- **abutment and pier**: the part of the arch's wall which balances the thrust; if it is in an intermediate position between two arches is called pier;
- **center**: the center point of the arch;
- **span**: the width of the arch's opening;
- **crown**: the top part of an arch;
- **intrados**: the inner curve of the arch;
- **extrados**: the outer curve of the arch;
- **spandrel**: a triangular walling enclosed by the extrados of the arch, a horizontal line from the crown and a perpendicular one from the springing of the outer curves;
- **depth of arch**: is the perpendicular distance between the intrados and extrados;
- **springing line**: is the imaginary line from which starts the arch;
- **springing stone or springer**: the first voussoir at springing level on either side of the arch;

- **rise**: is the distance from the springing line of the arch to the top of the arch;
- **skew back**: the surface of the abutments on which the arch rests;
- **haunch**: The lower half of the arch between the crown and skewback is called haunch.

In **Fig. 6.8** some typical shapes of arch are reported.

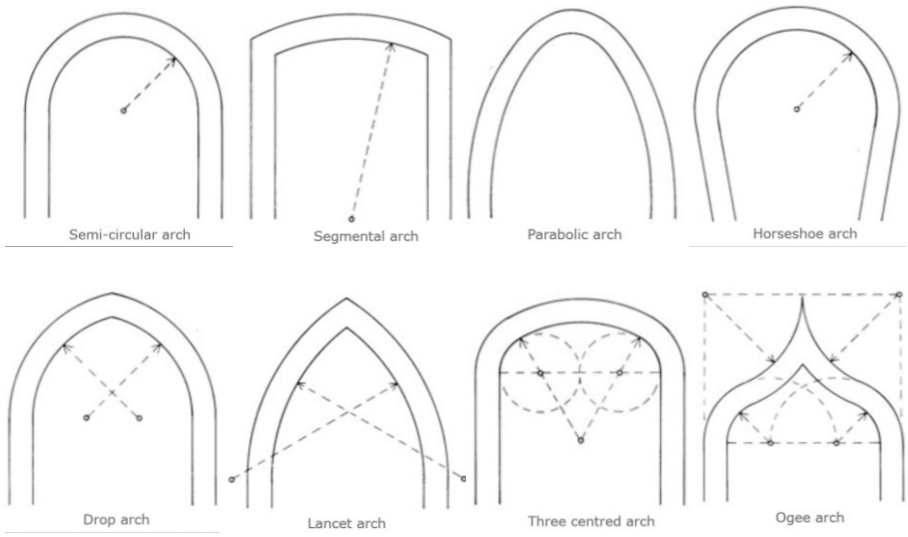

Fig. 6.8 - Some types of arch. Drawings from (Fisher, 1992).

■ 6.2 A Brief Historical Survey of the Mechanical Theory of the Masonry Arch

The Ancient Theory. The first static theories about the arches were formulated in the XVI centuries. Before them, even if magnificent constructions were built, the rules existing and used were only geometric. In **Fig. 6.9** is reported the so-called Derand's rule (Derand, 1643), a geometric empiric method used for proportioning the dimensions of the piers of a round arch (**Fig. 6.9a**) and a pointed one (**Fig. 6.9b**). It is well known that the thrust of the round arch is greater than that of the pointed one, and consequently the thickness of the pier in the first case must be greater.

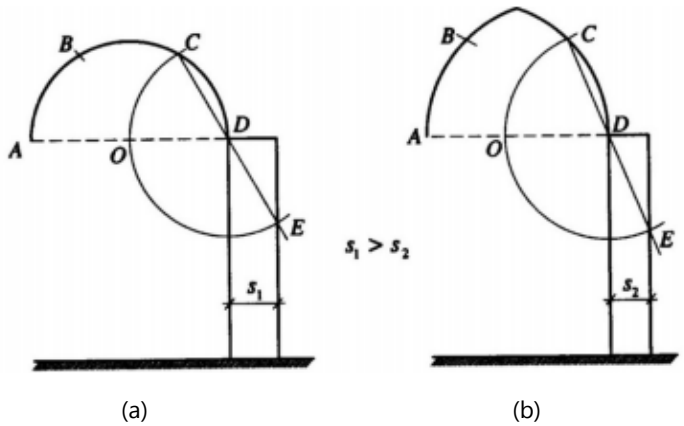

Fig. 6.9 –An ancient empirical rule used to proportion the thickness of the piers of a round arch (a) and a pointed one (b), derived from (Derand, 1643).

Leonardo Da Vinci. Probably, the first mechanical study on the arch was made by Leonardo Da Vinci. He gave also a definition which contains an in-depth understanding of the mechanical behaviour, namely:

> *"... arco non è altro che una fortezza causata da due debolezze, imperò che l'arco negli edifizi è composto di 2 parti di circulo, i quali quarti circuli, ciascuno debolissimo per sé, desidera cadere, e opponendosi alla ruina l'uno dell'altro, le due debolezze si convertano in unica fortezza..."* (Marcolongo, 1937).

> *"... an arch is nothing but a strength caused by two weaknesses; that is why an arch in buildings is composed of two quarter-circles; these quarter-circles, each very weak in itself, wish to fall, and opposing each other's ruin, convert weakness into a single strength..."* (Benvenuto, 1991).

As reported in a drawing of the Forster Codex (**Fig. 6.10a**), it seems that Leonardo, by making some experimental tests on an arch, came up with a criterion of safety reported in **Fig. 6.10b** and a failure rule reported in **Fig. 6.10c**: someone could think that the line depicted in **Fig. 6.10b and in Fig. 6.10c** represent a line of thrust due to a load acting at the key stone (**Fig. 6.10a**) and much larger than the self-weight of the arch. Leonardo synthetized the failure rule with these words:

> *... l'arco non si romperà se la corda dell'archi di fori non tocherà l'arco di dentro ..."*
>
> *"... the arch will not crack if the chord of the outer arch will not touch the inner arch ... "*

in which is possible to see a first a primitive formulation of the rule according to which the line of thrust has to lie within the arch geometry.

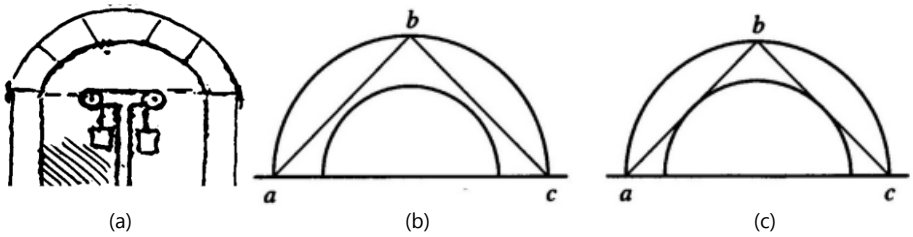

Fig. 6.10 - A famous drawing from the Forster Codex (a) which shows an experimental test on an arch made by Leonardo da Vinci. He formulated a safety criterion (b) and a failure rule (c).

* * *

Robert Hooke. The first rational study on the mechanics of the arch can be traced back to Robert Hooke. He knew the intimate physical behaviour of the arch, and during his career showed experiments on model arches, but during his life he did not provide the corresponding mathematical theory. Indeed, in a his famous work (Hooke, 1676) on helioscopes, he published a series of anagrams 'to fill the vacancy of the ensuing page'. Beside his famous *"ut tensio sic vis"* one of them is concerned with 'the true Mathematical and Mechanichal form of all manner of Arches for Building'. He wrote only the letters in an alphabetic order, namely:

> *«abccddeeeeefggiiiiiiiiillmmmmnnnnnooprrsssttttttuuuuuuuvx»*

and, deciphered, reads

> *"...ut pendet continuum flexile, sic stabit contiguum rigidum inversum..."*

"... as hangs the flexible line, so but inverted will stand the rigid arch...".

The solution of the anagram was published only after Hooke's death, but Hooke understood that if he could solve the catenary problem, he would at the same time have found the solution of the shape of the perfect arch carrying the same loads in compression. The search of the solution of the problem of the catenary was not trivial: **Leibniz** first (1691), and after **Huygens** and **John Bernoulli** also seem to have solved the problem at about the same time: anyhow their solutions were not rigorous mathematically. The problem, though with some mistakes, was solved some years later (1697) by **David Gregory**. Gregory states:

> *"In a vertical plane, but in an inverted situation, the chain will preserve its figure without falling, and therefore will constitute a very thin arch, or fornix; that is, infinitely small rigid and polished spheres disposed in an inverted arch of a cateneria will form an arch; no part of which will be thrust outwards or inwards by other parts, but, the lowest part remaining firm, it will support itself by means of its figure ... And, on the contrary, none but the catenaria is the figure of a true legitimate arch, or fornix.* ***And when an arch of any other figure is supported, it is because in its thickness some catenaria is included.*** *Neither would it be sustained if it were very thin, and composed of slippery parts. From Corol. 5 it may be collected, by what force an arch, or buttress, presses a wall outwardly, to which it is applied; for this is the same with that part of the force sustaining the chain, which draws according to a horizontal direction. For the force, which in the chain draws inwards, in an arch equal to the chain drives outwards."* (from (Ware, 1809): translation from the Latin)

The bold phrase was added by Ware, but it is completely clear that **Gregory realized that if the thrust line lies within the arch can be found, then the arch is stable**. Last but not least, Gregory understood that the horizontal action on the abutment of an arch is the same of the pull of an equivalent hanging chain. This approach, as we will see, was used in the middle of the XVIII century by **Poleni** in his studies on the stability of St Peter's dome in Rome.

* * *

Philippe de La Hire. La Hire gave important contributions to development of the static of the arch, applying for the first time the mechanics on the study of an arch, considered as composed by rigid bodies. In his first work (La Hire, 1695) he studied a semi-circular arch assembled from rigid voussoirs and considered the joints between them were frictionless.

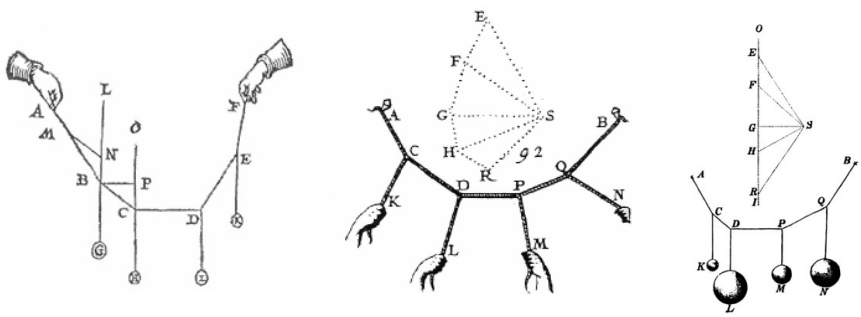

(a) (b) (c)

Fig. 6.11 - Three famous drawings about force equilibrium. **Stevin** (1586) introduced the parallelogram rule describing the equilibrium graphically: (a). **Varignon** introduced the polygon of forces and the funicular polygon in Nouvelle Mecanique ou Statique published posthumously in (1725): (b) and (c). Varignon in (c) described a way to construct graphically the form of a hanging rope with attached weights: this principle established the birth of the graphic statics, widely used in the 19th century.

The innovation in La Hire's consists in the use of the force polygon and the corresponding funicular polygon for the arch. Although the funicular polygon (**Fig. 6.11**) for an arch can be viewed as a "discrete" line of thrust (that is the shape of the inverted hanging chain) La Hire did not use these terms. He posed himself the problem of finding the weights of the voussoirs such that equilibrium should be maintained. Since he assumed that the contact joints are smooth, the line of thrust must be orthogonal to the joints conducting to a paradoxical statement: if the springing line is horizontal, it follows that the springing voussoirs must have an infinite weight for guarantee the stability of the arch.

La Hire, anyhow, noted that friction between the voussoirs would confer the necessary stability to the structure and in (La Hire, 1712) he returned to the arch, but he made a completely different hypothesis: the friction was taken to be so large that sliding could not occur. Then, the direction of the line of thrust was no longer fixed as before, and the line of thrust, is in this case, undetermined. He overcame this problem introducing a powerful idea to catch the arch behaviour. He asked himself: what happens if the abutments are too weak, showing some little outward settlements, and how would the arch behaviour be?

He answered to this question stating that the arch would break in a critical section LM between the springing and the keystone (**Fig. 6.12a**). In L, a hinge, needed to accommodate the abutments settlements, was formed and consequently the line of thrust became completely determined, being the thrust P tangential to the arch in L. From some considerations about the equilibrium of the portions LMF and LMI, he determined the value of P (**Fig. 6.12b**) and then the stability of the whole structure, writing the moment about the corner H, can be checked.

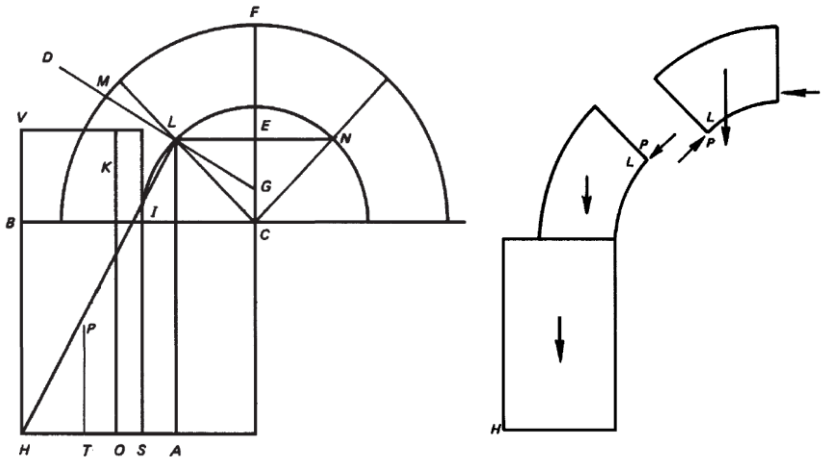

Fig. 6.12 - Two drawing from (La Hire, 1712). In (a) the section LM is taken to be critical and the increase of the outward settlements of the abutments is accommodated by a hinge in L: this point represents the only contact between the above portion LMF and the bottom portion LMI of the arch. In (b) the line of thrust has to pass tangentially through L. Knowing the weight of LMF, the value of the force P can be evaluated and can be used to check the stability of the whole structure around H.

Although there were some mistakes (conducting a conservative assessment) and no rule for finding the point L was given, this form of reasoning unlocks the statics of the arch and is the most important and original result achieved by La Hire.

Was in that period that the French engineer **Bernard Forest de Bélidor** made a widely use of the La Hire's method and in his work (Belidor, 1729) he spent an entire section on arches treating them approximately in this way but applying some changes with the basic aim to establish a set of design rules.

* * *

Pierre Couplet. In this historical context, Couplet wrote in (1729) and in (1730) two remarkable memoirs on arch thrust. In particular, in (Couplet, 1730) he noted that the voussoirs could not slide each other allowing only detachments and excluded from the calculation any resistance in compression of the masonry. In effect, Couplet implicitly assumed true the three basic assumptions of Heyman: no tensile strength, infinite compressive strength, and sliding cannot occur. Furthermore, Couplet formalized in this work two ways of approaching any structural problem: through equilibrium (statics), considering the thrust lines, and through deformation (mechanisms).

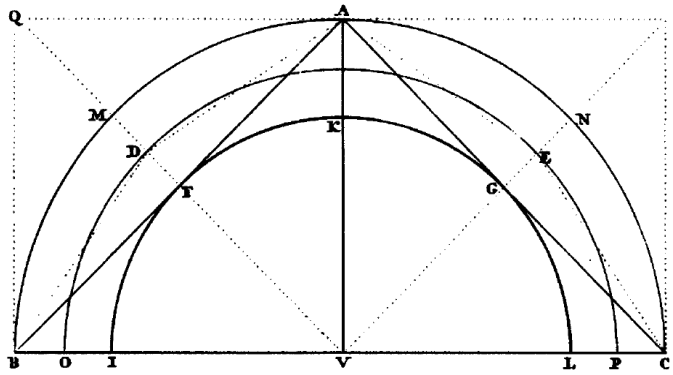

Fig. 6.13 - Drawing from (Couplet, 1730): the arch cannot collapse under a vertical force acting at the crown A if the straight lines AFB and AGC are entirely lying within the arch geometry

In particular, he states that an arch will not collapse if the chord of half the extrados does not touch the intrados, but is entirely lying within the arch geometry: this results comes out by considering a round arch of negligible self-weight subjected at the crown A to a single vertical force (**Fig. 6.13**). This safety criterion is very similar to that of Leonardo (**Fig. 6.10b**).

Couplet, in his work, tackled the problem to find the **minimum thickness** of a round arch subjected only its own weight. He hypothesized a mechanism (see **Fig. 6.14**) dividing the arch in four rigid pieces, connected each other by hinges R, T, A, K and F, where the hinges T and K are placed at 45°. Couplet solved the equilibrium problem and found a relation between the thickness s and the mean radius R_m of the arch, namely: $s/R_m = 0.101$.

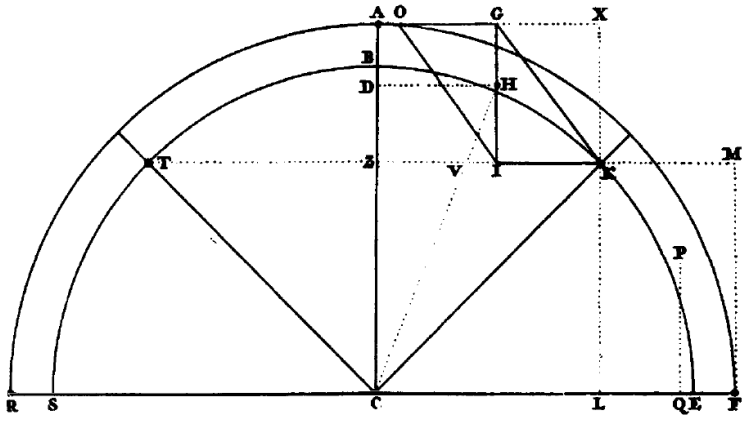

Fig. 6.14 - Drawing from (Couplet, 1730): a round arch of minimum thickness collapsing under its self-weight.

Remark 1|6. The correct solution was found first by **Heyman** in (Heyman, 1969) and later recalculated, with a different partition of the domain, by **Ochsendorf** in (Ochsendorf, 2006): the exact intrados position is at 31° rather than at 45°, anyhow the analysis is not sensitive to the position of this hinge, since the varying the hinge angle the correct value of t/R differs little. ■

Later, he reworks the La Hire and Belidor approaches in order to evaluate the abutment thrust and to assess the stability of the whole structure (**Fig. 6.15**).

> "*Couplet's contribution is outstanding. He had clear ideas of lines of thrust, and of mechanisms of collapse caused by the formation of hinges; he made explicit his simplifying assumptions; and he used these ideas to obtain an essentially correct and complete solution to the problem of arch design.*" from (Heyman, 1998).

The Couplet's work was noted immediately and had a big spread. Indeed, **Danyzy** in (Danyzy, 1732) made several tests in Montpellier following the Couplet's approach. He used arches made from plaster voussoirs and he found confirmations of Couplet's results. Although the Danyzy's results were clearly published not before 1778, **Frezier** reported in his work (Frézier, 1737-39) a plate showing the Danyzy's experimental tests (**Fig. 6.16**): all arches shown are in the collapse state with piers having the minimum dimension. The sketch 241 in **Fig. 6.16** confirms clearly the use of Couplet's approach.

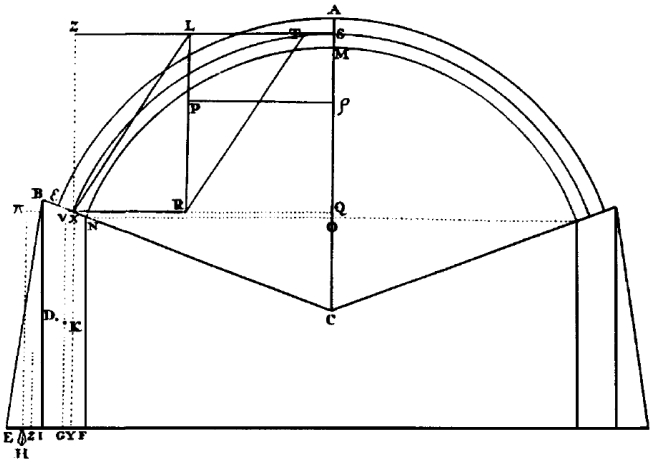

Fig. 6.15 - Drawing from (Couplet, 1730): the force system for design of abutments is shown. The thrust is referred to the curve centre line SX of the arch. The thrust at S is horizontal, and the weight of half the arch is represented in the line LR; by resolving the equilibrium Couplet valuates the magnitude of the abutment thrust (line LX) in order to size the piers and to assess the stability of the whole structure.

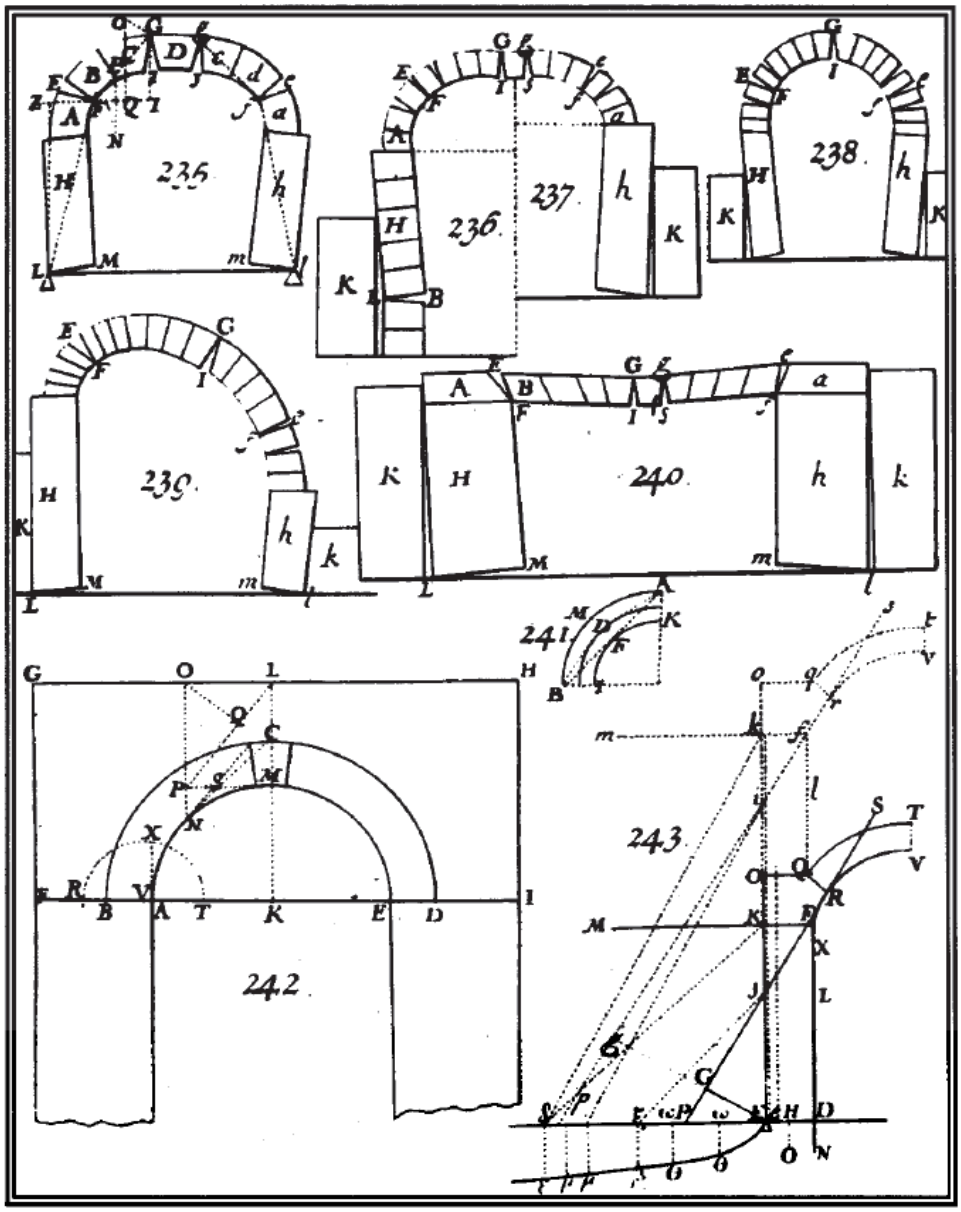

Fig. 6.16 - Drawing from (Frézier, 1737-39): the experimental tests made by Danyzy in Montpellier are reported. Danyzy follows the Couplet's approach (241) and obtain experimental confirmations of the Couplet's mechanism as shown in 241 (the exactly representation of the collapse mechanism predicted by Couplet and reported above in **Fig. 6.13**). The flat arch of 240 is in a collapse state because the abutments are tilting, otherwise it would be stable.

* * *

St Peter's Dome. Beginning these days and starting from these researches, it can be said that the mechanics of the arch is almost totally understood. This is completely demonstrated the story of the restructuring of St Peter's in Rome and in particular by the studies made by **Poleni**: **the first considerable application of the mechanics to the arches**.

The dome of St Peter's was designed by **Michelangelo** and constructed a century and a half earlier but a few years later, cracks began to develop and grow gradually. In the early years of the XVIII century the dome showed a widespread crack pattern (see e.g. **Fig. 6.17**). This is the description of Saverio Brunetti reported by Poleni in hi "Memorie istoriche della gran cupola del tempio Vaticano e de'danni di essa e detristoramenti loro, divisi in libri cinque" (1748):

> *"... the entire wall of the drum and the attic, together with the columns and buttresses, have rotated outwards, dilating the dome and lowering the lantern...."*

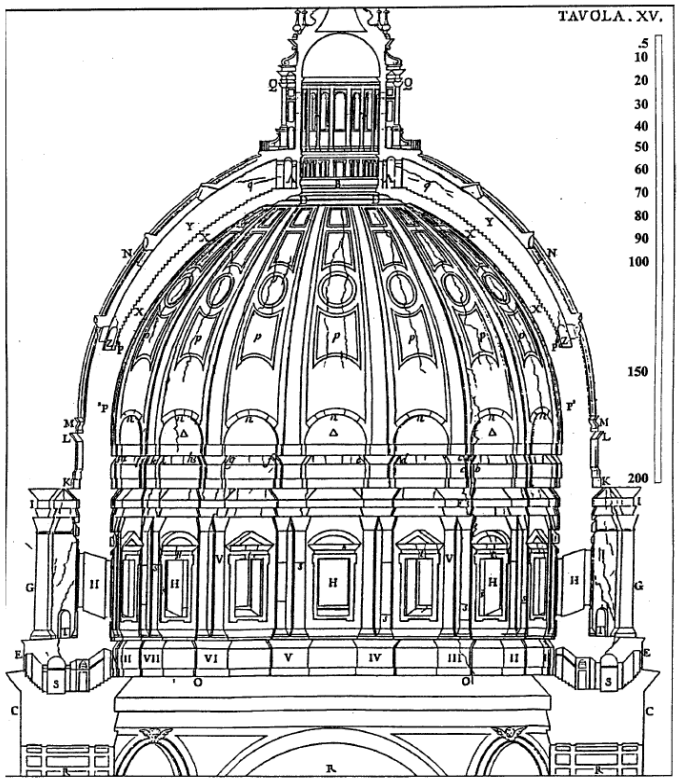

Fig. 6.17 – Drawing from (Poleni, 1748). The drawing, made by Vanvitelli, illustrates in detail the crack pattern running along the dome intrados.

The crack pattern was recognized during the years 1742 and 1743 by **Vanvitelli** and his drawings were even published in (Poleni, 1748) (**Fig. 6.17** and **Fig. 6.18**): meridian cracks, running up from the drum, divided the dome into many portions (lunes). The alarm grew up and then Pope Benedict XIV in 1742 called **Le Seur**, **Jacquier**, and **Boscovich** (the three scientists known as "**Tre Mattematici**") to report on the condition of the dome.

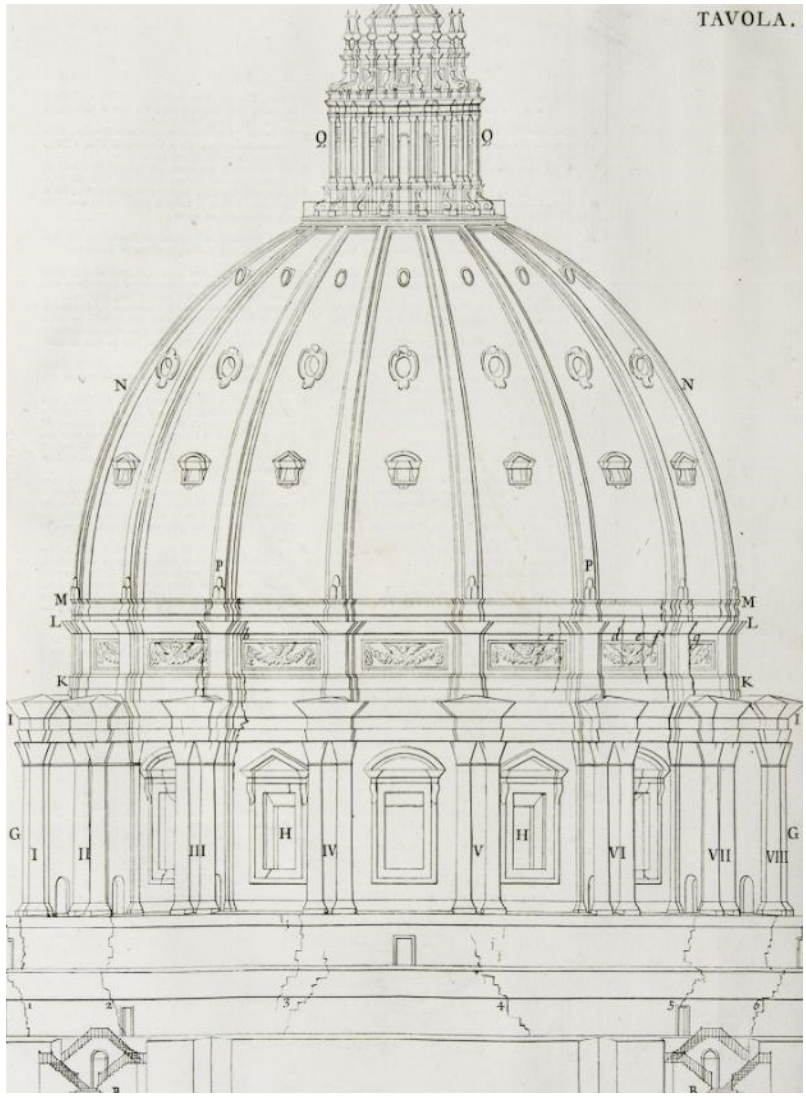

Fig. 6.18 - Drawing from (Poleni, 1748). The drawing is made by Vanvitelli and the crack pattern running along the dome extrados and affecting also the drum is shown.

These scientists probably knew the **virtual work principle** (see **Fig. 6.19**), although it was first formulated only in 1717 by **Giovanni Bernoulli** in a letter addressed to **Varignon** and published in (Varignon, 1725) though *"there is actually a misprint and the correct date of the letter is February 26th, 1715"* (Capecchi, 2012).

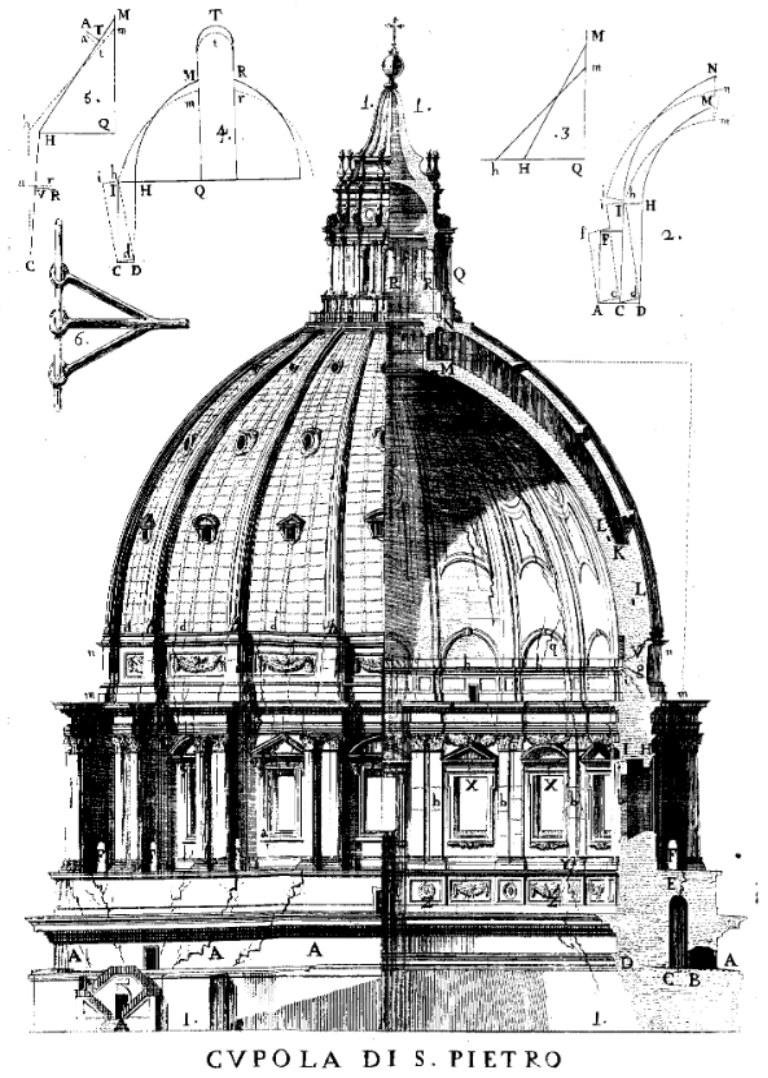

Fig. 6.19 - Drawing from (Le Seur, Jacquier and Boscovich, 1742): the crack pattern (a drawing of Vanvitelli) is reported. On the top, the mechanism analysed by the "tre mattematici" with the virtual work principle is depicted.

Using this principle, they assessed in their work *"Parere di tre mattematici sopra i danni che si sono trovati nella cupola di S. Pietro"* (1742) that the dome was damaged and needed an extensive restructuration: in addition to encircling the dome with iron

hoops, they also wanted to thicken the buttresses placing also on them heavy statues. Anyhow, Benedict XIV, not completely convinced of their proposal, decided to require the assessment of an important Italian scientist: **Giovanni Poleni**.

The analysis of Poleni estabilished that the Dome was safe and that the craks was caused by defects in construction and the use of poor masonry. Anyhow, the importance of this study stays in the application of main results achieved in the previous years. Indeed, in his Memoir (Poleni, 1748), Poleni showed a deep knowledge of the work of La Hire and Couplet and a profound understanding of the concept of Hooke's hanging chain (see **Fig. 6.21**).

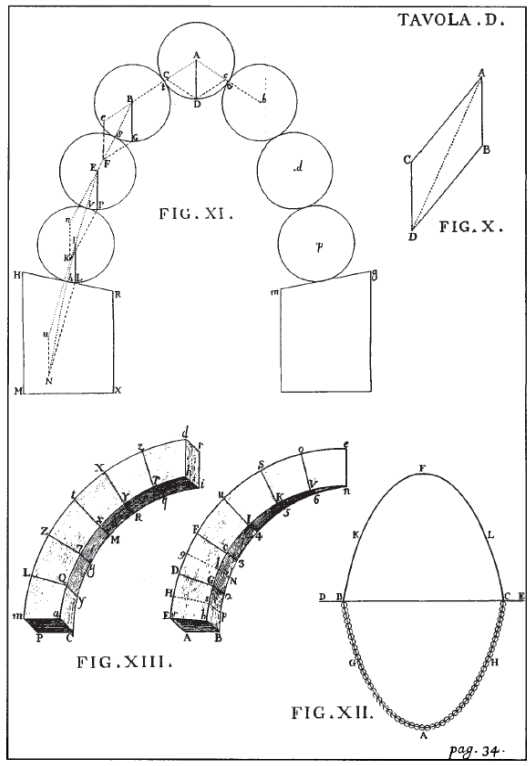

Fig. 6.20 – Drawing (Poleni, 1748): a deep knowledge of the Stirling's work (Stirling, 1717) is shown in Fig. XI with the use of an catenary formed by smooth spheres. Poleni sliced the dome hypothetically into 50 such lunes: a schematic view of a half "lune" is shown in Fig. XIII.

Furthermore, he quoted Gregory stating that an arch, in order to be stable, needs that the line of thrust has to lie within the geometry. He drew inspiration even from a work by **Stirling** (1717) (cited explicitly in (Poleni, 1748, p. 33)) using a catenary formed by smooth spheres (see "Fig. XI." in **Fig. 6.20**). Poleni treated the dome slicing it into 50 "lunes" and considering one of them solved the problem of equilibrium of

a two dimensional arch with almost zero thickness at the crown (see "FIG. XIII." in **Fig. 6.20**). The thrust line was determined experimentally by loading a flexible string with some spheres of variable mass considering also the loading of the superimposed lantern (see **Fig. 6.21**).

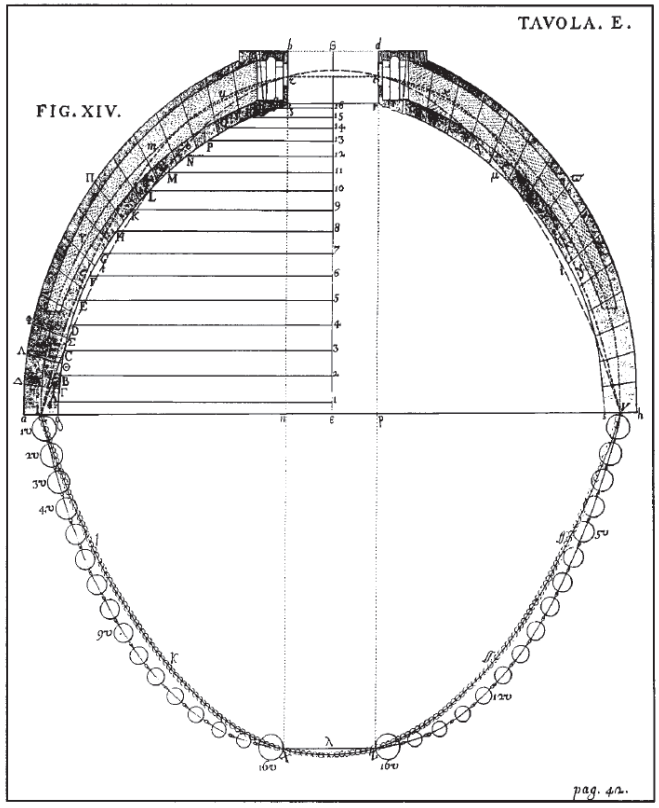

Fig. 6.21 – Drawing (Poleni, 1748). Poleni analysed a "lune" using the concept of hanging chain of Hook; He modelled the weight of a lune with 32 spheres of variable mass considering also the loading of the superimposed lantern.

The result of this experimental test, made in the laboratory in Padua, was that **the inverted chain lain within the thickness of the dome** and therefore each lune was safe and consequently the whole dome also. He concluded that crack pattern was due only to the poor material used for the inferior part of the construction. The Pope agreed the work of Poleni and entrusted to him the restructuration under the technical supervision of Vanvitelli: the dome was repaired and reinforced between 1743 and 1744 with iron hoops and the cracks were patched (through *"scuci e cuci"*) (see **Fig. 6.22**). No other restructuring was made during the last three centuries and the Dome is currently in a perfectly stable condition: the analysis of Poleni was correct.

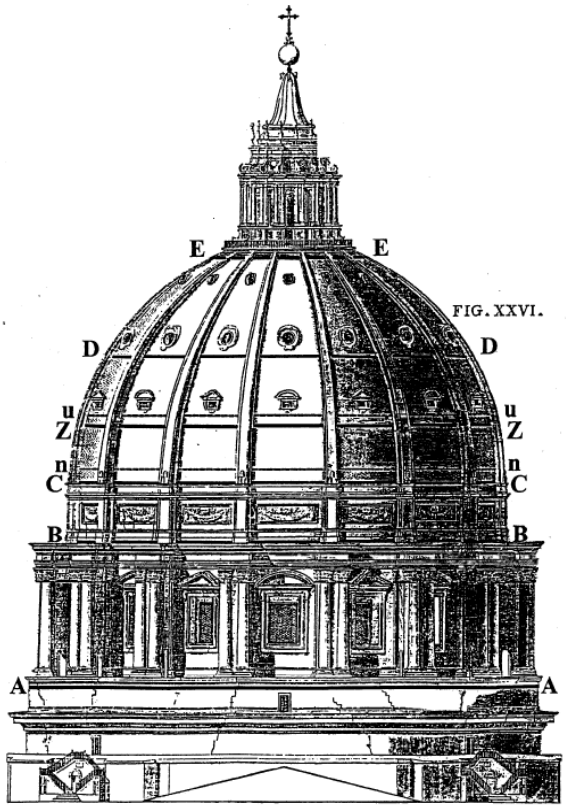

Fig. 6.22 - Drawing of Vanvitelli treated taken from (Poleni, 1748): six new iron hoops (A, B, C, D, E, Z) were installed under the supervision of Vanvitelli whilst (u,n) was already present.

* * *

Charles Augustin de Coulomb. The last further decisive development into the study of the arch was due to Coulomb. He in his famous memoir *"Essai sur une application des regies de maximis & minimis a quelques problemes de statique, relatifs a l'architecture"* (1773) made several contributions to many problems of civil engineering and in particular to the thrust of soil and the thrust of arches. In this work, Coulomb solved many problems considering failure imaginary planes along which the slip could occur in relation to the cohesion and the friction of the material. Nevertheless, with regard to the masonry arches Coulomb took into account marginally the strength of the material and assess the stability only with equilibrium considerations through principles *of maximum and minimum*. Furthermore, he stated that the failure of the arch could occur only with the formation of hinges between voussoirs, concluding that the friction was enough to prevent any sliding (see **Fig. 6.23**).

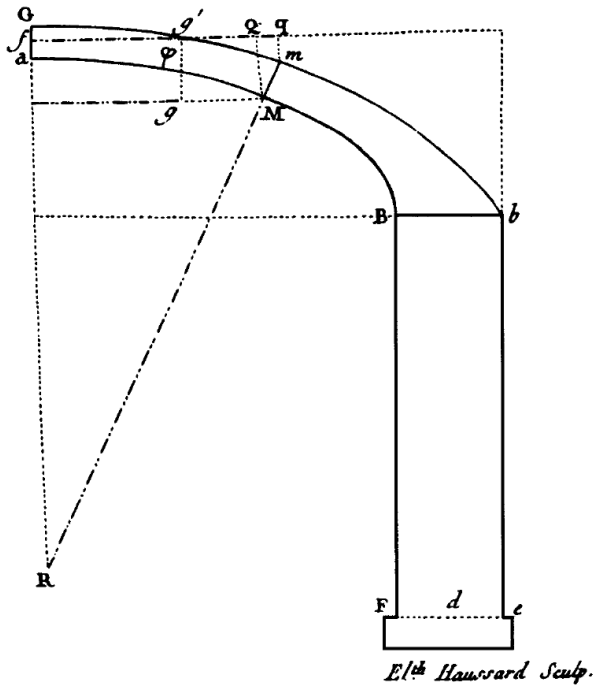

Fig. 6.23 - Drawing from (Coulomb, 1773): the equilibrium of an arch with a generic shape is shown. The half arch is in equilibrium and the thrust acts horizontally in f at the crown. Coulomb supposed that the failure could have been occurred at a generic joint between two voussoirs (defined by the section Mm). He considered two limit situations. First, supposing that a hinge was formed in the intrados in M, he wrote an expression for the value of the thrust H in M and stated that the exact position of M and the relative value of H could be found maximizing the value of H: this solution corresponds to the minimum value of H for which the arch is safe. With a specular reasoning, he found the position of the hinge that was formed in the extrados in m and the related value of H. Definitively, he did not fix the position of the section Mm, but considered it variable and furthermore he found a range to which H had to belong.

Furthermore, Coulomb made some consideration regarding the crushing failure when the stress is concentrated in a point, i.e. when a hinge was formed. Almost surely Coulomb did not know the studies of Couplet or Poleni and probably he had the only possibility to read the handbook of Belidor reporting La Hire's analysis. Nevertheless, during the years he had spent in Montpellier, he knew Danyzy, then he was surely aware of the collapse of the arch through the making of hinges. This mindset is particularly clear on his works, but **his main original result was to couple the definition of bounds regarding the thrust**: hinges may form in different positions and not uniquely at 45°.

* * *

The Coulomb's idea was demonstrated experimentally by **Barlow** (1846) at the Institution of Civil Engineers. He analysed the problem of the minimum thickness for the stability of the arches showing a deep knowledge either of the work of Coulomb and either of the equivalence between the line of thrust and the hanging chain (**Fig. 6.25**). Furthermore, he investigated the horizontal component *H* of the thrust on the abutments fixing the bounds corresponding to the least and greatest values of *H* (see **Fig. 6.24**).

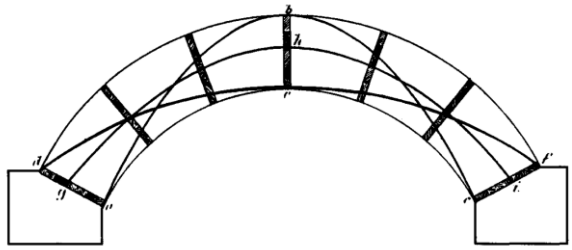

Fig. 6.24 - Drawing from (Barlow, 1846): the experimental model of a voussoir arch designed by Barlow with the alternative positions (experimentally verified) of the thrust line is shown.

Coulomb's work represented a milestone in the development of the mechanics of the arches, and also **Claude-Louis Navier** in (1833-38), although only in the second edition, dedicated a section to the arches theory following the Coulomb approach. Later, the French engineer **Yvon Villarceau** gave a complete exposition of arch theory in his *"L'établissement des arches de pont"* (1854). In particular, he understood clearly that since the arch is essentially a statically indeterminate structure, there exist an infinite number of equilibrated line of thrust.

It could seem strange, but although every other structural elements, during that period, were treated taking into account the material properties, at least until the end of the XIX the arch and some other masonry structures were analysed purely with equilibrium considerations neglecting all the characteristics regarding the resistance and the deformability widely used after **Galileo Galilei**.

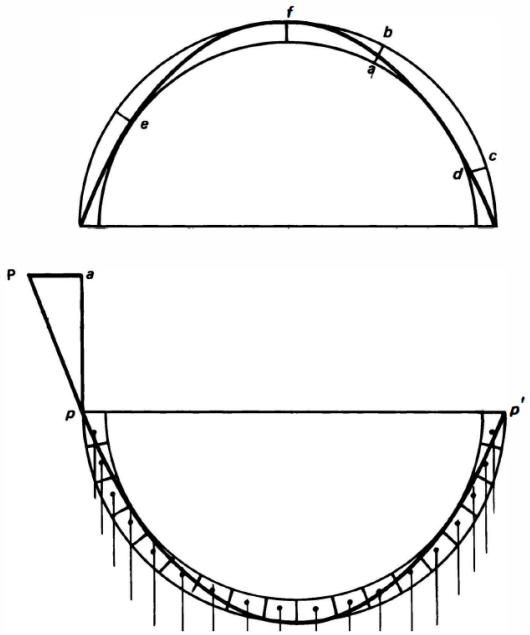

Fig. 6.25 - Drawing from (Barlow, 1846): the equivalence between the arch and the hanging chain. Barlow used this model to calculate the horizontal component of the abutment thrust (as Poleni before him).

Indeed, as we saw, until that period, generally in main works no questions about the failure or the ultimate load were posed, and if the fractures or the crack pattern were considered, they were used only to assess the working condition of the arch and to calculate in such a way the thrust.

* * *

Advent and spread of the Theory of Elasticity. Nevertheless, during the XIX century the fast development of both the elasticity and of graphic statics (with the milestone of **Culmann** (1866) and later with the works of **Luigi Cremona** [(1872),(1874)] on one hand rendered the study on masonry obsolescent and, on the other hand, marked the birth of the application of some elastic principles to masonry with particular regard to the arch: it was in that period that often the concept of line of thrust was associated with the elastic rule of the middle third. Indeed, e.g. **Alberto Castigliano** in his *"Théorie de l'équilibre des systèmes élastiques et ses applications"* (1879) his applied his elastic energy theorems also to the masonry bridge (see **Fig. 6.26**), considering the elastic properties of stones and mortar, and stating that the line of thrust had to lie into the "middle-third" of the section.

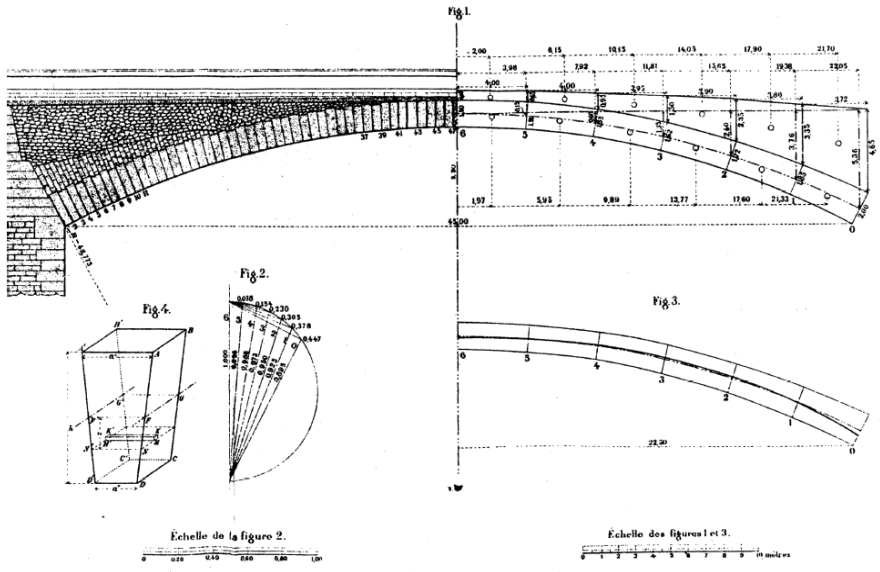

Fig. 6.26 – Drawing from (Castigliano, 1879): the *"Mosca Bridge"* in Turin.

At the beginning of the XX century, with the starting of the development of the **Plasticity**, **Pippard** in (Pippard et al, 1936) and in (Pippard and Ashby, 1939) made experimental tests modelling arches with steel voussoirs: Pippard noted that small imperfection of the abutments (e.g. settlements) were accommodated by the arch through hinges: the arch, initially hyperstatic, became statically determined (three-pin arch). Anyhow, Pippard interpreted wrongly his results using principles of minimum of elastic energy.

The urgency for the search of the actual line of thrust was actually extraneous to the inventors and the followers of the line of thrust, from (Hooke, 1676) to (Moseley, 1843), and is mainly motivated by elastic-like considerations [see also (Foce and Aita, 2003) and (Becchi and Foce, 2002)]. In modern times the stability of the arch falls within the frame of Limit Analysis, through which the degree of safety of the structure can be assessed.

* * *

The New Theory. The modern milestone study, which fills a theoretical gap of almost one hundred years existing in the scientific literature on voussoir arches, came with a new approach and is due to **Kooharian** with his work "*Limit Analysis of Voussoir (Segmental) and Concrete Arches*" (1952). This paper represents the starting point for the application of **Limit Analysis** to masonry structures. With this work, all the

applications of Poleni, Coulomb, Barlow and Yvon Villarceau based on "equilibrium approach" find finally a theoretical base.

Although Kooharian did not fix rigorously the basic assumptions necessary to apply the limit analysis theorems to masonry structures and considered only the problem of the voussoir arch, his work is the departure point of a new era. Indeed, few years later, **Heyman** in (Heyman, 1966) fixed a rigorous theoretical base through three clear fundamental hypotheses, sufficient for the application of Limit Analysis to masonry structures. In his work Heyman, studied in deep the arch and extended the analysis to a wide range of masonry structures, with particular reference to Gothic cathedrals and their peculiar structural elements.

Kooharian in (Kooharian, 1952) treated the voussoir arch, defined as a structure *"composed of many individual sections fitted one upon another"*. The basic assumption was: *"the voussoir arch can take large compressive stress but cannot take any tensile stress at its joints, even when the joints are filled by mortar"*, it is noticed that this assertion corresponds with two of the three hypotheses of Heyman). Starting from these considerations, he applied the two theorems of Limit Analysis to arches and clarified the secondary role of the middle third rule usually adopted since the later years of the XIX century.

Since the only action between two adjacent voussoirs is a compressive force and no tensile stress can be supported at joints, Kooharian browsed vary possible positions of the normal compressive stress *N* in an attempt to answer to this question: *where can the resultant N act?* (see **Fig. 6.27**)

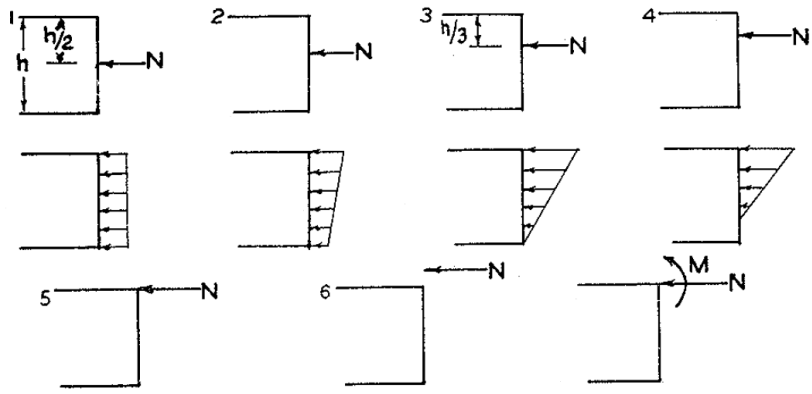

Fig. 6.27 - Drawing from (Kooharian, 1952): the compressive force N acting at various positions along a voussoir. The position 1, 2, 3, 4, 5 are certainly possible and safe. Position 3 corresponds to the "third-middle": in the elastic analysis of the arch it is considered, mistakenly, as a limit position.

He, assuming a linear distribution of stress due to the axial force N, checked which positions of N, qualitatively represented in **Fig. 6.27**, are safe. Firstly, Kooharian clarified the interpretation about the position 3, associate with middle-third rule: this position often gave rise to some misunderstanding since with elastic analysis it was interpreted as a limit position. Starting from many experimental tests of design and analysis of arches made in that years (e.g. Pippard), Kooharian stated firstly that this position is not only possible but even safe, that is the collapse does not occur. In short, he concluded by pointing out that the positions 1, 2, 3, 4, 5 (**Fig. 6.27**) are as possible as safe, and that the collapse occurs if and only if *N* acts outside the cross-section (position 6 of **Fig. 6.27**). Thus, the limit condition represented by the middle-third rule is replaced by another one schematically represented by a resultant *N* acting exactly on the edge of a section: in this state, we could image that two adjacent elements can exhibit a relative rotation about that edge.

In the same work he applied the two theorems of Limit Analysis on the arch and solved the problem concerning the determination of the *"exact"* line of thrust. In what follows we show the rationale behind the approach proposed by Kooharian.

In the previous centuries the stability of the arch was assessed searching a line of thrust (balancing the weight of the voussoirs and the acting loads) located within the arch. Since the number of all possible lines of thrust, compatible with the loads, is infinite, the search of the actual line of thrust is not trivial; furthermore the actual one depends on external factors that are far from being known. Nevertheless, was this empirical guess of the masters correct?

To answer this question, we need to introduce the theorems of Limit Analysis, proved at the beginning of the XX century and in particular, the Safe Theorem.

Safe Theorem. The collapse doesn't occur if a statically admissible internal force system, in equilibrium with the external loads, can be found. ■

The line of thrust represents geometrically a system of internal compressive forces *in equilibrium* with the loads, but when is it also statically admissible? In agreement with the observations made by Kooharian (**Fig. 6.27**), the *statically admissibility* is is owed to the fact that the line of thrust lies within the arch. Then, the **Safe Theorem** for the arch states: *the arch is safe under fixed loads if and only if there exists a line of thrust lying wholly within the geometry.* The relevance of the safe theorem resides in the fact that finding the actual line of thrust does not matter, it is sufficient that there exits at least one lying wholly in the masonry.

Then we can answer to the previous question: whenever in the past the analysis of an arch was led back to find of a line of thrust lying within the arch geometry, it was

applied unwittingly the Safe Theorem (the most relevant example was the work of Poleni on St Peter's dome).

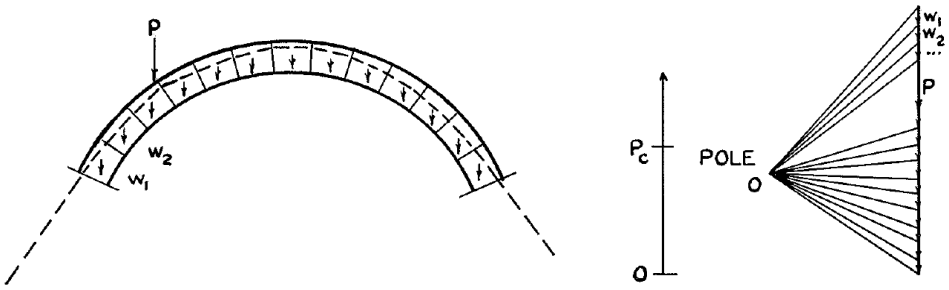

Fig. 6.28 - Drawing from (Kooharian, 1952). An application of the *Safe Theorem*: a graphical analysis through the funicular polygon of voussoir arch loaded by a force P is shown. The weight of each voussoir is think as concentrated in the relative center of gravity, and then the line of thrust coincides with the funicular polygon, and is uniquely determined fixing a pole O.

The Safe Theorem permits also to evaluate a lower bound multiplier for the load in the case of proportional loads. By applying the Safe Theorem a *safe or a lower bound value* of the load can be determined but it would be extremely important to know how safe it is: this could be done by determining an upper bound value of the collapse load. The **Kinematic Theorem** answers to this question being concerned with loads producing collapse. A structure reaches the collapse state when a sufficient number of plastic hinges form so as to reduce it to a mechanism.

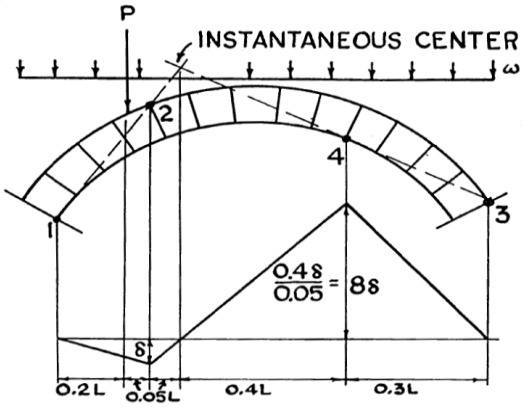

Fig. 6.29 - Drawing from (Kooharian, 1952): an application of the Kinematic Theorem.

A *"kinematical admissible"* collapse state is characterized by the condition that in a virtual displacement of the mechanism the work of the external loads must be at

least as large as that of the internal forces. Since an arch could view as a statically indeterminate structure with three unknown reactions, a generic collapse mechanism needs at least four hinges. A hinge for the voussoir arch form when the resultant of the compression stress N acts on the edge of a section: in this situation, relative rotation among two adjacent elements are allowed. The application of the Kinematic Theorem comes about with the choice of all possible mechanics for which the work of the external forces is greater than the work of internal one and consequently with a valuation of the minim of the upper bounds multipliers. In the case of proportional loadings, the integrated use of both safe and kinematic theorems allows to define an interval $[s', s'']$ to which the collapse multiplier has to belong. In a limit condition, that is $s' = s''$, the line of thrust touches the extrados and intrados in a certain number of point such that the structure becomes a mechanism (kinematic theorem).

* * *

Jaques Heyman. A rigorous framework for the application of the theorems of Limit Analysis to masonry, was given by (Heyman, 1966) by introducing these three necessary assumptions:

(i) masonry has no tensile strength,
(ii) masonry has infinite compressive strength,
(iii) sliding does not occur.

These assumption, and the subsequent application of Limit Analysis give a justification of the equilibrium approach of Poleni, Coulomb, Barlow and Yvon Villarceau. Assuming true the hypotheses (i) and (ii), the real yield surface (see **Fig. 6.30**) represented by the curved boundary *OCDEO* has to be replaced by the bilateral *AOB*.

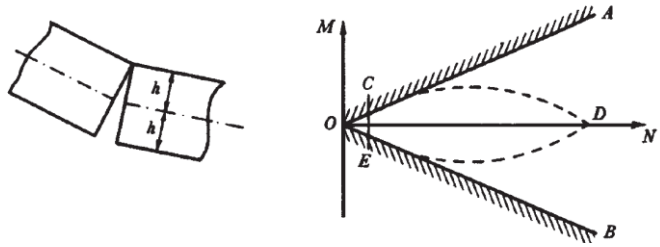

Fig. 6.30 – From (Heyman, 1966): an hinge (a) and the yield surface for masonry are shown.

However, although the simplification might seem substantial, Heyman pointed out that, generally, a typical value of permitted stress used in design is 10 per cent of the

crushing strength. For such a level of compressive stresses, the curved triangle *OCE* is practically coincident with the bilateral *AOB*.

For low stressed masonry structures, the compressive strength does not play any role, and the design rules consist only in static assessment in which the structural geometry becomes the pin point: that is the design rules become geometric rules.

Remark 2|6. As we have seen, 15 years before Kooharian had enunciated two of them, but it should be noted that Couplet in the XVIII century made already similar assumptions, although not so clearly. ■

Remark 3|6. The limit condition, represented by *N* acting on the edge of the section, obviously conducts to a concentration of compressive stress in that zone and could cause a failure by crushing. According to the basic assumption of infinite compressive strength, this kind of failure is neglected. Already Coulomb, at the end of the XVII century, made this observations and discussed also the necessary modifications if the stone were in danger of crushing. ■

Remark 4|6. In his milestone work (1966), Heyman never wrote anything about the elastic behaviour of masonry, neglecting completely any elastic behaviour of the masonry material. ■

■ 6.3 THE MASONRY ARCH: NUMERICAL MODEL AND BENCHMARKS

In this section, in order to test the PR method introduced in **Section 4.3**, we present some applications on arches by using the PR method (i.e. modelling the cracks as concentrated). The voussoir arch suggests directly the optimal partition (radial cuts) to be used and consequently a preliminary analysis, using the C^0 method (i.e. modelling the cracks as smeared), is not necessary. The application of the energy criterion (see **Chapter 4**) allows us to find directly the mechanism solution of the kinematical problem, considering variable both the given settlements (as show in **Section 6.4.1**) or the loads (**Sections 6.4.2** and **Sections 6.4.3**).

In what follows, we use as benchmark either well-known results or other results obtained analytically and reported in the appendix. In particular, the applications are:
- the analysis of a round arch subjected to given settlements;
- the evaluation of the minimum thickness;
- the analysis of the arch under horizontal actions.

As we will see, in all these cases, a perfect concordance between our numerical results and the benchmarks is obtained.

6.3.1 Arch, numerical analysis with PR method: model and discretization

In what follows, we consider a circular arch with a variable angle of embrace, subjected only to the self-weight q (**Fig. 6.31**).

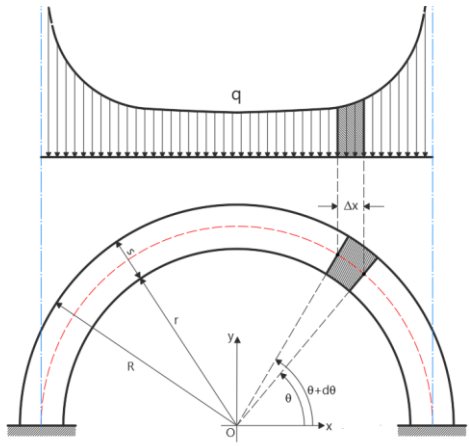

Fig. 6.31 - The discretization and the symbology used for the arch is shown. Since an arch could be thought of as composed by many individual sections fitted once upon another, the basic element of the discretization is chosen coinciding with a sector of annulus: this conducts to a distribution of the self-weight as depicted (see also **Section C.2**).

The application of the PR method to the arch proceeds through the following steps (specializing the procedure shown in **Section 4.3.2**).

* * *

1. The domain Ω_* representing the structural geometry of the arch is partitioned into M sectors of annulus Ω_{*i}. Each subdomain Ω_{*i} is approximated through a quadrilateral element Ω_i as shown in (**Fig. 6.32**) and then the domain:

$$\Omega = \mathrm{U}_{\mathrm{j}\in\{1\ldots M\}}\,\Omega_{\mathrm{j}}\,, \tag{6.1}$$

becomes *our structural model domain*. In particular, the set

$$\pi_M = \left\{\Omega_i \text{ with } j \in \{1 \ldots M\}\; s.t.\; \Omega_i \cap \Omega_{\mathrm{j}} \neq \emptyset \text{ for } i \neq j\right\}, \tag{6.2}$$

is a partition of the structural domain Ω constituted by a countable set of subdomains having finite perimeter, therefore, is a Caccioppoli partition of Ω in the sense of Chambolle et al (2007).

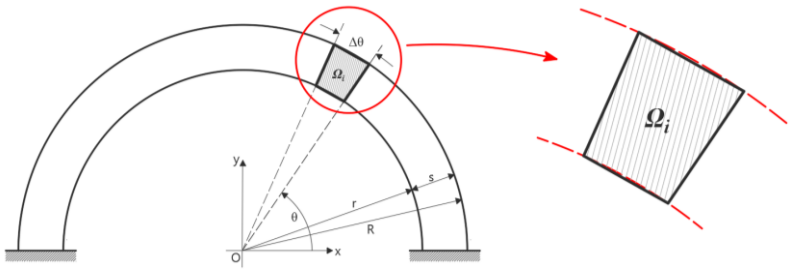

Fig. 6.32 - The basic element Ω_i of the partition π_M is depicted. The subdomain Ω_i approximates the sector of annulus Ω_{*i}, and consequently, increasing the number of elements M, Ω will tend to real arch domain Ω_*.

2. The displacement field $\boldsymbol{u} = \boldsymbol{u}(\boldsymbol{x})$**,** defined in Ω, is approximated as piecewise rigid. Since the number of elements of the discretization is M, the number of independent Lagrangian parameters is $3M$, collected in the vector:

$$\widehat{\boldsymbol{U}} = \left(U_1, V_1, \Phi_1, .., U_j, V_j, \Phi_j, .., U_M, V_M, \Phi_M\right)\,, \quad \widehat{\boldsymbol{U}} \in \mathbb{R}^{3M}\,. \tag{6.3}$$

* * *

3. The potential energy $\wp$ of the external forces can be expressed in terms of the components of $\widehat{\boldsymbol{U}}$ and is a linear function of $3M$ unknown Lagrangian parameters, symbolically expressed as follows:

$$\wp = \wp\left(\widehat{\boldsymbol{U}}\right) \ , \ \widehat{\boldsymbol{U}} \in \mathbb{R}^{3M} \ . \tag{6.4}$$

The problem can be formulated as a linear programming one, in the form:

$$\min_{\widehat{\boldsymbol{U}} \in \mathbb{K}^M} \wp\left(\widehat{\boldsymbol{U}}\right) , \tag{6.5}$$

$\mathbb{K}^M$ being the subset of $\mathbb{R}^{3M}$ defined by the unilateral and bilateral constraints associated to the contact and fixing conditions.

* * *

4. To fix ideas, let Ω_i and Ω_j be two contiguous subdomains, with the $l(A,B)$ side in common. Let $\boldsymbol{n}$ and $\boldsymbol{t}$ be the normal and tangential unit vectors to $l(A,B)$ (see **Fig. 6.33**), and $\boldsymbol{u}_j(A)$ the nodal displacement of the material point A belonging to the Ω_j subdomain.

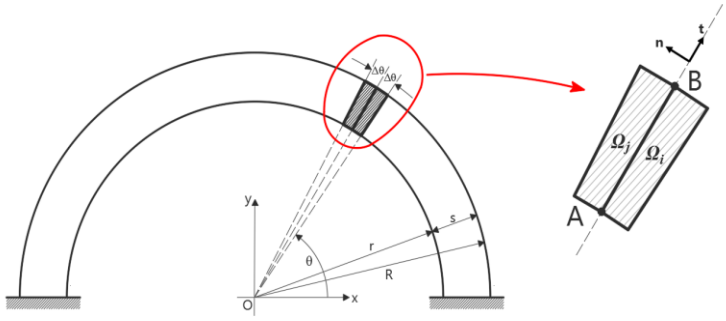

Fig. 6.33 - Two adjacent subdomains Ω_i and Ω_j are shown.

The kinematical conditions between Ω_i and Ω_j along $l(A,B)$ can be expressed as follows:

$$\left(\boldsymbol{u}_j(A) - \boldsymbol{u}_i(A)\right) \cdot \boldsymbol{n} \geq 0 \ , \tag{6.6}$$

$$\left(\boldsymbol{u}_j(B) - \boldsymbol{u}_i(B)\right) \cdot \boldsymbol{n} \geq 0 \ , \tag{6.7}$$

$$\left(\boldsymbol{u}_j(A) - \boldsymbol{u}_i(B)\right) \cdot \boldsymbol{t} = 0 \ . \tag{6.8}$$

These relations, written for all adjacent blocks, can be thought of as *constraints* on the displacement field $\boldsymbol{u}$ and then on the 3M Lagrangian parameters $\widehat{\boldsymbol{U}}$. Similar relations can be written to take into account the boundary conditions (see examples below).

Remark 5|6. It should be noted that previous restrictions imply that two adjacent voussoirs can rotate and detach each other, but cannot exhibit any relative sliding. ■

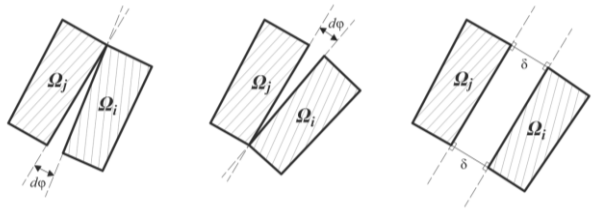

Fig. 6.34 - . All the three admissible relative displacements between two adjacent voussoirs are shown. The relative displacement between them represents the singular deformation $\boldsymbol{E}^s$.

Being M is the number of elements, the interfaces are $M+1$ ($M-1$ internal and 2 relative to the boundary) and consequently $3(M+1)$ is the total number of restrictions, both equalities and inequalities. These linear restrictions define a convex polytope $\mathbb{K}^M$ of the $\mathbb{R}^{3M}$ in which the solution $\widehat{\boldsymbol{U}}^0$ of the kinematical problem has to belong.

* * *

5. With the above approximation the structural problem is formulated as a minimum problem: "*find a piecewise rigid displacement* $\widehat{\boldsymbol{U}}^0$ *which minimizes the potential energy* $\wp$ *in* $\mathbb{K}^M$:

$$\min_{\widehat{\boldsymbol{U}}\in\mathbb{K}^M} \wp\left(\widehat{\boldsymbol{U}}\right) \text{ ."} \tag{6.9}$$

This linear programming problem is solved with the simplex method, or with the interior point method if the number of unknowns and conditions is large.

* * *

6. Found the minimizer $\widehat{\boldsymbol{U}}^0$, it is an easy task to evaluate the corresponding deformed shape of the arch, the hinges formed and the line of thrust. It will be noted that the moving part of the arch represents a one degree of freedom mechanism.

6.3.2 Benchmarks

The benchmarks we will present in the next sections refer to the following cases:

1. a round arch subjected to settlement:
    a. with supports subjected to given horizontal outward settlements;
    b. with supports subjected to given horizontal inward settlements;
    c. with a support subjected to a given vertical bottom settlement;
2. the assessment of the minimum thickness for:
    a. a round arch;
    b. a circular arch with a springing angle $\beta = 30°$;
    c. a circular arch with a springing angle $\beta = 60°$;
3. the assessment of the horizontal static multiplier for:
    a. a round arch;
    b. a circular arch with a springing angle $\beta = 15°$;
    c. a circular arch with a springing angle $\beta = 30°$;
    d. a circular arch with a springing angle $\beta = 45°$.

■ 6.4 BENCHMARK 1: THE EFFECT OF THE SETTLEMENTS

In this section, we present three cases regarding a round arch subjected to given settlements. In all these cases, the round arch, with an internal radius $r = 1m$ and a thickness s equals to 0.25m ($s/r = 0.25$), is discretized with 500 elements and loaded only by the self-weight applied at the centres of gravity of each element.

6.4.1 Round arch subjected to given outward settlements

In this example, both supports are subjected to given outward settlements δ as shown in **Fig. 6.35** (see also **Section 3.5**).

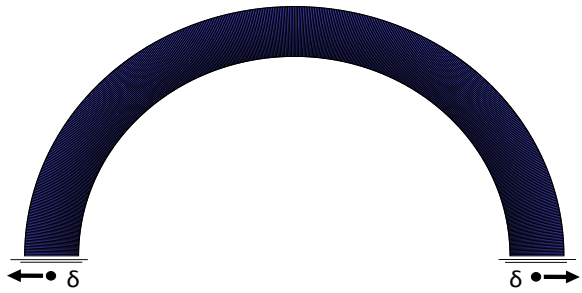

Fig. 6.35 - A round arch, loaded by the self-weight and discretized with 500 elements, is subjected to given horizontal outward settlements δ.

Remark 6|6. As for the implementation of the boudary constraints, with reference to the right base element Ω_k, let A and B the two contact points with the base support (**Fig. 6.36**).

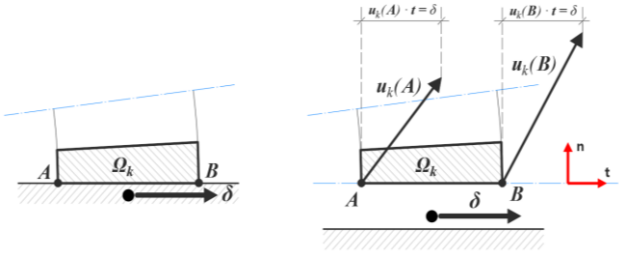

Fig. 6.36 - The way to implement the horizontal outward settlement δ with respect to the right base element Ω_k is shown.

The constraints, expressing the settlements, can be written as function of the displacements of the points A and B, namely:

$$\begin{array}{lll} \boldsymbol{u}_k(A)\cdot\boldsymbol{t}=\delta & \text{or} & \boldsymbol{u}_k(B)\cdot\boldsymbol{t}=\delta\ , \\ \boldsymbol{u}_k(A)\cdot\boldsymbol{n}\geq 0 & & \boldsymbol{u}_k(B)\cdot\boldsymbol{n}\geq 0\ . \end{array}$$

The first two relations express the support settlement, whilst the unilateral ones represent the unilateral contact with the base support. Similar relations have to be written for the left base element. These boundary relations combined with the internal ones will define the subset $\mathbb{K}^M$ in which the optimal solution has to be found. ■

Since the number of elements is 500, the total unknowns are 1500 (i.e. the dimension of $\widehat{\boldsymbol{U}}$). The number of relations, both equalities and inequalities, defining the subset of $\mathbb{K}^M \subseteq \mathcal{R}^{1500}$ is 1503. The solution $\widehat{\boldsymbol{U}}^0$ of the minimum problem:

$$\min_{\widehat{\boldsymbol{U}}\in\mathbb{K}^M} \wp\left(\widehat{\boldsymbol{U}}\right),$$

reached through the simplex method in 16.55s (with an Intel® Core™ i7-6700HQ), is shown in **Fig. 6.37**. It should be noted that the solution is symmetric and three hinges form (0.5027rad, $\pi/2$ and $(\pi-0.5027)$rad). Initially the arch was hyperstatic with many redundancies, but the formation of these three hinges turns it into an isostatic substructure.

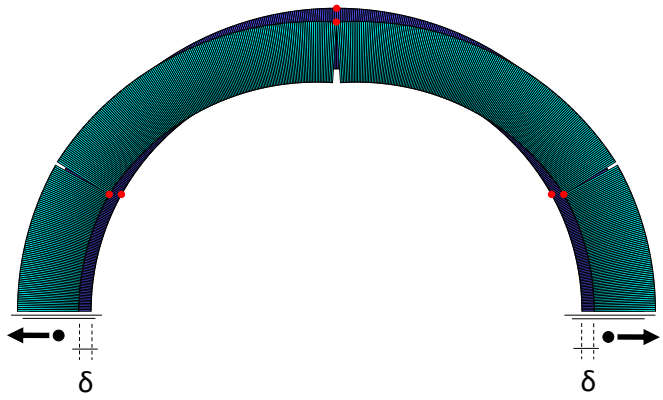

Fig. 6.37 - A graphical representation of the solution $\widehat{U}^0$ of the minimum problem obtained with the PR method: three hinges form and the arch becomes isostatic.

By adopting a thrust line solution for the stress, the position of the hinges determines three conditions, which are sufficient to determine a unique pressure line, as shown in **Fig. 6.38**.

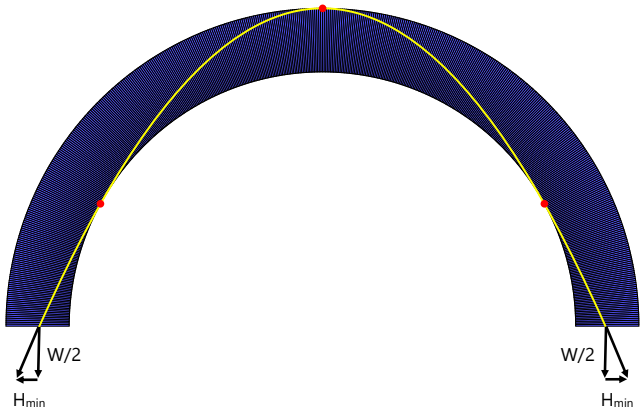

Fig. 6.38 - The hinges formed and the relative thrust line are represented. Since W indicates the weight of the whole structure, H_{min} represents the horizontal thrust on the base supports.

Remark 7|6. The solution of the problem does not depend on the value δ of the settlement: indeed, by varying the value of δ, the numerical solution is self-similar and returns exactly the same position of the hinges. ■

Remark 8|6. The outward settlements of the supporting structures represent the ultimate cause of the cracking at the in the intrados of the key section (often the only visible of the three ones) and, consequently, of the drop of the thrust with respect to the initial configuration. ■

6.4.2 Round arch subjected to given inward settlements

In this case, both supports are subjected to given inward settlements δ as shown in **Fig. 6.39**.

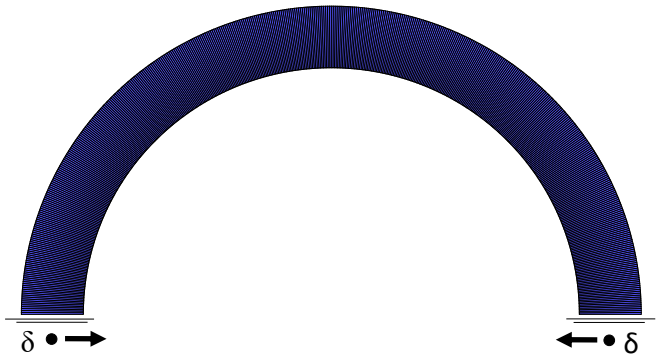

Fig. 6.39 - A round arch, loaded by the self-weight and discretized with 500 elements, is subjected to given horizontal inward settlements δ.

Remark 9|6. The supports settlements are expressed analytically through 6 indipendent relations involving only two base blocks. With reference to the right base element Ω_k (**Fig. 6.40**), the relations can be expressed as follows

$$\begin{matrix} \boldsymbol{u}_k(A)\cdot\boldsymbol{t}=-\delta \\ \boldsymbol{u}_k(A)\cdot\boldsymbol{n}\geq 0 \end{matrix} \quad \text{or} \quad \begin{matrix} \boldsymbol{u}_k(B)\cdot\boldsymbol{t}=-\delta\ , \\ \boldsymbol{u}_k(B)\cdot\boldsymbol{n}\geq 0\ . \end{matrix}$$

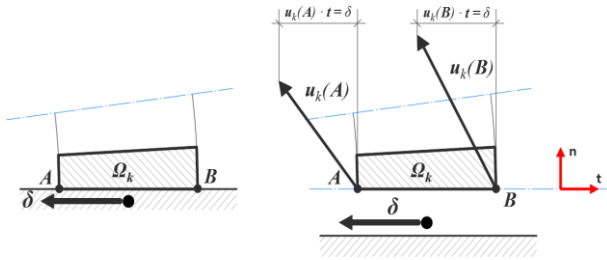

Fig. 6.40 - The way to implement the horizontal inward settlement δ with respect to the right base element Ω_k is shown.

The first two relations express the support settlement, whilst the unilateral ones represent the unilateral contact with the base support. Similar relations have to be written for the left base element. ■

The solution $\widehat{\boldsymbol{U}}^0$ of the minimum problem, reached both with the simplex method (19.82s with an Intel® Core™ i7-6700HQ) and with the interior point method (0.11s

with an Intel® Core™ i7-6700HQ), is shown in **Fig. 6.41** and in **Fig. 6.42**. Even in this case, the arch, initially hyperstatic with many redundancies, is turned into an isostatic substructure.

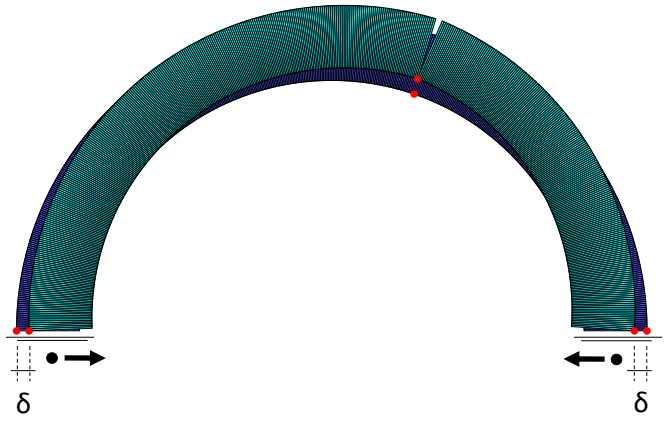

Fig. 6.41 - A graphical representation of the solution $\widehat{\boldsymbol{U}}^0$ obtained with the simplex method is reported: three hinges form respectively at 0.0 rad, 1.238rad and at π.

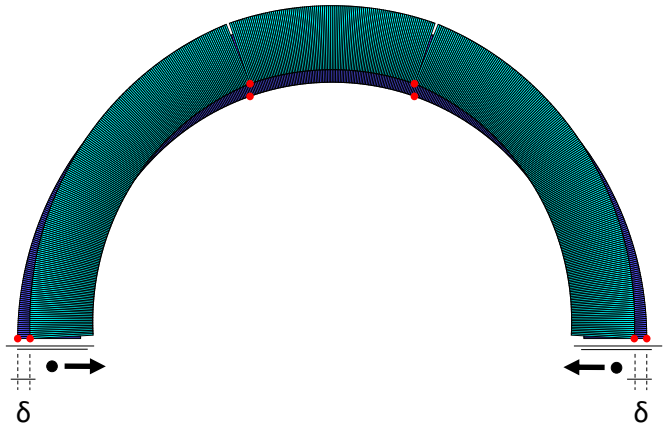

Fig. 6.42 - The solution $\widehat{\boldsymbol{U}}^0$ obtained with the interior point method is reported: four hinges form respectively at 0.0 rad, 1.238rad, $(\pi - 1.238)$rad and at π.

With reference to the solution obtained with the simplex method, by adopting a thrust line solution for the stress, the position of the hinges determines three conditions, which are sufficient to determine a unique pressure line, as shown in **Fig. 6.43.**

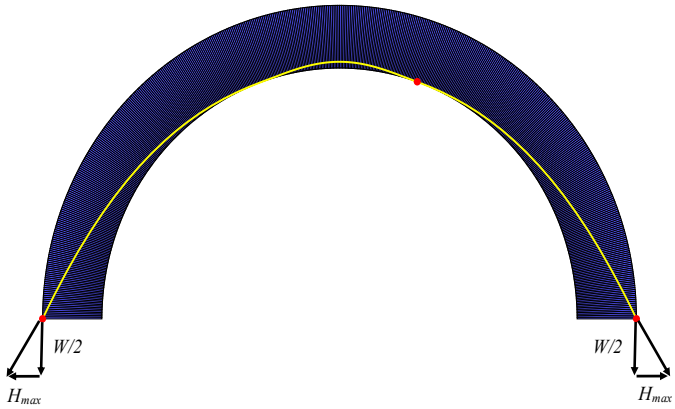

Fig. 6.43 - The hinges formed and the relative thrust line are represented. W indicates the weight of the whole structure whilst H_{max} the horizontal thrust on the base supports.

Remark 10|6. By comparing the lines of thrust depicted in **Fig. 6.43** and **Fig. 6.38**, since the weight of the arch is the same, the change of the angle of incidence on the supports causes the increase of the horizontal thrust from H_{min} to H_{max}: small changes in external conditions (an abutment gives way slightly or the external structure pushes the arch inward) force the thrust line to assume two widely different positions altering markedly the actual equilibrium state of the arch. In both cases, the arch accommodates the external changes by forming an isostatic substructure, i.e. a three-pin arch. ■

Remark 11|6. By comparing the solutions depicted in **Fig. 6.41** and in **Fig. 6.42**, the total relative rotation of two internal hinges shown in **Fig. 6.42** is equal to the relative rotation of the single hinge of **Fig. 6.41**. It should be noted that if there is a little asymmetric change, either in the geometry or in the load, one of the two hinges of **Fig. 6.42** will not form. ■

6.4.3 Round arch subjected to a given bottom settlement

Here, the right support is subjected to a given vertical settlement δ as shown in **Fig. 6.44.**

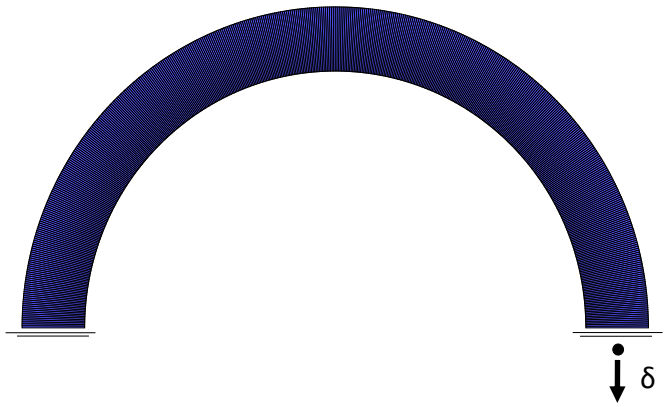

Fig. 6.44 - A round arch, loaded by the self-weight and discretized with 500 elements, is subjected to a given vertical settlement δ.

Remark 12|6. The settlement is expressed analytically (**Fig. 6.45**) through three relations involving only the right base element Ω_k:

$$\begin{aligned} &\boldsymbol{u}_k(A)\cdot\boldsymbol{t}=0 \quad \text{or} \quad \boldsymbol{u}_k(B)\cdot\boldsymbol{t}=0\ , \\ &\boldsymbol{u}_k(A)\cdot\boldsymbol{n}\geq-\delta \quad \boldsymbol{u}_k(B)\cdot\boldsymbol{n}\geq-\delta\ . \end{aligned}$$

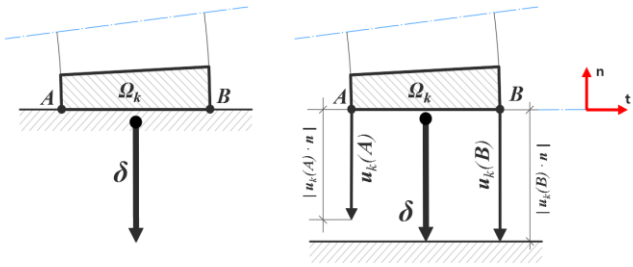

Fig. 6.45 - The way to implement the vertical settlement δ with respect to the subdomain Ω_k is shown.

The first two relations express the no sliding condition, whilst the unilateral ones represent the unilateral contact with the base support taking also into account the given vertical settlment. ■

The solution $\widehat{\boldsymbol{U}}^0$ of the minimum problem, reached both with the simplex method (20.56s with an Intel® Core™ i7-6700HQ) is shown in **Fig. 6.46**. Also in this case, the

arch, initially hyperstatic with many redundancies, is turned into an isostatic substructure.

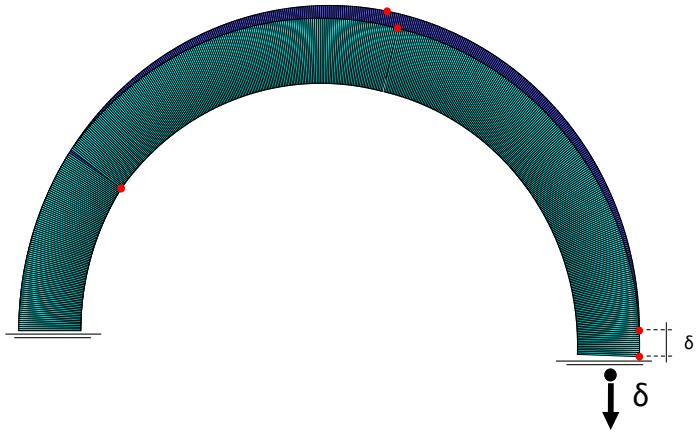

Fig. 6.46 - A graphical representation of the solution $\widehat{\boldsymbol{U}}^0$ obtained with the simplex method is reported: three hinges form respectively at 0.0 rad, 1.382rad and 2.564rad.

The positions of these three hinges return three conditions, which are sufficient to determine a unique pressure line, as shown in **Fig. 6.47**.

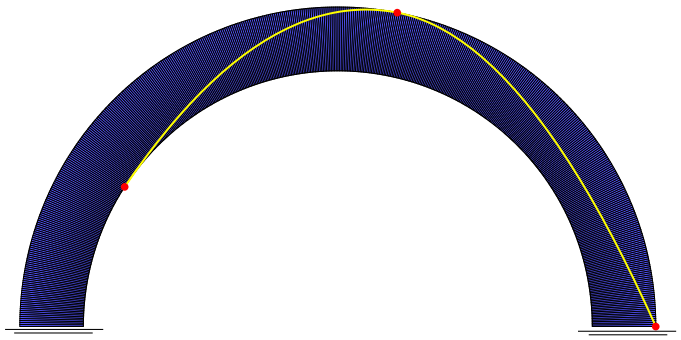

Fig. 6.47 - The hinges formed and the relative thrust line are represented.

■ 6.5 BENCHMARK 2: COUPLET'S PROBLEM

Let us consider the following problem: what is the minimum thickness for which an arch is yet safe under its own weight?

Remark 13|6. This is a well-known problem in literature, known as the minimum thickness problem or also the Couplet's problem because, the first who posed this question and gave a solution was Couplet. Almost two centuries later, Heyman (1969) solved the problem for a round arch (partitioning the domain with vertical cuts), and successively the solution was recalculated by Ochsendorf (2006) with a different partition of the domain (sectors of annulus). For a detailed analysis see **Appendix D** and (Heyman, 2009).

In this section, by using the PR method, we propose some applications concerning the evaluation of the minimum thickness of a circular arch (with an internal radius $r = 1.00m$) subjected only to the self-weight and with different springing angles β (i.e. the total angle of embrace is $\pi - 2\beta$).

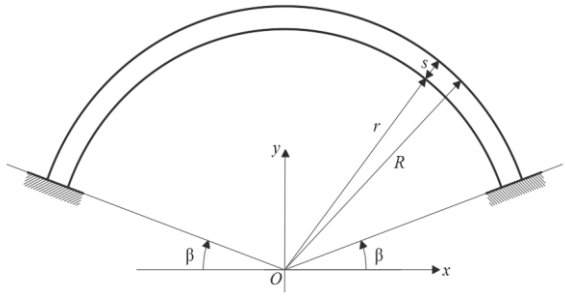

Fig. 6.48 – The symbology adopted for a circular arch with a springing angle β is shown.

When the thickness s reaches its minimum value, the arch becomes a mechanism: four rigid bodies hinged in five points as shown in **Fig. 6.49**. The positions of the hinges are defined by the angles θ_i.

The procedure of finding the solution is provided by the following observation.

Remark 14|6. With reference to a structure with a fixed discretization, the subset $\mathbb{K}^M$ of $\mathbb{R}^{3M}$, defined by the internal and boundary restrictions, can be thought of as the subset of all mechanisms compatible with the constraints: in this sense *the energy criterion is a selection criterion of the mechanism solving the kinematical problem in* $\mathbb{K}^M$.

If the boundary conditions are homogeneous, the homogeneous solution, i.e. $\widehat{\boldsymbol{U}}^0 = \mathbf{0}$, belongs to the subset $\mathbb{K}^M$. When the minimizer is $\widehat{\boldsymbol{U}}^0 = \mathbf{0}$ the initial configuration is safe and no one mechanism can occur. Instead, when then initial configuration is not stable, the solution $\widehat{\boldsymbol{U}}^0$ of the minimum problem is not homogeneous, that is $\widehat{\boldsymbol{U}}^0 \neq \mathbf{0}$.

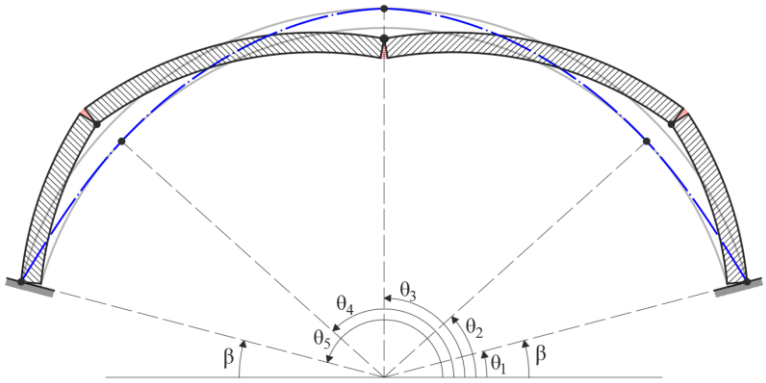

Fig. 6.49 - The mechanism associated with the solution of the Couplet's problem for an arch with springing angle $\beta = 15°$. The crosshatch in red represents the singular deformations $\boldsymbol{E}^s$ along the hinges whilst the dash-dotted blue line represents the support of the singular part $\boldsymbol{T}^s$ of the stress field.

We perform a numerical procedure based on the following two steps:

(i) initially we fix a value s_s of the thickness to which there corresponds a safe configuration (i.e. $\widehat{\boldsymbol{U}}^0 = \mathbf{0}$);

(ii) by decreasing the thickness s, we find the least value of s (say s_m) for which the arch becomes a mechanism (i.e. $\widehat{\boldsymbol{U}}^0 \neq \mathbf{0}$).

In this way, rather than find an exact value of s_{min}, we define an interval $[s_m, s_s]$ to which the minimum thickness, solution of the Couplet's problem, has to belong.

In what follows we evaluate the minimum thickness for a circular arch considering four springing angles β: 0°, 30°, and 60°. In **Tab. 6.1** (extracted from **Tab D.1**) the relative analytical solutions are reported.

β [°]	s_{min}/r	θ_2 [°]	$\theta_2 - \beta$ [°]
0.00	0.1135818	35.52	35.52
30.00	0.0231130	50.54	20.54
60.00	0.0015265	69.19	9.19

Tab. 6.1 - The minimum thickness s_{min}/r, the angle θ_2 and the angle $\theta_4 = \theta_2 - \beta$ as functions of the springing angle β are reported.

6.5.1 Couplet's problem: numerical solution for β=0°

A round with an internal radius $r = 1$m is discretized with 500 elements (**Fig. 6.50a)**. The only load considered is the self-weight applied at the centres of gravity of each voussoir. In **Fig. 6.50** the solutions corresponding to a safe value of s_s and to the unstable one s_m are shown.

Fig. 6.50 – In (a) the solutions corresponding to a safe value of the thickness (s_s = 0.11359). In (b) the mechanism corresponding to s_m = 0.11357.

The solution $\widehat{\boldsymbol{U}}^0$ of the minimum problem, reached through the simplex method, is practically coincident to the analytical one (**Tab. 6.2**) and corresponds exactly to that found by Ochsendorf (2006). The mechanism, the relative hinges and the associated line of thrust are depicted in **Fig. 6.51**.

$\beta = 0°$	s_{min}/r	ϑ_2 [°]
Numerical solution	[0.11357 , 0.11359]	35.64
Analytical solution	0.11358	35.52

Tab. 6.2 - The numerical solution reached with the simplex method and the analytical one (extracted from **Tab. D.1**) are reported.

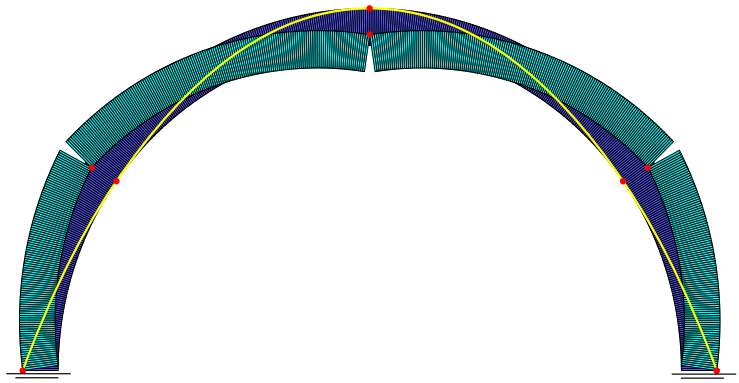

Fig. 6.51 - The mechanism, the hinges and the associated line of thrust corresponding to the value $s_m = 0.11357$ are shown.

6.5.2 Couplet's problem: numerical solution for β=30°

In this case we consider a circular arch, discretized with 100 elements, with a springing angle $\beta = 30°$ and an internal radius $r = 1$m (**Fig. 6.52a**). The arch is loaded by the self-weight. In **Fig. 6.52** the solutions corresponding to a safe value of s_s and to the unstable one s_m are shown.

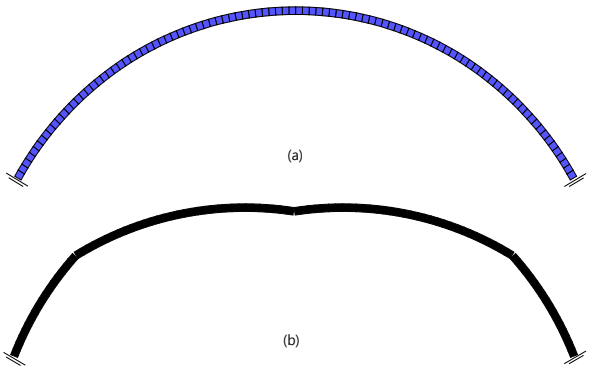

Fig. 6.52 - In (a) the solutions corresponding to a safe value of the thickness ($s_s = 0.0233$). In (b) the mechanism corresponding to $s_m = 0.0230$.

The solution $\widehat{\boldsymbol{U}}^0$ of the minimum problem, reached through the simplex method, is coincident to the analytical one (**Tab. 6.3**). The mechanism, the relative hinges and the associated line of thrust are depicted in **Fig. 6.53**.

$\beta = 30°$	s_{min}/r	ϑ_2 [°]
Numerical solution	[0.0230 , 0.0233]	50.40
Analytical solution	0.02311	50.54

Tab. 6.3 - The numerical solution reached with the simplex method and the analytical one (extracted from **Tab. D.1**) are reported.

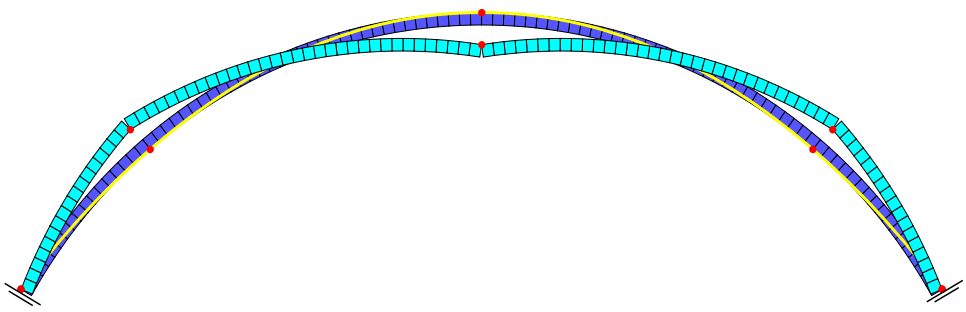

Fig. 6.53 - The mechanism, the hinges and the associated line of thrust corresponding to the value $s_m = 0.0230$ are shown

6.5.3 Couplet's problem: numerical solution for β=60°

The circular arch of **Fig. 6.54a** ($\beta = 60°, r = 1$m) is discretized with 500 elements and is subjected to its self-weight. In **Fig. 6.54** the solutions corresponding to a safe value of s_s and to the unstable one s_m are shown.

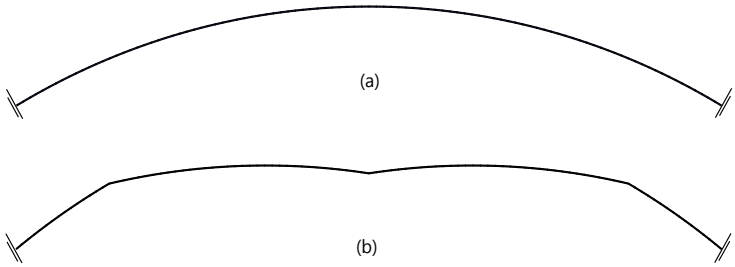

Fig. 6.54 - In (a) the solutions corresponding to a safe value of the thickness ($s_s = 0.00155$). In (b) the mechanism corresponding to $s_m = 0.00151$.

The solution $\widehat{\boldsymbol{U}}^0$ of the minimum problem, reached through the simplex method, is coincident to the analytical one (**Tab. 6.4**). The mechanism, the relative hinges and the associated line of thrust are depicted in **Fig. 6.55**.

$\beta = 60°$	s_{min}/r	ϑ_2 [°]
Numerical solution	[0.00151 , 0.00155]	69.00
Analytical solution	0.001526	69.19

Tab. 6.4 - The numerical solution reached with the simplex method and the analytical one (extracted from **Tab. D.1**) are reported.

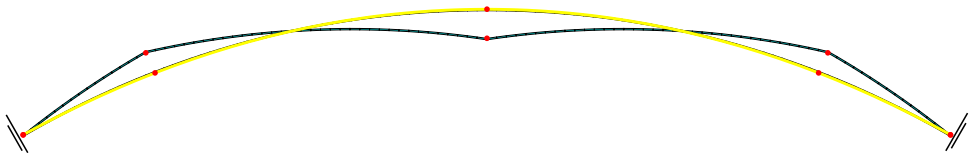

Fig. 6.55 - The mechanism, the hinges and the associated line of thrust corresponding to the value $s_m = 0.11357$ are shown.

■ 6.6 BENCHMARK 3: THE ARCH UNDER HORIZONTAL ACTION

In this section, we present some applications concerning the arch subjected to horizontal actions, as those produced by a seismic action. The only load considered is the self-weight and the horizontal incremental action is represented by forces, proportional to the mass through the scale parameter λ, and acting in centres of gravity of each block. (**Fig. 6.56**).

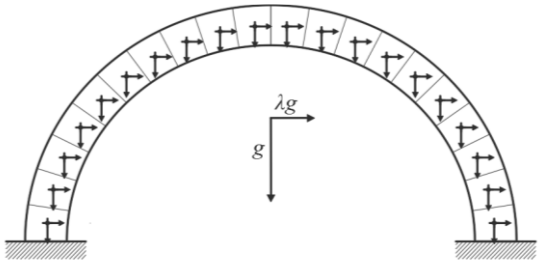

Fig. 6.56 - The arch is subjected to vertical and horizontal loads applied to the centroids of each voussoir.

When λ reaches a certain value, say λ_c, four hinges form and the arch becomes a mechanism (**Fig. 6.57**) with the moving part composed by three rigid blocks hinged in four points.

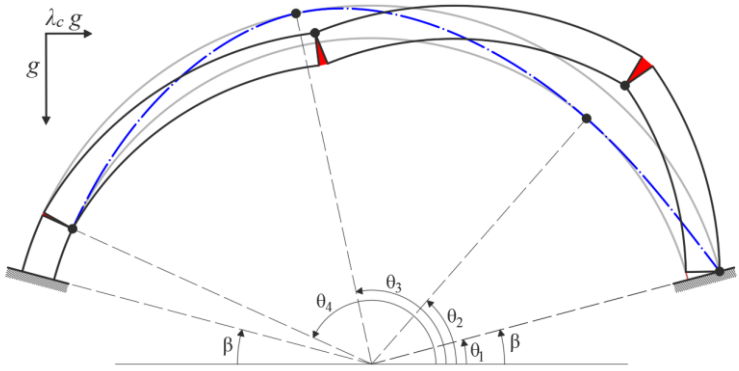

Fig. 6.57 - When the scale parameter λ reaches a certain value, the arch becomes a mechanism constituted by three rigid blocks hinged in four points.

The numerical strategy adopted to solve the problem is the same as that used for the minimum thickness problem. The interval $[\lambda_s, \lambda_m]$, to which the collapse multiplier λ_c has to belong, is found through a numerical procedure. In particular, λ_s represents an approximation of the supremum of the multipliers for which the initial configuration is still safe (i.e. the minimizer is homogeneous, namely $\widehat{\boldsymbol{U}}^0 = \mathbf{0}$), whilst

λ_m represents an approximation of the infimum of the multipliers for which the structure becomes a mechanism, that is $\widehat{\boldsymbol{U}}^0 \neq \mathbf{0}$.

In the next sections, we present some applications regarding a circular arch with a different springing angle, and, in order to test our numerical method, we compare these results to those obtained analytically (see **Appendix E**, **Tables E.1**, **E.2**, **E.3** and **E.4**).

The goal of this analysis is to search the exact position of four hinges (defined by the angles θ_i for $i \in \{1, \dots, 4\}$) and of the interval to which the collapse multiplier λ_c has to belong.

6.6.1 Circular arch under horizontal action: β=0°

In this section, we analyse a round arch ($\beta = 0°$) with an internal radius $r = 1.00m$, and thickness $s = 0.25m$. The arch is discretized with 80 rigid quadrangular elements (**Fig. 6.58a**).

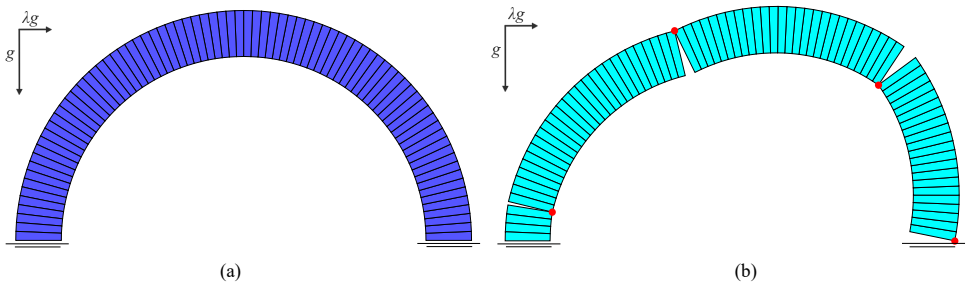

Fig. 6.58 – In (a) the round arch, discretized with 80 rigid elements, is depicted. In (b) the solution $\hat{U}^0$ corresponding to $\lambda = 0.340$ is reported.

The solution $\hat{U}^0$ of the minimum problem (**Fig. 6.58b**), reached through the simplex method, is close to the analytical one (**Tab. 6.5**). The mechanism, the relative hinges and the associated line of thrust are depicted in **Fig. 6.59**.

s =0.25m	λ_c	θ_4 [°]	θ_3 [°]	θ_2 [°]	θ_1 [°]
Numerical solution	[0.334 , 0.340]	171.00	108.00	47.25	0.00
Analytical solution	0.340	170.04	108.75	47.47	0.00

Tab. 6.5 - The numerical solution reached with the simplex method and the analytical one (extracted from **Tab. E.1**) are reported.

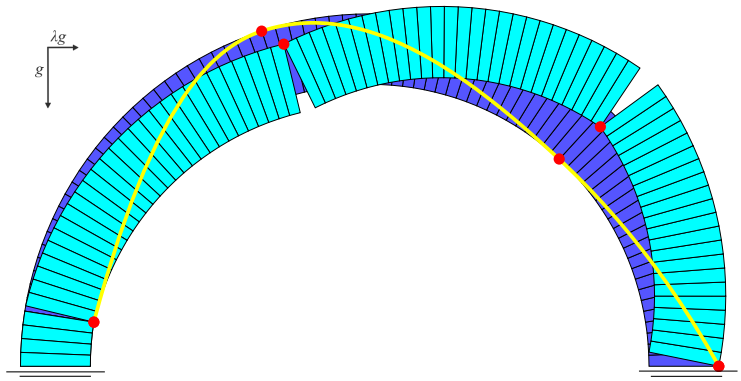

Fig. 6.59 - The mechanism corresponding to $\lambda = 0.340$, the hinges formed and the associated thrust line are represented.

6.6.2 Circular arch under horizontal action: β=15°

The circular arch with a total angle of embrace equals to $150°$ ($\beta = 15°$), internal radius $r = 1.00m$ and thickness $s = 0.15m$ is discretized with 100 rigid elements (**Fig. 6.60a**).

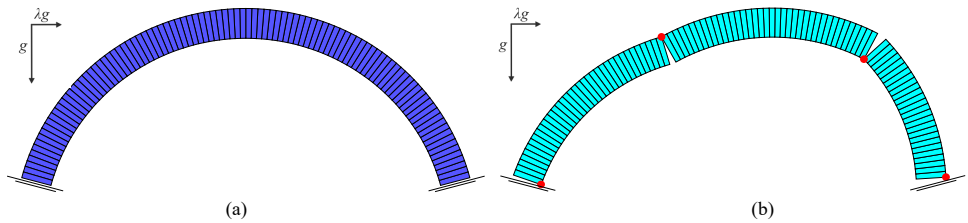

Fig. 6.60 - The depressed arch ($\beta = 15°$) is discretized with 100 rigid elements. In (b) the solution $\widehat{\boldsymbol{U}}^0$ corresponding to $\lambda = 0.395$ is reported.

The solution $\widehat{\boldsymbol{U}}^0$ of the minimum problem (**Fig. 6.60b**), reached through the simplex method, is coincident to the analytical one (**Tab. 6.6**).

s =0.15m	λ_c	θ_4 [°]	θ_3 [°]	θ_2 [°]	θ_1 [°]
Numerical solution	[0.390 , 0.395]	165.00	111.00	54.00	15.00
Analytical solution	0,392	165,00	111,32	54,29	15,00

Tab. 6.6 - The numerical solution reached with the simplex method and the analytical one (extracted from **Tab. E.2**) are reported.

The mechanism, the hinges formed and the line of thrust are reported in **Fig. 6.61**.

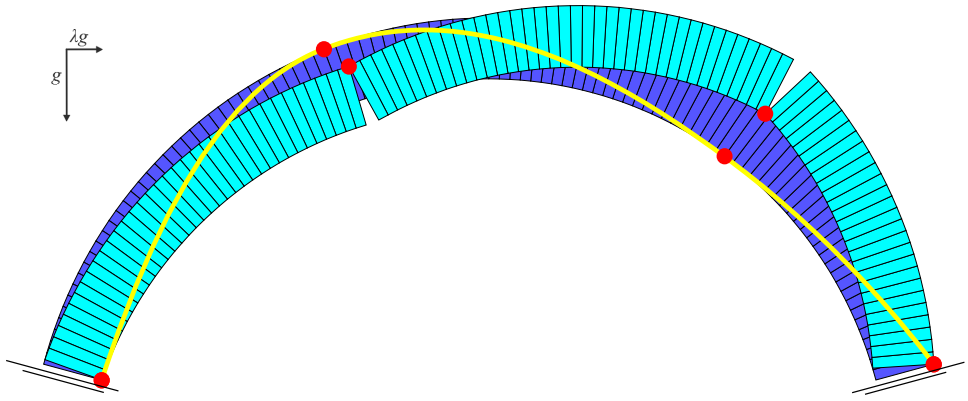

Fig. 6.61 - The mechanism corresponding to $\lambda = 0.395$, the hinges formed and the associated thrust line are represented.

6.6.3 Circular arch under horizontal action: β=30°

The circular arch with a springing angle $\beta = 30°$, internal radius $r = 1.00m$ and a thickness $s = 0.10m$ is discretized with 120 rigid elements (**Fig. 6.62a**).

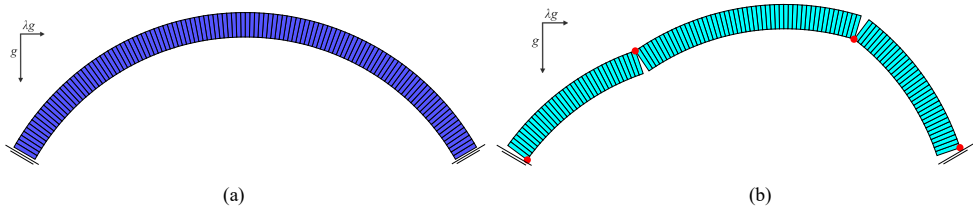

Fig. 6.62 – In (a) the depressed arch ($\beta = 30°$) is discretized with 120 rigid elements. In (b) the solution $\widehat{\boldsymbol{U}}^0$ corresponding to $\lambda = 0.549$ is reported.

The solution $\widehat{\boldsymbol{U}}^0$ of the minimum problem (**Fig. 6.62b**), reached through the simplex method, is coincident to the analytical one (**Tab. 6.7**).

s =0.10m	λ_c	θ_4 [°]	θ_3 [°]	θ_2 [°]	θ_1 [°]
Numerical solution	[0.548 , 0.549]	150.00	115.00	64.14	30.00
Analytical solution	0.549	150.00	114.97	63.59	30.00

Tab. 6.7 - The numerical solution reached with the simplex method and the analytical one (extracted from **Tab. E.3**) are reported.

The mechanism, the corresponding hinges and the line of thrust are reported **Fig. 6.63**.

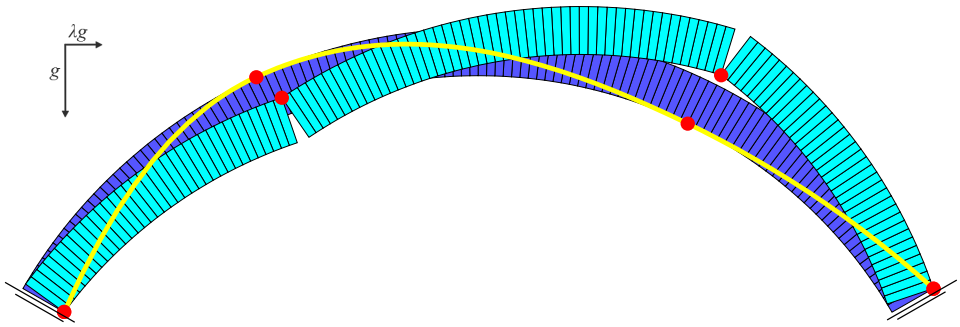

Fig. 6.63 - The mechanism corresponding to $\lambda = 0.549$, the hinges formed and the associated thrust line are represented.

6.6.4 Circular arch under horizontal action: β=45°

The circular arch with a total angle of embrace equals to 90° ($\beta = 45°$), internal radius $r = 1.00m$ and thickness $s = 0.03m$ is discretized with 120 rigid elements (**Fig. 6.64a**).

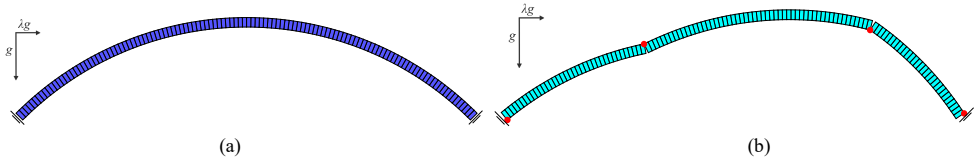

Fig. 6.64 - The depressed arch ($\beta = 45°$) is discretized with 120 rigid elements. In (b) the solution $\hat{\boldsymbol{U}}^0$ corresponding to $\lambda = 0.3700$ is reported.

The solution $\hat{\boldsymbol{U}}^0$ of the minimum problem (**Fig. 6.64b**), reached through the simplex method, is close to the analytical one (**Tab. 6.8**).

s =0.03m	λ_c	θ_4 [°]	θ_3 [°]	θ_2 [°]	θ_1 [°]
Numerical solution	[0.3765 , 0.3700]	135.00	107.25	67.75	45.00
Analytical solution	0.377	135.00	107.20	67.06	45.00

Tab. 6.8 - The numerical solution reached with the simplex method and the analytical one (extracted from **Tab. E.4**) are reported.

The mechanism, the hinges formed and the associated line of thrust are depicted in **Fig. 6.65**.

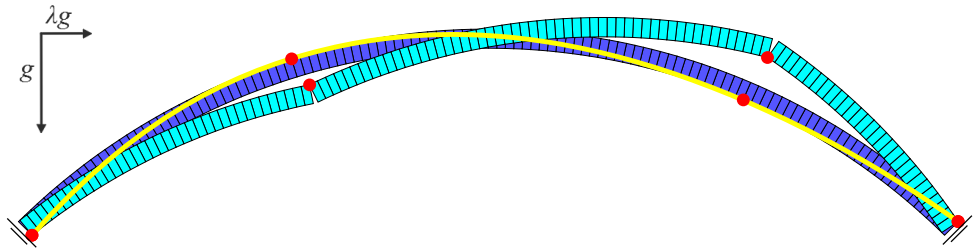

Fig. 6.65 - The mechanism corresponding to $\lambda = 0.340$, the hinges formed and the associated thrust line are represented.

Chapter 7

APPLICATIONS AND CASE STUDIES

Prologue. In the first part of this Chapter, we present some applications concerning simple portals analysed using the two numerical methods described in **Chapter 4**, namely the PR method, based on rigid blocks (modelling the cracks as concentrated), and the C^0 method, based on continuous functions (modelling the cracks as smeared). It will be seen that with the application of the continuous model, the solution will often give a hint on a partition into rigid blocks. In the central part of this Chapter, some examples regarding simple walls with openings, analysed with the PR method, are shown. In the final part, we present three case studies, developed with the PR method, in order to illustrate the way in which a particular fracture pattern can be identified.

■ 7.1 EXAMPLE 1: PORTAL (CASE A)

In this section, we present two applications concerning the same portal analysed with the two methods: the PR method (rigid blocks), and the C^0 method (based on continuous functions).

7.1.1 Numerical analysis with the PR method

The NRNT portal, subjected to a piecewise uniformly distributed load (represented in **Fig. 7.1a** with yellow strips), is discretized with rigid blocks using 1536 triangular elements (**Fig. 7.1a**). As shown in the figure, the right support is subjected to a given vertical settlement δ.

Remark 1|7. The settlement of the right support is expressed analytically on each interface through four restrictions:

$$\begin{aligned} \boldsymbol{u}_k(A)\cdot\boldsymbol{t} &= 0 \qquad & \boldsymbol{u}_k(B)\cdot\boldsymbol{t} &= 0\ , \\ \boldsymbol{u}_k(A)\cdot\boldsymbol{n} &\geq -\delta \qquad & \boldsymbol{u}_k(B)\cdot\boldsymbol{n} &\geq -\delta\ , \end{aligned}$$

being $\boldsymbol{t}$ and $\boldsymbol{n}$ the tangential and normal unit vectors whilest A and B represent the two end nodes of the interface.

The solution $\widehat{\boldsymbol{U}}^0$ of the minimum problem is reached through the interior point method in 6.04s with an Intel® Core™ i7-6700HQ (see **Fig. 7.1b**).

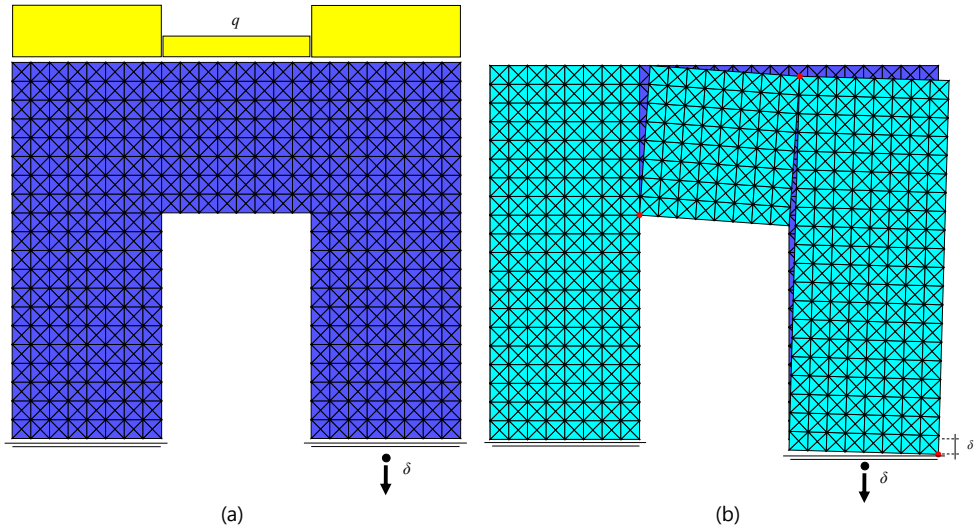

Fig. 7.1 - A portal of NRNT material, loaded by a piecewise uniformly distributed load (represented by the yellow strips) and subjected, on the right support, to a given vertical settlement, is discretized with 1536 triangular elements (a). The solution $\widehat{\boldsymbol{U}}^0$ obtained through the interior point method is reported in (b).

Three hinges form and then the moving part of the structure becomes isostatic. The corresponding line of thrust can be determined (**Fig. 7.2**).

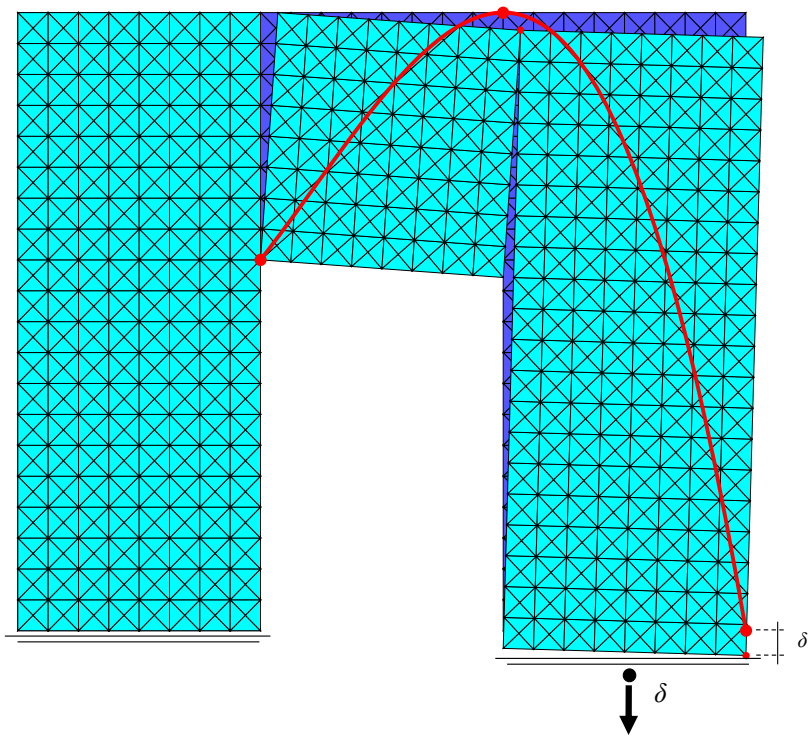

Fig. 7.2 - The hinges formed and the relative thrust line are represented.

7.1.2 Numerical analysis with the C^0 method

Here we analyse the same portal of **Fig. 7.1a** with the C^0 method, based on an approximation with continuous functions. The portal of NRNT material (**Fig. 7.3a**) is discretized using 96 9-nodes square elements (a second order Lagrangian quadrangular element) and is loaded by its self –weight represented with a piecewise uniformly distributed load (yellow strips). The right support is subjected to a given vertical settlement δ.

The solution $\widehat{\boldsymbol{U}}^0$ of the minimum problem is reached through the minimization of the energy into the finite element space defined in **Section 4.4**. The solution, obtained with the interior point method in 89.53s (with an Intel® Core™ i7-6700HQ), is shown graphically in **Fig. 7.3b**.

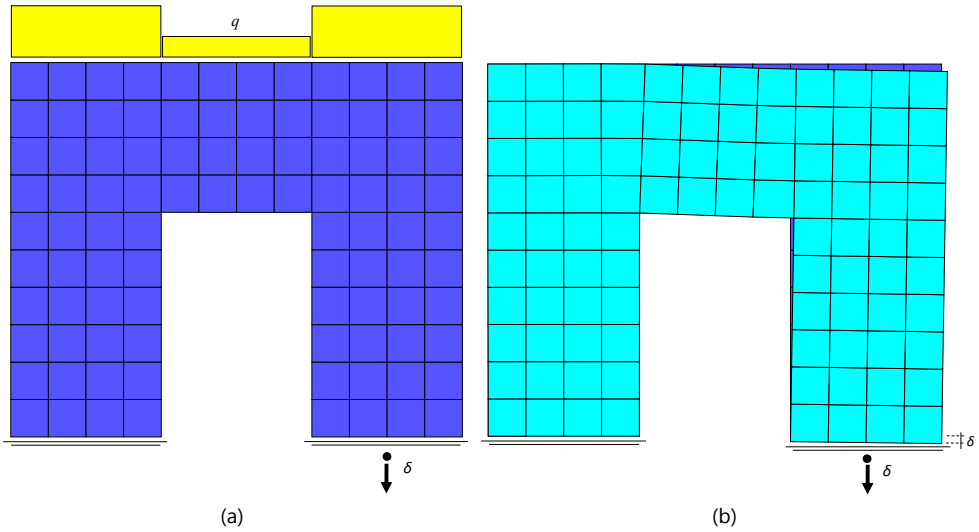

Fig. 7.3 – In (a) a portal of NRNT material, discretized with 96 9-nodes square elements and loaded by a piecewise uniformly distributed load (yellow strips), is subjected to a given vertical settlement δ at the right support. In (b): representation of the solution $\widehat{\boldsymbol{U}}^0$ obtained through the interior point method.

To represent the strain field $\boldsymbol{E}$, we report in **Fig. 7.4** a measure of the deformation, namely $|\boldsymbol{E}|^2 = tr(\boldsymbol{E}\boldsymbol{E}^T)$. From **Fig. 7.4** we see that the gradient of deformation is concentrated on two vertical strip of elements, whilst the other elements are characterized by strains whose norm is close to zero.

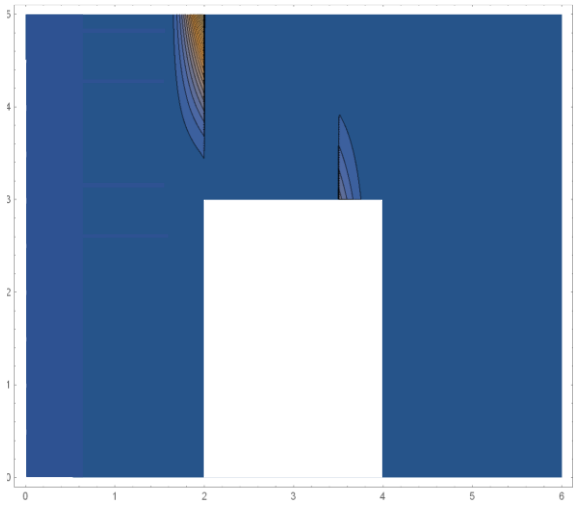

Fig. 7.4 - The field $|\boldsymbol{E}|^2 = tr(\boldsymbol{E}\boldsymbol{E}^T)$ is reported.

The skew-symmetric part of the displacement field, representing the local rotation field, is depicted in **Fig. 7.5**: it should be noticed that the gradient of rotation is essentially concentrated along two vertical lines.

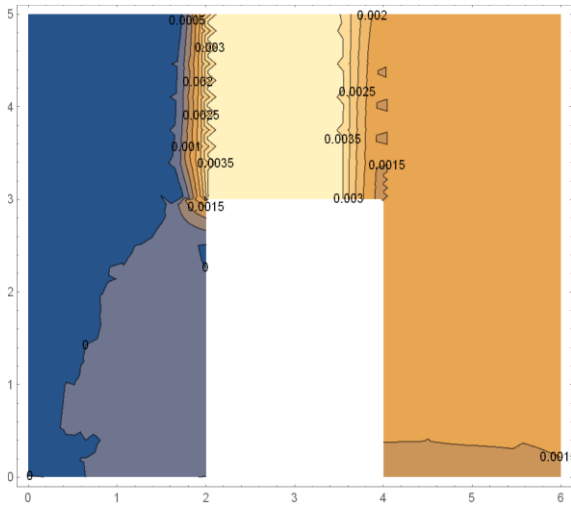

Fig. 7.5 - Rotation field over the whole domain.

■ 7.2 EXAMPLE 2: PORTAL (CASE B)

In this section, we present two applications concerning the same portal analysed with both methods introduced in **Chapter 4**. The portal studied here has a lintel with a larger span than that analysed in **Section 7.1**.

7.2.1 Numerical analysis with the PR method

The NRNT portal, shown in **Fig. 7.6a,** is subjected to a piecewise uniformly distributed load (yellow strips) and is discretized with rigid blocks using 1440 triangular elements. The right support is subjected to a given vertical settlement δ.

The solution $\widehat{\boldsymbol{U}}^0$ of the minimum problem is reached through the interior point method in 5.52s with an Intel® Core™ i7-6700HQ (**Fig. 7.6b**). Also in this case, three hinges form and the moving part of the structure becomes isostatic. It should be noted that the position of the "central" hinge changes: this is due to the larger span of the lintel relative to the pier.

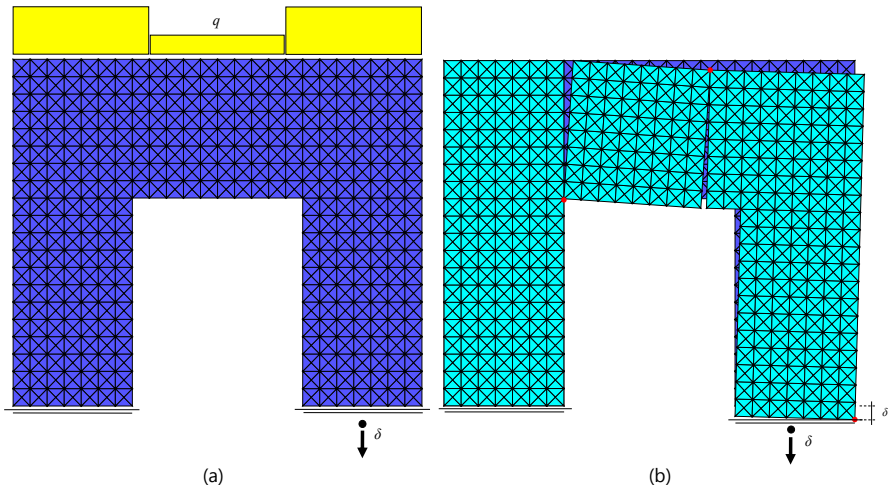

Fig. 7.6 – In (a) a NRNT portal, discretized with 1440 triangular elements, is loaded by a piecewise uniformly load (yellow strips) and is subjected to a given vertical settlement δ. In (b) a representation of the solution $\widehat{\boldsymbol{U}}^0$, obtained through the interior point method, is reported in (b): three hinges form and the moving part of the structure becomes isostatic.

Since the positions of the three hinges formed is known, the corresponding line of thrust can be determined (**Fig. 7.7**).

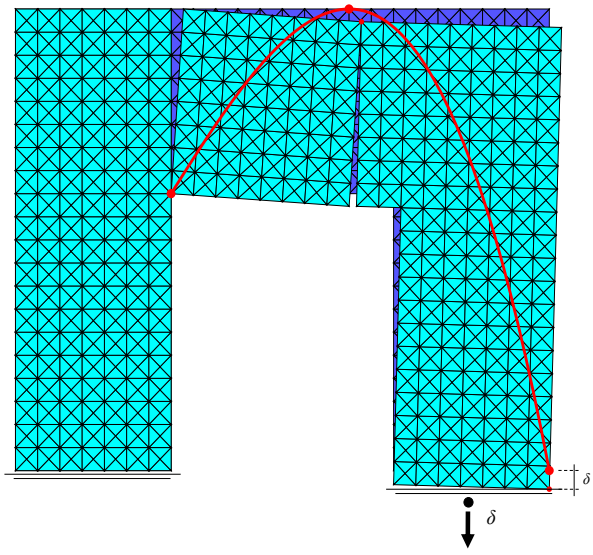

Fig. 7.7 - The hinges formed and the relative thrust line are represented.

7.2.2 Numerical analysis with the C^0 method

The same portal of **Fig. 7.6a** is here analysed with the C^0 method, based on an approximation with continuous functions. The portal of NRNT material, shown in **Fig. 7.8a**, is discretized using 360 9-nodes square elements (a second order Lagrangian quadrangular element) and is loaded by its self –weight represented with a piecewise uniformly distributed load (yellow strips). The right base support is subjected to a given vertical settlement δ.

The solution $\widehat{\boldsymbol{U}}^0$ of the minimum problem, obtained with the interior point method in 647.73s (with an Intel® Core™ i7-6700HQ) by using 16 tangent planes for each node, is shown graphically in **Fig. 7.8b**.

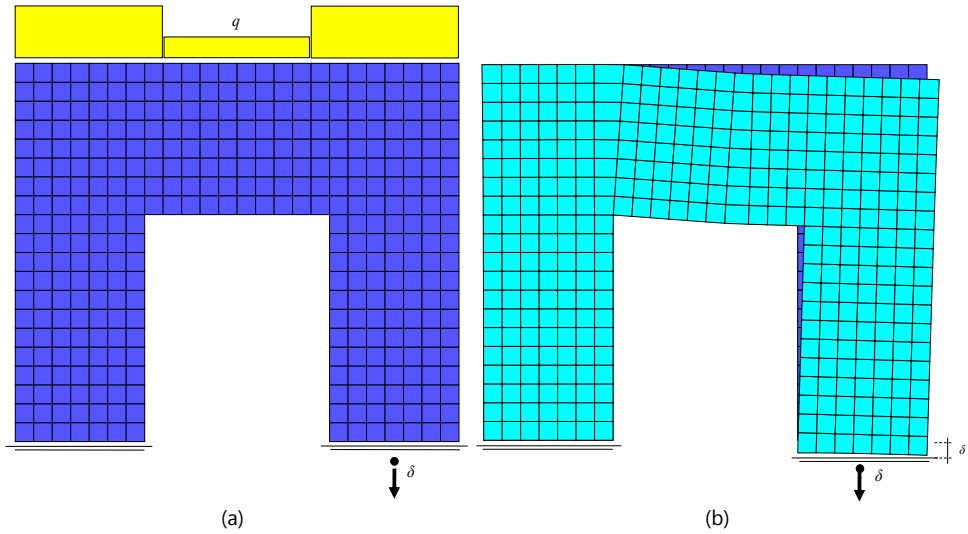

Fig. 7.8 – In (a) a NRNT portal, discretized through 360 square elements, is loaded by a piecewise uniformly distributed load and is subjected to a given vertical settlement δ at the right base support. In (b) a representation of the solution $\widehat{\boldsymbol{U}}^0$ obtained with the interior point method is reported: a perfect concordance with the solution obtained with the PR method is highlighted (see **Fig. 7.6b**).

To represent the strain field $\boldsymbol{E}$, we report in **Fig. 7.9** a measure of the deformation, namely $|\boldsymbol{E}|^2 = tr(\boldsymbol{E}\boldsymbol{E}^T)$. From **Fig. 7.9** we see that the gradient of deformation is concentrated on two vertical strips of elements, whilst the other elements are characterized by strains whose norm is close to zero.

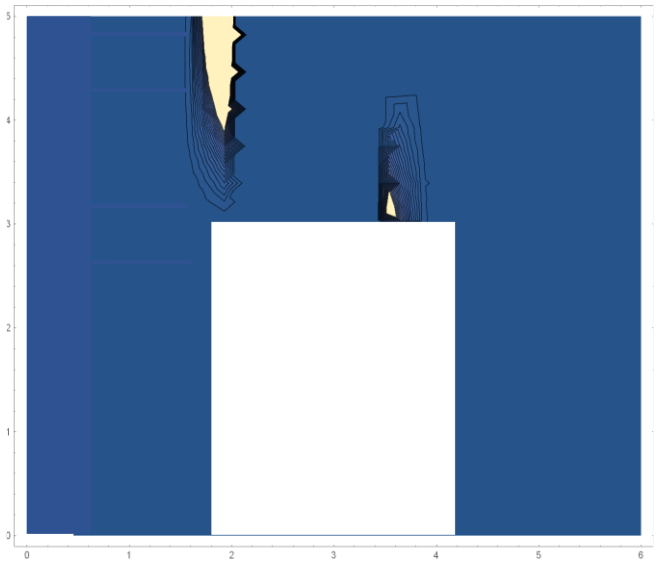

Fig. 7.9 - The field $|\boldsymbol{E}|^2 = tr(\boldsymbol{E}\boldsymbol{E}^T)$ is reported.

The skew-symmetric part of the displacement field, representing the local rotation field, is depicted in **Fig. 7.10**: it should be noticed that the gradient of rotation is essentially concentrated along two vertical lines.

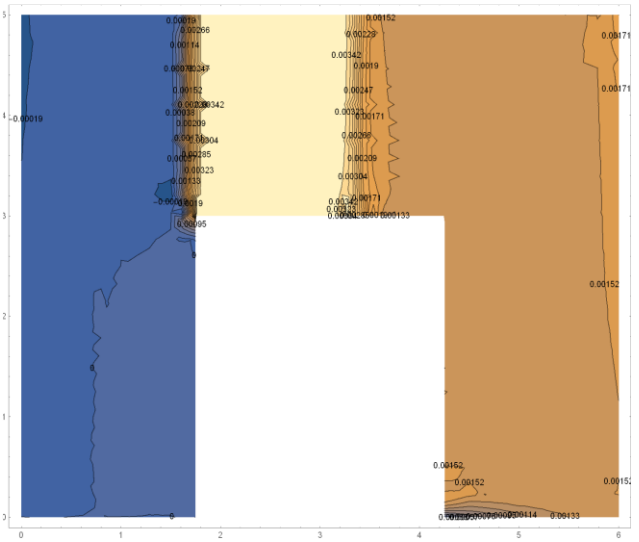

Fig. 7.10 - The rotation field over the whole domain.

■ 7.3 EXAMPLE 3: WALL WITH OPENINGS (CASE A)

In this section, as illustration of the PR method for a more complex structure, we present two applications concerning the same wall with openings on adopting two different discretizations.

7.3.1 Numerical analysis with the PR method

The wall with openings, discretized with 304 rigid triangular elements, is subjected to uniform loads (yellow strips) and to given vertical settlements as depicted in **Fig. 7.11**.

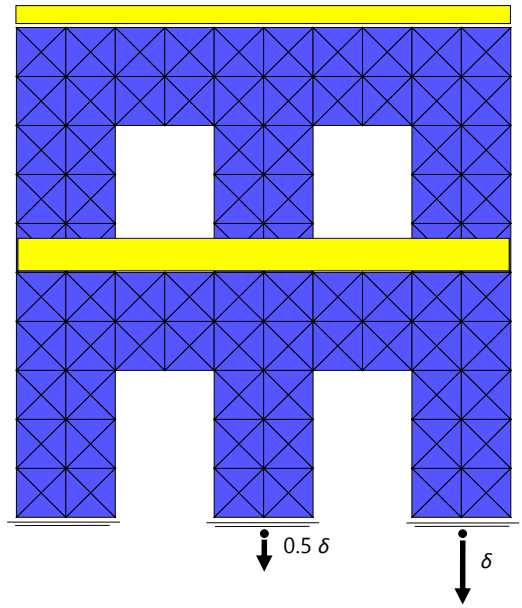

Fig. 7.11 - A NRNT structure, discretized through 304 triangular elements, is subjected to uniformly distributed loads represented by yellow strips and to given vertical settlements.

The number of restrictions, both equalities and inequalities, is 3384 whilst the number of unknowns is 912. The solution $\widehat{\boldsymbol{U}}^0$ of the minimum problem is reached through the interior point method in 0.23s with an Intel® Core™ i7-6700HQ (**Fig. 7.12**).

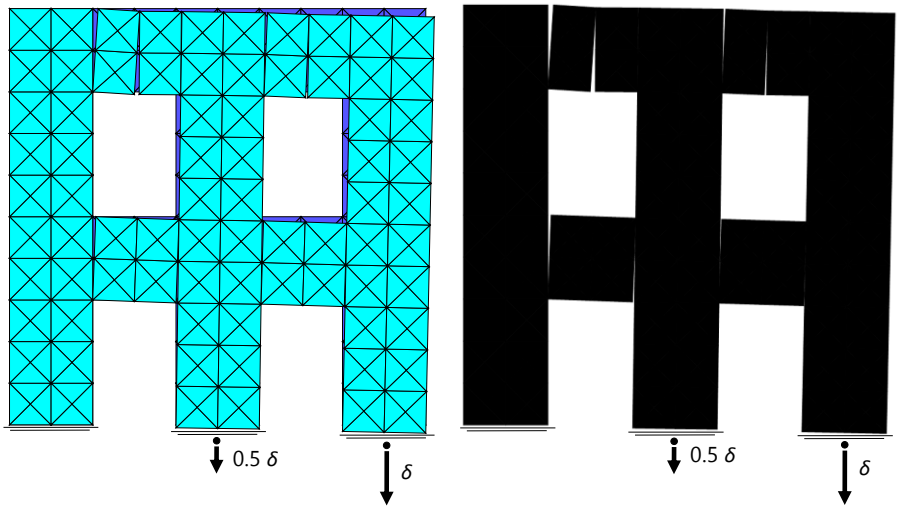

Fig. 7.12 – Two representations of the same solution $\widehat{\boldsymbol{U}}^0$, obtained through the interior point method, are reported.

7.3.2 Numerical analysis with the PR method on a denser discretization

The structure of **Section 7.3.1** is here discretized with 4864 triangular rigid elements. It is subjected to uniformly distributed loads represented by yellow strips and to given vertical settlements as shown in **Fig. 7.13**.

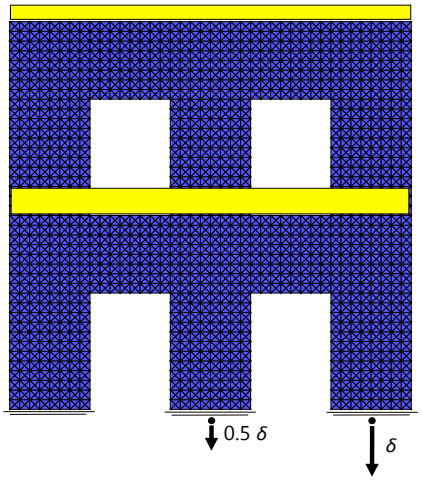

Fig. 7.13 - A NRNT structure, discretized with 4864 triangular elements, subjected to uniformly distributed loads (yellow strips) and to given vertical settlements.

The number of restrictions, both equalities and inequalities, is 57312 whilst the number of unknowns is 14592. The solution $\widehat{\boldsymbol{U}}^0$ of the minimum problem is reached through the interior point method in 15.83s with an Intel® Core™ i7-6700HQ (**Fig. 7.12**).

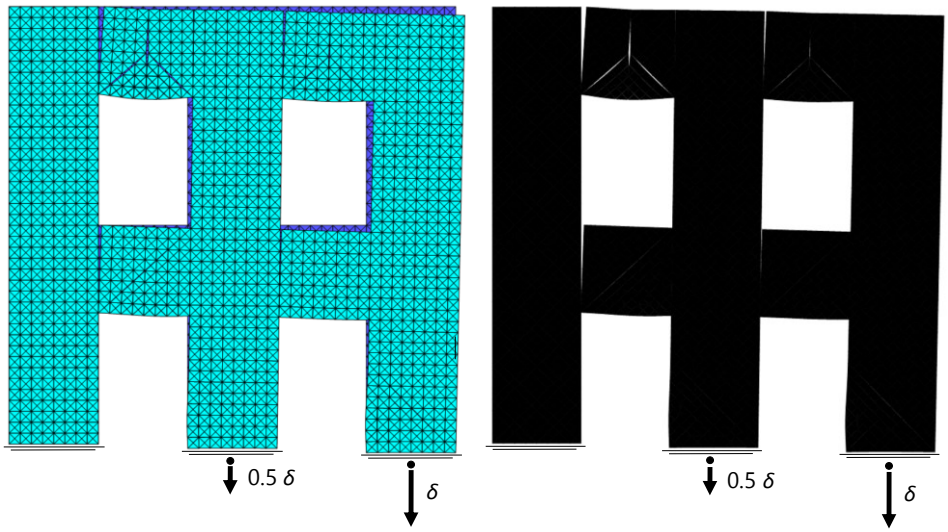

Fig. 7.14 – Two representation of the same solution $\widehat{\boldsymbol{U}}^0$, obtained through the interior point method, are reported.

■ 7.4 EXAMPLE 4: WALL WITH OPENINGS (CASE B)

In this section, we propose two examples regarding a wall with openings subjected to given vertical settlements increasing linearly inward. Both cases are analysed by using the PR method.

7.4.1 Numerical analysis with the PR method

A wall with openings, discretized with 1216 triangular elements, is subjected to piecewise uniformly loads (yellow strips) and to a given linear settlement distribution as shown in **Fig. 7.15a**.

The number of restrictions, both equalities and inequalities, is 3648 whilst the number of unknowns is 14064. The solution $\widehat{\boldsymbol{U}}^0$ of the minimum problem is reached through the interior point method in 1.86s with an Intel® Core™ i7-6700HQ (**Fig. 7.15b** and **Fig. 7.16**).

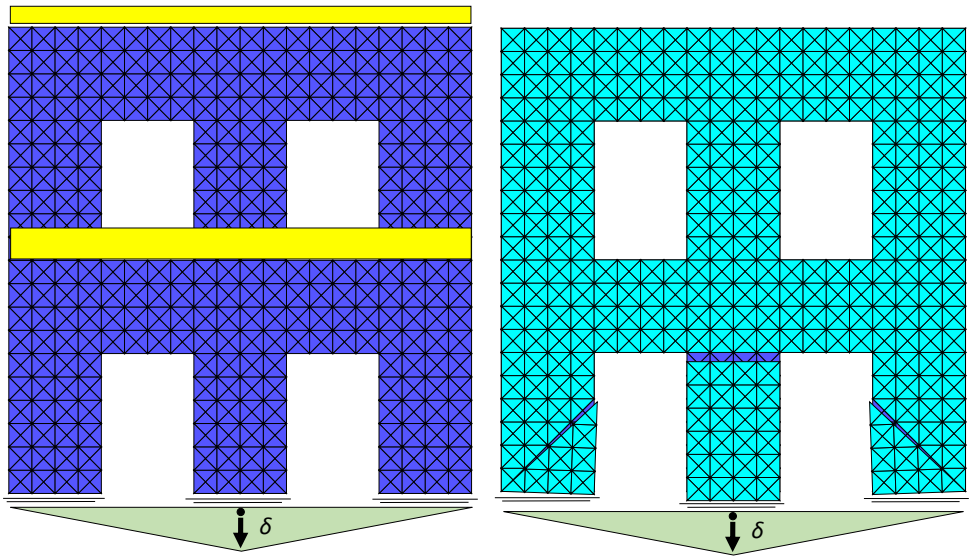

Fig. 7.15 – In (a) the wall with openings, discretized with 1216 rigid triangular elements, is subjected to uniformly loads (yellow strips) and to a given vertical settlement distribution. In (b) the solution $\widehat{\boldsymbol{U}}^0$ obtained through the interior point method is reported.

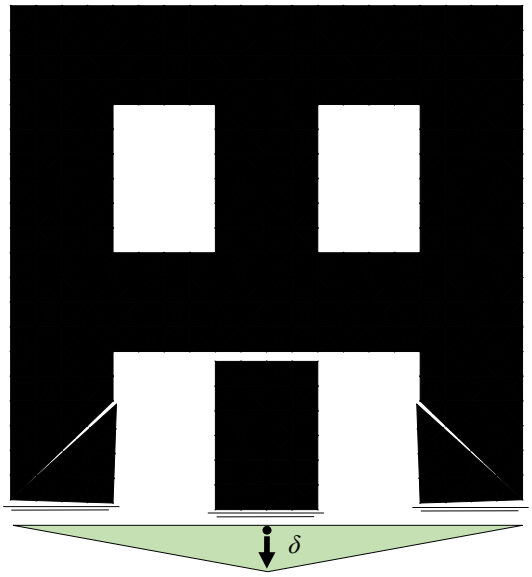

Fig. 7.16 - Another representation of the solution $\widehat{\boldsymbol{U}}^0$, obtained through the interior point method, is reported.

7.4.2 Numerical analysis with the PR method (larger openings)

The same structure analysed before (**Fig. 7.15a**) but with larger openings is discretized through 17920 triangular elements. It is subjected to uniformly distributed loads, represented by yellow stripes, and to given vertical linear settlements as shown in **Fig. 7.17**.

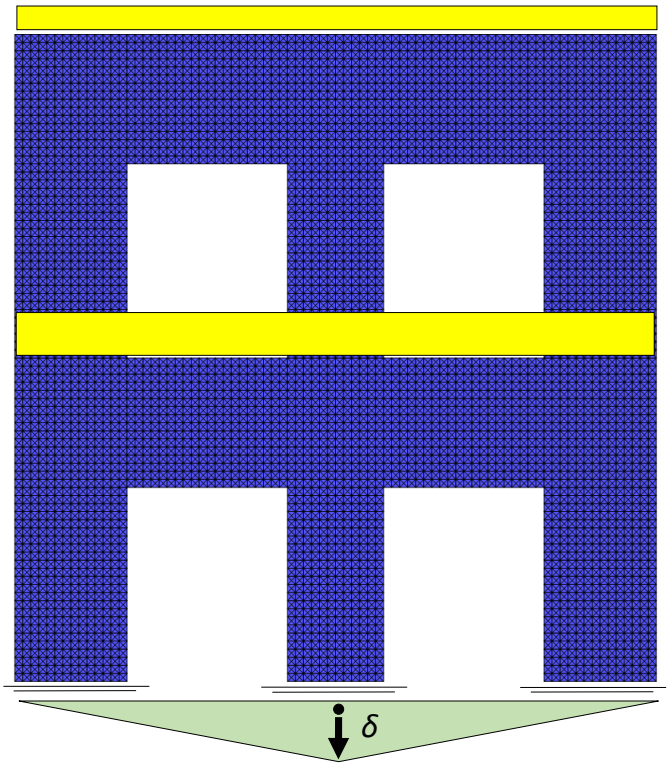

Fig. 7.17 - A wall with openings, discretized through 17920 triangular elements, is subjected to uniform loadings represented by yellow stripes and to a given vertical settlement distribution.

The number of restrictions, both equalities and inequalities, is 212832 whilst the number of unknowns is 53760. The solution $\widehat{\boldsymbol{U}}^0$ of the minimum problem is reached through the interior point method in 230s with an Intel® Core™ i7-6700HQ. A representation of the solution $\widehat{\boldsymbol{U}}^0$ is reported in **Fig. 7.18**.

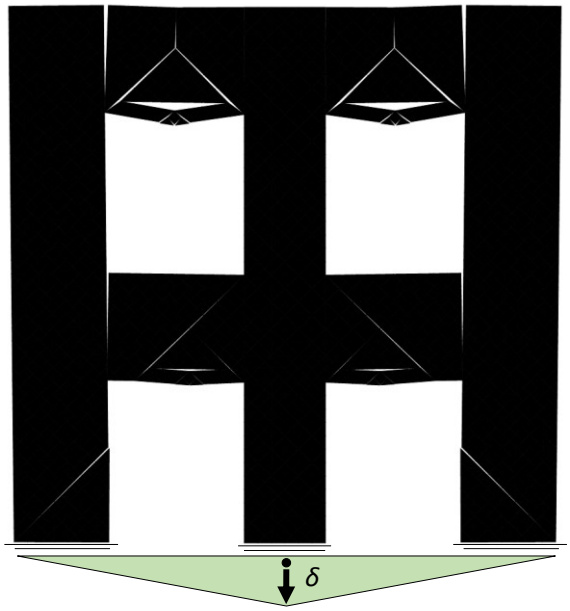

Fig. 7.18 - A representation of the solution $\widehat{U}^0$, obtained in 230s through the interior point method, is depicted.

■ 7.5 CASE STUDIES: DETECTING A CRACK PATTERN

In this section, we present three case studies in order to illustrate the way in which a particular fracture pattern can be identified as the one associated to the minimum of the energy in the class of piecewise rigid displacements (PR method, i.e. modelling the cracks as concentrated). The results in each case are obtained performing different iterations each corresponding to a different settlement scenario, in order to find the optimal form of the foundation settlements as that giving the best qualitative fit with the real crack pattern, see also (Iannuzzo et al, 2016).

7.5.1 Case study 1: XVII century building in Bergamo

As first example concerning the identification of the crack pattern, we propose the analysis of the façade of the structure depicted in **Fig. 4.1**. This masonry construction, due to an evident foundation settlement, exhibits a widespread cracking on its main façade (see also **Fig. 7.19**).

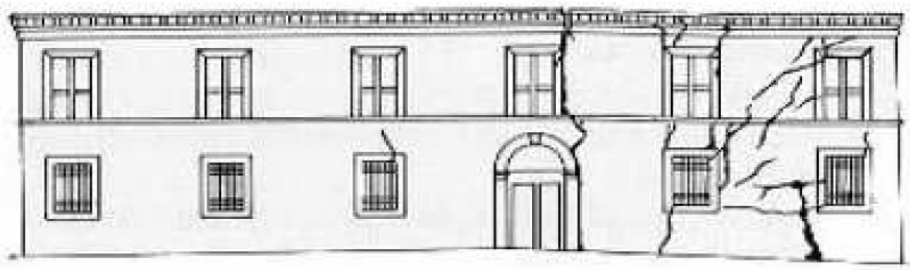

Fig. 7.19 - Front view and crack pattern of the façade of a XVII century building in Bergamo, presenting an extensive cracking due to an evident differential settlement of the foundation (redrawn from the site of the Fire workers of Bergamo. Courtesy of Paolo Faccio).

In the simulation, the main façade, loaded by two uniformly distributed loads, represented by yellow strips, is discretized with 7192 rigid triangular elements (**Fig. 7.20**). The effect of a differential settlement of the right part of the foundation is considered and the analysis is restricted to the right part of the structure, on the right side of the red vertical line depicted in (**Fig. 7.20**). We consider as data of the problem the foundation settlements defining the known terms of some of the restrictions considered as constraints in the LP program.

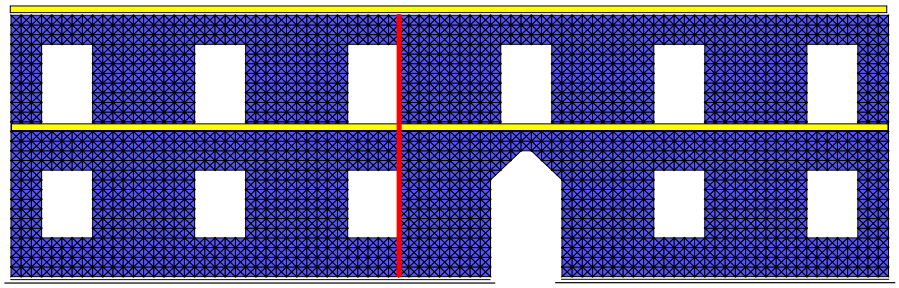

Fig. 7.20 – The structure shown in **Fig. 7.19** is discretized with 7192 rigid triangular elements.

The discretization of the extract structure is constituted by 4048 triangular elements and then the number of unknowns is 12144. The total number of restrictions, both equalities and inequalities (including internal and external boundary conditions) is 47508. The piecewise rigid displacement field, with support on the triangular elements, produced by the settlement is obtained by minimizing the potential energy $\wp(\widehat{\boldsymbol{U}})$ with respect to the generalized displacement $\widehat{\boldsymbol{U}}$, as described in **Section 4.3**.

The optimal profile of the given settlements, controlled by three parameters, was obtained by executing a parametric analysis for various runs of the program on the

grid of possible values of the parameters. The shapes of both vertical and horizontal settlements which better reflect the real crack pattern are shown in **Fig. 7.21**. The solution $\widehat{\boldsymbol{U}}^0$ of LP problem is reached through the interior point method in 61.82s with an Intel® Core™ i7-6700HQ (**Fig. 7.21** and **Fig. 7.22**).

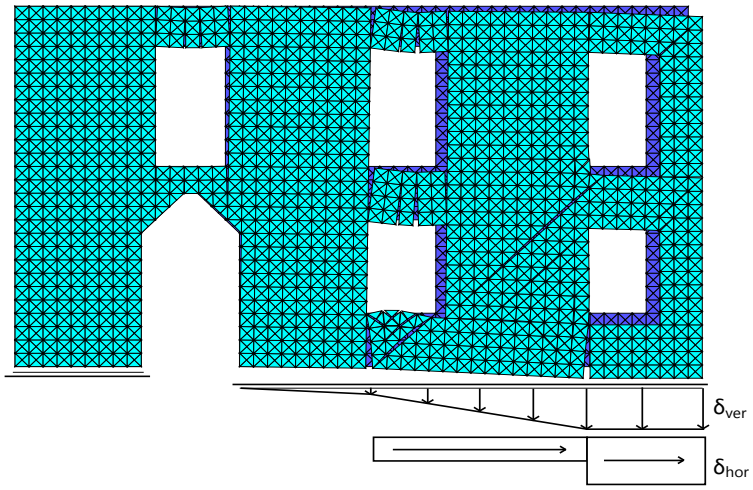

Fig. 7.21 - A representation of the optimal solution $\boldsymbol{u}^0$, corresponding to the minimizer $\widehat{\boldsymbol{U}}^0$ of the LP problem, and of both vertical and horizontal foundation settlements giving the best qualitative fit with the real crack pattern (see **Fig. 7.19**) are depicted.

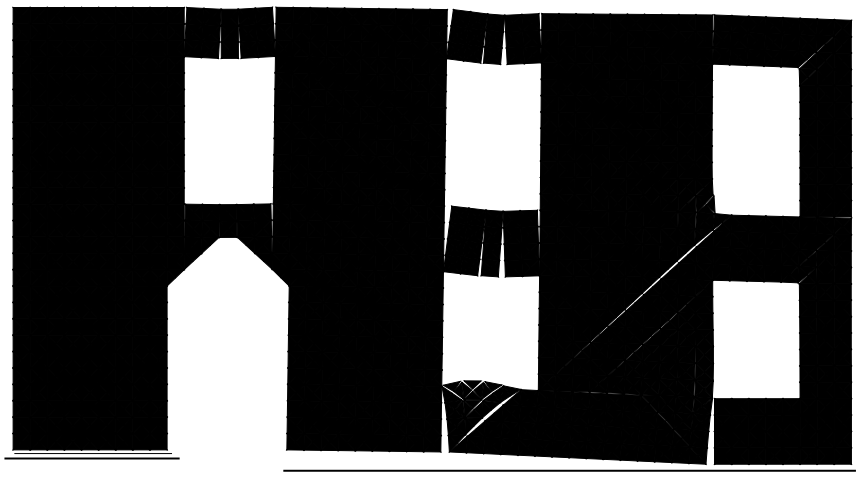

Fig. 7.22 – Another representation of the minimizer $\widehat{\boldsymbol{U}}^0$ of the LP problem.

7.5.2 Case study 2: XVIII century building in Torre Annunziata (Naples)

In this section, we present the analysis of the façade of a XVIII century historical buildings, made of local tuff stone, located in via Nazionale, Torre Annunziata. In **Fig. 7.23** the front of the building with the drawing of the cracks (obtained through a photographic image reconstruction), and its second floor plan are shown.

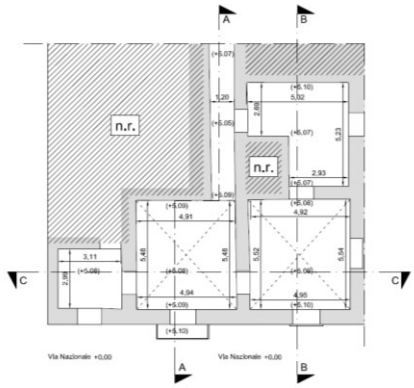

(a)

(b)

Fig. 7.23 - Front view of a XVIII century building in Torre Annunziata (Naples): (a). In (a) the crack pattern, traced through digital image reconstruction from the photo, is also reported. Plan of the second floor of the building: (b), some parts of the plan are not shown.

With reference to **Fig. 7.24a**, we observe that the parapet inside the dashed rectangle is a non-structural element and then is not considered in the analysis. The masonry structure in the dot-dashed rectangle is a semi-detached construction and therefore is not considered in the analysis either. In the model we construct (see **Fig. 7.24b**), we use 490 identical square elements of side 0.80 m, for which the

corresponding number of unknowns is 1470. As external load we consider the self-weight only, on assuming a masonry density of 1600 kg/m^3, applied at the centroids of each rigid block.

(a) (b)

Fig. 7.24 – The front view of the building (a) and rigid block discretization (b) are shown. The zone of crushing is highlighted with two light yellow strips.

We consider as data of the problem both foundation settlements and given eigenstrains concentrated along the two light yellow strips, located above two of the ground floor masonry panels. The eigenstrains simulate a widespread crushing of such wall panels, caused by the enlargement of the adjacent openings (**Fig. 7.24**). Both settlements and eigenstrains represent the known terms of some of the inequalities considered as constraints in the LP program. The total number of restrictions, both equalities and inequalities (including internal and external boundary conditions) is 5244.

Since the exact distribution and the relative amplitude of the set of settlements and distortions which caused the cracks were not known exactly, we considered a set of simple forms of such settlements defined by a few parameters and performed some qualitative parametric analyses to identify the relative values of such parameters choosing the value that gave the better description of the detected crack pattern. The foundation settlement and eigenstrains shape which better reflect the real crack pattern are shown in **Fig. 7.25**. We used the interior point routine implemented in the program Mathematica ® to solve the related LP problem.

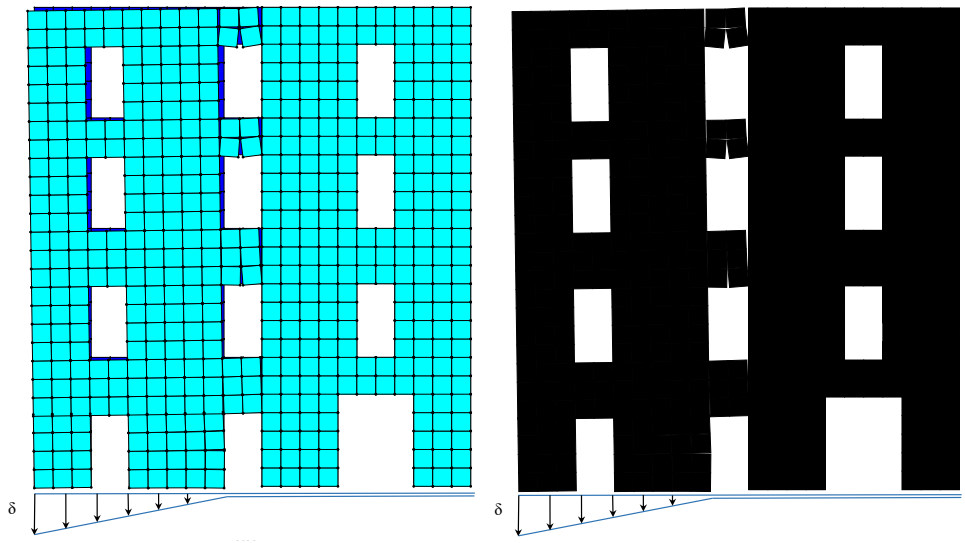

Fig. 7.25 – Two representation of the same optimal solution $\boldsymbol{u}^0$ corresponding to the minimizer $\tilde{\boldsymbol{U}}^0$ of the LP problem are depicted.

7.5.3 Case study 3: XVII century Church (Naples)

The third example concerns the analysis of "Chiesa di Santa Maria Incoronatella della Pietà dei Turchini", a XVII century church located in via Monteoliveto in Naples. In **Fig. 7.26a** and **Fig. 7.26b**, the plan and a lateral view of the structure are reported.

The discretized model we construct, is constituted by 3183 square blocks of side 0.52m (see **Fig. 7.26c**). As external loads, in addition to the self-weight of the structure (ρ=1800 kg/m^3), uniformly distributed tractions (applied as shown in **Fig. 7.26c**) representing the action of the secondary structures, and whose values are also reported in **Fig. 7.26c**, are also considered. The total unknowns of the problem are 9549 and the number of restrictions, both equalities and inequalities, is 36256. Performing a few different runs for different relative values of the four prescribed settlements, we found the particular form of the vertical settlements, shown in **Fig. 7.27**, as that giving the best qualitative fit with the real crack pattern. Two representations of the result, in terms of rigid body displacements of the blocks, are reported in **Fig. 7.27**. In **Fig. 7.28** we report the result of the analysis of the same wall of the Church, considering the effect of a tie, represented in **Fig. 7.28** by the thick red line.

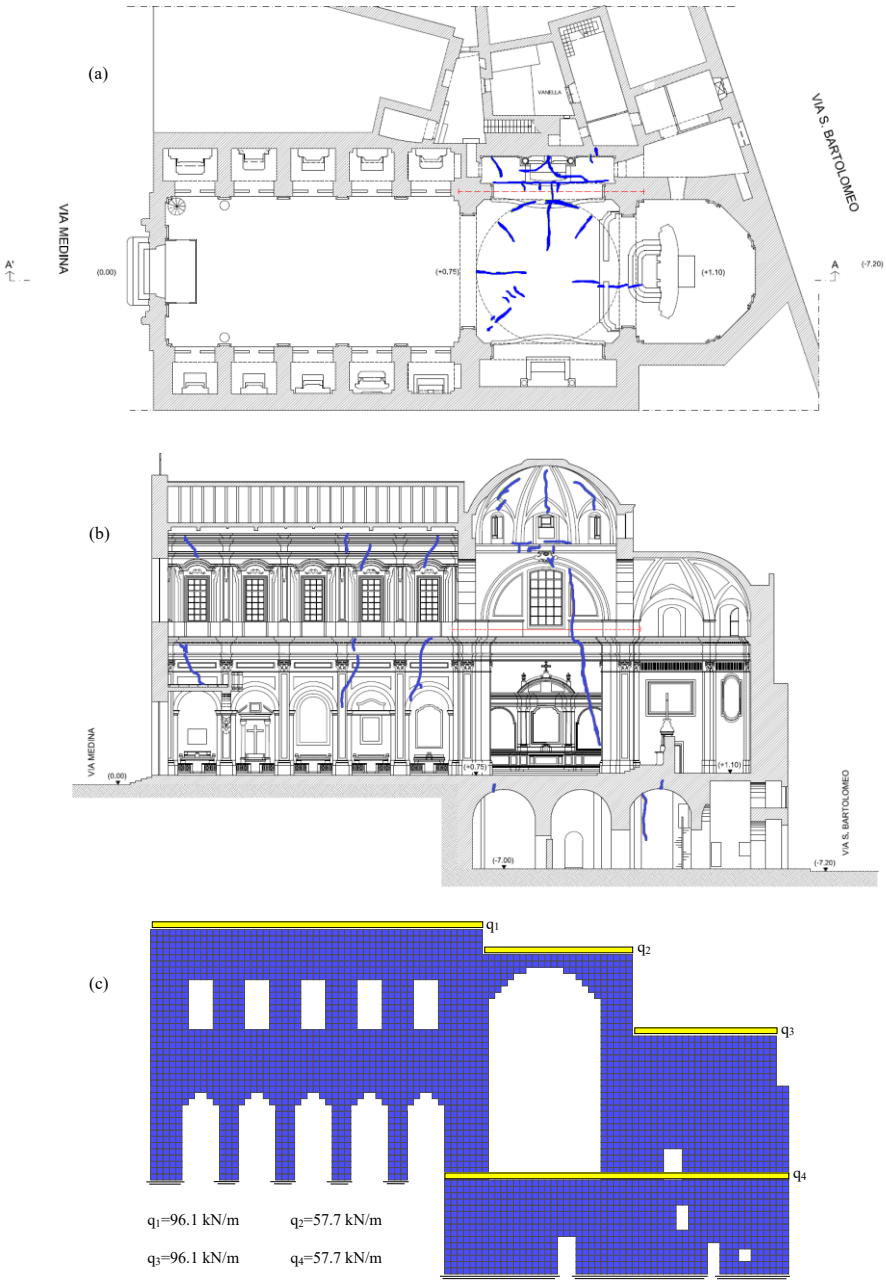

Fig. 7.26 - Plan (a) and section A-A' (b) of the church and the rigid block discretization (c). The crack pattern, reconstructed from a photographic survey, is shown in (a) and (b). The distributed loads due to the secondary structures are reported in (c) with yellow strips.

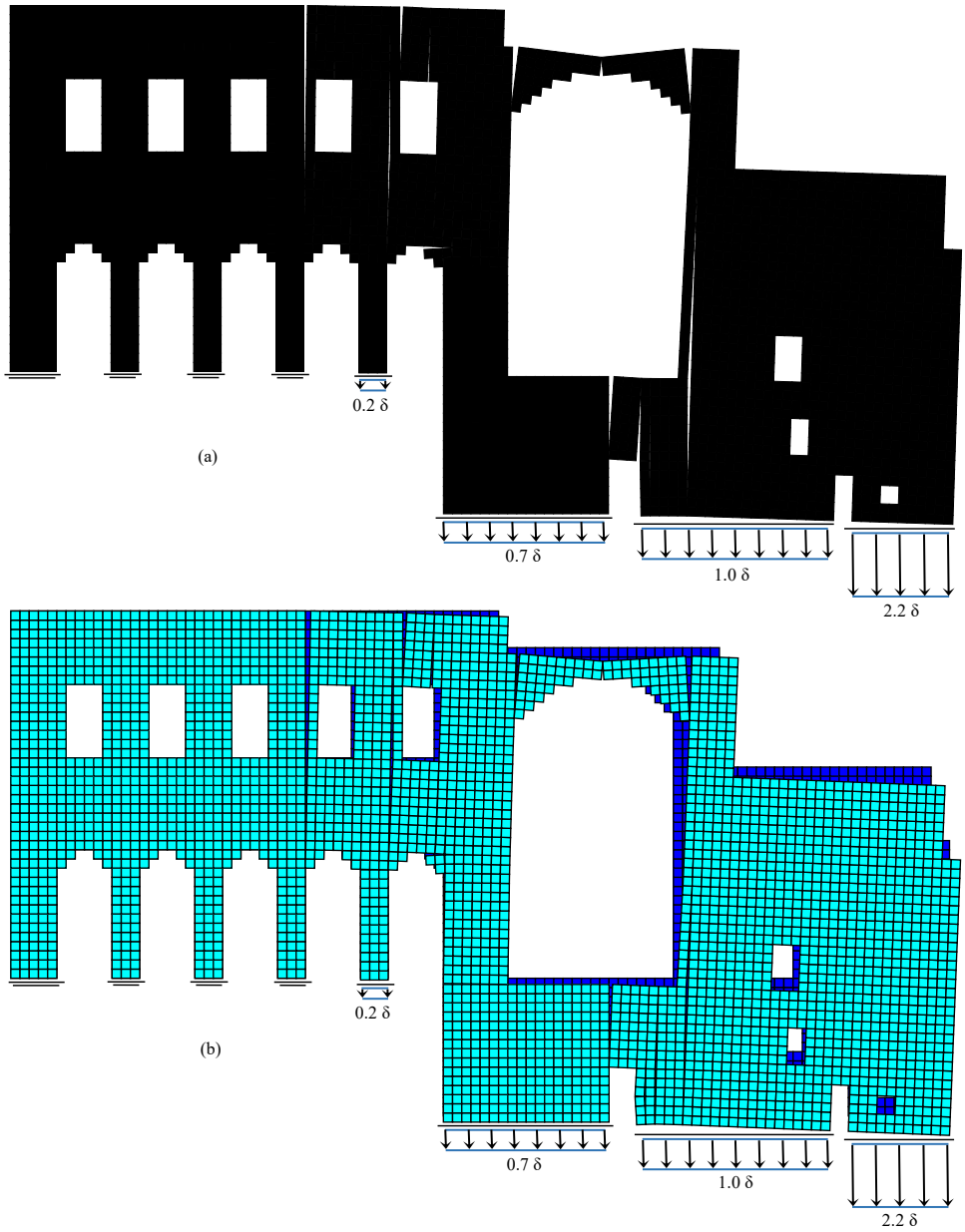

Fig. 7.27 - Two representations of the same minimizer $\widehat{\boldsymbol{U}}^0$ of the LP problem corresponding to the vertical foundation settlements giving the best qualitative fit with the real crack pattern (see **Fig. 7.26a** and **Fig. 7.26b**) are depicted.

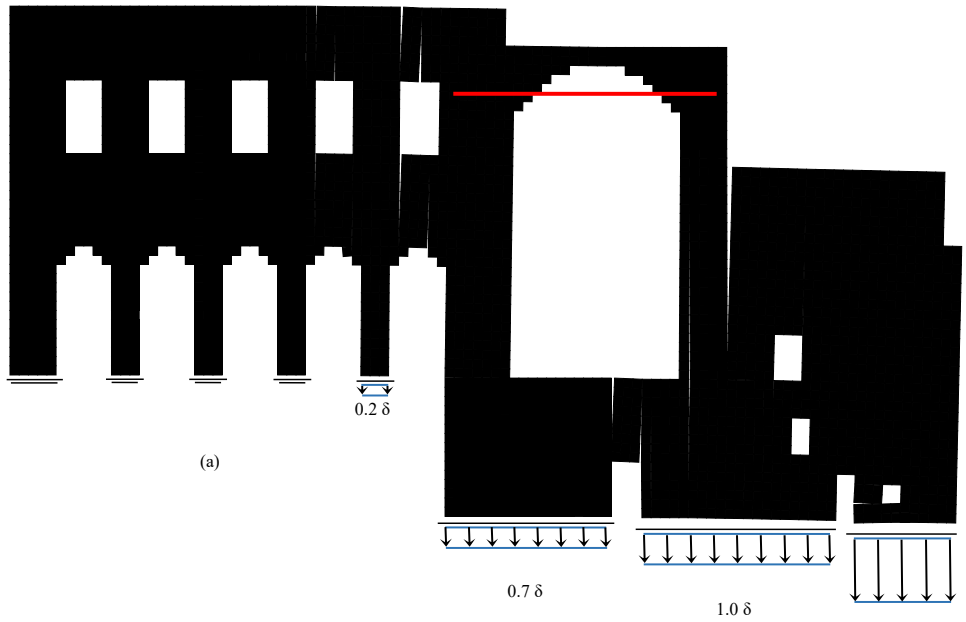

Fig. 7.28 - Representation of the solution $\boldsymbol{u}^0$ corresponding to the analysis of the structure subjected to the optimal value of the vertical foundation settlements found in the previous analysis and to the effect of a tie (red thick line).

Chapter 8

MASONRY STRUCTURES UNDER HORIZONTAL ACTIONS

Prologue. In this Chapter, some applications concerning the analysis of simple masonry structures under horizontal actions are presented. First cases concern either portals or double portals analyzed with both numerical methods. The numerical strategy adopted to solve the problem is the same used for the circular arch (see **Section 6.6**). Furthermore, we illustrate how the use of the C^0 method based on continuous functions could simplify the problem providing an indication of the partition of the structure into rigid blocks. Finally as a case study, an arch under horizontal shaking action is considered. We find the static collapse multiplier with the PR method, and then, by using the partition obtained through the rigid block model, we develop a dynamic analysis based on the model of rocking of a rigid block.

■ 8.1 EXAMPLE 1: PORTAL UNDER HORIZONTAL ACTION

In this section, we present some applications concerning portals under horizontal actions analysed by using the PR method (rigid blocks) and varying the discretization. Our numerical strategy to solve the problem of a structure under horizontal action is the same adopted for the arches (see **Section 6.6**). In short, if λ denotes the scale factor of the horizontal actions (loads or displacements), we can find an interval $[\lambda_s, \lambda_m]$ to which the collapse multiplier λ_c has to belong. In particular, λ_s represents an approximation of the supremum of the multipliers for which the initial configuration is still safe (i.e. $\widehat{\boldsymbol{U}}^0 = \mathbf{0}$), whilst λ_m represents an approximation of the infimum of the multipliers for which the structure becomes a mechanism (i.e. $\widehat{\boldsymbol{U}}^0 \neq \mathbf{0}$).

8.1.1 Numerical analysis with the PR method

The NRNT portal, discretized with 384 rigid triangular elements, is loaded on the top edge by a piecewise uniformly distributed load (represented by yellow strips) as shown in **Fig. 8.1**. The external horizontal action is represented by the horizontal distribution of loads (represented by grey strips) proportional to the vertical ones through the scale factor λ as shown in figure **Fig. 8.1.**

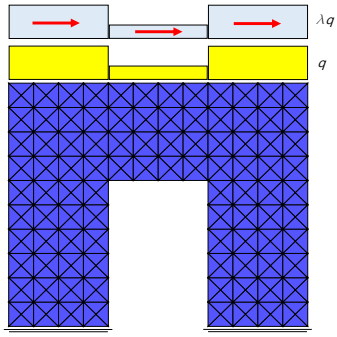

Fig. 8.1 – A NRNT portal, discretized with 384 rigid triangular elements, loaded by a piecewise uniformly distributed vertical load (yellow strip) and by a similar horizontal load distribution λq (represented with the grey strips).

The collapse multiplier λ_c belongs to the interval $[0.252\,,0.253]$. The mechanism corresponding to the value $\lambda = 0.253$, reached through the interior point method in 0.31s with an Intel® Core™ i7-6700HQ, is depicted in **Fig. 8.2**.

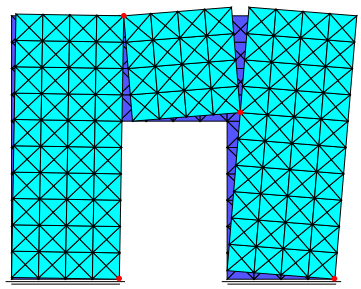

Fig. 8.2 – A representation of the solution $\widehat{U}^0$ for $\lambda = 0.253$ and obtained through the interior point method: four hinges form and the structure becomes a mechanism.

8.1.2 Numerical analysis with the PR method on a denser discretization

The previous portal of **Fig. 8.1**, subjected to the same load conditions, is here discretized with 1536 rigid triangular elements as depicted in **Fig. 8.3**.

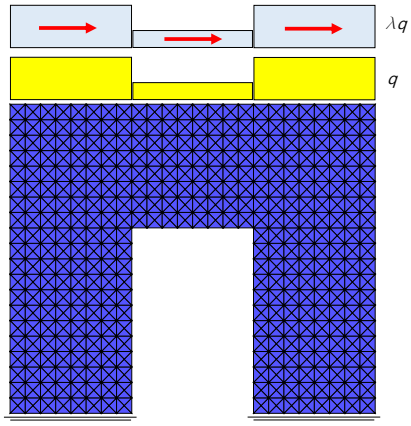

Fig. 8.3 - The portal analysed in **Section 8.1.1** is discretized with 1536 triangular elements.

The number of restrictions, both equalities and inequalities, is 18048 whilst the number of unknowns is 4608. The collapse multiplier λ_c belongs to the interval $[0.249\,,0.250]$. The solution $\widehat{\boldsymbol{U}}^0$ corresponding to the value $\lambda = 0.250$, reached through the interior point method in 3.53s with an Intel® Core™ i7-6700HQ, is depicted in **Fig. 8.4.** From **Fig. 8.4**, it should be noted that fours hinges form and the structure becomes a mechanism.

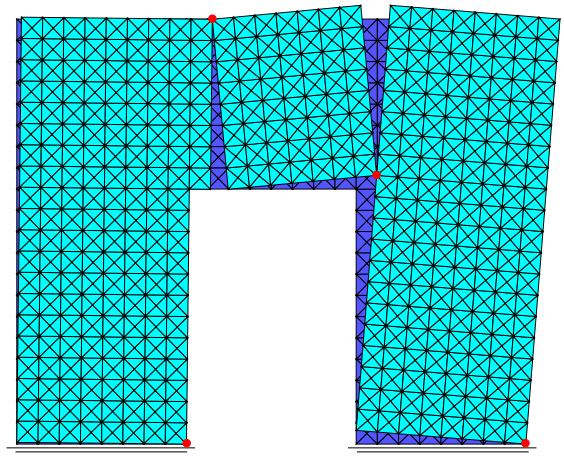

Fig. 8.4 - A representation of the solution $\widehat{\boldsymbol{U}}^0$ corresponding to $\lambda = 0.250$ is depicted.

8.1.3 Numerical analysis with the C^0 method

The same portal of **Fig. 8.1** is here analysed with the C^0 method, based on an approximation with continuous functions. The portal of NRNT material is discretized using 384 9-nodes square elements (a second order Lagrangian quadrangular element) and is loaded as shown in **Fig. 8.5a**.

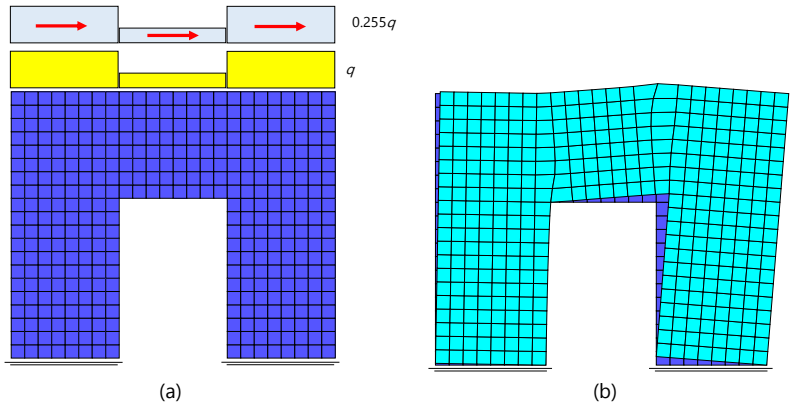

Fig. 8.5 –In (a): the NRNT portal, discretized with 384 9-nodes square elements, is loaded by a piecewise uniformly distributed vertical load (yellow strip) and by a similar horizontal load distribution 0.255q (represented with the grey strips). In (b): a representation of the solution is depicted.

The solution $\widehat{\boldsymbol{U}}^0$ of the minimum problem, obtained with the interior point method in 716.78s (with an Intel® Core™ i7-6700HQ) by using 16 tangent planes for each node, is shown graphically in **Fig. 8.5b**. The streamlines of the displacement field are reported in **Fig. 8.6**.

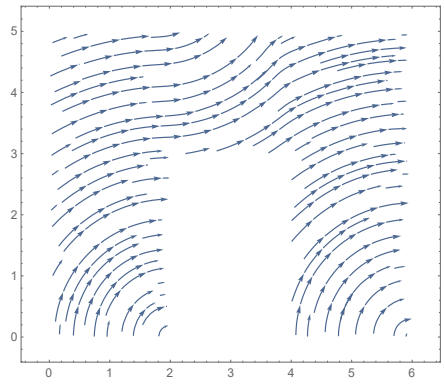

Fig. 8.6 - The stream plot of the displacement field is reported: the centres of rotation can be identified.

To represent the strain field $\boldsymbol{E}$, in **Fig. 8.7** we report a measure of the deformation, namely $|\boldsymbol{E}|^2 = tr(\boldsymbol{E}\boldsymbol{E}^T)$.

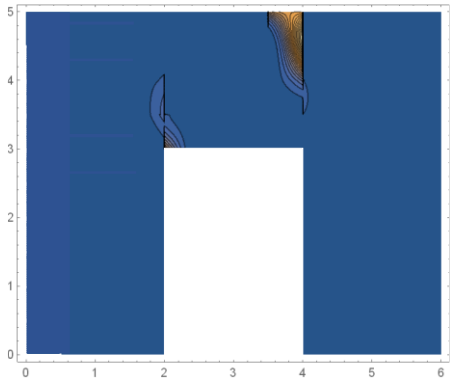

Fig. 8.7 - The field $|\boldsymbol{E}|^2 = tr(\boldsymbol{E}\boldsymbol{E}^T)$ is reported.

The skew-symmetric part of the displacement field is depicted in **Fig. 8.8a**. It should be noticed that the gradient of rotation is essentially concentrated along two vertical lines. By depicting the positive rotations in red and the negative ones in blue (**Fig. 8.8b**), we obtain a neat subdivision of the domain into three blocks. Such blocks deform essentially as rigid bodies since the rotation is piece-wise constant and the deformation is practically constant (see **Fig. 8.7**). The partition is the same obtained with the PR method (see **Fig. 8.2** and **Fig. 8.4**).

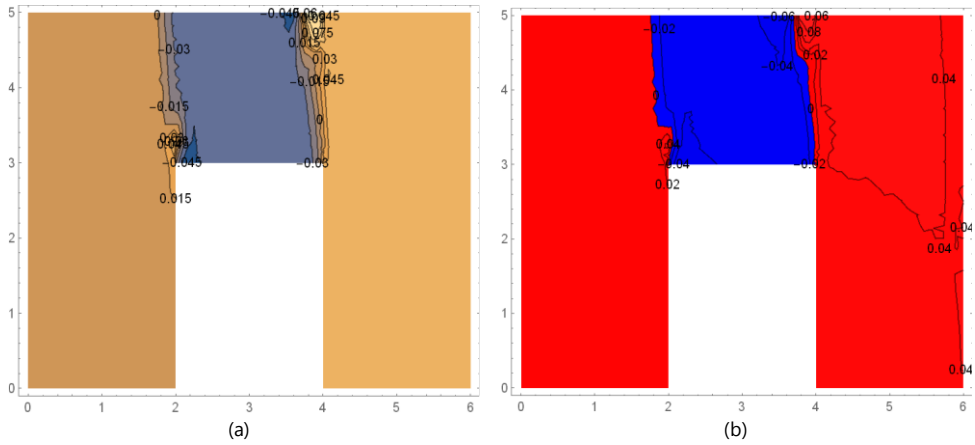

Fig. 8.8 – In (a) the rotation field over the whole domain. In (b) by depicting the positive rotations in red and the negative ones in blue, a neat partition of the whole domain into three rigid blocks can be seen.

■ 8.2 EXAMPLE 2: PORTAL UNDER HORIZONTAL ACTION

In this section, the portal of **Section 8.1** is here analysed with both two numerical methods but varying the mode of application of the horizontal load. Our numerical strategy to solve the problem of a structure under horizontal action is the same adopted in **Section 6.6** for the arches (see also **Section 8.1**).

8.2.1 Numerical analysis with the PR method

A NRNT portal, discretized with 384 rigid triangular elements, is loaded on the top edge by a piecewise uniformly distributed load (represented by yellow strips) as shown in **Fig. 8.9a**. The external horizontal action is here represented by the force λQ where Q is equal to the resultant of the acting vertical loads and λ is the scale factor.

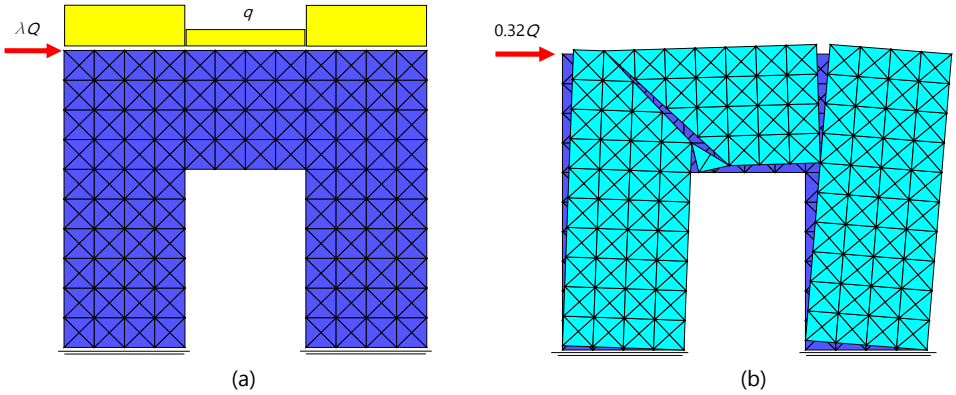

Fig. 8.9 – In (a): the NRNT portal, discretized with 384 rigid triangular elements, is subjected to a piecewise uniformly distributed load q and to the horizontal force λQ. In (b): a representation of the solution $\hat{U}^0$ corresponding to $\lambda = 0.32$ and obtained through the interior point method is depicted: four hinges form and the structure becomes a mechanism.

The collapse multiplier λ_c belongs to the interval $[0.31, 0.32]$. The mechanism corresponding to the value $\lambda = 0.32$, reached through the interior point method in 0.27s with an Intel® Core™ i7-6700HQ, is depicted in **Fig. 8.9b**.

8.2.2 Numerical analysis with the PR method on a denser discretization

The same NRNT portal of **Section 8.2.1**, subjected to the same load conditions, is here discretized with 1536 rigid triangular elements as depicted in **Fig. 8.10**.

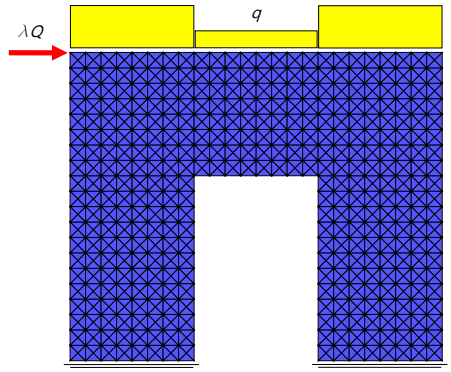

Fig. 8.10 – The NRNT portal, discretized with 1536 rigid triangular elements, is loaded by the piecewise uniform load q and by the horizontal force λQ.

The collapse multiplier λ_c belongs to the interval $[0.30\,,0.31]$. The mechanism corresponding to the value $\lambda = 0.31$, reached through the interior point method in 2.35s with an Intel® Core™ i7-6700HQ, is depicted in **Fig. 8.11**.

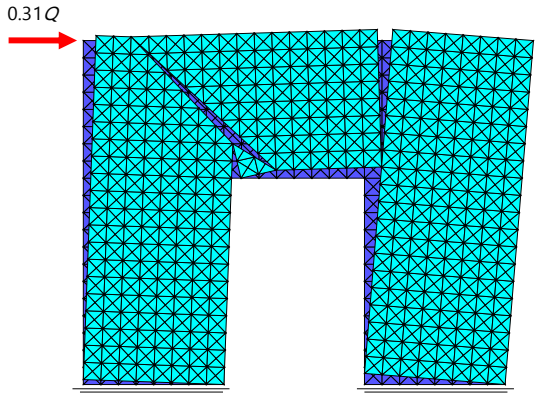

Fig. 8.11 – A representation of the solution $\hat{\boldsymbol{U}}^0$ corresponding to $\lambda = 0.31$ and obtained through the interior point method is depicted: four hinges form and the structure becomes a mechanism.

8.2.3 Numerical analysis with the C^0 method

The same NRNT portal of **Fig. 8.9**, subjected to the same load conditions, is here analysed with the C^0 method, based on an approximation with continuous functions. The portal, shown in **Fig. 8.12a**, is discretized using 384 9-nodes square elements (a second order Lagrangian quadrangular element).

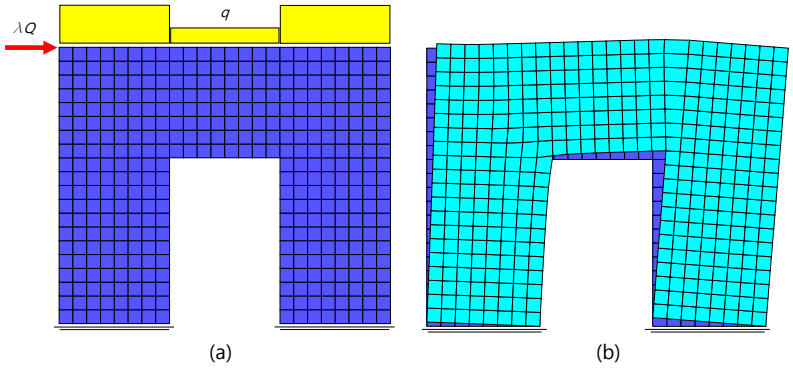

Fig. 8.12 –In (a) the NRNT portal, discretized with 384 9-nodes square elements, is loaded by a piecewise uniformly distributed vertical load (yellow strip) and by a similar horizontal load distribution 0.32q (represented with the grey strips). In (b) a representation of the solution is depicted.

The solution $\widehat{\boldsymbol{U}}^0$ of the minimum problem, obtained with the interior point method in 716.78s (with an Intel® Core™ i7-6700HQ) by using 16 tangent planes for each node, is shown graphically in **Fig. 8.12b**. The streamlines of the displacement field are reported in **Fig. 8.13**.

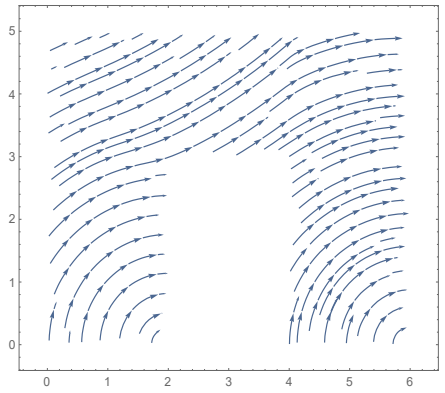

Fig. 8.13 - The stream plot of the displacement field is reported: the centres of rotation can be identified.

To represent the strain field $\boldsymbol{E}$, in **Fig. 8.14** we report a measure of the deformation, namely $|\boldsymbol{E}|^2 = tr(\boldsymbol{E}\boldsymbol{E}^T)$.

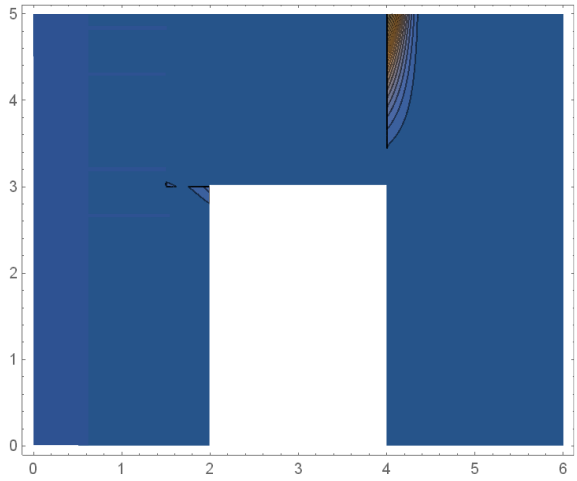

Fig. 8.14 - The field $|\boldsymbol{E}|^2 = tr(\boldsymbol{E}\boldsymbol{E}^T)$ is reported.

The skew-symmetric part of the displacement field is depicted in **Fig. 8.15a**. It should be noted that the gradient of rotation is essentially concentrated along two lines. By depicting the positive rotations in red and the negative ones in blue (**Fig. 8.15b**), we obtain a neat subdivision of the domain into three blocks. Such blocks deform essentially as rigid bodies since the rotation is piece-wise constant and the deformation is practically constant (see **Fig. 8.14**). The partition is the same obtained with the PR method (**Fig. 8.9b** and **Fig. 8.11**).

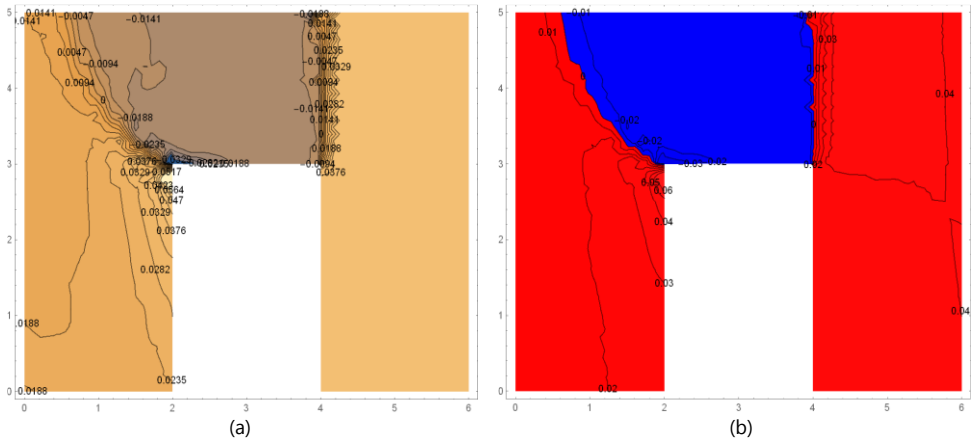

Fig. 8.15 – In (a) the rotation field over the whole domain. In (b) by depicting the positive rotations in red and the negative ones in blue, a neat partition of the whole domain into three rigid blocks can be seen.

■ 8.3 EXAMPLE 3: DOUBLE PORTAL UNDER HORIZONTAL ACTIONS

In this section, we present three solutions concerning a double portal analysed by using both two numerical methods described in **Chapter 4**, namely the PR method, based on rigid blocks (modelling the cracks as concentrated), and the C^0 method, based on continuous functions (modelling the cracks as smeared). In the first two cases the external actions are represented through two concentrated forces depending on a scale factor λ, whilst in the third one the structure is subjected to a horizontal linear displacement.

8.3.1 Numerical analysis with the PR method

A NRNT double portal, discretized with 12288 triangular elements, is loaded by two piecewise uniformly distributed loads (represented by yellow strips). The external horizontal action is represented by the two forces $(0.5\lambda Q, \lambda Q)$ where Q is in norm equal to the resultant of the acting loads at the same level and λ is the scale factor (**Fig. 8.16a**).

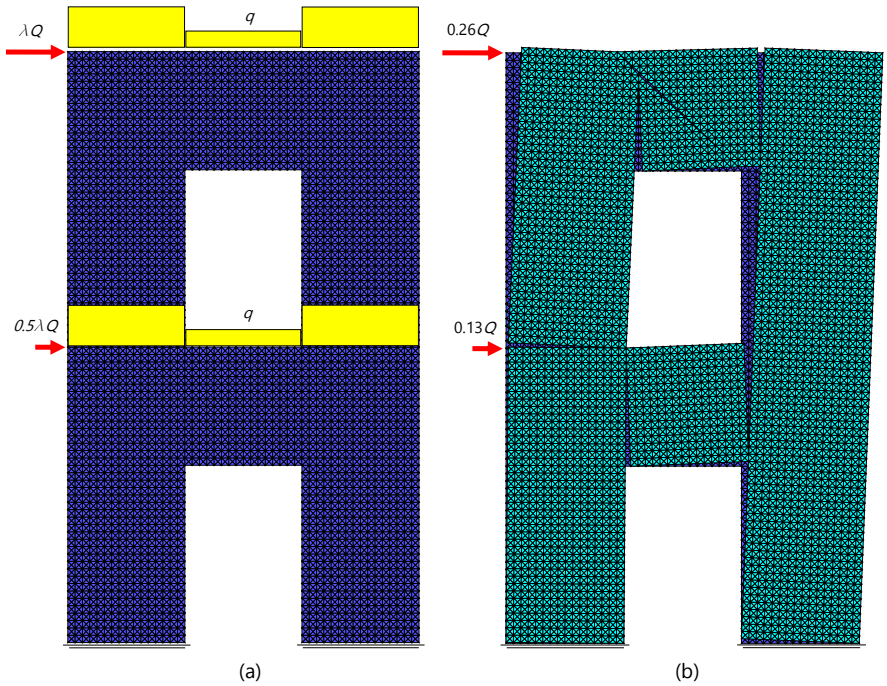

Fig. 8.16 – In (a) the NRNT double portal is discretized with 12288 triangular elements. In (b) a representation of the solution $\widehat{\boldsymbol{U}}^0$ corresponding to $\lambda = 0.26$.

The number of restrictions, both equalities and inequalities, is 146048 whilst the number of unknowns is 36864. The collapse multiplier λ_c belongs to the interval $[0.25\,, 0.26]$. The mechanism corresponding to the value $\lambda = 0.26$, reached through the interior point method in 49.98s with an Intel® Core™ i7-6700HQ, is depicted in **Fig. 8.16a** and in **Fig. 8.17.**

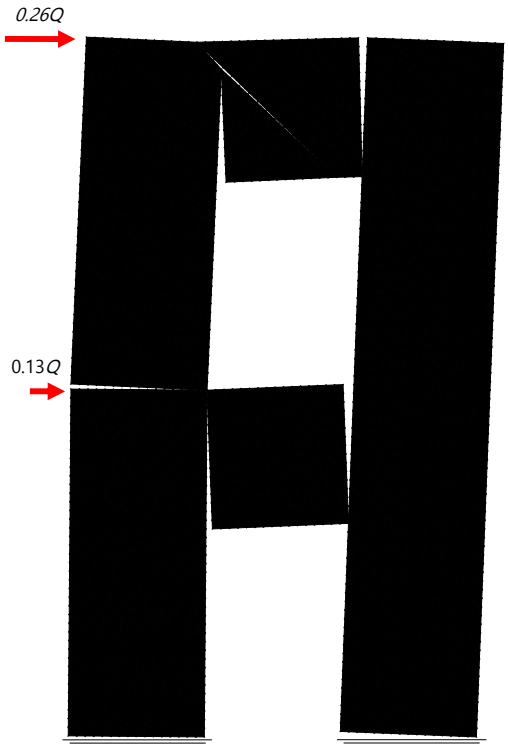

Fig. 8.17 - Another representation of the solution $\widehat{\boldsymbol{U}}^0$ corresponding to $\lambda = 0.26$.

8.3.2 Numerical analysis with the C^0 method (horizontal forces)

The NRNT double portal of **Section 8.3.1** is here analysed with the C^0 method, considering the same load condition. The structure is discretized using 384 9-nodes square elements (a second order Lagrangian quadrangular element) as shown in **Fig. 8.18a**.

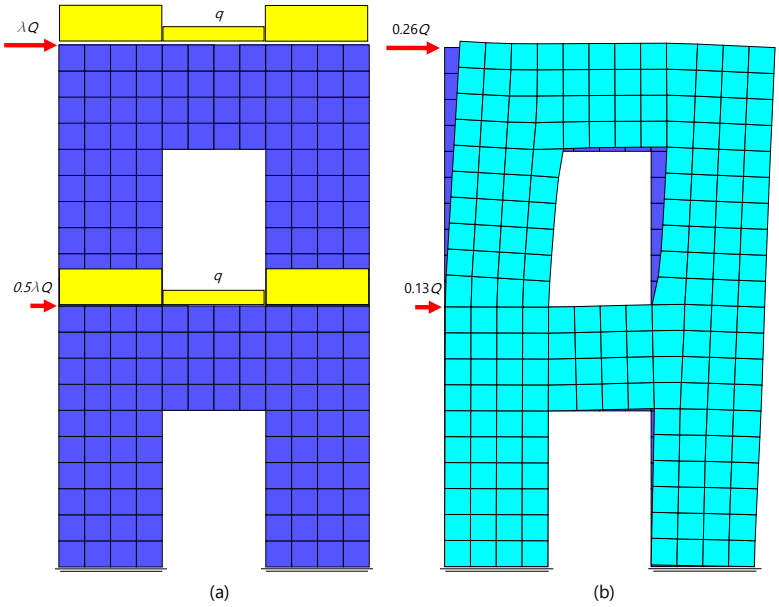

Fig. 8.18 – In (a): the NRNT double portal, discretized with 384 9-nodes square elements. In (b): a representation of the solution $\widehat{\boldsymbol{U}}^0$ corresponding to $\lambda = 0.26$.

The solution $\widehat{\boldsymbol{U}}^0$ of the minimum problem, obtained with the interior point method in 287.43s (with an Intel® Core™ i7-6700HQ) by using 16 tangent planes for each node, is shown graphically in **Fig. 8.18b**.

To represent the strain field $\boldsymbol{E}$, in **Fig. 8.19a** we report a measure of the deformation, namely $|\boldsymbol{E}|^2 = tr(\boldsymbol{E}\boldsymbol{E}^T)$. The streamlines of the displacement field are reported in **Fig. 8.19b**.

The skew-symmetric part of the displacement field is depicted in **Fig. 8.20a**. It should be noticed that the gradient of rotation is essentially concentrated along lines. By depicting the positive rotations in red and the negative ones in blue (**Fig. 8.20b**), we obtain a neat subdivision of the domain into five blocks. Such blocks deform essentially as rigid bodies since the rotation is piece-wise constant and the deformation is practically constant (see **Fig. 8.19a**). The partition is similar to that obtained with the PR method (see **Fig. 8.17**).

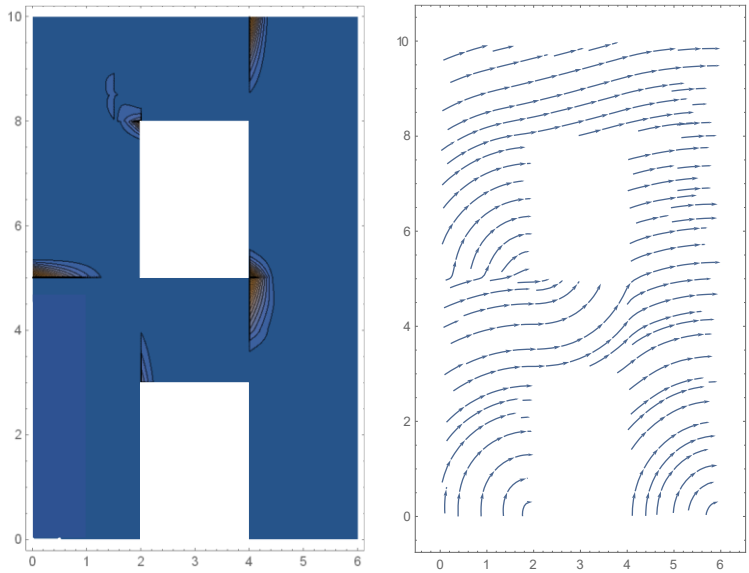

Fig. 8.19 - The field $|\boldsymbol{E}|^2 = tr(\boldsymbol{E}\boldsymbol{E}^T)$ is reported.

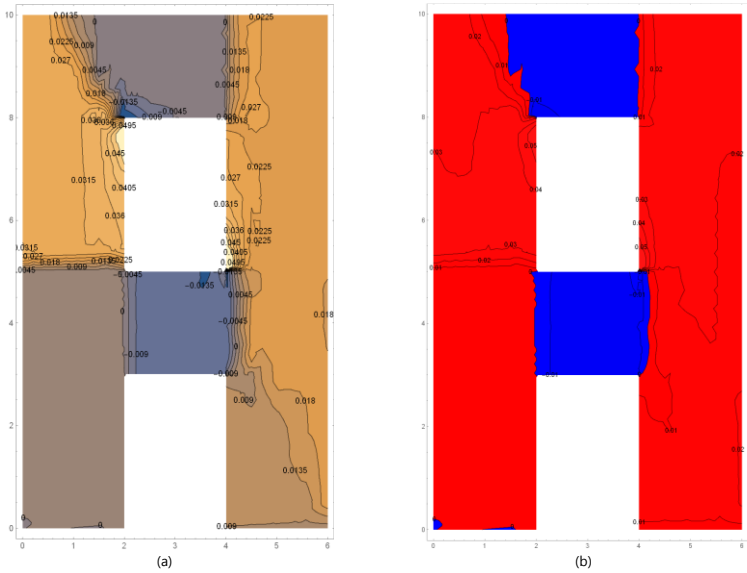

Fig. 8.20 – In (a) the rotation field over the whole domain. In (b) by depicting the positive rotations in red and the negative ones in blue, a partition of the whole domain into five rigid blocks can be seen.

8.3.3 Numerical analysis with the C^0 method (horizontal displacements)

The NRNT double portal of **Section 8.3.1**, here analysed by using the C^0 method, is loaded by a piecewise uniformly distributed loads (represented by yellow strips as shown in **Fig. 8.21a**) and by horizontal actions modelled with linear displacement imposed to the left side of the structure. The double portal is discretized using 768 9-nodes square elements (a second order Lagrangian quadrangular element).

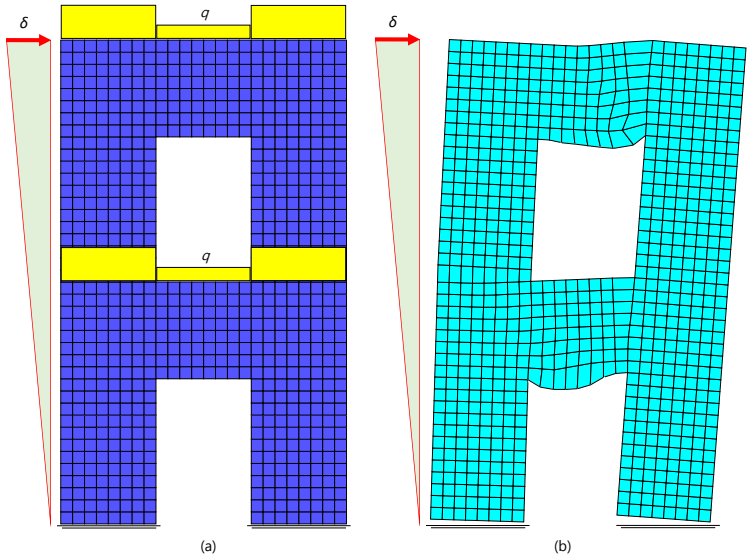

Fig. 8.21 – In (a): the NRNT double portal, discretized with 768 9-nodes square elements, is loaded by a piecewise uniformly distributed loads (yellow strips) and is subjected at left side to a linear distribution of displacements. In (b): a representation of the solution is depicted.

The solution $\widehat{\boldsymbol{U}}^0$ of the minimum problem is reached through the minimization of the energy into the finite element space defined previously (see **Section 4.4**). The solution obtained with the interior point method in 600s (with an Intel® Core™ i7-6700HQ) is shown graphically in **Fig. 8.21b**. The horizontal component of the displacement corresponding to the solution $\widehat{\boldsymbol{U}}^0$ is reported in **Fig. 8.22**: the gradient of the displacement field is concentrated essentially along lines.

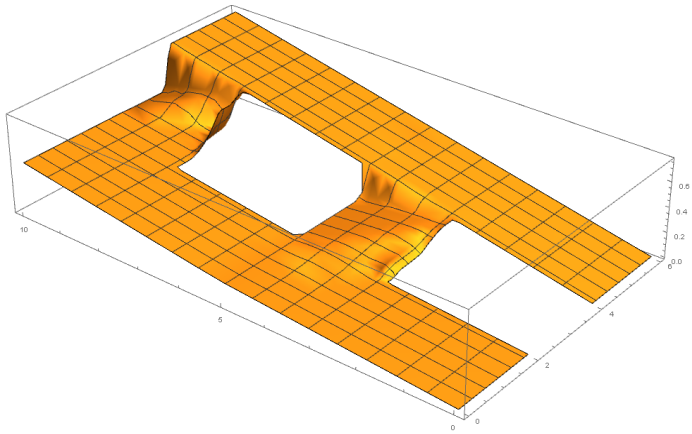

Fig. 8.22 – Graph of the horizontal component of the displacement field corresponding to the solution $\widehat{\boldsymbol{U}}^0$.

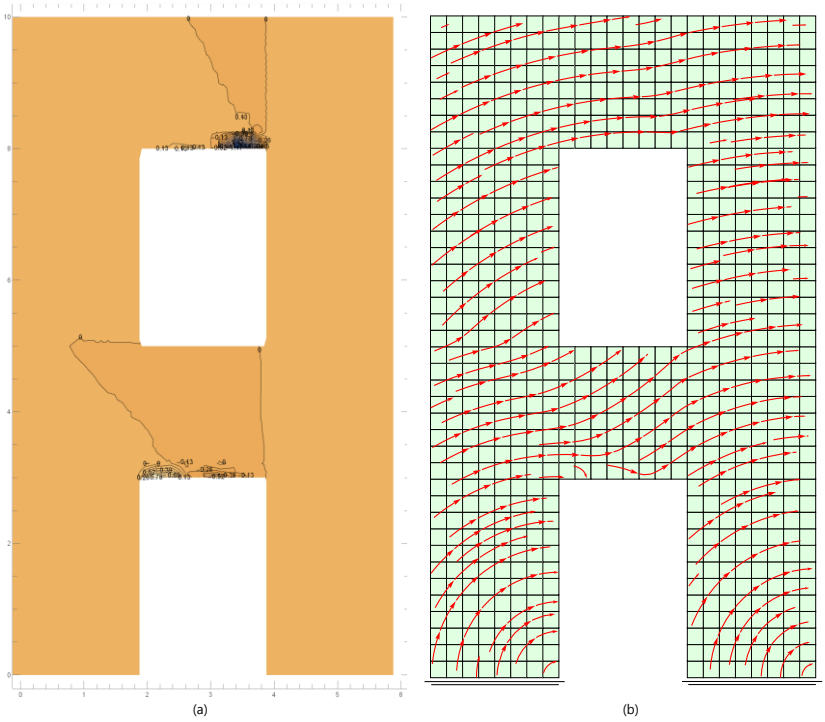

Fig. 8.23 – Rotation field over the whole domain: (a). Stream plot of the displacement field: (b).

The skew-symmetric part of the displacement field (representing the local rotation) is depicted in **Fig. 8.23a**. It should be noticed that the gradient of rotation is essentially concentrated along lines (**Fig. 8.23a**). A stream plot of the displacement field over the whole domain is reported in **Fig. 8.23b**; from **Fig. 8.23b** the centres of rotation can be clearly identified.

By depicting the positive rotations in red and the negative ones in blue (**Fig. 8.24a**), we obtain a neat subdivision of the domain into five blocks **Fig. 8.24b**. Such blocks deform essentially as rigid bodies since the rotation and the deformation are piecewise constant. Notice that the strain, though we are using continuous functions, is practically all concentrated on lines.

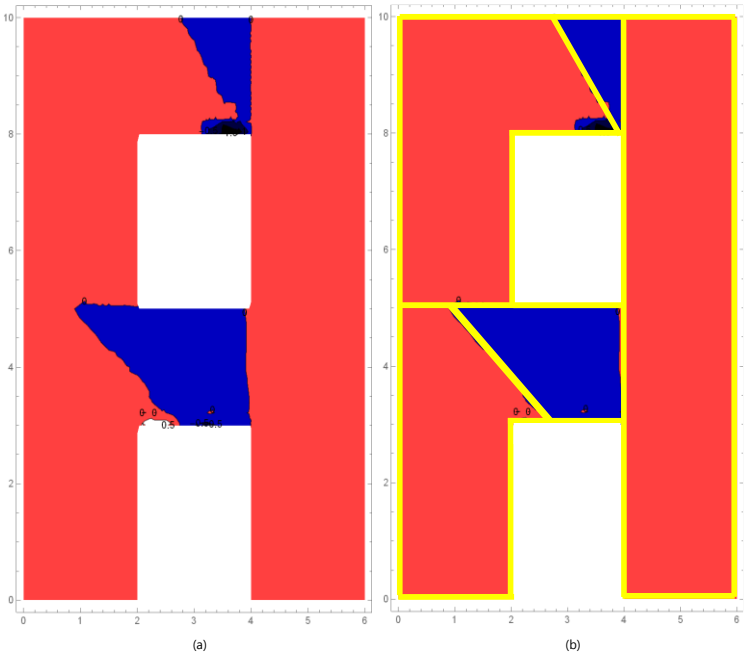

Fig. 8.24 - By depicting the positive rotations in red and the negative ones in blue (a), a neat partition of the whole domain into five rigid blocks can be seen (b).

■ 8.4 ARCH UNDER HORIZONTAL LOAD: A CASE STUDY

In this section, we analyse a real barrel vault, built and tested at the DIST laboratory (Department of Structures for Engineering and Architecture, Università degli Studi di Napoli Federico II): we refer to the work of Ramaglia et al (2016) for more details on the realization and testing of this artefact.

For the numerical strategy used to solve the problem of the arch under horizontal action we refer to **Section 6.6**. We approach the analysis by using the PR method in order to evaluate a static collapse multiplier and to obtain a partition of the domain into rigid blocks. Starting from this rigid block mechanism, and considering that a masonry structure under variable actions shows a typical SDOF unilateral dynamic behaviour, such mechanisms can be used to perform a dynamic analysis with the same approach used for the dynamic analysis model of rocking of a rigid block (see **Appendix F** and (Ochsendorf, 2006)).

8.4.1 Arch, case study: static analysis

The numerical analysis presented her is based on the PR method. The analytic solution is given in the appendix (see **Section E.2**). The structural geometry of the arch is shown in **Fig. 8.25**. The arch presents an internal radius $r = 1.54m$, a thickness $s = 0.12m$ and a springing angle β equal to 17.17°.

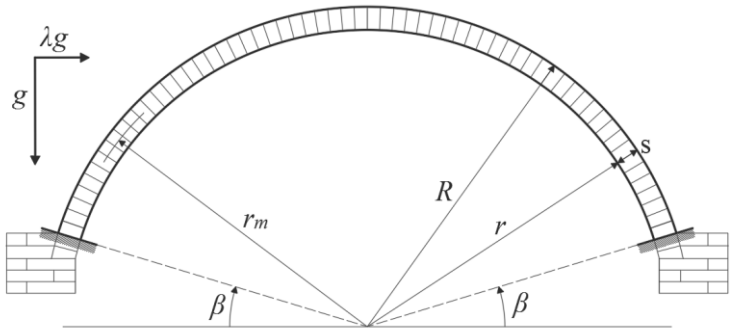

Fig. 8.25 - Structural geometry of the tested arch.

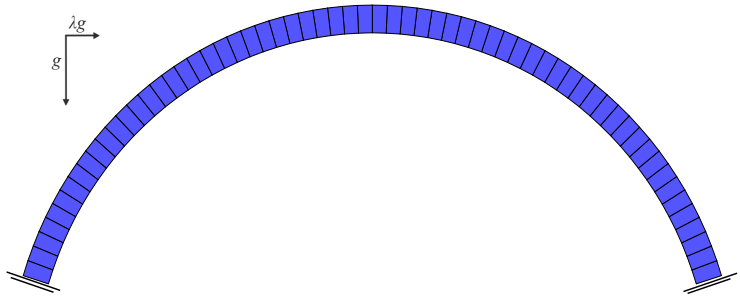

Fig. 8.26 - The circular arch with $\beta = 17.17°$ is discretized with 62 rigid elements.

The arch is discretized with 62 rigid quadrangular elements as shown in **Fig. 8.26**. A representation of the solution $\widehat{\boldsymbol{U}}^0$ of the minimum problem, reached through the simplex method, is reported in **Fig. 8.27**. The solution is close to the analytical one (**Tab. 8.1**). The mechanism, the relative hinges and the associated line of thrust are depicted in **Fig. 8.28**.

s =0.12m	λ_c	θ_4 [°]	θ_3 [°]	θ_2 [°]	θ_1 [°]
Numerical solution	[0.1594 , 0.1595]	151.08	99.40	47.71	17.17
Analytical solution	0.1593	149.90	99.05	48.20	17.17

Tab. 8.1 - The numerical solution reached with the simplex method and the analytical one (extracted from **Tab. E.5**) are reported.

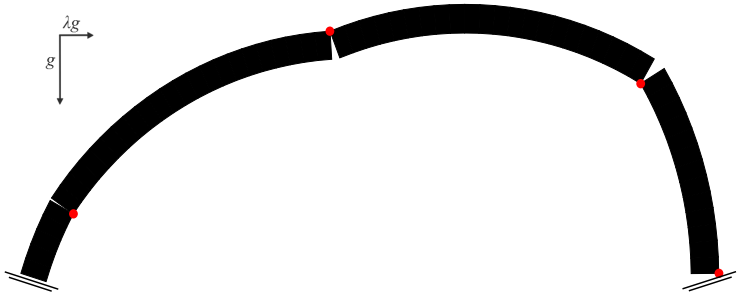

Fig. 8.27 - Solution $\widehat{\boldsymbol{U}}^0$ corresponding to $\lambda = 0.1595$, obtained through the simplex method.

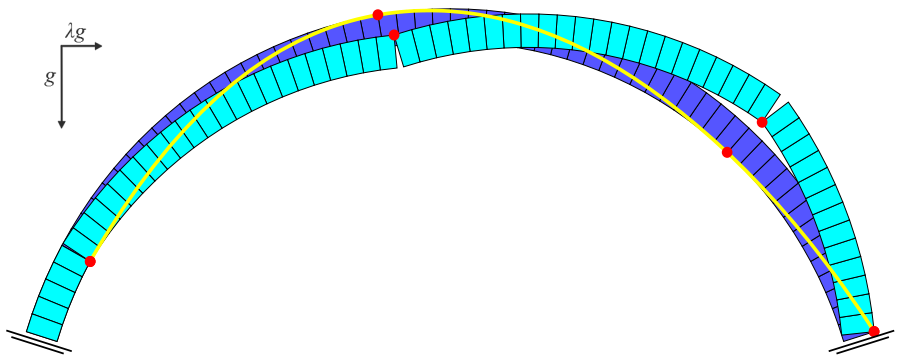

Fig. 8.28 - The mechanism corresponding to $\lambda = 0.1595$, the hinges formed and the associated thrust line.

8.4.2 Arch, case study: dynamic analysis

The previous analysis gives a close approximation of the static collapse multiplier, anyhow, once the arch reaches this limit condition, represented by the above SDOF mechanism, it starts moving dynamically. If the external action be constant the collapse will certainly occur. If the external action is variable action (e.g. seismic action), a dynamic analysis has to be performed. Indeed, during the motion, the arch oscillates between the two qualitative configurations reported in **Fig. 8.29**.

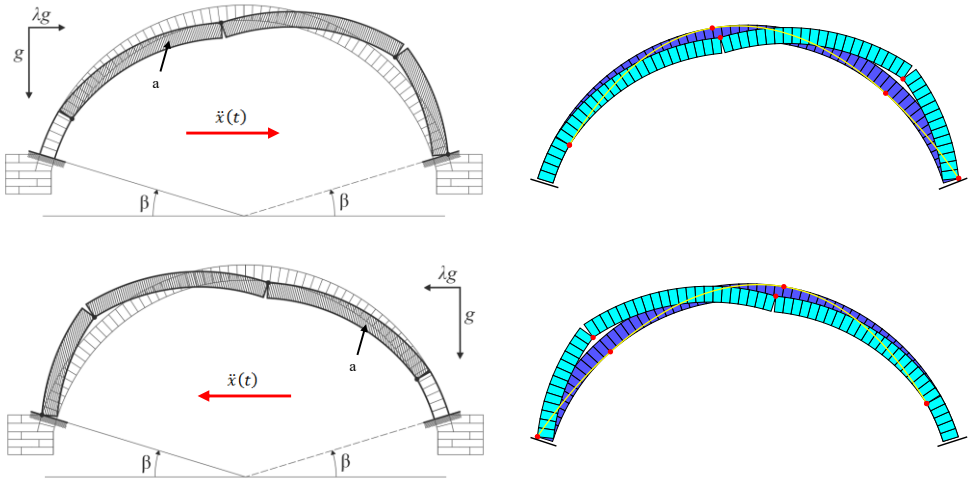

Fig. 8.29 - The two pattern configurations among which the arch oscillates under a variable action.

The arch shows a typical unilateral dynamic behaviour, and it can be treated with the model of rocking of a rigid block (see **Appendix F**). By using the mechanisms shown in **Fig. 8.29** in both directions and by evaluating all the dynamic properties of the rigid blocks in which the arch decomposes, the dynamic analysis can be performed. The equation of motion is derived from the Lagrangian of the whole system and reads:

$$0.639\text{Sign}\left(\vartheta(t)\right) - 0.3207\ddot{x}_g(t) + 0.393\ddot{\vartheta}(t) = 0$$

where ϑ identifies the Lagrangian parameter of the rotation of the blocks (labelled with the letter "a" in **Fig. 8.29**) and $\ddot{x}_g(t)$ is the ground motion. The integration of the previous ODE is performed numerically. In **Fig. 8.30** an analysis considering a restitution coefficient $r = 0.9$ and a sinusoidal impulse with a duration $T = 15s$ expressed by:

$$\ddot{x}_g(t) = \alpha g Sin(\omega t)$$

where $\alpha = 0.25$ and $\omega = 2\pi f$, with $f = 2Hz$ is presented.

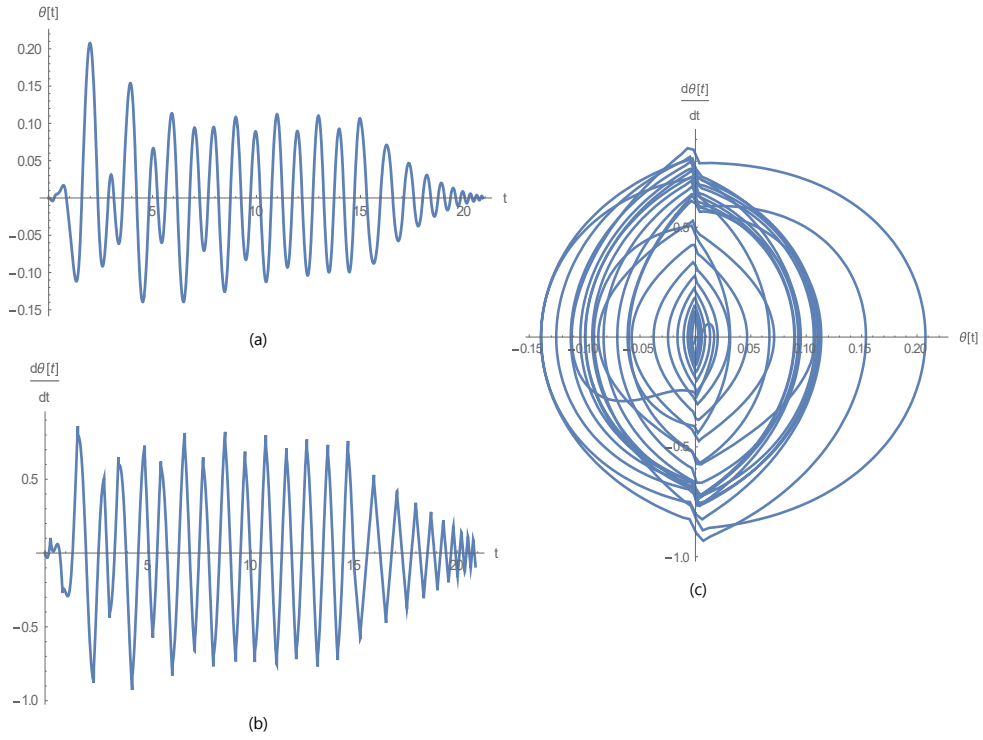

Fig. 8.30 - The rotation (a), the angular velocity (b) and the related phase plane (c) are reported.

PART IV

CONCLUSIONS

Chapter 9

CONCLUSIONS

Prologue. The results of this dissertation are discussed in three parts: 1) a general description on the general framework of the theory; 2) the sense and the motivation behind the two numerical procedures which are proposed; 3) a discussion on the applications and results concerning 2d structures subjected either to prescribed settlements or variable loads.

■ 9.1 RIGID BLOCK MODEL METHODOLOGY

This dissertation presents a new rigid block model for the analysis of masonry elements and structures. The basic idea behind this work is that real masonry structures exhibit such rigid block mechanisms when subject to severe settlements or when shaken by serious earthquakes. To model this behaviours the Normal Rigid No-Tension (NRNT) model is adopted, that is the material is rigid in compression, but extensional deformations, at zero energy price, are allowed. The NRNT model represents a natural extension of the Heyman's theory to continuum models.

The boundary value problem (bvp) dealt with by using a displacement approach, is formulated as a minimum energy search. Such energy criterion allows to select, among all kinematically admissible mechanisms, the mechanism solving the bvp.

Two ways to discretize the displacement space are adopted, and for each of them a numerical solution strategy is introduced, namely: the PR method and C^0 method. With the PR method (i.e. rigid blocks), the energy is minimized within the set of piecewise rigid (PR) displacements under Heyman's restrictions: the latent strain is concentrated along lines and only concentrated cracks are allowed. With the C^0

method the minimum of the energy is searched among continuous (C^0) displacement fields (according to a classical finite element approximation). The problem is reduced to a standard Linear Programming by introducing a special set of linearized constraint conditions, in order to enforce the semi-positiveness of the latent strain tensor: the fractures appears as smeared. The main result of the C^0 method is that, even if continuous functions are considered, the solution will often return an approximate partition of the whole structure into rigid blocks, confirming the validity of the PR method.

After the two methods are introduced, some trivial problems are proposed to explore the numerical performances of the two approaches and the "pro et contra" of these two strategies. **Chapter 6** is completely dedicated to the study of the arch as benchmark case, whilst in the final Chapters some applications to common structures are proposed. The method for determining the effects of settlements, for identifying a settlement distribution producing a given crack pattern and for assessing the static multiplier due of horizontal actions, are illustrated. The main conclusion is that if an optimal partition of the structural domain is correctly guessed the results obtained with the PR methods are satisfactory, otherwise the C^0 method can be used to identify the optimal partition. The results we present, show that a masonry structure either forms an isostatic substructure in order to accommodate the effect of the given settlements, or reduces to a Single Degree of Freedom mechanism, if driven into to a limit state under the effect of variable forces (e.g. due to seismic actions). This last observation leads to the possibility of applying to the formed SDOF mechanism the model of rigid block rocking in order to analyse its dynamical behaviour.

■ 9.2 RIGID BLOCK MODEL: APPLICATIONS

Both PR and C^0 methods allow the user to analyse 2d masonry structures using:

- different discretizations of the domain with a generic choice of the element type;
- a generic distribution (e.g. vertical or horizontal) of external forces, implemented as concentrated and applied at generic points of the domain;
- a generic distribution of prescribed settlements along the boundary of the structural domain, implemented either with bilateral or unilateral constraints;
- the possibility to consider in the PR method eigenstrains (e.g. to simulate crushing), modelled as relative, non-homogeneous unilateral constraints;

In our analysis, with reference to the C^0 method, we tested various finite element types, but the best choice, balancing accuracy and simplicity, turned out to be a second order Lagrangian quadrangular element (**Fig. 4.6**).

The benchmarks and the applications analysed prove the valid numerical performances of the two approaches and show the "pro et contra" of these two strategies. The main result of the C^0 method is that, even if continuous functions are considered, the solution will often return an approximate partition of the whole structure into rigid blocks, confirming the validity of the PR method.

Remark 1|9. In this respect, we have to point out that the appearance of piece-wise rigid mechanisms (producing concentrated strains) rather than continuous mechanisms (entailing diffuse strains), is often due, in real structures, to mechanical characteristics, such as cohesion, toughness and finite friction, which are not accounted for by the NRNT model.

For bvp's concerning NRNT materials, there are essentially two legitimate ways to encourage rigid block mechanisms over diffuse deformations. The first one consists in trasplacing the loads, along their lines of action, from their actual points of application to the boundary, essentially exploiting small tensile stresses. The second one is to add, all over the loaded boundary, a scant uniform pressure, of the order of a small fraction of the atmospheric pressure. This last trick is sufficient to add to the bvp the so-called "safe load condition", necessary, with the known theorems, to show the existence of a displacement solution for the parent problem concerning NENT materials, (see (Giaquinta and Giusti, 1985), (Anzellotti ,1985)).

The C^0 method being more time consuming, is more appropriate in the analysis of simple structure or as a preliminary analysis to be implemented in combination with the PR method. Indeed, as discussed in **Section 5.3** (p. 97) and noted explicitly with **Remark 2|5** and **Remark 4|5**, the sluggishness of the rigid block approximation in reproducing "slanted" cracks (that is cracks not developing along the boundary of the rigid elements), is one of the main critical issues inherent to the PR approximation. Then, when the stereotomy of the structure does not give sufficient restrictions on the discretization, this constitutes a reason to use at the same time the C^0 approximation can be used in combination with the PR approximation, as a preliminary analysis for suggesting the optimal rigid block partition.

If an "optimal" discretization of the domain is suggested by the stereotomy of the real structural geometry (e.g. the voussoirs in the arch), the results, obtained by using the PR method, are good and the time required for the analysis is of the order of a few seconds. Instead, when the structure has a complex stereotomy and no information about an opportune discretization into rigid blocks is available, the C^0 method can be used to select an optimal partition into rigid blocks to be fed into the PR method.

By fixing an optimal partition, the coupled use of both methods allows the user, for a generic 2d structure in:

- to assess the effects of given settlements;
- to explore the equilibrium under given loads;
- to define a geometrical safety factor for the structure;
- to explore the effect of horizontal actions and consequently to find the collapse mechanism and the interval to which the horizontal static multiplier has to belong;
- to identify the distribution of the settlements producing a given crack pattern.

The use of the rigid block model for the analysis of a structure under horizontal actions return the collapse mechanism and the interval to which the static horizontal collapse multiplier has to belong. Starting from this rigid block mechanism, and considering that a masonry structure under variable actions shows a typical SDOF unilateral dynamic behaviour, such mechanisms can be used to perform a dynamic analysis with the same approach used for the dynamic analysis model of rocking of a rigid block (see **Appendix F**). In fact, by using the mechanisms found in both directions and by evaluating all the dynamic properties of the rigid blocks in which the structure decomposes, the dynamic analysis can be performed integrating directly the equation of the motion derived from the Lagrangian of the whole system.

PART V

APPENDICES

Appendix A

PRELIMINARIES

Prologue. In this section, we give the essential definitions and the basic tools (both of tensors algebra and convex analysis) used in this dissertation with particular regard to the strain and stress by adopting conventions of (Gurtin, 1972).

■ A.1 PRELIMINARIES FROM TENSOR ALGEBRA

Let V be the two-dimensional vector space associated to the 2d Euclidean space $\mathcal{E}^2$. In this text, we adopt the Einstein summation convention: when an index variable appears twice in a single term and is not otherwise defined, it implies summation of that term over all the values of the index.

With Lin one denotes the set of all second order tensor on V, seen as linear transformations from V to V. The scalar product of two elements $\boldsymbol{A}, \boldsymbol{B} \in Lin$ is defined by

$$\boldsymbol{A} \cdot \boldsymbol{B} = tr(\boldsymbol{A}\boldsymbol{B}^T) \,. \tag{A.1}$$

Sym indicates the subspace of Lin of all symmetric linear transformation whilst Skew of all antisymmetric ones.

It is well-known that the eigenvalues of any symmetric tensor are real and the relative eigenvectors can be chosen such that they are orthogonal to each other. Thus, with regards to a generic symmetric tensor $\boldsymbol{A} \in Sym$, it is possible to fix an orthonormal base of eigenvectors $(\boldsymbol{e}^1, \boldsymbol{e}^2)$ which results also an orthonormal base of the vector

space V. Then, with regards to this base, a symmetric tensor $\boldsymbol{A} \in Sym$ admits a spectral decomposition defined as follows:

$$\boldsymbol{A} = \alpha_i \boldsymbol{e}^i \otimes \boldsymbol{e}^i \quad \forall\, \boldsymbol{A} \in Sym\,, \tag{A.2}$$

where α_i, with $i \in \{1,2\}$, is the eigenvalues related to the eigenvector $\boldsymbol{e}^i$. This spectral decomposition exists and is unique.

Definition 1|A. Two symmetric tensors $\boldsymbol{A}, \boldsymbol{B} \in Sym$ are **coaxial** if and only if they admit a spectral decomposition with the same orthonormal basis of eigenvectors.

Definition 2|A. Two symmetric tensors $\boldsymbol{A}, \boldsymbol{B} \in Sym$ **commute** if and only if:

$$\boldsymbol{A}\boldsymbol{B} = \boldsymbol{B}\boldsymbol{A}. \tag{A.3}$$

The following result allows to connect the previous two definitions.

Theorem 1|A. Two symmetric tensors $\boldsymbol{A}, \boldsymbol{B} \in Sym$ commute if and only if they are coaxial.

In this dissertation, we often treat with two particular subspaces of Lin: Sym^+ and Sym^-; therefore it would be useful point out the minimal characterization of these subspaces need to the readers. We denote with Sym^+ [Sym^-] the subspace of Sym of all semidefinite positive [negative] symmetric tensors. It is well known that a semidefinite positive [negative] symmetric tensor has as spectral decomposition with all non-negative [non-positive] eigenvalues, namely:

$$\boldsymbol{A} = \alpha_i \boldsymbol{e}^i \otimes \boldsymbol{e}^i \in Sym^+ \Leftrightarrow \alpha_i \geq 0 \;\; \forall\, i \in \{1,2\}\,, \tag{A.4}$$
$$\boldsymbol{B} = \beta_i \boldsymbol{e}^i \otimes \boldsymbol{e}^i \in Sym^- \Leftrightarrow \beta_i \leq 0 \;\; \forall\, i \in \{1,2\}\,. \tag{A.5}$$

Theorem 2|A. Let $\boldsymbol{A}$ be a semidefinite positive [negative] symmetric tensor, i.e. $\boldsymbol{A} \in Sym^+$ [$\boldsymbol{A} \in Sym^-$], if there exists a vector $\boldsymbol{u} \in V$ such that $\boldsymbol{u} \cdot \boldsymbol{A}\boldsymbol{u} = 0$, then $\boldsymbol{u}$ is an eigenvector of $\boldsymbol{A}$ associating with an eigenvalue equals to 0, namely:

$$\boldsymbol{u} \cdot \boldsymbol{A}\boldsymbol{u} = 0 \Rightarrow \boldsymbol{A}\boldsymbol{u} = \boldsymbol{0}\,. \tag{A.6}$$

Proof. Suppose $\boldsymbol{A} \in Sym^+$ [$\boldsymbol{A} \in Sym^-$] and assuming for $\boldsymbol{A}$ the following spectral decomposition:

$$\boldsymbol{A} = \alpha_i \boldsymbol{e}^i \otimes \boldsymbol{e}^i \;\text{ with }\; \alpha_i \geq 0\; [\alpha_i \leq 0]\,, \tag{A.7}$$

it easy to verify that results:

$$\boldsymbol{Au} = \alpha_i \boldsymbol{f}^i, \tag{A.8}$$
$$\boldsymbol{u} \cdot \boldsymbol{Au} = \alpha_i (u^i)^2, \tag{A.9}$$

where $\boldsymbol{f}^i = u^i \boldsymbol{e}^i$ and $u^i = (\boldsymbol{e}^i \cdot \boldsymbol{u})$. Recalling that α_i is non-negative [non-positive], if $\boldsymbol{u} \cdot \boldsymbol{Au} = 0$ results that each term in the summation (A.9) has to be zero, that is $\alpha_i (u^i)^2 = 0 \;\; \forall\, i \in \{1,2\}$ or rather at least one of the two following relations have to hold:

$$\alpha_i = 0 \quad \text{or} \quad u^i = (\boldsymbol{e}^i \cdot \boldsymbol{u}) = 0\,. \tag{A.10}$$

Then from (A.8) results that $\boldsymbol{Au} = \boldsymbol{0}$: $\boldsymbol{u}$ is an eigenvector of $\boldsymbol{A}$ associating with an eigenvalue equals to 0.■

Since in our treatment we often handle two symmetric tensors, one belongs to Sym^+ and the other to Sym^-, the following characterization are relevant.

Theorem 3|A. Let $\boldsymbol{B}$ be symmetric tensor, it results:

$$\boldsymbol{A} \cdot \boldsymbol{B} \geq 0 \;\; \forall \boldsymbol{A} \in Sym^+ \;\; [\,\forall \boldsymbol{A} \in Sym^-\,] \;\Rightarrow\; \boldsymbol{B} \in Sym^+ \;\; [\boldsymbol{B} \in Sym^-]\,. \tag{A.11}$$

Theorem 4|A. Let $\boldsymbol{A} \in Sym^+$, if $\boldsymbol{B} \in Sym^+$ $[\boldsymbol{B} \in Sym^-]$ then

$$\boldsymbol{A} \cdot \boldsymbol{B} \geq 0 \;\; [\boldsymbol{A} \cdot \boldsymbol{B} \leq 0]\,. \tag{A.12}$$

Theorem 5|A. Let $\boldsymbol{A} \in Sym^+$ and $\boldsymbol{B} \in Sym^-$, it results:

$$\boldsymbol{A} \cdot \boldsymbol{B} = 0 \Rightarrow \boldsymbol{AB} = \boldsymbol{BA} = 0\,. \tag{A.13}$$

From **Theorem 1|A** and **5|A,** if these three relations hold:

$$\boldsymbol{A} \in Sym^+ \;\;,\;\; \boldsymbol{B} \in Sym^- \;\;,\;\; \boldsymbol{A} \cdot \boldsymbol{B} = 0 \;\;, \tag{A.14}$$

then $\boldsymbol{A}$ and $\boldsymbol{B}$ are coaxial.

■ A.2 PRELIMINARIES FROM CONVEX ANALYSIS

One briefly introduces some concepts about convex analysis, in particular three geometrical definitions regarding the convex cone, the dual cone and the polar cone.

Let $V_{\mathbb{R}}$ be the two-dimensional vector real space associated to the 2d Euclidean space $\mathcal{E}^2$ and let K be a non-empty subset of $V_{\mathbb{R}}$. In this section, we made the particular request that V is a vector space over the real field $\mathbb{R}$ because, as it can see below, we need to consider into the following definitions the concept of non-negative (or positive) scalar.

Definition 3|A. K is a **cone** (or linear cone) if and only if:

$$\forall \boldsymbol{x} \in K \Rightarrow \gamma \boldsymbol{x} \in K \qquad \forall \gamma \in \mathbb{R}_0^+. \tag{A.154}$$

Definition 4|A. K is a **convex cone** if it is closed under linear combinations with non-negative coefficients:

$$K \; convex \; cone \Leftrightarrow \forall \boldsymbol{x}, \boldsymbol{y} \in K \Rightarrow \alpha \boldsymbol{x} + \beta \boldsymbol{y} \in K \quad \forall \alpha, \beta \in \mathbb{R}_0^+ . \tag{A.16}$$

It is noticed that assuming $\boldsymbol{y} = \boldsymbol{x}$ and $\alpha = \beta = \gamma/2$, a convex cone is a special case of linear cone. In some books, one defines a convex cone K using strictly positive scalars and so, the origin does not belong to the cone: this is the case of the convex *"blunt"* cone K, otherwise the cone is called *"pointed"*. In our treatment, we consider only pointed cone. It is noticed that, since the scaling parameters α and β are non-limited, the cones are infinite in extent and not bounded.

It follows from the above properties that *a convex cone is as a linear cone that is closed under convex combinations*. More succinctly, a set K is a convex cone if and only if $\alpha K = K$ and $K + K = K$, for any positive scalar α.

Examples. The empty set, the space $V_{\mathbb{R}}$, and any linear subspace of $V_{\mathbb{R}}$ are convex cones. A convex combination of a finite set of vectors in $\mathbb{R}^n$ is a convex cone. The intersection of two convex cones in the same vector space is again a convex cone, but their union may fail to be one. The set of semidefinite matrices, both Sym^+ and Sym^-, are convex cone. ■

Below one supposes the vector space $V_{\mathbb{R}}$ is equipped either by the inner product $\langle \cdot, \cdot \rangle$ and either by the relative induced norm $|\cdot|$. One introduces the notions of projection of a point on a convex cone and the normal cone of a set.

Definition 5|A. Let $K \subseteq V_{\mathbb{R}}$ be a convex cone of a vector space $V_{\mathbb{R}}$ equipped by the norm $|\cdot|$ induced by inner product $\langle \cdot, \cdot \rangle$. A point $\boldsymbol{y} \in K$ is the **orthogonal projection** of a point $\boldsymbol{x} \in V_{\mathbb{R}}$ if

$$|\boldsymbol{y} - \boldsymbol{x}| = min\{|\boldsymbol{z} - \boldsymbol{x}|, \forall \boldsymbol{z} \in K\} . \tag{A.17}$$

Furthermore, it is possible to demonstrate that if K is also closed, the projection exists and is unique. Starting from this definition, if K is a closed convex cone, the following statement holds:

Theorem 6|A. Let K be a closed convex cone, $\boldsymbol{y} \in K$ is the orthogonal projection of a point $\boldsymbol{x} \in V_{\mathbb{R}}$ onto K if and only if the following two conditions hold:

$$\langle \boldsymbol{w}, \boldsymbol{x} - \boldsymbol{y} \rangle \leq \boldsymbol{0} \quad \forall \boldsymbol{w} \in K, \tag{A.18}$$

$$\langle \boldsymbol{y}, \boldsymbol{x} - \boldsymbol{y} \rangle = \boldsymbol{0}\,. \tag{A.19}$$

It is useful to give another geometrical characterization of projection of a point, that is a geometric one based on the concept of *"normal cone"* of a set $S \subseteq V_{\mathbb{R}}$ in a fixed point $\boldsymbol{y} \in V_{\mathbb{R}}$.

Definition 6|A. Let S be a non-empty subset of $V_{\mathbb{R}}$, and let $\boldsymbol{y} \in V_{\mathbb{R}}$, the **normal cone** to S in $\boldsymbol{y}$ is

$$Norm(S, \boldsymbol{y}) = \{\boldsymbol{x} \in V_{\mathbb{R}} \mid \langle \boldsymbol{z} - \boldsymbol{y}, \boldsymbol{x} \rangle \leq 0 \; \forall \boldsymbol{z} \in S\}\,. \tag{A.20}$$

When $S = K$ is a closed convex cone, it is possible introduce the following characterization.

Definition 7|A. Let $K \subseteq V_{\mathbb{R}}$ be a closed convex cone, for any $\boldsymbol{y} \in K$, the **normal cone** in $\boldsymbol{y}$ to K is:

$$Norm(K, \boldsymbol{y}) = \{\boldsymbol{x} \in V_{\mathbb{R}} \mid \langle \boldsymbol{z}, \boldsymbol{x} \rangle \leq 0 \; \forall \boldsymbol{z} \in K \; with \; \langle \boldsymbol{y}, \boldsymbol{x} \rangle = 0\}\,. \tag{A.21}$$

Starting from the last definition, one demonstrates that the following statement holds:

Theorem 7|A. The point $\boldsymbol{y} \in K$ is the **orthogonal projection** (with respect the inner product) of a point $\boldsymbol{x} \in V_{\mathbb{R}}$ onto a closed convex cone K if and only if:

$$(\boldsymbol{x} - \boldsymbol{y}) \in Norm(K, \boldsymbol{y})\,. \tag{A.22}$$

Below we introduce the definition and the main geometrical characterizations of the dual cone of a generic set $K \subseteq V_{\mathbb{R}}$. Let $V_{\mathbb{R}}^*$ be the dual space of $V_{\mathbb{R}}$, that is the set of the linear and continuous functionals on $V_{\mathbb{R}}$.

Definition 8|A. The (algebraic) **dual cone** of $K \subseteq V_{\mathbb{R}}$ is the subspace of $V_{\mathbb{R}}^*$ of all the linear and continuous functionals that are non-negative on K, namely:

$$K^* = \{\boldsymbol{v} \in V_{\mathbb{R}}^* \mid \quad \boldsymbol{v}(\boldsymbol{w}) \geq 0 \quad \forall\, \boldsymbol{w} \in S\}\,. \tag{A.23}$$

If the space is equipped by the inner product $\langle \cdot\,, \cdot \rangle$, from the previous definition it descends:

Definition 9|A. Let $K \subseteq V_{\mathbb{R}}$ be a non-empty set, the dual cone of K is the set:

$$K^* = \{\boldsymbol{v} \in V_{\mathbb{R}} \mid \langle \boldsymbol{w}, \boldsymbol{v} \rangle \geq 0 \quad \forall\, \boldsymbol{w} \in S\}\,. \tag{A.24}$$

Since in finite dimensions every dimensional linear functional is continuous and every continuous linear functional in an inner product space induces a linear isomorphism from $V_{\mathbb{R}}^*$ to $V_{\mathbb{R}}$ (see Riesz representation theorem), the previous two definitions of the dual cone are essentially the same. If K is equal to its dual cone K^*, then K is called self-dual.

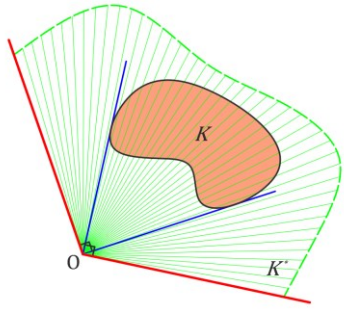

Fig. A.1 - A set K and the its dual cone K^*.

Let $K \subseteq V_{\mathbb{R}}$ be a non-empty set (not necessary a convex cone), the set:

$$K^O = \{\boldsymbol{v} \in V_{\mathbb{R}} \mid \langle \boldsymbol{w}, \boldsymbol{v} \rangle \leq 0 \quad \forall\, \boldsymbol{w} \in S\}\,. \tag{A.25}$$

Is the polar cone of K and it coincides with the negative of the dual cone K^*, i.e. $K^O = -K^*$, as shown in **Fig. A.2**.

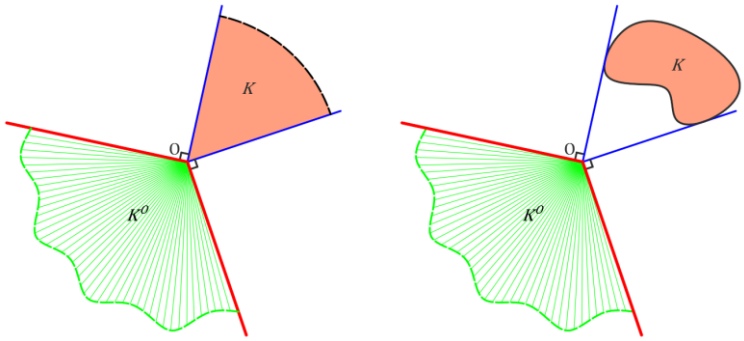

Fig. A.2 - Two sets and their relative polar cones.

Appendix B

ELASTIC-PLASTIC CONSTITUTIVE LAW

Prologue. In this section, we introduce the basic concepts of Plasticy, following closely the approach set out both in the course notes of Prof. Luciano Nunziante (2005) and in the book (2011).

■ B.1 ANELASTIC BODY AND INTERNAL VARIABLES

A **Cauchy-elastic material** is one in which the stress at each point is determined only by the current state of deformation. On contrary, a body is **anelastic** when its deformation is function of the past history and other internal variables (*materials with memory*). The theory that deals with these materials, in the linear case, is called *linear viscoelasticity*. A way of representing the parameters on which depends the behaviour of an anelastic body, is to introduce internal variables collected in the vector $\boldsymbol{\xi} = [\xi_1, \xi_2, \dots, \xi_n]^T$. Therefore, the strain $\boldsymbol{E} = [\varepsilon_{ij}]$ can be expressed as follows:

$$\boldsymbol{E} = \boldsymbol{E}(\boldsymbol{T}, \boldsymbol{\xi}, T) \,, \tag{B.1}$$

where $\boldsymbol{T} = [\sigma_{ij}]$ is the Cauchy stress tensor and T is the temperature. The presence of these additional variables requires additional constitutive equations. For anelastic bodies, with infinitesimal deformation, the strain can be additively decomposed into an elastic and an anelastic parts as follows:

$$\boldsymbol{E} = \boldsymbol{E}^e + \boldsymbol{E}^a \,, \tag{B.2}$$

where the elastic part is determined by the current stress state, namely:

$$\boldsymbol{E}^e = \mathbb{C}^{-1}\boldsymbol{T}\,, \tag{B.3}$$

whilst the anelastic components depend on the internal variables. The body is said to be in **equilibrium** if its state does not change spontaneously when the external actions remain constant. Since in this context the focus is on the plastic behaviour of materials and structures, the plastic strain $\boldsymbol{E}^p = \boldsymbol{E}^a$, representing the permanent deformation of the material, takes the role of an internal variable, and from here on we express the deformation as follows:

$$\boldsymbol{E} = \boldsymbol{E}^e + \boldsymbol{E}^p\,. \tag{B.4}$$

■ B.2 PLASTIC FLOW

The plastic behaviour of the material is non-conservative, in the sense that, during an increasing load process, part of the external energy is dissipated in other forms of energy, related to the development of irreversible deformations (or fractures) that arise within the material. In the following, we express the strains $\boldsymbol{E}$ and the stress $\boldsymbol{T}$ as column vectors in $\mathbb{R}^9$, namely:

$$\boldsymbol{\varepsilon} = [\varepsilon_1, \varepsilon_2, \dots, \varepsilon_9]^T = [\varepsilon_{11}, \varepsilon_{12}, .., \varepsilon_{33}]^T\,, \tag{B.5}$$

$$\boldsymbol{\sigma} = [\sigma_1, \sigma_2, \dots, \sigma_9]^T = [\sigma_{11}, \sigma_{12}, .., \sigma_{33}]^T\,. \tag{B.6}$$

If the load process is time dependent, (B.4) can be rewritten in the following incremental form:

$$\dot{\boldsymbol{\varepsilon}} = \dot{\boldsymbol{\varepsilon}}^e + \dot{\boldsymbol{\varepsilon}}^p\,. \tag{B.7}$$

The experimental results show that in many structural materials the anelastic strains arise when both a certain stress limit level $\boldsymbol{\sigma}$ and a certain level of the stress increment $d\boldsymbol{\sigma}$ are reached. In particular, the **plastic function** f_0 defines a yield domain, describing all the limit stress states $\boldsymbol{\sigma}$, that is:

$$f_0(\boldsymbol{\sigma}) = 0\,, \tag{B.8}$$

in the stress space in $\mathbb{R}^9$, or, for isotropic materials (by restricting to the principal stresses) in stress space $\mathbb{R}^3$ (**Fig. B.1**).

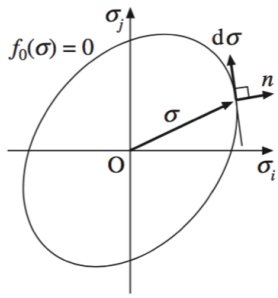

Fig. B.1 – Drawing from Nunziante (2005): a schematic representation of the yield domain.

It is usually assumed that the function f_0 is almost everywhere (*a.e.*) differentiable. From here on, we restrict to consider "perfect plasticity", in which plastic deformations arise if the two following conditions are met:

$$f_0(\boldsymbol{\sigma}) = 0\,, \tag{B.9}$$

$$df_0(\boldsymbol{\sigma}) = \left(\frac{df_0}{d\sigma_i}\right)_{\boldsymbol{\sigma}} = \nabla f_0 \cdot d\boldsymbol{\sigma} = 0\,, \tag{B.10}$$

where (B.9) expresses that the stress vector $\boldsymbol{\sigma}$ belongs to the yield domain, whilst (B.10) requires that the stress increase $\mathrm{d}\boldsymbol{\sigma}$ belongs to the tangent plane to the limit domain at $\boldsymbol{\sigma}$, and consequently that is orthogonal to the normal $\boldsymbol{n}$ defined through the gradient vector of f_0, namely:

$$\left(\frac{df_0}{d\sigma_i}\right)_{\boldsymbol{\sigma}}\,. \tag{B.11}$$

An internal point ($f_0(\boldsymbol{\sigma}) < 0$) corresponds to an elastic state, whilst the stress states external to the plastic domain are not admissible for elastic perfectly plastic materials. The plastic strain increase $d\boldsymbol{E}^p$ or $d\boldsymbol{\varepsilon}^p$ can be expressed in the following form:

$$d\boldsymbol{E}^p = d\lambda\,\boldsymbol{\Pi}\quad,\quad d\boldsymbol{\varepsilon}^p = d\lambda\,\boldsymbol{\pi}\,, \tag{B.12}$$

where $\boldsymbol{\Pi} = [\pi_{ij}]$ is a second order symmetric tensor and $\boldsymbol{\pi}$ is its representation in $\mathbb{R}^9$ space. The scalars π_{ij} determine the *shape* of the plastic strain increment, whilst $d\lambda$ the *norm* of the plastic strain increment. This assumption is in accordance to experimental results for which, in a perfectly plastic material, the plastic strains arise when a limit stress state is attained (B.9) along specific planes of plastic flow depending on the material and on the level stress. Moreover, the plastic strain increase does not depend neither on the direction nor on the magnitude of the stress

increment $d\boldsymbol{\sigma}$ (B.10). Then, the incremental strain of the material can be characterized by the three following relations:

$$d\lambda \geq 0\,,\;\; f_0(\boldsymbol{\sigma}) = 0\,,\;\; df_0(\boldsymbol{\sigma}) = 0\,, \tag{B.13}$$

$$d\lambda = 0\,,\;\; f_0(\boldsymbol{\sigma}) = 0\,,\;\; df_0(\boldsymbol{\sigma}) < 0\,, \tag{B.14}$$

$$d\lambda = 0\,,\;\; f_0(\boldsymbol{\sigma}) < 0\,, \tag{B.15}$$

respectively **plastic state**, **elastic return** and **elastic state**.

Remark 1|B. Some metallic materials (e.g. steel) have a structure made of polycrystalline aggregates where each crystal is an assembly of atoms, with their own regular structure. These crystal aggregates, though in elastic conditions present an isotropic macroscopic behaviour, show plastic strains (or plastic slips) on special crystal planes in response to shear stresses therein. Such planes are those where the strength is minimal and define the mechanism of slip.

Based on these experimental evidences (**Remark 1|B**), the direction of the strain increment is ruled by a function $P(\boldsymbol{\sigma})$ called **plastic potential**. This potential is the generator of the scalars π_i (or equivalently π_{ij}) through the following relation:

$$\pi_i = \frac{\partial P(\boldsymbol{\sigma})}{\partial \sigma_i}\,. \tag{B.16}$$

Generally, for many materials, it is assumed that the plastic potential function $P(\boldsymbol{\sigma})$ coincides with the yield function $f_0(\boldsymbol{\sigma})$, namely:

$$P(\boldsymbol{\sigma}) = \;\; f_0(\boldsymbol{\sigma})\,, \tag{B.17}$$

and the **Associated Plastic Potential** hypothesis (B.17) defines standard (or associated) materials. Hence, the constitutive law, in the case of plastic condition, can be rewritten as follows:

$$d\boldsymbol{\varepsilon}^p = d\lambda \frac{\partial f_0}{\partial \boldsymbol{\sigma}}\,, \tag{B.18}$$

and it is also known as **Normality Law**. Condition (B.18) states that the direction of $d\boldsymbol{\varepsilon}^p$ is the same of the normal $\boldsymbol{n}$ to the boundary of the yield domain $f_0 = 0$ at the stress point $\boldsymbol{\sigma}$ (see **Fig. B.2a**).

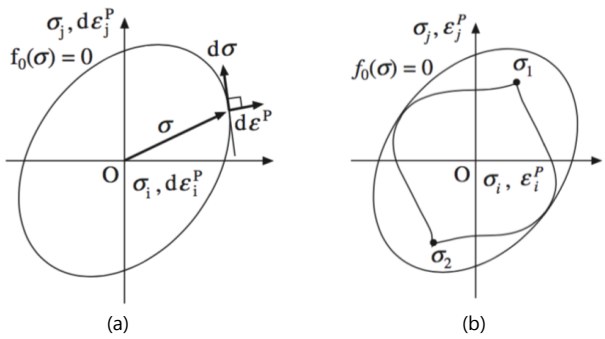

Fig. B.2 - Drawings from Nunziante (2005). By overlapping the vector space referred to $d\boldsymbol{\varepsilon}^p$ with that referred to $\boldsymbol{\sigma}$ (with coincident bases) we can represent in the same plane the vectors $\boldsymbol{\sigma}, d\boldsymbol{\sigma}, d\boldsymbol{\varepsilon}^p$. In (a) the Normality Law is symbolically represented. In (b): if we consider two different transformations Γ_1, Γ_2 with the same ends points $\boldsymbol{\sigma}_1, \boldsymbol{\sigma}_2$, in general different values of plastic strain increase $\Delta\boldsymbol{\varepsilon}^p$ can be reached: $d\boldsymbol{\varepsilon}^p$ is not an exact differential.

It should be noted that $d\boldsymbol{\varepsilon}^p$ is not an exact differential (see **Fig. B.2b**). When the increments are time-dependent, the condition (B.18) can be rewritten as follows:

$$\dot{\varepsilon}_i^p = \dot{\lambda}\left(\frac{\partial f_0(\boldsymbol{\sigma})}{\partial \sigma_i}\right)_{\boldsymbol{\sigma}}, \tag{B.19}$$

with:

$$\dot{\lambda} \geq 0 \quad if \quad f_0(\boldsymbol{\sigma}) = 0\,, \quad \dot{f}_0(\boldsymbol{\sigma}) = 0\,, \tag{B.20}$$

$$\dot{\lambda} = 0 \quad if \quad f_0(\boldsymbol{\sigma}) = 0\,, \quad \dot{f}_0(\boldsymbol{\sigma}) < 0\,, \tag{B.21}$$

$$\dot{\lambda} = 0 \quad if \quad f_0(\boldsymbol{\sigma}) < 0\,. \tag{B.22}$$

If the plasticization function f_0 is assigned through m functions (i.e. $f_{01}(\boldsymbol{\sigma}), \dots, f_{0m}(\boldsymbol{\sigma})$), the strength domain is defined by m inequalities, namely:

$$f_{01}(\boldsymbol{\sigma}) \leq 0, \dots, f_{0m}(\boldsymbol{\sigma}) \leq 0\,, \tag{B.23}$$

and the yield condition becomes:

$$sup f_{0i}(\boldsymbol{\sigma}) = 0,\ i \in \{1, \dots, m\}\,. \tag{B.24}$$

Each function $f_{0i}(\boldsymbol{\sigma}) = 0$ represents a surface, within which the function f_{0i} is differentiable, while in the edge points the function f_{0i} is not differentiable (**Fig. B.3**).

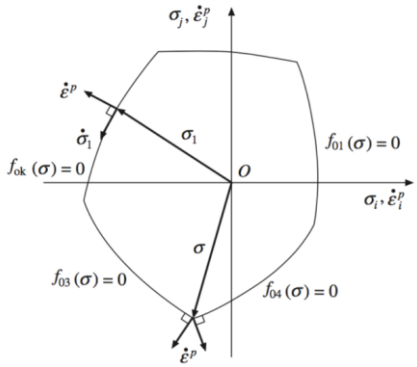

Fig. B.3 – Drawing from Nunziante (2005): yield plastic domain defined by m functions.

Conditions (B.19-22) can be generalized as follows:

$$\dot{\varepsilon}_i^p = \sum_{k=1}^{m} \dot{\lambda}_k \frac{\partial f_{0k}}{\partial \sigma_i}, \tag{B.25}$$

with:

$$\dot{\lambda}_k \geq 0 \ \ where \ \ f_{0k}(\boldsymbol{\sigma}) = 0 \ \ , \ \ \dot{f}_{0k}(\boldsymbol{\sigma}) = 0 \,, \tag{B.26}$$

$$\dot{\lambda}_k = 0 \ \ where \ \ f_{0k}(\boldsymbol{\sigma}) = 0 \ \ , \ \ \dot{f}_{0k}(\boldsymbol{\sigma}) < 0 \,, \tag{B.27}$$

$$\dot{\lambda}_k = 0 \ \ where \ \ f_{0k}(\boldsymbol{\sigma}) < 0 \,, \tag{B.28}$$

where $\dot{\lambda}_k$ refers to the k-th plane of the plastic domain and $\partial f_{0t}/\partial \sigma_i$ defines the gradient vector of the active planes f_{0t} in the stress space. Condition (B.25) expresses the vector of plastic strain increase as a non-negative linear combination ($\dot{\lambda}_t \geq 0$) of the gradient vectors of the active planes: for this reason $\dot{\boldsymbol{\varepsilon}}^p$ belongs to the **cone of the outward normal vectors** to the yield surfaces corresponding to the active stresses (**Fig. B.3**).

■ B.3 STABLE MATERIAL (DRUCKER POSTULATE)

With reference to the $\sigma - \varepsilon$ plot (**Fig. B.4**) if we consider the state A, defined by $(\sigma_1, \varepsilon_1)$, and apply the positive stress increment $\dot{\sigma}_1 dt$, a positive strain increment $\dot{\varepsilon}_1 dt$ arises and the specific power increment is positive, namely:

$$\dot{\sigma}_1 \dot{\varepsilon}_1 > 0 \,. \tag{B.29}$$

The material in the state A is defined **stable**. Instead, in the state B, defined by $(\sigma_2, \varepsilon_2)$, a positive strain increment $\dot{\varepsilon}_2 dt$ is associated to a negative stress increment $\dot{\sigma}_2 dt$ and consequently $\dot{\sigma}_2 \dot{\varepsilon}_2$ is negative: the material in B is **unstable**.

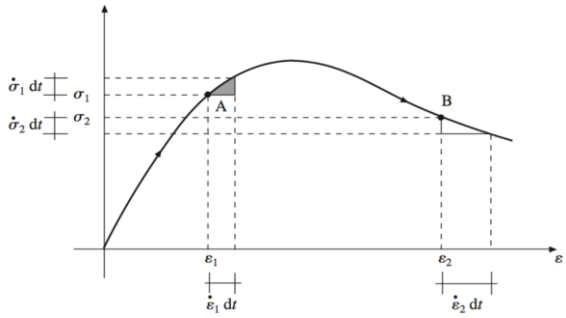

Fig. B.4 - Drawing from Nunziante (2005): typical one-dimensional stress test showing a ductile behaviour. In A the material is stable ($\dot{\sigma}_1 \dot{\varepsilon}_1 > 0$), whilst in B ($\dot{\sigma}_1 \dot{\varepsilon}_1 < 0$) is unstable.

From these observations, the **Drucker's stability postulate** descends: if a material is stable, the following inequality must be satisfied:

$$\oint \dot{\boldsymbol{\sigma}} \cdot \dot{\boldsymbol{\varepsilon}}\, dt \geq 0\,, \tag{B.30}$$

where the integral is done over a closed stress cycle (loading-unloading path in the stress space). From (B.30) descends that in a cycle of plastic deformation the second degree plastic work is always non negative:

$$\dot{\boldsymbol{\sigma}} \cdot \dot{\boldsymbol{\varepsilon}}^p \geq 0\,, \tag{B.31}$$

hence, it should be noted that the Drucker stability postulate is in line with the normality ($\dot{\boldsymbol{\sigma}} \cdot \dot{\boldsymbol{\varepsilon}}^p = 0$) and with hardening materials ($\dot{\boldsymbol{\sigma}} \cdot \dot{\boldsymbol{\varepsilon}}^p > 0$). Furthermore, for an elastic plastic material with an associate plastic potential, with respect to a limit stress state $\boldsymbol{\sigma}$ and to the corresponding $\dot{\boldsymbol{\varepsilon}}^p$ (see **Fig. B.5a**), the following inequalities holds:

$$(\boldsymbol{\sigma} - \boldsymbol{\sigma}^a) \cdot \dot{\boldsymbol{\varepsilon}}^p \geq 0\,, \tag{B.32}$$

for all admissible stress state $\boldsymbol{\sigma}^a$ (an admissible stress state is defined by $f(\boldsymbol{\sigma}^a) \leq 0$). Starting from the Drucker's stability postulate it is possible to demonstrate that the **plastic domain has to be convex**: in **Fig. B.5b** a geometric counterexample, showing how a non-convex domain contradicts condition (B.32) is reported.

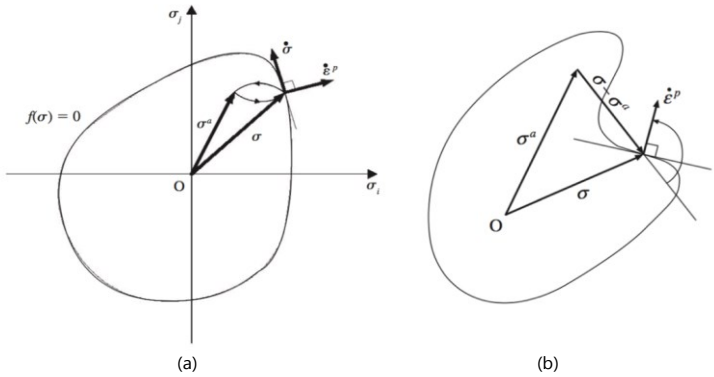

Fig. B.5 – Drawings from Nunziante (2005): a convex limit domain (a) and a non convex domain (b) are depicted.

■ B.4 THEOREMS OF LIMIT ANALYSIS

We refer to a normal material: an elastic-plastic material with an associate plastic potential according to the normality law and the Drucker's stability postulate. The body, occupying the domain $V \subseteq \mathbb{R}^3$ and subjected to the volume load $\boldsymbol{b}$, is loaded by given tractions on the complementary part $\partial V_N = \partial V - \partial V_D$ of the boundary, where ∂V_D is the constrained part.

The body is in a **plastic collapse state** if the load system $(\boldsymbol{b}, \bar{\boldsymbol{s}})$ cannot be further amplified: the strains and the associated displacements can grow indefinitely, defining the **collapse mechanism**. A stress field $\boldsymbol{\sigma}^a$ is **statically admissible** if it satisfies the equilibrium equations (B.33) and the boundary equations (B.34):

$$div\boldsymbol{\sigma}^a + \boldsymbol{b} = \boldsymbol{0} \ , \ \boldsymbol{x} \in V \ , \tag{B.33}$$

$$\boldsymbol{\sigma}^a \cdot \boldsymbol{n} = \bar{\boldsymbol{s}} \ \ , \ \boldsymbol{x} \in \partial V_N \ , \tag{B.34}$$

as well as the compatibility condition:

$$f(\boldsymbol{\sigma}^a) \leq 0 \ , \tag{B.35}$$

being $\boldsymbol{n}$ the outward normal at the boundary ∂V of the domain V. A load system $(\boldsymbol{b}, \bar{\boldsymbol{s}})$ in equilibrium with an admissible stress field $\boldsymbol{\sigma}^a$ is said an **admissible load** and the set $(\boldsymbol{b}, \bar{\boldsymbol{s}}, \boldsymbol{\sigma}^a)$ is defined equilibrated. The collapse load system $(\boldsymbol{b}, \bar{\boldsymbol{s}})$ and the stress $\boldsymbol{\sigma}$ at collapse represent the admissible load-stress system $(\boldsymbol{b}, \bar{\boldsymbol{s}}, \boldsymbol{\sigma})$ that occurs under the collapse of the structure.

A stress field $\boldsymbol{\sigma}^s$ is a **safe stress field** if it satisfies (B.33), (B.34) and the compatibility condition:

$$f(\boldsymbol{\sigma}^s) < 0\,. \tag{B.36}$$

A load system $(\boldsymbol{b}^s, \overline{\boldsymbol{s}}^s)$ in equilibrium with a safe stress field is said a **safe load system**. A set $(\dot{\boldsymbol{u}}_0, \dot{\boldsymbol{\varepsilon}}_0)$, where the infinitesimal strain rate field is expressed as follows:

$$\dot{\varepsilon}_{0ij} = \frac{1}{2}\left(\frac{\partial \dot{u}_{0i}}{\partial x_j} + \frac{\partial \dot{u}_{0j}}{\partial x_i}\right) \quad \boldsymbol{x} \in \partial V\,, \tag{B.37}$$

is said an **admissible kinematism**, if the displacement rate field $\dot{\boldsymbol{u}}_0$ satisfies the following relation on the constrained boundary:

$$\dot{\boldsymbol{u}}_{\boldsymbol{0}} = \underline{\dot{\boldsymbol{u}}}_{\boldsymbol{0}}\ ,\ \boldsymbol{x} \in \partial V_D\,. \tag{B.38}$$

B.4.1 Safe Theorem of Plastic Collapse

Safe Theorem - Part I. If a load program is assigned, the existence of a statically safe stress field $\boldsymbol{\sigma}^s$, for each instant of the load program, is a sufficient condition so that the plastic collapse will not occur. ■

Safe Theorem - Part II. The structure cannot bear an external load system if does not exist an admissible stress distribution $\boldsymbol{\sigma}^a$. Hence, the existence of a statically admissible stress field $\boldsymbol{\sigma}^a$ is a necessary condition so that the plastic collapse will not occur. ■

It should be noted that in the collapse state results:

$$\dot{\boldsymbol{\sigma}} = \boldsymbol{0}\ ,\ \dot{\boldsymbol{\varepsilon}}^e = \boldsymbol{0}\,,\ \dot{\boldsymbol{\varepsilon}} = \dot{\boldsymbol{\varepsilon}}^p\,. \tag{B.39}$$

B.4.2 Kinematic Theorem of Plastic Collapse

Let $(\dot{\boldsymbol{u}}^0, \dot{\boldsymbol{\varepsilon}}^0)$ be an admissible mechanism, $(\boldsymbol{b}, \overline{\boldsymbol{s}}, \boldsymbol{\sigma})$ the collapse load-stress set, $(\dot{\boldsymbol{u}}, \dot{\boldsymbol{\varepsilon}})$ the actual collapse mechanism $(\dot{\boldsymbol{u}}, \dot{\boldsymbol{\varepsilon}})$, and $\boldsymbol{\sigma}^0$ a statically admissible stress state satisfying the normality law with respect to the $\dot{\boldsymbol{\varepsilon}}^{0p}$, namely:

$$\boldsymbol{\sigma} \cdot \dot{\boldsymbol{\varepsilon}}^{0p} \leq \boldsymbol{\sigma}^0 \cdot \dot{\boldsymbol{\varepsilon}}^{0p}\,. \tag{B.40}$$

By denoting with $\dot{D}$ the power dissipation (or internal power):

$$\dot{D} = \int_V \boldsymbol{\sigma}^0 \cdot \dot{\boldsymbol{\varepsilon}}^{0p}\, dV\,, \tag{B.41}$$

and with $\dot{W}$ the external power (or load power):

$$\dot{W} = \int_{\partial V} \overline{\boldsymbol{s}} \cdot \dot{\boldsymbol{u}}^0\, dS - \int_V \boldsymbol{b} \cdot \dot{\boldsymbol{u}}^0\; dV\,, \tag{B.42}$$

it is possible to demonstrate that the functional $(\dot{D} - \dot{W})$ is always non negative, namely. The *kinematic theorem of plastic collapse* states that the functional $(\dot{D} - \dot{W})$ exhibits its minimum value in correspondence of the actual collapse mechanism resulting:

$$\dot{D} = \dot{W}\,. \tag{B.43}$$

By using the functionals $\dot{D}$ and $\dot{W}$ the kinematic theorem can be expressed through the following statements.

Kinematic Theorem - Part I. The existence of a kinematical admissible mechanism, for which the following condition occurs:

$$\dot{D} < \dot{W}\,, \tag{B.44}$$

represents a sufficient condition so that the plastic collapse will not occur. ■

Kinematic Theorem - Part II. When the following condition, with reference to each kinematically admissible mechanism, occurs:

$$\dot{W} \leq \dot{D}\,, \tag{B.45}$$

this represents a necessary condition so that the structure is able to sustain the loads, and the plastic collapse will not occur. ■

Kinematic Theorem - Part III. When the following condition, with reference to each kinematically admissible mechanism, occurs:

$$\dot{W} < \dot{D}\,, \tag{B.46}$$

this represents a sufficient condition so that the structure is able to sustain the loads. ■

Appendix C

THE CATENARY

■ C.1 THE CATENARY

The catenary is the geometrical curve describing the configuration of a chain simply supported at its two end points and subjected only to its weight. Since a chain cannot support compression (then, cannot opposite any resistance to flexion), it exhibits only tensile force everywhere tangent to the curve. The catenary, then, represents a geometrical configuration through which the chain supports its weight only with tangent tensile stresses. One considers a chain of length L suspended (see **Fig. C.1**) at the two end points $\boldsymbol{P}_1$ and $\boldsymbol{P}_2$ and let $\boldsymbol{\gamma}(s) = \big(x(s), y(s)\big)$ be, in an orthonormal reference system (O, x, y), the parametric curve which describe the deformed equilibrium configuration of the chain.

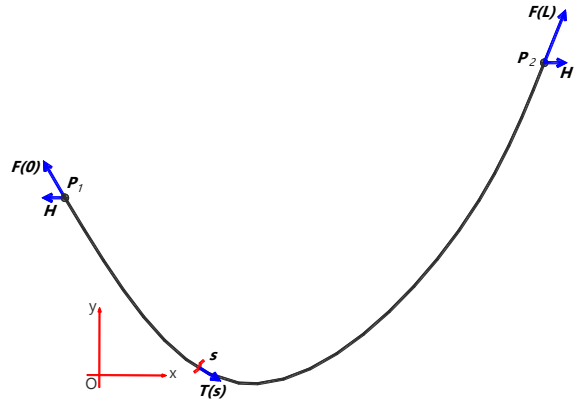

Fig. C.1 – The deformed configuration of a chain simple supported at its two end points.

Let $s \in [0, L]$ be the curvilinear abscissa, $\mu = \mu(s)$ the mass per unit length, and $\boldsymbol{g} = (0, -g)$ the acceleration of gravity. Furthermore, one supposes that the elastic deformation can be neglected and the chain is homogenous (i.e. μ is constant and independent of the particular deformed shape.).

Since the chain is at rest, also its part between $\boldsymbol{P}_1$ and the section $\boldsymbol{S}$ is in equilibrium: the resultant of the acting forces must be zero, namely:

$$\boldsymbol{0} = \boldsymbol{F}(0) + \int_0^s \boldsymbol{g}\, \mu(s) ds + \boldsymbol{T}(s)\,. \tag{C.1}$$

where $\boldsymbol{F}(0)$ indicates the force acting in $\boldsymbol{P}_1$ and $\boldsymbol{T}(s)$ is the internal force at s. Since $\boldsymbol{g}$, $\mu(s)$ and $\boldsymbol{F}(0)$ are constant, deriving the previous vectorial equation with respect to s, one obtains:

$$\boldsymbol{g}\, \mu + \frac{d\boldsymbol{T}(s)}{ds} = \boldsymbol{0}\,, \tag{C.2}$$

this is a differential equation whose two components along the x-axis and y-axis are:

$$\left(\boldsymbol{g}\, \mu + \frac{d\boldsymbol{T}(s)}{ds}\right) \cdot \boldsymbol{i} = 0 \;\Rightarrow\; \frac{d\boldsymbol{T}(s)}{ds} \cdot \boldsymbol{i} = 0\,, \tag{C.3}$$

$$\left(\boldsymbol{g}\, \mu + \frac{d\boldsymbol{T}(s)}{ds}\right) \cdot \boldsymbol{j} = 0 \;\Rightarrow\; -g\, \mu + \frac{d\boldsymbol{T}(s)}{ds} \cdot \boldsymbol{j} = 0\,. \tag{C.4}$$

Since $\boldsymbol{T}(s)$ is tangent to the curve $\boldsymbol{\gamma}$, it can be write as:

$$\boldsymbol{T}(s) = T(s)\, \frac{d\boldsymbol{\gamma}(s)}{ds} = T(s)\, \boldsymbol{t}(s)\,, \tag{C.5}$$

and (C.3) and (C.4) can be written as:

$$\frac{d}{ds}\left(T(s)\frac{dx}{ds}\right) = 0\,, \tag{C.6}$$

$$g\, \mu + \frac{d}{ds}\left(T(s)\frac{dy}{ds}\right) = 0\,, \tag{C.7}$$

where $\frac{dx(s)}{ds}$ and $\frac{dy(s)}{ds}$ denote the projections of the tangent vector $\boldsymbol{t}(s)$ on the two coordinate axes. From (C.6), we can derive that the horizontal component of $\boldsymbol{T}(s)$ is constant with respect to s:

$$T(s)\frac{dx}{ds} = const\,, \tag{C.8}$$

From (C.1), by assuming $\boldsymbol{F}(0)\cdot\boldsymbol{i} = H$, (C.6) and (C.7) can be rewritten as:

$$T(s)\frac{dx}{ds} = H\,, \tag{C.9}$$

$$-g\,\mu + \frac{d}{ds}\left(H\frac{dy}{dx}\right) = 0\,, \tag{C.10}$$

and recalling that

$$ds = \sqrt{1+\left(\frac{dy}{dx}\right)^2}\,dx\,, \tag{C.11}$$

(C.9) and (C.10) can be combined as:

$$H\frac{d^2y}{dx^2} = g\,\mu\sqrt{1+\left(\frac{dy}{dx}\right)^2}\,. \tag{C.12}$$

This is the ordinary differential equation governing the problem, whose integral is expressed by:

$$y(x) = \frac{H}{g\,\mu}cosh\left(\frac{g\,\mu}{H}x + c_1\right) + c_2\,, \tag{C.13}$$

where H is the horizontal component of the internal traction and c_1 and c_2 are the two constants of integration depending on the position of the two end-points of the chain. The length of the chain is fixed and can be expressed as:

$$L = \int_{\boldsymbol{P}_1}^{\boldsymbol{P}_2} ds = \int_{\boldsymbol{P}_1}^{\boldsymbol{P}_2}\sqrt{1+\left(\frac{dy}{dx}\right)^2}\,dx\,. \tag{C.14}$$

By equation (C.14) the horizontal component H can be determined.

Remark 1|C. The problem of the catenary can be formulated as a problem of calculus of variations, i.e. as an isoperimetric problem since the length of the chain has to be constant. The chain of length L, simply supported at the two end points $\boldsymbol{P}_1$ and $\boldsymbol{P}_2$, has mass per unit length $\mu = \mu(s)$. In an equilibrated configuration, the total mechanical energy, being the kinetic energy equals to

zero, coincides with the potential energy and achieves there a minimum. By using (C.11), the potential energy can be written as:

$$E(y) = \int_{P_1}^{P_2} \mu g\, y(s) ds = \int_{P_1}^{P_2} \mu g\, y(x) \sqrt{1 + \left(\frac{dy}{dx}\right)^2}\, dx\,, \tag{C.15}$$

and the length of the chain as:

$$L = \int_{P_1}^{P_2} ds = \int_{P_1}^{P_2} \sqrt{1 + \left(\frac{dy}{dx}\right)^2}\, dx\,. \tag{C.16}$$

Definitely, the catenary can be regarded as a curve $\boldsymbol{\gamma}(s) = \big(x, y(x)\big)$ where $y(x) \in \mathrm{C}^1[a,b]$ minimizes the functional $E(y)$ under the condition (C.16). ■

■ C.2 THE CATENARY AND THE ARCH: THE LINE OF THRUST

It is well-known the parallelism between the catenary and the line of thrust (see **Section 6.2**). Since the acting loads (including the self-weight) are fixed and do not depend on the final configuration, the differential equation which governs the shape of the thrust line derived from (C.12) and is:

$$\frac{d^2y}{dx^2} = -\frac{q(x)}{H}, \tag{C.17}$$

where $q(x)$ represents the value of the external load including the self-weight. If we consider only the self-weight, it should be noted that $q(x)$ can assume different profiles depending on how the load is transferred to the line of thrust. In **Fig. C1**, with regard to a round arch, two qualitative distributions of the self-weigh are reported: in **Fig. C1a** the load is transmitted vertically whilst in **Fig. C1b** radially.

Anyhow, even if these two distribution are different, the results using them are close to each other. Indeed, in **Fig. C2** we report the representations (for a round arch with internal radius equals to 1.00m and a thickness equals to 0.25m) deriving from these two partition of the domain

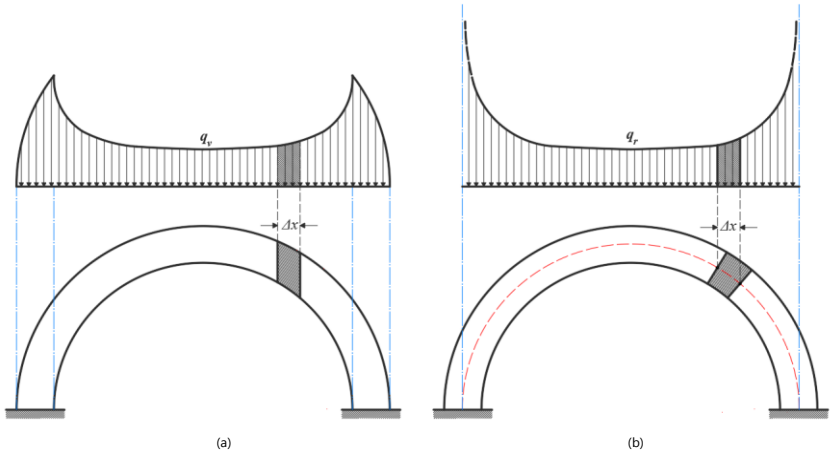

Fig. C.1 - Two qualitative distributions of the self-weigh are reported: one (a) is related to vertical cuts and the other (b) to radial ones.

The value of the resultant (**Fig. C2a**) in these two cases are very close. Also the value of the loads are similar, in particular are practically the same on the central part of the arch, and they differ only near the springings (**Fig. C2b**). Anyhow, as it possible to see from many figures reported in the **Chapter. 6**, the hinges form often in the central part of the arch, and in these sense the choose of a partition rather than the other one conducts to small errors.

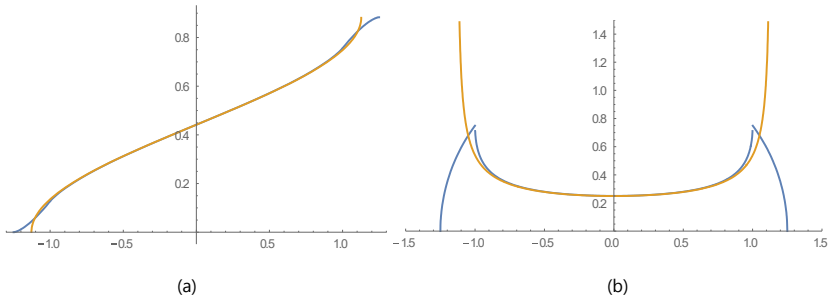

Fig. C.2 - The resultant (a) of the self-weight (valued starting from the left-hand side) and the self -weight distribution (b) deriving from the two different partition of the domain for a round arch (internal radius r=1.00m and a thickness s=0.25m) are reported

Finally, for this reason it is noticed that also the use of a constant distribution of the self-weight is currently practice (**Fig. C3**, thick red line) and consequently the line of thrust can be interpreted as a parabola ($q(x)$ constant).

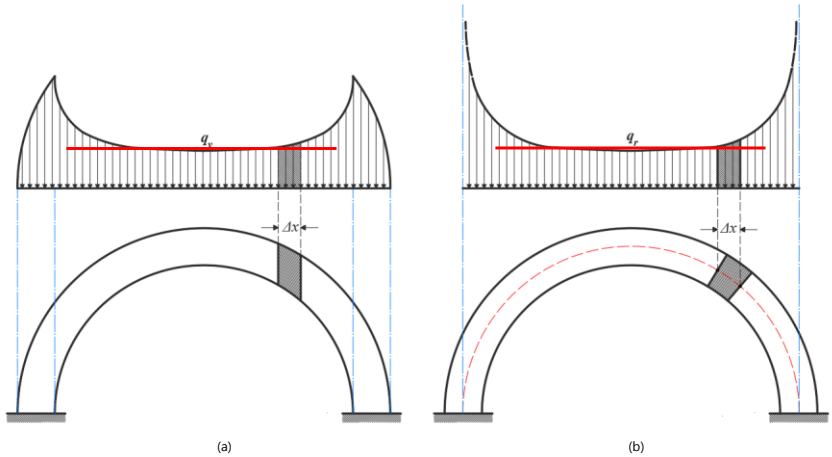

Fig. C.3 - Considering the self-weight constant implies that the thrust is a parabola since $q(x)$ is constant: the error made is usually small.

Appendix D

COUPLET'S PROBLEM

■ D.1 COUPLET'S PROBLEM

Suppose we consider an arch with a fixed internal radius *r* and imagine a decreasing process of the thickness s, what is the minimum thickness for which the arch is yet safe under only its own weight?

This is a well-known problem, known as the minimum thickness problem or, since Couplet was the first who posed this question, it is also known as the Couplet's (see **Section 6.2**).

What happens when the minimum thickness is reached? From **Fig. D.1**, when the thickness reaches its minimum value, the line of thrust touches the arch geometry in 5 five points (**Fig. D.1a**) and the arch becomes a mechanism (**Fig. D.1b**).

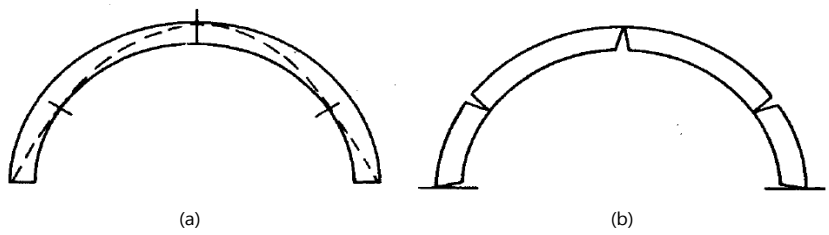

Fig. D.1 – Drawing from (Heyman, 1995): the hinges formed (b) and the associated thrust line (a).

This condition represents a limit equilibrium state: the line of thrust passes through the hinges of the corresponding mechanism. If only the self-weight is considered,

the solution depends only by a geometrical factor, e.g. r, and usually is given using the relative number s/r.

The mechanism associated with the solution of the Couplet's problem ($\beta = 0$) is shown in **Fig. D.2**. It involves four rigid bodies, and since the kinematism is symmetric, the only variables are the angle θ_2 (defining the position of hinges C_{12} and C_{34}, see **Fig. D.2**) and the thickness s. Couplet evaluated the solution fixing a priori the position of the intrados hinge C_{12} (i.e. $\theta_2 = 45°$). He found a relation between the thickness s and the mean radius R_m, i.e. $s/R_m = 0.101$.

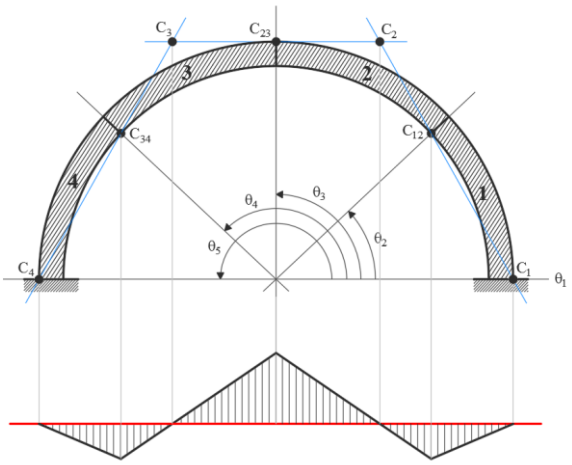

Fig. D.2 - The mechanism corresponding to the solution of Couplet's problem for a round arch ($\beta = 0$) involves four rigid bodies hinged in five points.

Almost two centuries later, Heyman (1969)solved the problem for a round arch considering a partition of the domain made by vertical cuts, and successively the solution was recalculated by Ochsendorf (2006) with a different partition of the domain (sector of annulus, see also **Remark 1|6** and **Section 6.5**). The minimum thickness, for a round arch with regard the internal radius *r*, is:

$$\frac{s}{r} = 0.114 \quad \rightarrow \quad \text{Ochsendorf (2006)} \ [radial\ cuts]\,,$$

$$\frac{s}{r} = 0.112 \quad \rightarrow \quad \text{Heyman (1969)} \ [vertical\ cuts]\,.$$

The exact intrados position of hinge C_{12} is at 31° rather than at 45° (Couplet, 1730), anyhow the analysis is not sensitive to the position of this hinge, since varying the hinge angle, the correct value of s/R_m differs little.

■ D.2 MINIMUM THICKNESS: ANALYTICAL SOLUTION

In this section, we develop an analytical procedure in order to solve the problem of the minimum thickness with reference to a generic circular arch (see **Fig. D.3**), whose geometry is defined by the internal radius r, the thickness s and the springing angle β (i.e. the total angle of embrace is $\pi - 2\beta$).

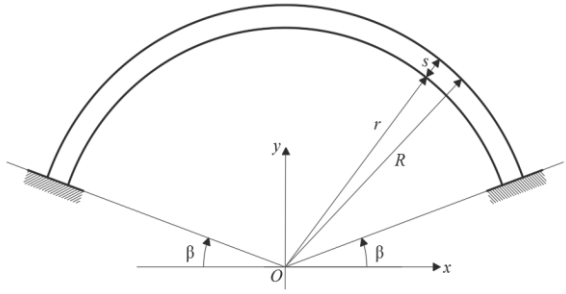

Fig. D.3 - The circular arch with a springing angle β is shown. For $\beta = 0$, it turns a rounded arch.

The circular arch is partitioned through radial cuts. Fixing a generic mechanism (see **Fig. D.4**), we evaluate the analytical expression of the virtual work made by the external forces (i.e. self-weight).

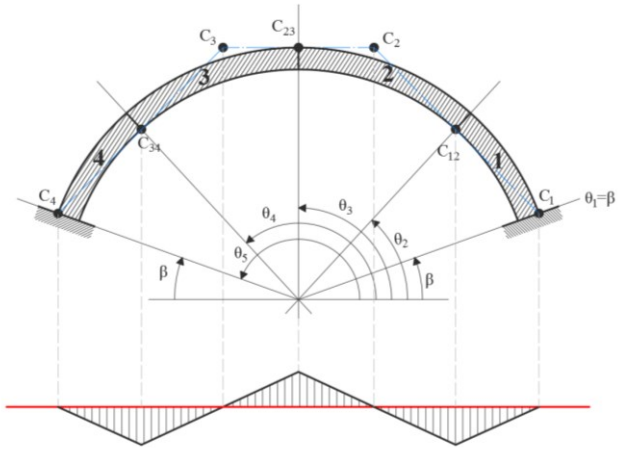

Fig. D.4 - The generic mechanism, for a depressed arch. The hinges formed divide the arch into four rigid blocks identified by the angles ϑ_i with $i \in \{1, \dots, 5\}$.

Then, we find the values of the variables for which the virtual work is zero, and finally, between them we select both the value of the minimum thickness and the positions of the hinges.

Remark 1|D. We use the polar transformation to characterize the geometric proprieties of the four rigid sectors of annulus. In particular, the polar transformation is a diffeomorphism from $\mathbb{R}^2$ to $\mathbb{R}^2$, defined as:

$$\boldsymbol{\varphi}: (\rho,\theta) \in [0,2\pi[\times]0,+\infty[\rightarrow \big(x_0 + \rho\, cos(\theta), y_0 + \rho\, sin(\theta)\big), \tag{D.1}$$

where $(x_0, y_0) = \boldsymbol{p}_0$ is the pole of the transformation (in our case $(0,0) = \boldsymbol{p}_0$). Using this function, we can express all the geometrical measures of the arch as functions of the polar coordinates of the hinges.

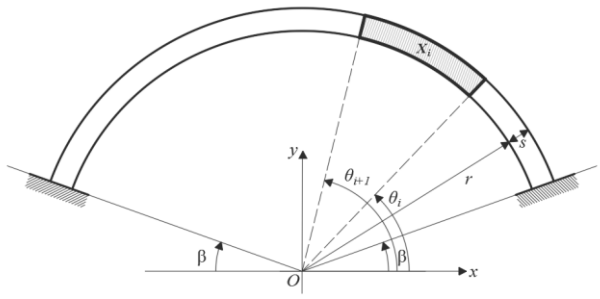

Fig. D.5 - The depressed arch is partitioned through radial cuts, and then the polar transformation is used to calculate the geometric proprieties of a generic sector of annulus X_i.

With reference to the **Fig. D.5**, let X_i the domain occupied by the rigid block i and coinciding with the sector of annulus between θ_i and θ_{i+1}: it corresponds to the domain Ω_i of the polar plane individuated by the set:

$$\Omega_i = [\theta_i, \theta_{i+1}] \times [r, r+s]\,. \tag{D.2}$$

Since, in our case, the pole is $\boldsymbol{p}_0 = (0,0)$ and recalling that the Jacobian of $\boldsymbol{\varphi}$ is constant and results $J(\boldsymbol{\varphi}) = \rho$, it is possible to evaluate the area $\boldsymbol{A}(i)$ and the coordinates of the centroid $\boldsymbol{G}(i) = \big(x_G(i), y_G(i)\big)$ of the rigid block i as:

$$A(i) := \iint_{X_i} dxdy = \iint_{\Omega_i} \rho\, d\rho d\theta\,, \tag{D.3}$$

$$\boldsymbol{G}(i) := \frac{\iint_{X_i}(x,y)dxdy}{\iint_{X_i} dxdy} = \frac{\iint_{\Omega_i} \rho\big(\rho\cos(\theta), \rho\sin(\theta)\big)\, d\rho d\theta}{\iint_{\Omega_i} \rho\, d\rho d\theta}, \tag{D.4}$$

and by using (D.1), it results:

$$A(i) := \frac{1}{2} s\,(2r+s)(\theta_{i+1} - \theta_i)\,, \tag{D.5}$$

$$\boldsymbol{G}(i) := \tfrac{2\,(3r^2+3rs+s^2)}{3(2r+s)(\theta_i - \theta_{i+1})} \cdot \big(\sin(\theta_i) - \sin(\theta_{i+1})\,, \cos(\theta_{i+1}) - \cos(\theta_i)\big)\,. \tag{D.6}$$

Since the problem is symmetric, it results $\vartheta_4 = \pi - \vartheta_2$ and:

$$\vartheta_1 = \beta \ , \ \vartheta_3 = \frac{\pi}{2} \ , \ \vartheta_5 = \pi - \beta \ . \tag{D.7}$$

Since the unknowns of the problem are (θ_2, s, β, r), by solving analytically the kinematical problem and by using expressions (D.5) and (D.6), the virtual work of the external forces can be expressed as:

$$L(\theta_2, s, \beta, r) = -\frac{A_r + B_r}{C_r}, \tag{D.8}$$

where:

- $A_r = 3s(r+s)(2r+s)(\pi - 2\beta)\cos(\beta)\big(r + s - r\sin(\theta_2)\big)$;
- $B_r = s(\sin(\beta) - 1)\big(3r(r+s)(2r+s)(\pi - 2\theta_2)\cos(\theta_2) + 4s(3r^2 + 3rs + s^2)\sin(\theta_2)\big)$
- $C_r = 6\big(r + s - r\sin(\theta_2)\big)$.

For $r = 1$, the virtual work can be particularized in:

$$L(\theta_2, s, \beta) = -\frac{A + B}{C}, \tag{D.9}$$

with

- $- A = 3s(1+s)(2+s)(\pi - 2\beta)\cos(\beta)\big(1 + s - \sin(\theta_2)\big)$;
- $B = s(\sin(\beta) - 1)\big(3(1+s)(2+s)(\pi - 2\theta_2)\cos(\theta_2) + 4s(3 + s(3+s))\sin(\theta_2)\big)$;
- $C = 6\big(1 + s - \sin(\theta_2)\big)$.

The minimum thickness s_{min} of a depressed arch with a given springing angle $\bar{\beta}$ is:

$$s_{min} = \max\big\{s \in \mathbb{R} \mid L\big(\theta_2, s(\theta_2), \bar{\beta}\big) = 0\big\} . \tag{D.10}$$

In **Fig. D.6** and in **Tab. D.1** the minimum thickness (expressed through the ratio s_{min}/r), the angle θ_2 and the angle $\theta_2 - \beta$ as funciotns of β are reported.

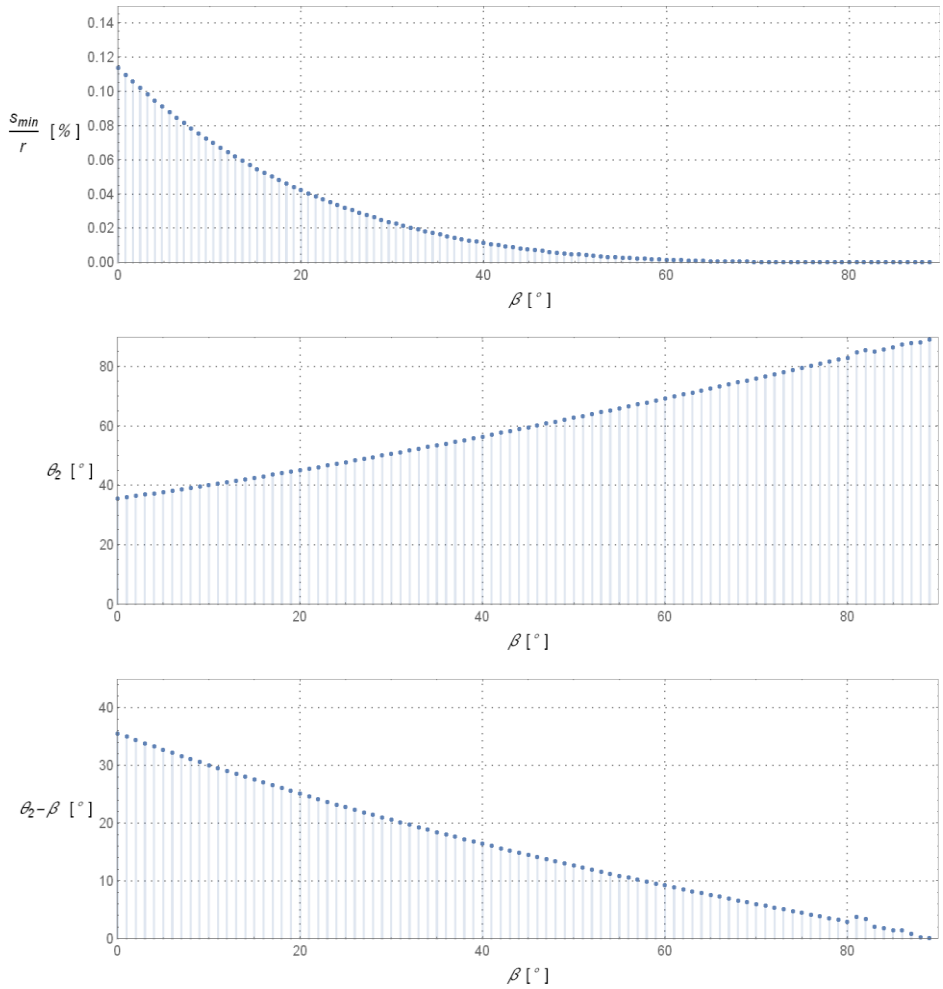

Fig. D.6 - The minimum thickness through the ratio s_{min}/r , the angle θ_2 and the angle $\theta_2 - \beta$ as functions of β are reported.

The minimum thickness decreases with β, and it reaches very small values for β greater than 60°:increasing the springing angle the imaginary line joining the centroids of each voussoir becomes closer to the thrust line.

β [°]	s_{min}/r	θ_2 [°]	$\theta_2 - \beta$ [°]
0.00	0.1135818	35.52	35.52
5.00	0.0903698	37.71	32.71
10.00	0.0710907	40.04	30.04
15.00	0.0551706	42.50	27.50
20.00	0.0421305	45.07	25.07
25.00	0.0315624	47.75	22.75
30.00	0.0231130	50.54	20.54
35.00	0.0164709	53.43	18.43
40.00	0.0113582	56.41	16.41
45.00	0.0075243	59.49	14.49
50.00	0.0047419	62.64	12.64
55.00	0.0028047	65.88	10.88
60.00	0.0015265	69.19	9.19
65.00	0.0007416	72.56	7.56
70.00	0.0003057	75.98	5.98
75.00	0.0000972	79.45	4.45
80.00	0.0000193	82.94	2.94
85.00	0.0000012	86.47	1.47

Tab. D.1 - The minimum thickness s_{min}/r , the angle θ_2 and the angle $\theta_2 - \beta$ as functions of β are reported

Remark 2|D. It is possible to define a safe factor due to the self-weight as the ratio between the thickness of the real arch and the relative s_{min}, e.g. considering an arch with $\beta = 60°$ and a thickens $s = 0.10m$, the minimal thickness to have a collapse under the self-weight results $s_{min} = 0{,}0015$m (see **Tab. D.1**) and so the safe factor is 65.5.

Remark 3|D. This result holds even in the case of other external loads having a distribution similar to that of the self-weight.

Remark 4|D. Let us imagine that under a certain distribution of loads the arch is stable but close to its limit state. If these external loads increase proportionally the internal equilibrated thrust line does not change and the collapse will not occur, even if the load multiplier is very high (the collapse will be governed by the compressive stresses and the arch could collapse only for crushing). However, if there will be some little changes into the distribution of external forces the arch could collapse instantly.

■ D.3 MINIMUM THICKNESS: ANALYTICAL SOLUTION FOR A ROUND ARCH

In this section, we particularize the previous analytical procedure with reference to a round arch ($\beta = 0$) with internal radius r and thickness s (**Fig. D.7**). The strategy to search the minimum thickness will be explained more accurately.

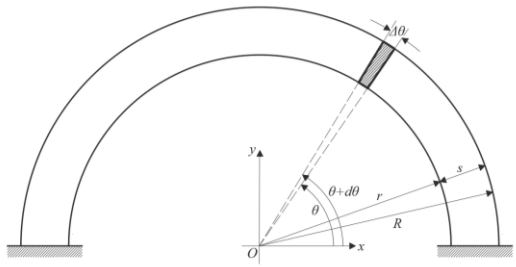

Fig. D.7 - A circular arch with radial cuts.

When s reaches its minimum value, the arch becomes a mechanism: four symmetric rigid bodies hinged in five symmetric points (**Fig. D.8**).

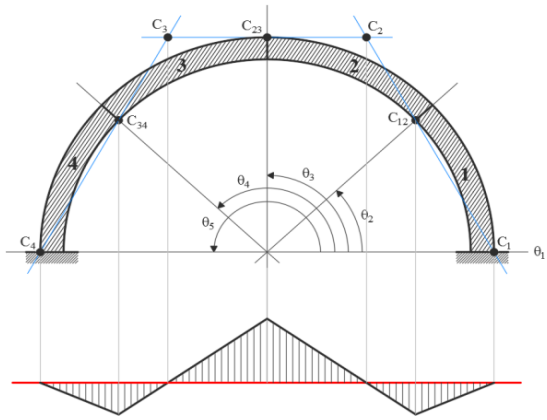

Fig. D.8 - The mechanism associated with the solution of the Couplet's problem for a round arch.

The four rigid bodies are identified by the angles ϑ_i with $i \in \{1, \ldots, 5\}$ (see **Fig. D.8**). Since the mechanism is symmetric the hinges C_1 and C_2 are located at the base of the arch on the extrados, whilst the hinge C_{23} on the extrados of the key. We fix the position of these hinges as:

$$\vartheta_1 = 0 \ , \ \vartheta_3 = \frac{\pi}{2} \ , \ \vartheta_5 = \pi \ . \tag{D.11}$$

The remaining two hinges (C_{12}, C_{34}) appear on the intrados and are identified by the angle ϑ_2. With reference to the mechanism shown in **Fig. D.8**, the infinitesimal displacements $(U_G(i), V_G(i), \Phi_G)$ of the centroid of each annulus (block) can be obtained as function of the rotation of, e.g., the block 4, namely:

$$\Phi_G(4) = -\phi, \tag{D.11}$$

and the mechanism is described by the following parameters:

- $\Phi_G(1) = \phi$
- $U_G(1) = -y_G(1)\,\phi$
- $V_G(1) = -\big(r + s - x_G(1)\big)\,\phi$
- $\Phi_G(2) = -\dfrac{r\,sin(\theta_2)}{r + s - r\,sin(\theta_2)}\phi$
- $U_G(2) = -\dfrac{r\,sin(\theta_2)\,\big(r + s - y_G(2)\big)}{r + s - r\,sin(\theta_2)}\phi$
- $V_G(2) = \dfrac{(-(r+s)^2 + r(r+s)\big(cos(\theta_2) + sin(\theta_2)\big) - r\,sin(\theta_2)x_G(2)\big)}{r + s - r\,sin(\theta_2)}\phi$
- $\Phi_G(3) = \dfrac{r\,sin(\theta_2)}{r + s - r\,sin(\theta_2)}\phi$
- $U_G(3) = \dfrac{r\,sin(\theta_2)\big(r + s - y_G(3)\big)}{r + s - r\,sin(\theta_2)}\phi$
- $V_G(3) = \dfrac{-(r+s)^2 + r(r+s)\,cos(\theta_2) + r\,sin(\theta_2)\,\big(r + s + x_G(3)\big)}{r + s - r\,sin(\theta_2)}\phi$
- $\Phi_G(4) = -\phi$
- $U_G(4) = y_G(4)\phi$
- $V_G(4) = -\big(r + s + x_G(4)\big)\phi$

where $\big(x_G(i), y_G(i)\big)$ represents the unknown position of the centre of gravity of the block i. The virtual work of the external forces is symbolically expressed as follows:

$$L(\theta_2, s) = \sum_{i=1}^{4} A(i) \cdot V_G(i)\,, \tag{D.12}$$

and expressing the unknown area of each block through equation (D.5) and the unknown position of each gravity centre $\big(x_G(i), y_G(i)\big)$ through (D.6), (D.12) becomes:

$$L(\theta_2, s) = \frac{-3s(1+s)(2+s)\big(\pi\big(1+s-cos(\theta_2)\big)+2\theta_2 cos(\theta_2)\big)+s\big(3\pi(2+3s+s^2)+4s\big(3+s(3+s)\big)\big)sin(\theta_2)}{6\big(1+s-sin(\theta_2)\big)}. \tag{D.13}$$

In **Fig. D.9** the function $L(\theta_2, s)$ for $(\theta_2, s) \in [0,2\pi] \times [0,0.30]$ is reported.

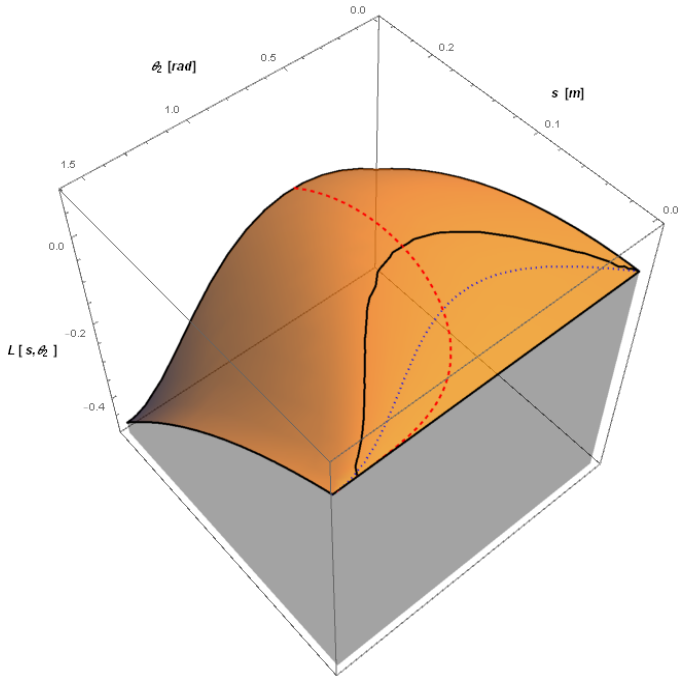

Fig. D.9 - A 3d plot of the virtual work $L(\theta_2, s)$ is reported. The thick black line represents the line on which $L(\theta_2, s) = 0$. The dashed red line is the projection on the surface of the points (θ_2, s) such that $\frac{\partial L(\theta_2, s)}{\partial \theta_2} = 0$ whilst the dotted one of the points where $\frac{\partial L(\theta_2, s)}{\partial \theta_2} = 0$.

It should be noted that the geometric location of the points such that $L(\theta_2, s) = 0$, namely the set:

$$\gamma = \{(\theta_2, s) \in \mathbb{R}^2 \mid L(\theta_2, s) = 0\}, \tag{D.13}$$

constitutes a curve (**Fig. D.10**). The minimum thickness of the arch corresponds to the maximum value of s reached in the following set:

$$s_{min} = \max\{s \in \mathbb{R} \mid L(\theta_2, s(\theta_2) = 0)\}. \tag{D.14}$$

The solution for a round arch is:

$$s_{min} = 0.113582\text{m} \ , \ \theta_2 = 0.61987\text{rad} \ , \tag{D.15}$$

which corresponds exactly to that obtained by Ochsendorf (2006).

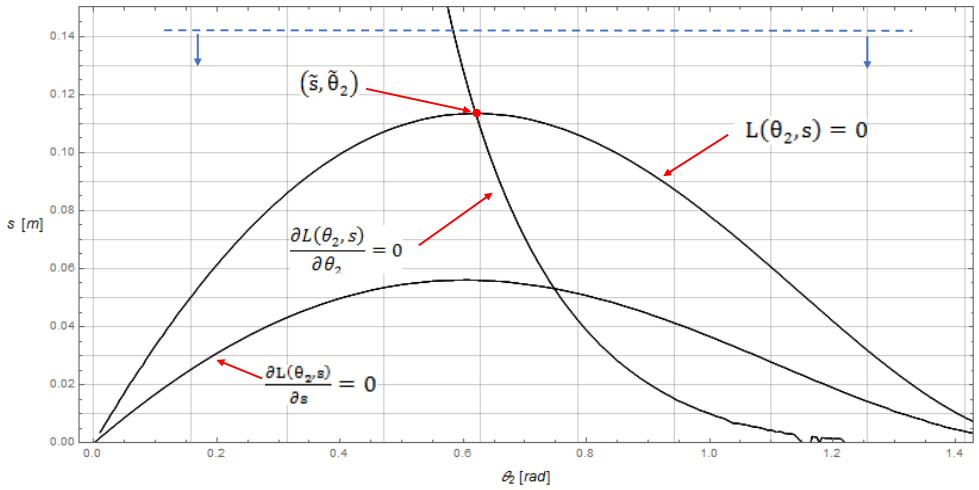

Fig. D.10 - The decreasing imaginary process of the thickness is represented by the downward movement of the blue dashed line. When this line touches the curve γ, the arch is in critical situation, in which the thrust line becomes tangent to the geometry in five points and the arch becomes a mechanism. In this sense the minimal thickness s_{min} is represented by the maximum value of s in the set $L(\theta_2, s(\theta_2)) = 0$.

Remark 5|D. Let s_{min} be the minimum thickness (that is the maximum of s in γ) and $\tilde{\theta}_2$ the associated angle, since results

$$\left.\frac{\partial L(\theta_2, s)}{\partial s}\right|_{(\tilde{s}, \tilde{\theta}_2)} \neq 0 \,,$$

applying the Dini's theorem, it is possible express locally s as a function of θ_2, namely $s = s(\theta_2)$ (depicted in **Fig. D.10**). While examining **Fig. D.10**, the numerical solution for the minimum thickness is stable varying θ_2.

Appendix E

ARCH UNDER HORIZONTAL ACTIONS

Prologue. In this section, we present an analytical evaluation of the horizontal collapse multiplier for a circular arch with a generic springing angle. In the last part of the section, we specialize this analysis with reference to the arch tested at the DIST laboratory (Department of Structures for Engineering and Architecture, University of Naples Federico II).

■ E.1 ANALYTICAL SOLUTION

In this section, we propose the analytical study of a circular arch subjected to horizontal forces (i.e. a seismic action). The circular arch is loaded by horizontal actions, as those produced by a seismic action. The only load considered is the self-weight and the horizontal incremental action is represented by forces, proportional to the mass through the scale parameter λ, and acting in centres of gravity of each voussoirs. (**Fig. E.1**).

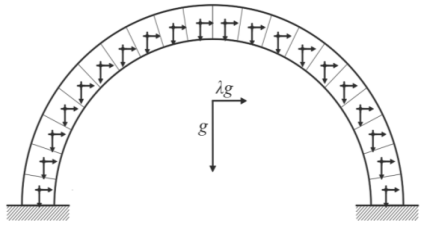

Fig. E.1 - The arch is subjected to vertical and horizontal loads applied to the centroids of each voussoir.

When λ reaches a certain value, say λ_c, four hinges form and the arch becomes a mechanism (**Fig. E.2**) with the moving part of the arch composed by three rigid blocks hinged in four points: a four-bar chain exhibiting a displacement with one degree of freedom. Considering finite displacement, it could be viewed as a well-known mechanism used in mechanical engineering: a four-bar linkage.

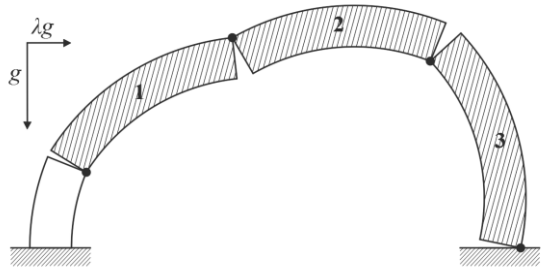

Fig. E.2 - When the scale parameter λ reaches a certain value, the arch becomes a mechanism constituted by three rigid blocks (each of them is a sector of annulus) hinged in four points.

The goal of this analysis is the search of the exact position both of the four hinges and of load multiplier λ_c. The position of the hinges, identified by the angles θ_i for $i \in \{1, \dots, 4\}$, and the value λ are then assumed as unknowns of the problem. Let we fix a generic mechanism as that shown in the **Fig. E.3**.

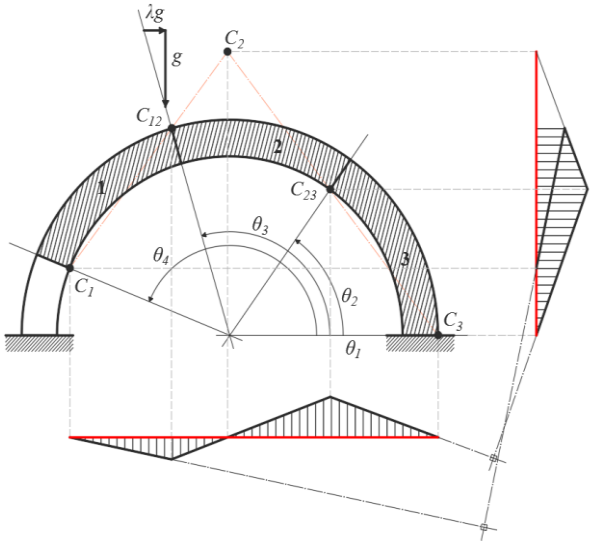

Fig. E.3 - Vertical and horizontal displacements of a generic failure mechanism for a round arch under horizontal forces. The unknowns of the problem are the position of the hinges (i.e. the angle θ_i for $i \in \{1, \dots, 4\}$) and the collapse load multiplier λ_c.

The solution strategy is similar to that used for the minimum thickness problem (see **Appendix D**) but, in this case, the search of the solutions is numerically more complex. Indeed, since the problem is not symmetric and no one a priori information about hinge positions is available, the virtual work of the external forces, as function of the unknowns, is symbolically represented by the following function:

$$L(\theta_1, \theta_2, \theta_3, \theta_4, \lambda) = \sum_{i=1}^{3} A(i) g(1, \lambda) \cdot \left(U_G(i), V_G(i)\right), \tag{E.1}$$

where $A(i)$ is the area measure of the block i and $\left(U_G(i), V_G(i)\right)$ represents the the position of its centroid.

By using (D.5) and (D.6) (see **Appendix D**), it is possible to express analytically the function (E.1). Such expression is very complex and is not reported. We develop a numerical code in order to search the value of the collapse multiplier λ_c in the set of all $(\theta_1, \theta_2, \theta_3, \theta_4, \lambda)$ such that $L(\theta_1, \theta_2, \theta_3, \theta_4, \lambda) = 0$, that is:

$$\lambda_c = \max\{\lambda \in \mathbb{R} \mid L(\theta_1, \theta_2, \theta_3, \theta_4, \lambda) = 0\}. \tag{E.2}$$

With reference to a circular arch with internal radius $r = 1.00m$ and a given springing angle β, below we report the numerical solutions as functions of the thickness s, showing:

- the horizontal collapse multiplier λ_c;
- the position of hinges identified through the values $\theta_1, \theta_2, \theta_3, \theta_4$;
- $\Delta\theta_{12} = \theta_2 - \theta_1$, $\Delta\theta_{23} = \theta_3 - \theta_2$ and $\Delta\theta_{43} = \theta_4 - \theta_3$;
- the ratio $\Delta\theta_{12}/\Delta\theta_{23}$ and $\Delta\theta_{12}/\Delta\theta_{23}$.

The parameter $\Delta\theta_{ij}$ identify the amplitude of the sectors of annulus, whilst $\Delta\theta_{ij}/\Delta\theta_{kl}$ the ratio between the angles identifying two sectors of annulus.

In particular we consider the following values of springing angle: $\beta = 0°$ (**Fig. E.1**) $\beta = 15°$ (**Fig. E.2**), $\beta = 30°$ (**Fig. E.3**), $\beta = 45°$ (**Fig. E.4**) and $\beta = 17.17°$ (**Fig. E.11**).

Remark 1|E. It should be noted that the position of the hinge C_{12} is the intersection between the extrados and the straight line passing through the centre of the arch and having the slope equals to $arctan(\lambda)$ (**Fig. E.3**). Indeed, when there is a horizontal action, the axis of the line of thrust rotates through $arctan(\lambda)$.

Remark 2|E. By observing the diagrams relative to the collapse multiplier λ_c, it should be noted that λ_c is equal to zero when the thickness s corresponds to s_{min} of the Couplet's problem.

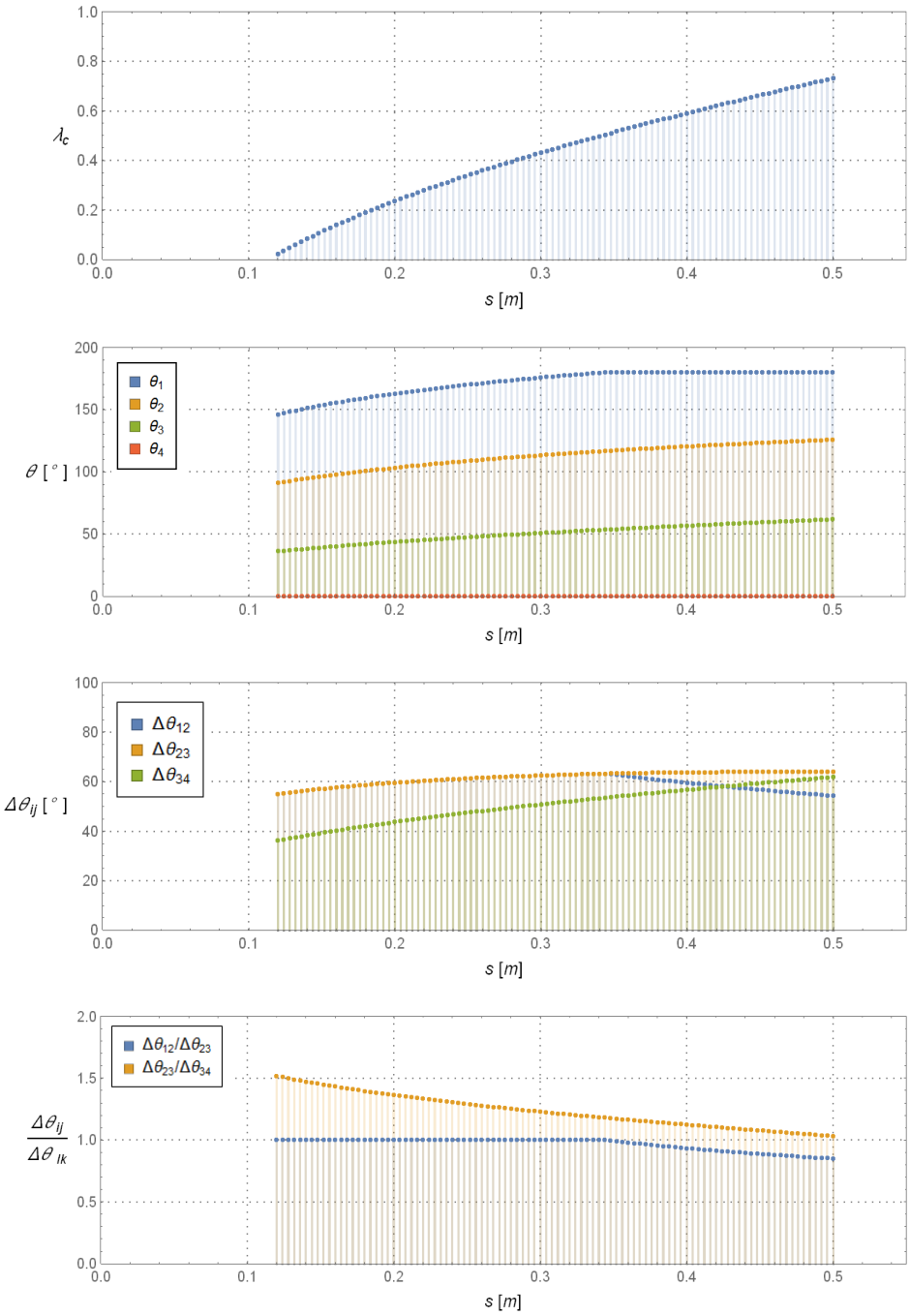

Fig. E.4 - Round arch ($\beta = 0°$) with internal radius $r = 1.00m$: the horizontal collapse multiplier λ_c, the hinge positions (identified by $\theta_1, \theta_2, \theta_3, \theta_4$) and the geometrical characterization of the sectors of annulus (by using $\Delta\theta_{ij}$ and the ratio $\Delta\theta_{ij}/\Delta\theta_{kl}$) are reported.

s [m]	λ_c	θ_4 [°]	θ_3 [°]	θ_2 [°]	θ_1 [°]
0.12	0.022	146.24	91.24	36.23	0.00
0.13	0.053	148.81	93.06	37.30	0.00
0.14	0.083	151.21	94.76	38.32	0.00
0.15	0.112	153.45	96.37	39.30	0.00
0.16	0.139	155.55	97.89	40.24	0.00
0.17	0.164	157.53	99.34	41.15	0.00
0.18	0.189	159.39	100.71	42.02	0.00
0.19	0.213	161.15	102.01	42.87	0.00
0.20	0.236	162.83	103.26	43.69	0.00
0.21	0.258	164.41	104.45	44.49	0.00
0.22	0.279	165.92	105.59	45.26	0.00
0.23	0.300	167.36	106.69	46.02	0.00
0.24	0.320	168.73	107.74	46.75	0.00
0.25	0.340	170.04	108.75	47.47	0.00
0.26	0.359	171.29	109.73	48.17	0.00
0.27	0.377	172.49	110.67	48.86	0.00
0.28	0.396	173.63	111.58	49.53	0.00
0.29	0.413	174.73	112.46	50.19	0.00
0.30	0.431	175.79	113.31	50.83	0.00
0.31	0.448	176.80	114.13	51.46	0.00
0.32	0.465	177.77	114.93	52.09	0.00
0.33	0.481	178.70	115.70	52.70	0.00
0.34	0.497	179.60	116.45	53.30	0.00
0.35	0.513	180.00	117.18	53.89	0.00
0.36	0.529	180.00	117.88	54.47	0.00
0.37	0.545	180.00	118.55	55.04	0.00
0.38	0.560	180.00	119.21	55.60	0.00
0.39	0.575	180.00	119.84	56.16	0.00
0.40	0.590	180.00	120.46	56.71	0.00
0.41	0.605	180.00	121.05	57.25	0.00
0.42	0.620	180.00	121.63	57.78	0.00
0.43	0.634	180.00	122.19	58.31	0.00
0.44	0.649	180.00	122.74	58.83	0.00
0.45	0.663	180.00	123.27	59.35	0.00
0.46	0.677	180.00	123.78	59.86	0.00
0.47	0.691	180.00	124.29	60.37	0.00
0.48	0.705	180.00	124.78	60.87	0.00
0.49	0.718	180.00	125.25	61.37	0.00
0.50	0.732	180.00	125.72	61.86	0.00

Tab. E.1 - The horizontal collapse multiplier λ_c and the hinges position (identified by $\theta_1, \theta_2, \theta_3, \theta_4$) expressed as functions of the thickness s are reported with reference to a round arch (i.e. $\beta = 0°$) with internal radius $r = 1.00m$.

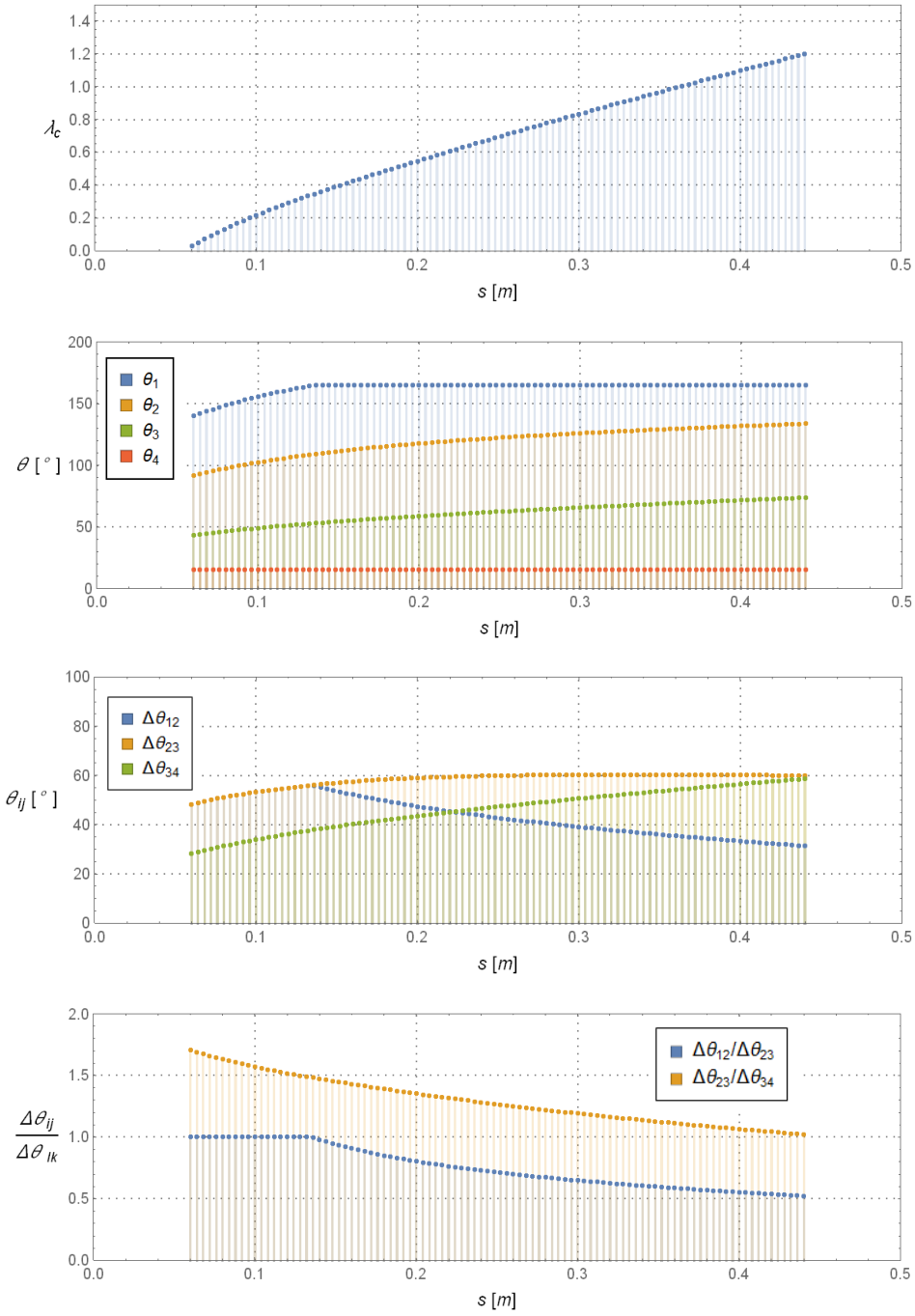

Fig. E.5 - Circular arch with $\beta = 15°$ and internal radius $r = 1.00m$: the horizontal collapse multiplier λ_c, the hinge positions (identified by $\theta_1, \theta_2, \theta_3, \theta_4$) and the geometrical characterization of the sectors of annulus (by using $\Delta\theta_{ij}$ and the ratio $\Delta\theta_{ij}/\Delta\theta_{kl}$) are reported.

s [m]	λ_c	θ_4 [°]	θ_3 [°]	θ_2 [°]	θ_1 [°]
0.06	0.028	139.93	91.62	43.31	15.00
0.07	0.082	144.49	94.69	44.88	15.00
0.08	0.130	148.53	97.43	46.33	15.00
0.09	0.175	152.16	99.91	47.67	15.00
0.10	0.216	155.45	102.19	48.92	15.00
0.11	0.255	158.46	104.29	50.11	15.00
0.12	0.291	161.24	106.24	51.23	15.00
0.13	0.326	163.81	108.06	52.30	15.00
0.14	0.359	165.00	109.76	53.32	15.00
0.15	0.392	165.00	111.32	54.29	15.00
0.16	0.424	165.00	112.77	55.22	15.00
0.17	0.455	165.00	114.10	56.11	15.00
0.18	0.486	165.00	115.34	56.97	15.00
0.19	0.517	165.00	116.50	57.80	15.00
0.20	0.547	165.00	117.59	58.60	15.00
0.21	0.577	165.00	118.61	59.38	15.00
0.22	0.606	165.00	119.58	60.14	15.00
0.23	0.635	165.00	120.50	60.87	15.00
0.24	0.664	165.00	121.37	61.59	15.00
0.25	0.693	165.00	122.20	62.29	15.00
0.26	0.721	165.00	123.00	62.98	15.00
0.27	0.749	165.00	123.76	63.65	15.00
0.28	0.777	165.00	124.49	64.31	15.00
0.29	0.805	165.00	125.20	64.95	15.00
0.30	0.832	165.00	125.88	65.59	15.00
0.31	0.859	165.00	126.54	66.21	15.00
0.32	0.886	165.00	127.17	66.83	15.00
0.33	0.913	165.00	127.79	67.44	15.00
0.34	0.940	165.00	128.39	68.04	15.00
0.35	0.967	165.00	128.98	68.63	15.00
0.36	0.993	165.00	129.54	69.21	15.00
0.37	1.019	165.00	130.10	69.79	15.00
0.38	1.045	165.00	130.64	70.36	15.00
0.39	1.071	165.00	131.16	70.93	15.00
0.40	1.097	165.00	131.68	71.49	15.00
0.41	1.123	165.00	132.18	72.05	15.00
0.42	1.148	165.00	132.68	72.60	15.00
0.43	1.174	165.00	133.16	73.15	15.00
0.44	1.199	165.00	133.64	73.69	15.00

Tab. E.2 - The horizontal collapse multiplier λ_c and the hinges position (identified by $\theta_1, \theta_2, \theta_3, \theta_4$) expressed as functions of the thickness s are reported with reference to a circular arch with $\beta = 15°$ and internal radius $r = 1.00m$.

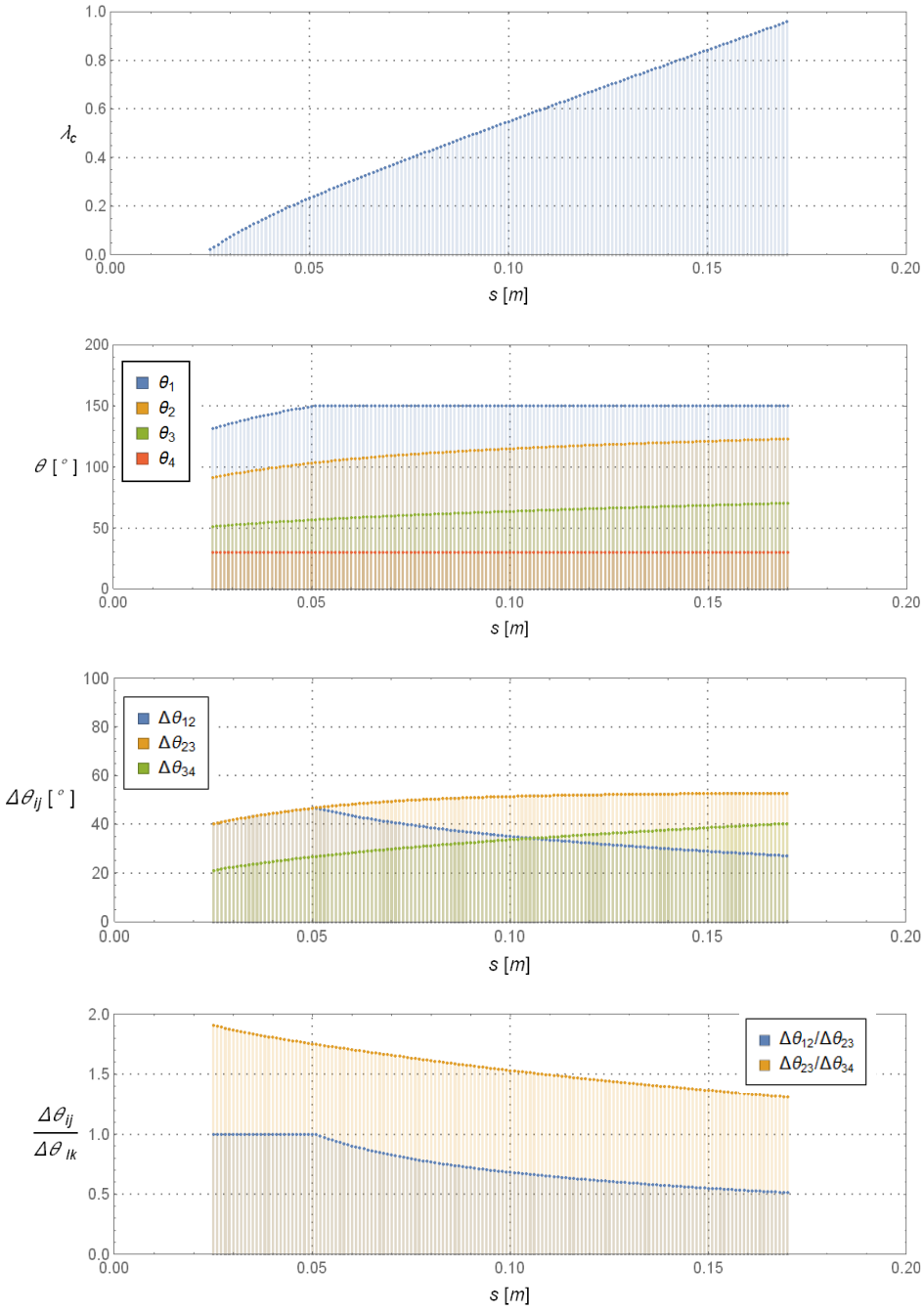

Fig. E.6 - Circular arch with $\beta = 30°$ and internal radius $r = 1.00m$: the horizontal collapse multiplier λ_c, the hinge positions (identified by $\theta_1, \theta_2, \theta_3, \theta_4$) and the geometrical characterization of the sectors of annulus (by using $\Delta\theta_{ij}$ and the ratio $\Delta\theta_{ij}/\Delta\theta_{kl}$) are reported.

s [m]	λ_c	θ_4 [°]	θ_3 [°]	θ_2 [°]	θ_1 [°]
0.025	0.021	131.37	91.22	51.07	30.00
0.030	0.073	135.94	94.16	52.37	30.00
0.035	0.118	139.95	96.75	53.55	30.00
0.040	0.160	143.52	99.07	54.63	30.00
0.045	0.198	146.74	101.19	55.64	30.00
0.050	0.233	149.69	103.14	56.58	30.00
0.055	0.267	150.00	104.91	57.46	30.00
0.060	0.300	150.00	106.49	58.29	30.00
0.065	0.333	150.00	107.90	59.07	30.00
0.070	0.365	150.00	109.19	59.81	30.00
0.075	0.396	150.00	110.35	60.51	30.00
0.080	0.427	150.00	111.42	61.17	30.00
0.085	0.458	150.00	112.41	61.81	30.00
0.090	0.488	150.00	113.32	62.43	30.00
0.095	0.519	150.00	114.17	63.02	30.00
0.100	0.549	150.00	114.97	63.59	30.00
0.105	0.578	150.00	115.72	64.14	30.00
0.110	0.608	150.00	116.43	64.68	30.00
0.115	0.638	150.00	117.10	65.20	30.00
0.120	0.667	150.00	117.75	65.71	30.00
0.125	0.697	150.00	118.36	66.21	30.00
0.130	0.726	150.00	118.95	66.69	30.00
0.135	0.755	150.00	119.51	67.17	30.00
0.140	0.784	150.00	120.06	67.63	30.00
0.145	0.814	150.00	120.58	68.09	30.00
0.150	0.843	150.00	121.09	68.54	30.00
0.155	0.872	150.00	121.59	68.98	30.00
0.160	0.901	150.00	122.07	69.42	30.00
0.165	0.930	150.00	122.54	69.85	30.00
0.170	0.959	150.00	122.99	70.27	30.00

Tab. E.3 - The horizontal collapse multiplier λ_c and the hinges position (identified by $\theta_1, \theta_2, \theta_3, \theta_4$) expressed as functions of the thickness s are reported with reference to a circular arch with $\beta = 30°$ and internal radius $r = 1.00m$.

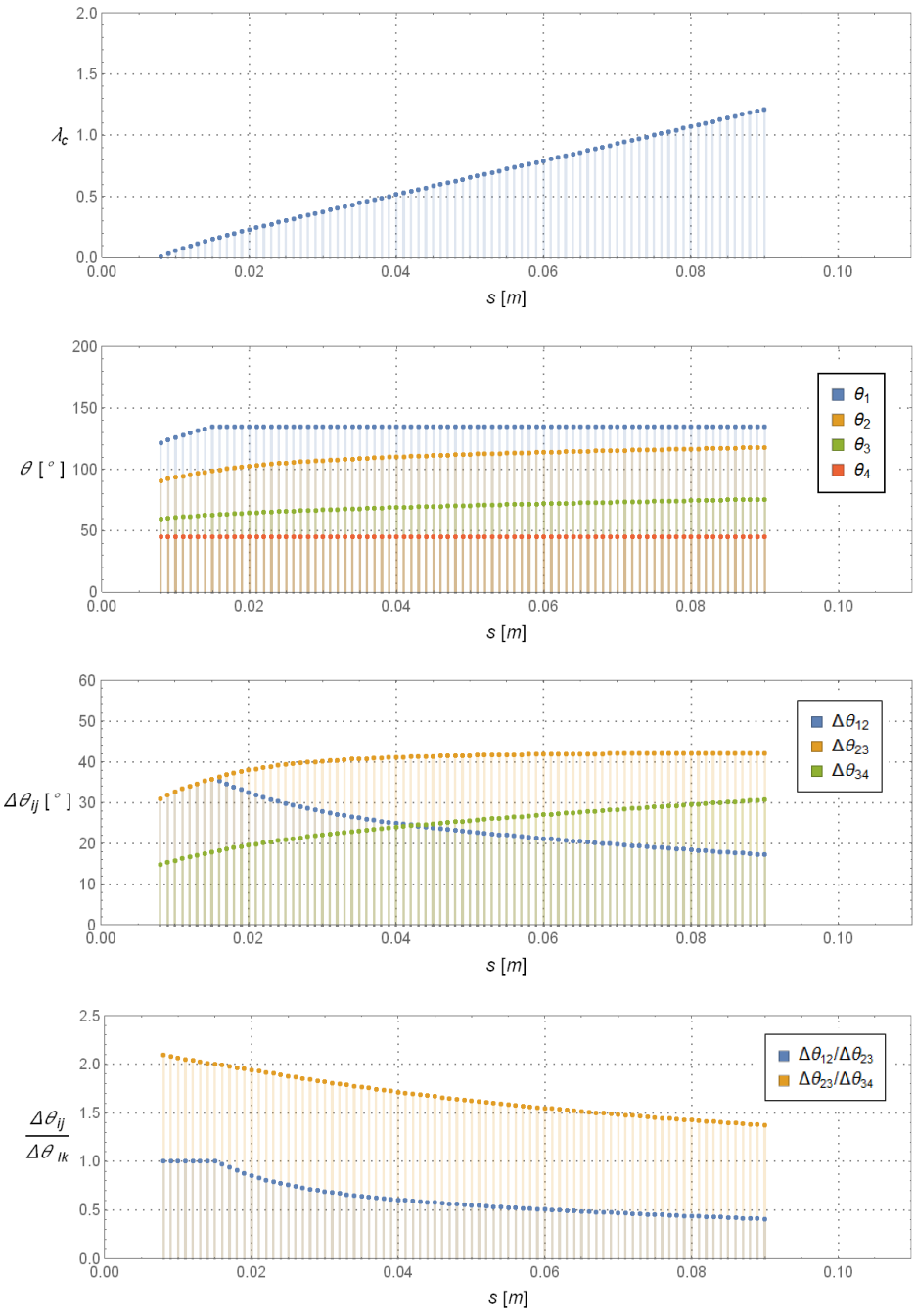

Fig. E.7 - Circular arch with $\beta = 45°$ and internal radius $r = 1.00m$: the horizontal collapse multiplier λ_c, the hinge positions (identified by $\theta_1, \theta_2, \theta_3, \theta_4$) and the geometrical characterization of the sectors of annulus (by using $\Delta\theta_{ij}$ and the ratio $\Delta\theta_{ij}/\Delta\theta_{kl}$) are reported.

s [m]	λ_c	θ_4 [°]	θ_3 [°]	θ_2 [°]	θ_1 [°]
0.008	0.012	121.67	90.71	59.75	45.00
0.010	0.059	126.01	93.40	60.78	45.00
0.012	0.100	129.73	95.71	61.69	45.00
0.014	0.136	133.00	97.75	62.51	45.00
0.016	0.169	135.00	99.59	63.26	45.00
0.018	0.201	135.00	101.17	63.94	45.00
0.020	0.231	135.00	102.53	64.56	45.00
0.022	0.261	135.00	103.71	65.13	45.00
0.024	0.290	135.00	104.74	65.66	45.00
0.026	0.320	135.00	105.65	66.16	45.00
0.028	0.348	135.00	106.47	66.62	45.00
0.030	0.377	135.00	107.20	67.06	45.00
0.032	0.405	135.00	107.87	67.48	45.00
0.034	0.433	135.00	108.48	67.88	45.00
0.036	0.461	135.00	109.05	68.26	45.00
0.038	0.489	135.00	109.57	68.62	45.00
0.040	0.517	135.00	110.06	68.97	45.00
0.042	0.544	135.00	110.52	69.31	45.00
0.044	0.572	135.00	110.95	69.64	45.00
0.046	0.599	135.00	111.36	69.96	45.00
0.048	0.627	135.00	111.76	70.27	45.00
0.050	0.655	135.00	112.13	70.57	45.00
0.052	0.682	135.00	112.49	70.87	45.00
0.054	0.710	135.00	112.84	71.16	45.00
0.056	0.737	135.00	113.17	71.44	45.00
0.058	0.765	135.00	113.49	71.72	45.00
0.060	0.792	135.00	113.81	71.99	45.00
0.062	0.820	135.00	114.11	72.26	45.00
0.064	0.848	135.00	114.41	72.52	45.00
0.066	0.875	135.00	114.70	72.78	45.00
0.068	0.903	135.00	114.98	73.04	45.00
0.070	0.931	135.00	115.25	73.29	45.00
0.072	0.959	135.00	115.52	73.54	45.00
0.074	0.987	135.00	115.79	73.79	45.00
0.076	1.015	135.00	116.05	74.03	45.00
0.078	1.043	135.00	116.31	74.27	45.00
0.080	1.071	135.00	116.56	74.51	45.00
0.082	1.099	135.00	116.81	74.75	45.00
0.084	1.127	135.00	117.05	74.98	45.00
0.086	1.156	135.00	117.29	75.21	45.00

Tab. E.4 - The horizontal collapse multiplier λ_c and the hinges position (identified by $\theta_1, \theta_2, \theta_3, \theta_4$) expressed as functions of the thickness s are reported with reference to a circular arch with $\beta = 45°$ and internal radius $r = 1.00m$.

■ E.2 ANALYTICAL SOLUTION FOR A CASE STUDY

In this section, we analyse a barrel vault tested at the DIST laboratory (Department of Structures for Engineering and Architecture, University of Naples Federico II) and we refer to the work of Ramaglia et al (2016). The geometry of the barrel vault is reported in **Fig. E.8**.

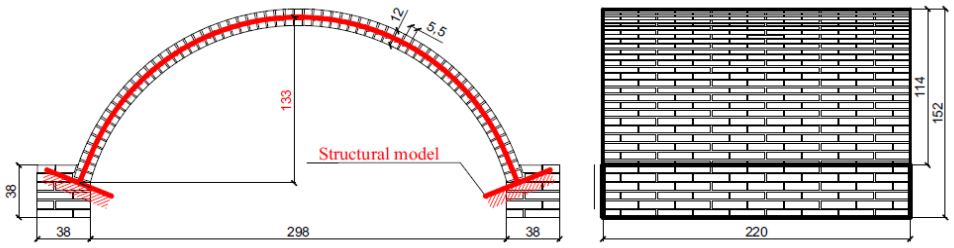

Fig. E.8 - Drawing from (Ramaglia et al, 2016): the geometry of the barrel vault is shown.

The structural geometry of the circular arch, reported in **Fig. E.9**, is characterized by a springing angle $\beta = 17.17°$, an internal radius $r = 1.54m$ and a thickness $s = 0.12m$.

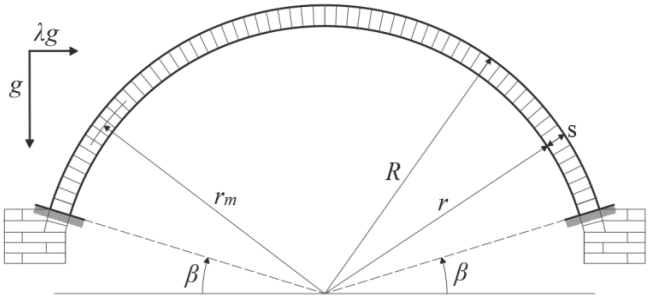

Fig. E.9 - The structural geometry of the tested arch is shown.

We develop the analysis shown in **Section E.1** with reference to the structural geometry shown in **Fig. E.9**. The generic mechanism considered is reported in **Fig. E.10** and the unknowns of the problem are the positions of the hinges and the horizontal multiplier, namely: $(\theta_1, \theta_2, \theta_3, \theta_4, \lambda)$. By expressing the work of external forces through these unknowns and by maximizing the value of λ in the set of all $(\theta_1, \theta_2, \theta_3, \theta_4, \lambda)$ such that the virtual work is equal to zero $L(\theta_1, \theta_2, \theta_3, \theta_4, \lambda) = 0$, we find the horizontal collapse multiplier λ_c.

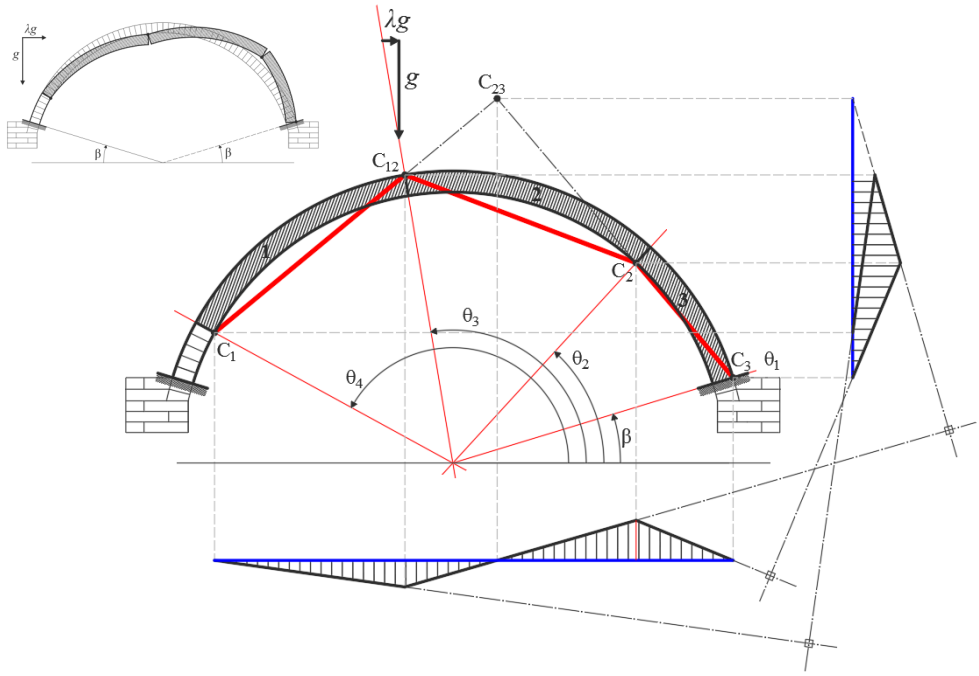

Fig. E.10 - Vertical and horizontal displacements of the generic failure mechanism related to the circular arch shown in **Fig. E.9**.

The analytical results in this case (s=0.12m) are extracted from the subsequent **Tab.E.5** (highlighted with the red rectangle) and reported below.

s =0.12m	λ_c	θ_4 [°]	θ_3 [°]	θ_2 [°]	θ_1 [°]
Analytical solution	0.1593	149.90	99.05	48.20	17.17

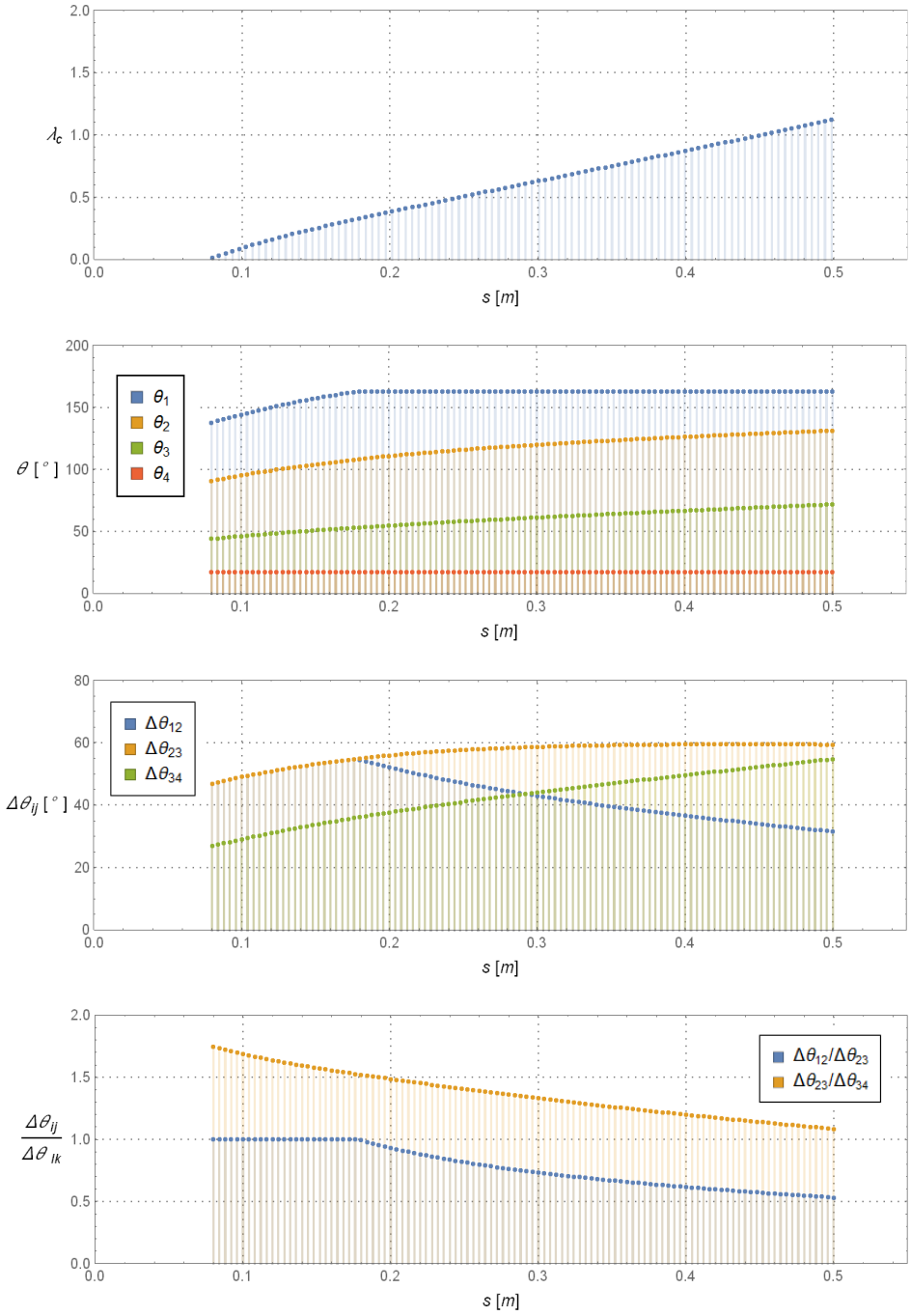

Fig. E.11 - Circular arch with $\beta = 17.17°$ and internal radius $r = 1.54m$: the horizontal collapse multiplier λ_c, the hinge positions (identified by $\theta_1, \theta_2, \theta_3, \theta_4$) and the geometrical characterization of the sectors of annulus (by using $\Delta\theta_{ij}$ and the ratio $\Delta\theta_{ij}/\Delta\theta_{kl}$) are reported.

s [m]	λ_c	θ_4 [°]	θ_3 [°]	θ_2 [°]	θ_1 [°]
0.08	0.014	137.58	90.78	43.98	17.17
0.09	0.054	141.05	93.09	45.13	17.17
0.10	0.091	144.23	95.22	46.21	17.17
0.11	0.126	147.17	97.20	47.23	17.17
0.12	0.159	149.90	99.05	48.20	17.17
0.13	0.191	152.45	100.79	49.13	17.17
0.14	0.221	154.84	102.44	50.03	17.17
0.15	0.249	157.10	104.00	50.89	17.17
0.16	0.277	159.24	105.48	51.72	17.17
0.17	0.304	161.26	106.90	52.53	17.17
0.18	0.330	162.81	108.25	53.31	17.17
0.19	0.355	162.83	109.53	54.07	17.17
0.20	0.381	162.83	110.74	54.80	17.17
0.21	0.406	162.83	111.87	55.52	17.17
0.22	0.431	162.83	112.94	56.21	17.17
0.23	0.456	162.83	113.96	56.88	17.17
0.24	0.481	162.83	114.92	57.54	17.17
0.25	0.505	162.83	115.84	58.19	17.17
0.26	0.530	162.83	116.72	58.82	17.17
0.27	0.555	162.83	117.56	59.44	17.17
0.28	0.579	162.83	118.36	60.05	17.17
0.29	0.603	162.83	119.14	60.65	17.17
0.30	0.628	162.83	119.88	61.24	17.17
0.31	0.652	162.83	120.60	61.82	17.17
0.32	0.677	162.83	121.30	62.39	17.17
0.33	0.701	162.83	121.97	62.95	17.17
0.34	0.725	162.83	122.63	63.51	17.17
0.35	0.750	162.83	123.26	64.07	17.17
0.36	0.774	162.83	123.88	64.61	17.17
0.37	0.799	162.83	124.48	65.16	17.17
0.38	0.823	162.83	125.07	65.69	17.17
0.39	0.848	162.83	125.64	66.23	17.17
0.40	0.873	162.83	126.21	66.76	17.17
0.41	0.897	162.83	126.76	67.28	17.17
0.42	0.922	162.83	127.30	67.81	17.17
0.43	0.947	162.83	127.83	68.33	17.17
0.44	0.972	162.83	128.35	68.85	17.17
0.45	0.997	162.83	128.86	69.36	17.17
0.46	1.022	162.83	129.36	69.88	17.17

Tab. E.5 - The horizontal collapse multiplier λ_c and the hinges position (identified by $\theta_1, \theta_2, \theta_3, \theta_4$) expressed as functions of the thickness s are reported with reference to a circular arch with springing angle $\beta = 17.17°$ and internal radius $r = 1.54m$.

Appendix F

ROCKING OF A RIGID BLOCK

Prologue. In this appendix, we present a basic introduction of rocking of a rigid block. Some applications, developed by using a numerical code implemented in Mathematica Wolfram, are shown in order to illustrate some typical well-known behaviours.

■ F.1 INTRODUCTION

Structural engineering generally deals with structures subjected to dynamic loads under the hypothesis of deformable behaviour. However, in some cases the simplified model of a rigid block supported unilaterally on a rigid plane can be useful to catch out the dynamical behaviour of some objects: e.g. isolated columns, statues, tanks of oil storage, water towers, nuclear reactors, mechanical and electrical hospital and laboratory equipments, that can lose their functionality because of earthquake motions. A block subjected to the base excitation can exhibit five types of motion: free flight, rest, slide, slide-rocking, rocking. Here we focus only on rocking motion.

The rocking motion of a block is a typical example of unilateral SDOF dynamics, identified, then, by a single Lagrangian coordinate (e.g. the rotation about a base corner). When the rocking motion starts, the block rotates around a base corner. If the block doesn't overturn, an instantaneous impact with the base will occur at a given moment. It is generally assumed that after the impact with the foundation, the block will continue in its state of rocking around the opposite vertex, as experimental data show (Monaco et al, 2014). The dynamic analysis of the rocking motion is very complex and involves highly nonlinear differential equations, taking into account

transitions of motion from one vertex to another (change of differential equation) and non-linearity associated with the impact, see (Sinopoli, 1987) and (Augusti and Sinopoli, 1992).

The first investigation on the dynamics of a slender rigid body, simply supported on a rigid ground with friction, is due to (Housner, 1963) at the beginning of sixties (i.e. during the Chilean earthquakes in 1960). In the piecewise model by Housner, the block can only rotate around the base corners, and the friction coefficient is large enough to prevent any sliding. With his study, Housner showed the existence of a **scale effect** necessary to explain why the larger of two geometrically similar blocks can support forcing actions for which the smaller block could overturn.

Later, experimental results on concrete blocks under various strong motion accelerograms, recorded during the San Fernando earthquake, showed in fact the chaotic nature of the problem (Aslam et al, 1978). The development of the study on rocking had a strong input in the '80s when the seismic safety of nuclear reactors became a theme of particular importance even in countries with low seismic activity. In 1984, Spanos and Koh (1984) defined some basic concepts about the periodic motions: symmetry/non-symmetry, order of an orbit, stability of symmetric orbits were examined. In the following years Hogan, on adopting these classifications in terms of response, extended the analysis to orbits of any order and verified the existence of motions with non-periodic and chaotic response (Hogan, 1989). Furthermore, since the sensitivity to initial conditions and geometrical dimensions creates uncertainty in the prediction of the asymptotic dynamics, Hogan bypassed the problem considering the transient phase having a duration comparable with a severe earthquake.

Successively Yim et al (1991) decided that the problem should be examined from a probabilistic point of view. Using a limited number of simulated ground motions the authors numerically solved the equation of the problem and produced fragility curves giving the probability of the body overturn. In (1999), Shao and Tung, following the same approach of (Yim et al, 1991), used two types of base motions: 50 artificial earthquakes simulated in a way identical to that of Yim and 75 real earthquakes. Shao reached the same conclusion as Yim et al. but showed that real earthquakes give less probability of overturning that simulated earthquakes do. Under realistic conditions, the rocking response of a rigid block is affected by additional factors such as the vertical component of the ground acceleration and the additional energy loss due to plastic deformations at the pivot points. In general, while rocking response under deterministic excitation has received considerable attention (Gesualdo et al, 2016b), the corresponding studies on stochastic behaviour are sparse.

Recent works (Prieto and Lourenço, 2005) have tried to unify the piecewise formulation by Housner, with the same hypothesis of large friction coefficient. The traditional piecewise equations are replaced by a single ordinary differential equation, and damping effects are no longer introduced by means of a coefficient of restitution, but are understood as the presence of impulsive forces. The results are in agreement with the classical formalism, and can be set in direct analogy with either a two-body central problem in the complex plane, or an inverted pendulum through simple variable transformations. Unfortunately these elegant formulations are unsuitable when rocking motion is to be avoided and sliding motion is welcome.

Recent attempts to derive equivalence between the single rocking block and various rocking mechanisms, in order to give indication for real structures (e.g. see **Section 8.4.1**) has been made by DeJong and Dimitrakopoulos (2014).

■ F.2 MOTION

The model to be analysed is shown in the following **Fig. F.2**. It is assumed that the block, rigid, has a constant density and the distance from both base corners is R. The friction coefficient between the block and the foundation is considered large enough to prevent slide and slide-rock. It is assumed that the impact is perfectly plastic and that there is no rebound.

The contact surface is assumed rigid and flat, so that the rocking motion is characterized by only one Lagrangian parameter.

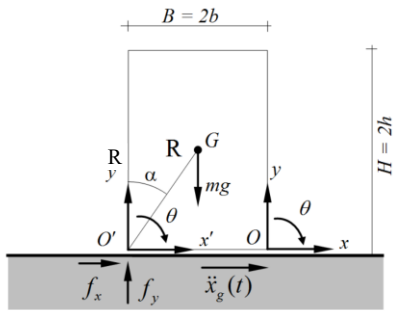

Fig. F.2 – Configuration of a rigid block in rocking.

Since the rotation about the corner O is assumed be positive whilst that about O' negative, a generic configuration is identified biunivocally by the angle θ or by the ratio x between the angle θ and the angle α defining the slenderness of the block. It should be noted that if $x = 1$ the block is in a configuration of unstable equilibrium and (for free oscillations) the condition $x > 1$ (with $\dot{x} > 0$) ensures the overturning.

Instead, in forced oscillations, it is possible to find a confined motion with $|x| > 1$. Clearly the geometric boundary condition is $\alpha x = \mp \pi/2$.

Shenton (1996) has shown that five starting motions response type (free flight, rest, slide, slide-rocking, rocking) are possible when an oscillation occurs, and in (Shenton, 1996) a diagram for individuation of initial response is given. Furthermore, taking into account only slide-rock and rocking motion, the transition between them, during the motion, is given in (Augusti and Sinopoli, 1992) considering the role of in determining this phenomena. The transition condition is:

$$\mu_s = \frac{3(B/H)}{4 + (B/H)^2}. \tag{F.1}$$

In conditions of free oscillations the region of pure rocking is that above the curve reported in **Fig. F.2**, while the region of slide-rocking is the one below (pointed area):

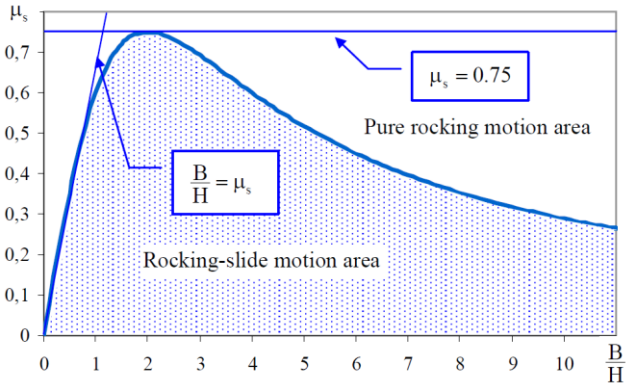

Fig. F.2 – Transition regions in the case of free oscillations.

■ F.3 IMPACT PROBLEM

As above said, the dynamic evolution of a rigid block is strongly influenced by impact, friction coefficient and ratio form of the block. When an impact occurs the pivot point changes instantly. The basic hypothesis generally assumed is that the impact is perfectly plastic or that there are not variations in the configuration of the block, but only in velocity. The problem of the impact is an impulsive-motion type, assuming that the cause of the sudden change of velocity is due to a force of "high intensity" agent in an “infinitesimal interval” so that the correspondent impulse is defined. But these considerations are not sufficient for the resolution of the problem: an additional hypothesis based on the definition of the impulsive force position is

needed. The problem can be overcome by using a restitution coefficient r. It could be defined as "energy" ratio and represented for symmetric block as follows:

$$r_i = \frac{\frac{1}{2}J_0\dot{\theta}^2(t_i^+)}{\frac{1}{2}J_0\dot{\theta}^2(t_i^-)} = \left(\frac{\dot{\theta}(t_i^+)}{\dot{\theta}(t_i^-)}\right)^2 , \tag{F.2}$$

where t_i represents the time of the $i-th$ impact and superscripts "-" and "+" identify the time before and after the impact. Anyhow, the introduction of a coefficient of restitution is often given simply through the ratio between the angular velocities before and after the impact, namely:

$$r_i = \frac{\dot{\theta}(t_i^+)}{\dot{\theta}(t_i^-)} . \tag{F.3}$$

If we assume constant the restitution coefficient r during the motion, in free oscillation the mechanical energy E_{tot}^N after N impacts can be expressed as follows:

$$E_{tot}^N = E_{tot}^0 r^{2N} , \tag{F.4}$$

where E_{tot}^0 is the mechanical energy at the instant $t = 0$. Alternatively, there is the approach proposed by Housner and consisting in the theoretical evaluation of the coefficient of restitution through the conservation of angular momentum. In fact, by relating the angular velocity of a symmetric body after the impact through relation (F.3), the conservation of angular momentum about O' just before the impact and right after the impact is:

$$J_0 - 2\mathrm{mrb}\sin\alpha\,\dot{\theta}(t_i^-) = J_0\dot{\theta}(t_i^+) . \tag{F.5}$$

The value of r for a rectangular symmetric block can be expressed as:

$$r = 1 - \frac{1}{2}\sin^2\alpha , \tag{F.6}$$

and r is independent of both the energy level of the pre-impact and the type of material, being a function only of the slenderness parameter α. The analogy between the dynamic behaviour of the pendulum and the rocking block (as inverted pendulum) is represented in **Fig F.3** by plotting on the phase plane $(x, \dot{x})$ the normalized mechanical energy $E_{tot}(x, \dot{x})$. In **Fig F.3b** the motion path, in free oscillation and for $r < 1$, is reported. It should be noted that whenever an impact occurs, a jump discontinuity on the angular velocity $\dot{x}$ happens and the total mechanical energy reduces and the path belongs to a lower energetic level set.

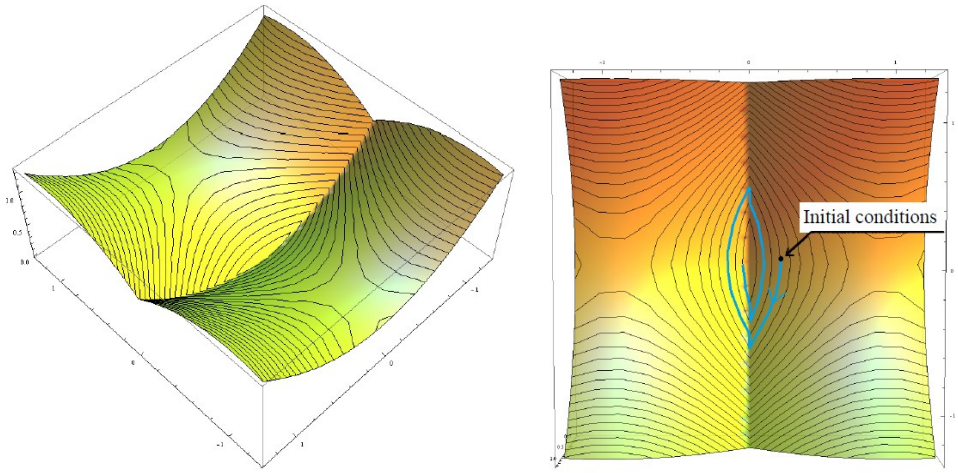

(a) (b)

Fig. F.3 – In (a) the normalized mechanical energy $E_{tot}(x, \dot{x})$ plotted on the phase plane $(x, \dot{x})$ is depicted. In (b) the path in free oscillations for $r < 1$ is shown.

■ F.4 EQUATIONS OF MOTION

With reference to **Fig. F.1**, it is possible to derive the equations of motion of the block in rocking by using the d'Alembert relations or derived directly from Lagrangian of the whole system.

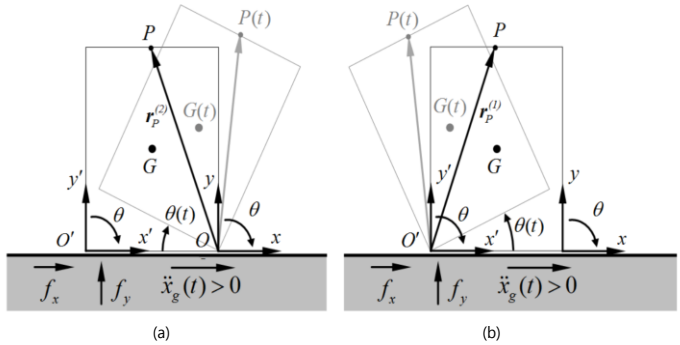

Fig. F.4 – Qualitative configurations for positive rotation (a) and negative ones (b).

In the numerical code developed, it is possible to assign any form of the external excitation, but the examples below proposed regard an external action expressed as follows:

$$\ddot{x}_g(\tau) = \beta\alpha g \cos(\Omega\tau + \phi)\,, \tag{F.7}$$

where:

- $\ddot{x}_g$ is the external horizontal forcing acceleration;
- β is the relative amplitude of the loading pulse ;
- g is the gravity acceleration;
- Ω is the frequency of the external actions;
- τ is the time variable;
- ϕ is the phase angle.

On defining the rocking frequency parameter p as the pendulum frequency of the block hanging about its corner, it is possible to express the differential equations governing the motion as a function of both two dimensionless parameters, namely the dimensionless time parameter $t = p\tau$ and the dimensionless frequency $\omega = \Omega/p$. It should be noted that the rocking frequency parameter for a symmetric rectangular block is $p = \sqrt{3g/4R}$. Definitively, the system of equations governing the motion of a generic rigid block is constituted by three relations: two nonlinear differential equations and an equation relating the angular velocities before and after the impact. The differential-algebraic equations (DAEs) can be expressed as follows:

$$\begin{cases} \alpha\ddot{x} + \sin\big(\alpha(1-x)\big) = -\alpha\beta\cos\big(\alpha(1-x)\big)\cos(\omega t) & for\ x > 0 \\ \alpha\ddot{x} - \sin\big(\alpha(1+x)\big) = -\alpha\beta\cos\big(\alpha(1+x)\big)\cos(\omega t) & for\ x < 0 \\ \dot{x}(t_i^+) = r\dot{x}(t_i^+) \end{cases}, \tag{F.8}$$

while for slender blocks the dependence on the angle α of the system (F.8) is lacking:

$$\begin{cases} \ddot{x} - x + 1 = -\beta\cos(\omega t) & for\ x > 0 \\ \ddot{x} - x - 1 = -\beta\cos(\omega t) & for\ x < 0 \\ \dot{x}(t_i^+) = r\dot{x}(t_i^+) \end{cases}. \tag{F.9}$$

It should be noted that the solution of the system, even in the simplified case of slender blocks, is complex as always in the case of nonlinear ordinary differential equations. In particular, in the ideal case with $r = 1$, the DAEs (F.8) can be condensed only in the following differential equation:

$$\alpha\ddot{x} + \mathrm{sgn}(x)\sin\big(\alpha(1 - \mathrm{sgn}(x)x)\big) = -\alpha\beta\cos\big(\alpha(1 - \mathrm{sgn}(x)x)\big)\cos(\omega t), \tag{F.10}$$

and equivalently the system (F.9) in:

$$\ddot{x} - x + \mathrm{sgn}(x) = -\beta\cos(\omega t), \tag{F.11}$$

where

$$\mathrm{sgn}(x): x \in \mathbb{R} \to \begin{cases} +1 & x > 0 \\ -1 & x < 0 \end{cases}. \tag{F.12}$$

■ F.5 EXAMPLES

In this section, we present some numerical results concerning first the case of free oscillations and later the case of forced ones in order to show some typical rocking behaviours.

F.5.1 Free oscillations

In this section, some typical time histories regarding free motion are proposed. In **Fig. F.5** three simple solutions for $r = 1$ obtained through the integration of differential equation (F.10) on assuming different initial conditions are depicted.

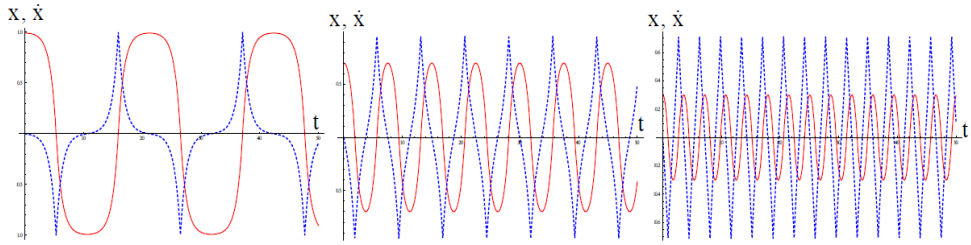

Fig. F.5 – Typical time histories for free motion with $r = 1$ (B=1.6, H=1) and considering different initial conditions: in (a): $(x(0), \dot{x}(0)) = (0.99, 0.00)$, in (b): $(x(0), \dot{x}(0)) = (0.70, 0.00)$ and in (c):dd $(x(0), \dot{x}(0)) = (0.30, 0.00)$.

In **Fig. F.6** a typical time history for a rigid block (H=3.0m, B=1.0m) in free oscillations with a restitution coefficient r=0.925 obtained by the numerical integration of (F.8) is depicted.

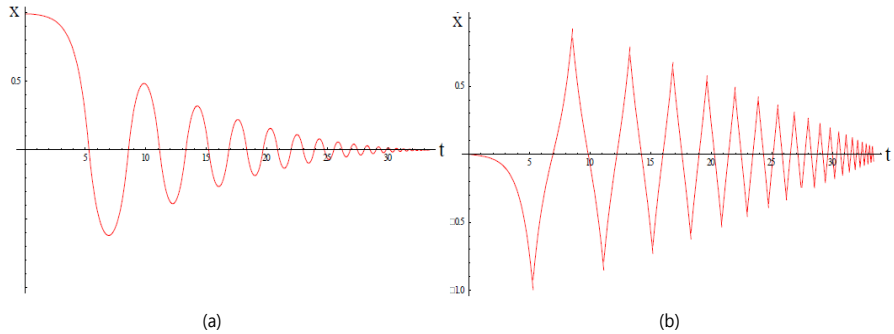

Fig. F.6 – Typical time histories for free motion with $r = 0.925$ and with initial conditions $(x(0), \dot{x}(0)) = (0.99, 0.00)$.

F.5.2 Forced oscillations

In this section, some typical response motions of a rigid block under sinusoidal excitations are presented. The variation of amplitude and frequency give several answers. The response diagrams are evaluated considering the nonlinear differential equations (F.8). In **Fig. F.7** the time histories of a typical unconfined motion are presented.

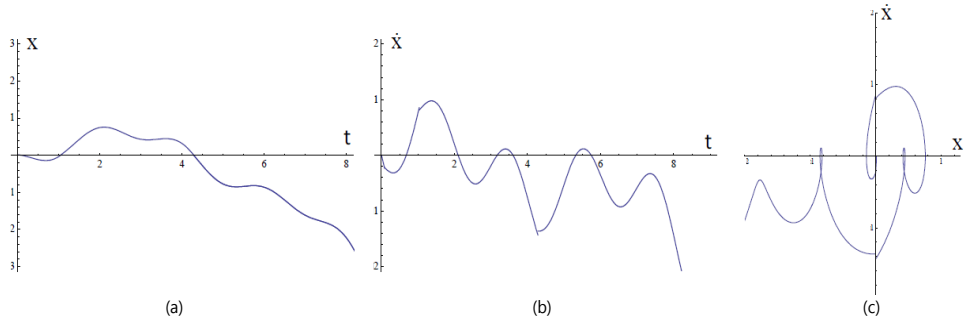

Fig. F.7 – Typical unconfined response (or overturning response): $r = 0.925$, $\omega = 3.14$, $\beta = 1.75$ and $\alpha = 0.5$. In (a): rotation, in (b): angular velocity, in (c) the related phase plane.

In **Figs. F.8**-**13** the results of the analyses, according to the definition of "orbit" given in (Spanos and Koh, 1984), are shown in order to test our numerical code and to illustrate some typical behaviour reported also in Hogan. The parameters of the external action are reported in every caption. In particular **Fig. F.12** illustrates a quasi periodic response whilst in **Fig. F.13** a typical chaotic response is reported: limited, casual and unpredictable, although with a certain order in the shape of motion, even if the excitation is periodical.

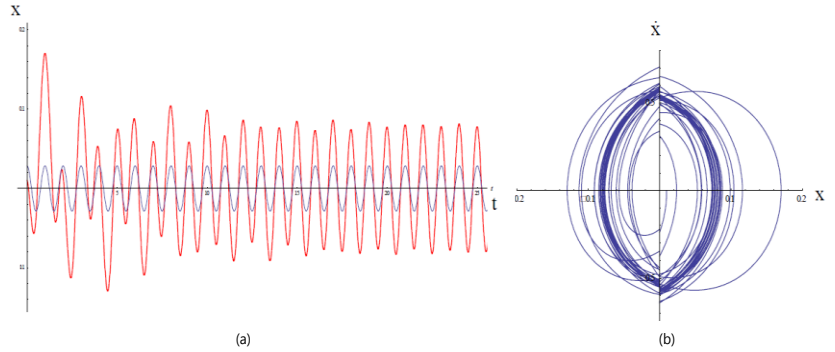

Fig. F.8 – Typical harmonic response with orbit of order (1,1): $r = 0.925$, $\omega = 6.28$, $\beta = 2.00$ and $\alpha = 0.5$. In (a): rotation, in (b): angular velocity, in (c) the related phase plane

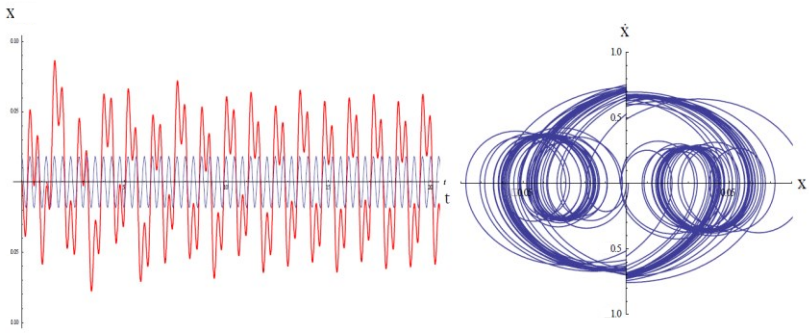

Fig. F.9 – Sub-harmonic response with orbit of order (1,3): $r = 0.925$, $\omega = 15.71$, $\beta = 6.50$ and $\alpha = 0.5$. In (a): rotation, in (b): angular velocity, in (c) the related phase plane.

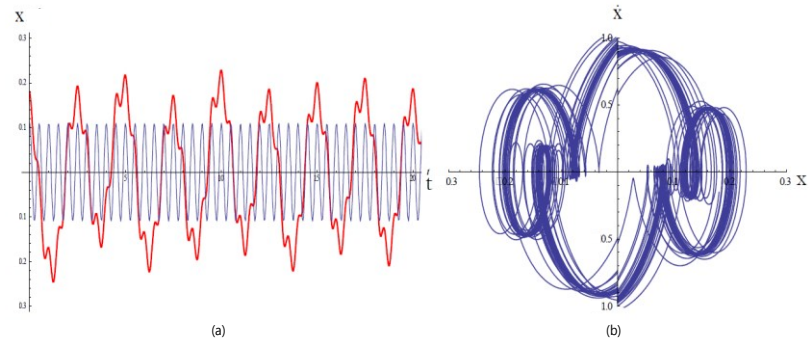

Fig. F.10 – Sub-harmonic response with orbit of order (1,5): $r = 0.925$, $\omega = 12.57$, $\beta = 5.50$ and $\alpha = 0.5$. In (a): rotation, in (b): angular velocity, in (c) the related phase plane.

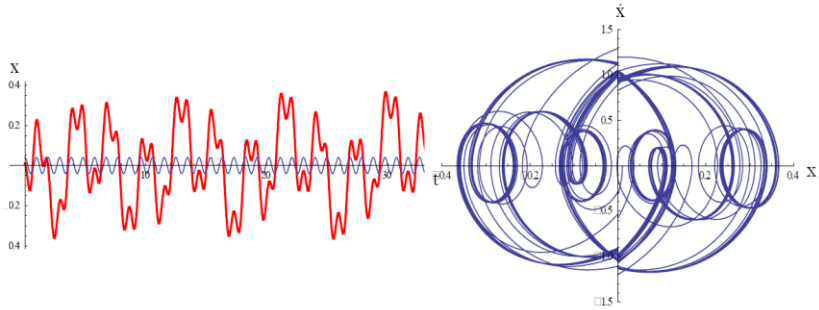

Fig. F.11 – Sub-harmonic response with orbit of order (3,9): $r = 0.925$, $\omega = 6.55$, $\beta = 4.00$ and $\alpha = 0.5$. In (a): rotation, in (b): angular velocity, in (c) the related phase plane.

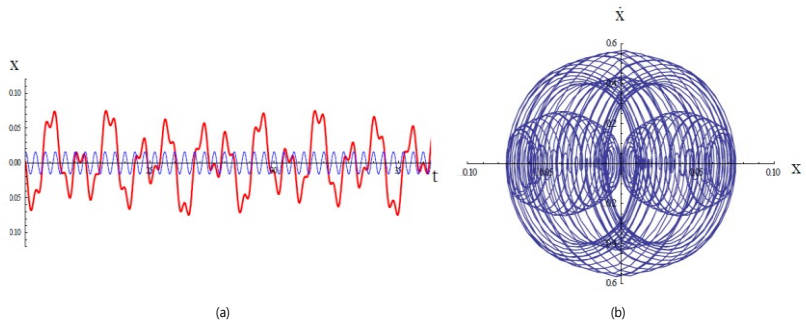

Fig. F.12 – Quasi periodic response: $r = 1.00$, $\omega = 15.71$, $\beta = 4.00$ and $\alpha = 0.46$. In (a): rotation, in (b): angular velocity, in (c) the related phase plane.

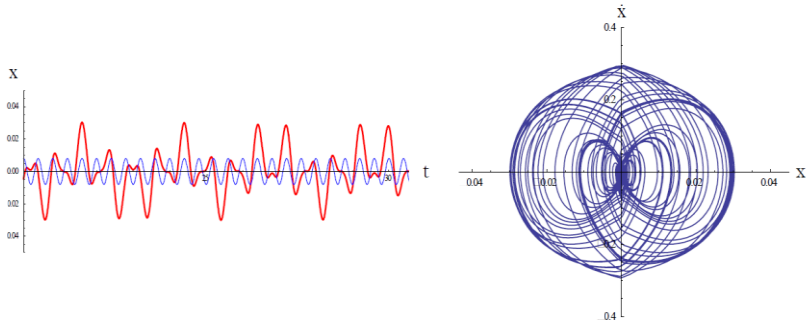

Fig. F.13 – Chaotic response: $r = 1.00$, $\omega = 15.71$, $\beta = 2.00$ and $\alpha = 0.46$. In (a): rotation, in (b): angular velocity, in (c) the related phase plane.

References

AA.VV. (1999). *Manuale per la riabilitazione e la ricostruzione postsismica degli edifici.* Roma: DEI.

Ambrosio, L., Fusco, N., & Pallara, D. (2000). *Functions of bounded variation and free discontinuity problems*. Oxford university press.

Angelillo, M. (1993). Constitutive relations for no-tension materials. *Meccanica, 28*, 195–202.

Angelillo, M. (Ed.). (2014a). *Mechanics of masonry structures.* Vienna: Springer.

Angelillo, M. (2014b). Practical applications of unilateral models to Masonry Equilibrium. In M. Angelillo (Ed.), *Mechanics of Masonry Structures* (pp. 109-210). Vienna: Springer.

Angelillo, M., & Rosso, F. (1995). On statically admissible stress fields for a plane masonry-like structure. *Quarterly of applied mathematics, 53(4)*, 731-751.

Angelillo, M., Babilio, E., & Fortunato, A. (2012). Numerical solutions for crack growth based on the variational theory of fracture. *Computational Mechanics, 50(3)*, 285-301.

Angelillo, M., Cardamone, L., & Fortunato, A. (2010). A numerical model for masonry-like structures. *Journal of Mechanics of Materials and Structures, 5(4)*, 583-615.

Angelillo, M., Fortunato, A., Montanino, A., & Lippiello, M. (2014). Singular stress fields in masonry structures: Derand was right. *Meccanica, 49(5)*, 1243-1262.

Anzellotti, G. (1985). A class of convex non-coercive functionals and masonry-like materials. In *Annales de l'IHP Analyse non linéaire*, (2)(4), 261-307).

Aslam, M., Godden, W. G., & Scalise, D. T. (1978). Rocking and Overturning response of rigid bodies to earthquake motions. *Lawrence Berkeley National Laboratory*.

Augusti, G., & Sinopoli, A. (1992). Modelling the dynamics of large block structures. In *Masonry Construction* (p. 195-211). Springer Netherlands.

Bagi, K. (2014). When Heyman's Safe Theorem of rigid block systems fails: Non-Heymanian collapse modes of masonry structures. *International Journal of Solids and Structures, 51(14)*, 2696-2705.

Baratta, A., Toscano, R. (1982). Stati tensionali in pannelli di materiale non resistente. *Atti del VII Congresso Nazionale AIMETA.* Genova.

Barlow, W. H. (1846). On the existence (practically) of the line of equal horizontal thrust in arches, and the mode of determining it by geometrical construction. In *Minutes of the Proceedings of the Institution of Civil Engineers* (Vol. 5, p. 162-172).

Bathe, K. J., & Wilson, E. L. (1976). *Numerical methods in finite element analysis.* Prentice-Hall.

Becchi, A., & Foce, F. (2002). *Degli archi e delle volte – Arte del costruire tra meccanica e stereotomia.* Venezia: Marsilio Editori.

Belidor, B. F. de (1729). *La science des ingenieurs dans la conduite des travaux de fortification et d'architecture civile.* Paris: Claude Jombert.

Benvenuto, E. (1991). *An Introduction to the History of Structural Mechanics. Part I: Statics and Resistance of Solids. Part II: Vaulted Structures and Elastic Systems.* New York: Springer.

Block, P. (2009). *Thrust network analysis: exploring three-dimensional equilibrium.* Doctoral dissertation, Massachusetts Institute of Technology.

Block, P., DeJong, M., & Ochsendorf, J. (2006). As hangs the flexible line: Equilibrium of masonry arches. *Nexus Network Journal, 8(2)*, 13-24.

Brandonisio, G., Mele, E., & De Luca, A. (2015). Closed form solution for predicting the horizontal capacity of masonry portal frames through limit analysis and comparison with experimental test results. *Engineering Failure Analysis, 55*, 246-270.

Brandonisio, G., Mele, E., & De Luca, A. (2017). Limit analysis of masonry circular buttressed arches under horizontal loads. *Meccanica*, 1-19.

Calderoni, B. (2015). *Edifici esistenti in muratura: comportamento strutturale e valutazione della resistenza sismica.* Dipartimento di Strutture per l'Ingegneria e l'Architettura Università degli Studi di Napoli Federico II.

Capecchi, D. (2012). *History of virtual work laws: a history of mechanics prospective.* Springer Science & Business Media.

Castellano, G. (1988). Un modello cinematico per i materiali non resistenti a trazione. *Cinquantenario della Facoltà di Architettura di Napoli: Franco Jossa e la sua opera* (p. 241-256). Napoli: Giannini.

Castigliano, A. (1879). *Théorie de l'équilibre des systèmes élastiques et ses applications.* Turin: Negro.

Cennamo, C., De Serio, F., Fortunato, A., Gesualdo, A., Iannuzzo, A., Montanino, A., & Angelillo, M. (2017). The kinematical problem for masonry-like structures: an energetical approach. *submitted*.

Chambolle, A., Giacomini, A., & Ponsiglione, M. (2007). Piecewise rigidity. *Journal of Functional Analysis, 244(1)*, 134-153.

Como, M. (1992). Equilibrium and collapse analysis of masonry bodies. In *Masonry Construction* (p. 185-194). Springer Netherlands.

Como, M. (2013). *Statics of historic masonry constructions.* Berlin-Heidelberg: Springer Verlag.

Como, M., & Grimaldi, A. (1985). A unilateral model for the limit analysis of masonry walls. In *Del Piero, G., & Maceri, F. (Eds.) Unilateral Problems in Structural Analysis* (pp. 25-45). Vienna: Springer.

Coulomb, C. A. (1773). Essai sur une application des regles de maximis & minimis a quelques problemes de statique: Relatifs a l'architecture. *Mémoires de mathématique & de physique, présentés à l'Académie Royale des Sciences par divers savans, 7*, 343-82. Paris : De l'Imprimerie Royale, 1776.

Couplet, P. (1729). De la poussée des voûtes. *Mémoires de l'Académie Royale des Sciences*, 79-117.

Couplet, P. (1730). Seconde partie de l'examen de la poussée des voûtes. *Mémoires de l'Académie Royale des Sciences*, 117-141.

Cremona, L. (1872). *Le figure reciproche nella statica grafica.* Milano: Tipografia di G. Bernardoni.

Cremona, L. (1874). *Elementi di calcolo grafico.* Torino: stamperia reale di G.B. Paravia e c.

Culmann, C. (1866). *Die graphische statik.* Zürich: Meyer & Zeller.

Cundall, P. (1971). A computer model for simulating progressive large scale movements in blocky rock systems. *Proceedings of the Symposium of the International Society of Rock Mechanics*, *1(II-8).* Nancy, France.

Dantzig, G. (2016). *Linear programming and extensions.* Princeton university press.

Dantzig, G. B., Orden, A., & Wolfe, P. (1955). The generalized simplex method for minimizing a linear form under linear inequality restraints. *Pacific Journal of Mathematics, 5(2)*, 183-195.

Danyzy, A. A. (1732). Méthode générale pour déterminer la résistance qu'il faut opposer à la poussée des voûtes. *Histoire de la Société Royale des Sciences établie à Montpellier, 2(1718-1745)*, 40-56. Published : Lyon 1778.

De Buhan, P., & De Felice, G. (1997). A homogenization approach to the ultimate strength of brick masonry. *Journal of the Mechanics and Physics of Solids, 45(7)*, 1085-1104.

De Maria, A. (s.d.). *Costruzioni in muratura e meccanismi di collasso. Materiale del Corso di Teoria delle Strutture.*

De Serio, F., Angelillo, M., De Chiara, E., Gesualdo, A., Iannuzzo, A., & Pasquino, M. (2016). Masonry structures made of monolithic blocks with an application to spiral stairs. *Submitted*.

DeJong, M.J., & Dimitrakopoulos, E.G. (2014). Dynamically equivalent rocking structures. *Earthquake Engineering and Structural Dynamics, 43(10)*, 1543-1564.

Del Piero, G. (1989). Constitutive equation and compatibility of the external loads for linear elastic masonry-like materials. *Meccanica, 24(3)*, 150-162.

Del Piero, G. (1996). Materiali non resistenti a trazione e analisi limite. *Proceedings of the Meeting Giornata di Studio AIDIS, Capri 1995.* Bari: Levante srl.

Del Piero, G. (1998). Limit analysis and no-tension materials. *International Journal of Plasticity, 14(1-3)*, 259-271.

Derand, F. (1643). *L'Architecture des voûtes ou l'art des traits et coupe des voûtes.* Paris: Sébastien Cramoisy.

Di Pasquale, S. (1984). *Statica dei solidi murari: teoria ed esperienze.* Università di Firenze: Atti Dipartimento Costruzioni.

Drucker, D. C., Prager, W., & Greenberg, H. J. (1952). Extended limit design theorems for continuous media. *Quarterly of Applied Mathematics, 9(4)*, 381-389.

Faccio, P. (a.a. 2014-15). *Consolidamento degli edifici storici.* Dispense del prof. Paolo Faccio, Università IUAV di Venezia, Dipartimento di Costruzioni dell'Architettura.

Fisher, R. C. (1992). *Visual lexicon of the South African dwelling.* Cape Town : Unibook Publishers (Pty) Ltd.

Foce, F., & Aita, D. (2003). The masonry arch between «limit» and «elastic» analysis. A critical re-examination of Durand-Claye's method. *Proceedings of the First International Congress on Construction History*, (p. 20-24). Madrid.

Forgács, T., Sarhosis, V., & Bagi, K. (2017). Minimum thickness of semi-circular skewed masonry arches. *Engineering Structures, 140*, 317-336.

Fortunato, A., Babilio, E., Lippiello, M., Gesualdo, A., & Angelillo, M. (2016). Limit Analysis for Unilateral Masonry-like Structures. *The Open Construction and Building Technology Journal, 10(Suppl 2:M12)*, 346-362.

Fortunato, A., Fraternali, F., & Angelillo, M. (2014). Structural capacity of masonry walls under horizontal loads. *Ingegneria Sismica, 31(1)*, 41-49.

Fraternali, F., Angelillo, M., & Fortunato, A. (2002). A lumped stress method for plane elastic problems and the discrete-continuum approximation. *International journal of solids and structures, 39(25)*, 6211-6240.

Frézier, A. F. (1737-39). *La théorie et la pratique de la coupe de pierres et des bois pour la construction des voûtes et autres parties des bâtiments civils et militaires, ou traité de stéréotomie à l'usage de l'architecture (3 vols).* Strasbourg/Paris: Jean Daniel Doulsseker - L. H. Guerin.

Gesualdo, A., & Monaco, M. (2015). Constitutive behaviour of quasi-brittle materials with anisotropic friction. *Latin American Journal of Solids and Structures, 12(4)*, 695-710.

Gesualdo, A., Cennamo, C., Fortunato, A., Frunzio, G., Monaco, M., & Angelillo, M. (2016a). Equilibrium formulation of masonry helical stairs. *Meccanica*, 1-12.

Gesualdo, A., Iannuzzo, A., Guadagnuolo, M. T., Guerriero, A., Monaco, M., & Savino, M. T. (2016b). Numerical analysis of rigid body behaviour. *Applied Mechanics & Materials, 847*, 240-247.

Giaquinta, M., & Giusti, E. (1985). Researches on the equilibrium of masonry structures. *Archive for Rational Mechanics and Analysis, 88(4)*, 359-392.

Giuffrè, A. (1991). *Letture sulla Meccanica delle Murature Storiche.* Edizioni Kappa.

Giuffrè, A. (1993). *Sicurezza e conservazione dei centri storici. Il caso Ortigia.* Bari: Laterza.

Gregory, D. (1697). Catenaria. *Phil. Trans, 19(231)*, 637-652.

Gurtin, M. E. (1972). The linear theory of elasticity. In C. A. Truesdell, & S. Flugge (Ed.), *Handbuch der Physik* (Vol. VIa/2, pp. 1-295). Berlin-Heidelberg-New York: Springer Verlag.

Heyman, J. (1966). The stone skeleton. *International Journal of solids and structures, 2(2)*, 249-279.

Heyman, J. (1969). The safety of masonry arches. *International Journal of Mechanical Sciences, 11(4)*, 363-385.

Heyman, J. (1995). *The stone skeleton: structural engineering of masonry architecture.* Cambridge: Cambridge University Press.

Heyman, J. (1998). *Structural analysis: a historical approach*. Cambridge : Cambridge University Press.

Heyman, J. (2009). La coupe des pierres. In *Proceedings 3rd International Congress on Construction History* , (2),807-812).

Hogan, S. J. (1989). On the dynamics of rigid-block motion under harmonic forcing. *Proceedings of the Royal Society of London A: Mathematical, Physical and Engineering Sciences, 425(186)*, 441-476.

Hooke, R. (1676). *A description of helioscopes, and some other instruments.* London: T.R. for John Martyn.

Housner, G. W. (1963). The behavior of inverted pendulum structures during earthquakes. *Bulletin of the seismological society of America, 53(2)*, 403-417.

Huerta, S. (2002). The medieval 'scientia'of structures: the rules of Rodrigo Gil de Hontañón.

Huerta, S. (2006). Galileo was wrong: the geometrical design of masonry arches. *Nexus Network Journal, 8(2)*, 25-52.

Huerta, S. (2008). The analysis of masonry architecture: a historical approach: to the memory of professor Henry J. Cowan. *Architectural Science Review, 51(4)*, 297-328.

Iannuzzo, A., Angelillo, M., De Chiara, E., De Guglielmo, F., De Serio, F., Ribera, F., & Gesualdo, A. (2016). Modelling the cracks produced by settlements in masonry structures. *Meccanica, Under review*.

Kooharian, A. (1952). Limit Analysis of Voussoir (Segmental) and Concrete Archs. *Journal of the American Concrete Institute, 24(4)*, 317-328.

Kupfer, H. (1973). Behavior of Concrete under Multiaxial Short Term Loading, with Emphasis on Biaxial Loading. *Deutscher Ausschuss fur Stahlbeton*, *254* . Berlin.

La Hire, P. de (1695). *Traité de mécaniqueo: ou l'on explique tout ce qui est nécessaire dans la pratique the arts, & les propriétés des corps pesants lesquelles ont un plus grand usage dans la Physique.* Paris: de l'Imprimerie Royale et se vend chez Jean Anisson.

La Hire, P. de. (1712). Sur la construction des voûtes dans les édifices. *Mémoires de l'Académie Royale des Sciences*, 69-77.

Le Seur, T., Jacquier, F., & Boscovich, R. G. (1742). *Parere di tre mattematici sopra i danni che si sono trovati nella cupola di S. Pietro sul fine dell'anno 1742*. Roma.

Lebon, F. (2014). Modeling the interfaces in masonry structures. In M. Angelillo (Ed.), *Mechanics of Masonry Structures* (pp. 213-240). Vienna: Springer.

Leibniz, G.W. (1691). De solutionibus problematis catenarii vel funicolaris. *Ada Eruditorum*, 435-439.

Livesley, R. K. (1978). Limit analysis of structures formed from rigid blocks. *International Journal for Numerical Methods in Engineering, 12(12)*, 1853-1871.

Lourenço, P. B., & Milani, G. (2014). Homogenization and seismic assessment: review and recent trends. In M. Angelillo (Ed.), *Mechanics of Masonry Structures* (pp. 293-341). Vienna: Springer.

Lucchesi, M., Šilhavý, M., & Zani, N. (2013). On the choice of functions spaces in the limit analysis for masonry bodies. *Journal of Mechanics of Materials and Structures, 7(8)*, 795-836.

Marcolongo, R. (1937). *Studi Vinciani, Memorie sulla geometria e la meccanica di Leonardo da Vinci.* Napoli: S.I.E.M. - Stabilimento Industrie Editoriali Meridionali.

Marmo, F., & Rosati, L. (2017). Reformulation and extension of the thrust network analysis. *Computers & Structures, 182*, 104-118.

Mastrodicasa, S. (1988). *Dissesti statici delle strutture edilizie.* Milano: Hoepli.

Mehrotra, S. (1992). On the implementation of a primal-dual interior point method. *SIAM Journal on optimization, 2(4)*, 575-601.

Milani, G. (2011). Simple lower bound limit analysis homogenization model for in-and out-of-plane loaded masonry walls. *Construction and Building Materials, 25(12)*, 4426–4443.

Monaco, M., Guadagnuolo, M., & Gesualdo, A. (2014). The role of friction in the seismic risk mitigation of freestanding art objects. *Natural hazards, 73(2)*, 389-402.

Moreau, J.J. (1974). On unilateral constraints, friction and plasticity. In *New variational techniques in mathematical physics* (p. 171-322).

Moseley, H. (1843). *The mechanical principles of engineering and architecture*. London: Longman, Brown, Green and Longmans.

Navier, C. (1833-38). *Résumé des leçons données à l'Ecole des Ponts et Chaussées, sur l'application de la mécanique à l'établissement des construcions et des machines. Deuxième édition corrigée et augmentée (3 vols).* Paris: Carilian-Goeury.

Nunziante, L. (2005). *Plasticità e Analisi Limite, Seminari introduttivi.* Napoli.

Nunziante, L., Gambarotta, L., & Tralli, A. (2011). *Scienza delle costruzioni* (3rd ed.). McGraw-Hill.

Ochsendorf, J. (2006). Masonry arch on spreading supports. *Structural Engineer, 84(2)*, 29-34.

Papa, F., & Zuccaro G. (2001). *CD Multimediale MEDEA - Manuale di Esercitazione sul Danno ed Agibilità per edifici ordinari. CAR Progetti srl per DPC-USSN*.

Pippard, A.J.S., & Ashby, R.J. (1939). An experimental study of the voussoir arch. *Journal of the Institution of Civil Engineers, 12(8)*, 371-372.

Pippard, A.J.S., Tranter, E. and Chitty, L. (1936). The mechanics of the voussoir arch. *Journal of the Institution of Civil Engineers, 4(2)*, 281-306.

Poleni, G. (1748). *Memorie istoriche della gran cupola del tempio Vaticano e de'danni di essa e detristoramenti loro, divisi in libri cinque.* Padova: Nella stamperia del seminario.

Prager, W. (1957). On ideal locking materials. *Transactions of the Society of Rheology, 1(1)*, 169-175.

Prieto, F., & Lourenço, P. B. (2005). On the rocking behavior of rigid objects. *Meccanica, 40(2)*, 121-133.

Ramaglia, G., Lignola, G. P., & Prota, A. (2016). Collapse analysis of slender masonry barrel vaults. *Engineering Structures, 117*, 86-100.

Romano, G., & Sacco, E. (1985). Analisi limite e collasso plastico per materiali non standard ben posti. *Riv. Ital. Geotecnica, 1*, 37-41.

Romano, G., Romano, M. (1979). Sulla soluzione di problemi strutturali in presenza di legami costitutivi unilaterali. *Accademia Nazionale dei Lincei, LXVII*, 1-10.

Sacco, E. (2009). A nonlinear homogenization procedure for periodic masonry. *European Journal of Mechanics-A/Solids, 28(2)*, 209-222.

Sacco, E. (2014). Micro, multiscale and macro models for masonry structures. In M. Angelillo (Ed.), *Mechanics of Masonry Structures* (pp. 241-291). Vienna: Springer.

Sarhosis, V., Bagi, K., Lemos, J. V., & Milani, G. (Eds.). (2016). *Computational Modeling of Masonry Structures Using the Discrete Element Method.* IGI Global.

Shao Y., & Tung C.C. (1999). Seismic Response of Unanchored Bodies. *Earthquake Spectra, 15(3)*, 523-536.

Shenton III, H. W. (1996). Criteria for initiation of slide, rock, and slide-rock rigid-body modes. *Journal of Engineering Mechanics*, *122*(7), 690-693.

Šilhavý, M. (2014). Mathematics of the masonry–like model and limit analysis. In M. Angelillo (Ed.), *Mechanics of Masonry Structures* (pp. 29-69). Vienna: Springer.

Simon, J., & Bagi, K. (2016). Discrete element analysis of the minimum thickness of oval masonry domes. *International Journal of Architectural Heritage, 10(4)*, 457-475.

Sinopoli, A. (1987). Dynamics and impact in a system with unilateral constraints the relevance of dry friction. *Meccanica, 22(4)*, 210-215.

Spanos, P. D., & Koh, A. S. (1984). Rocking of rigid blocks due to harmonic shaking. *Journal of Engineering Mechanics, 110(11)*, 1627-1642.

Stevin, S. (1586). *De Beghinselen der Weeghconst*. (In The Principal Works of Simon Stevin, vol. 1, Leyden, 1955).

Stirling, J. (1717). *Lineae tertii ordinis Neutonianae, sive, Illustratio tractatus D. Neutoni De enumeratione linearum tertii ordinis: cui subjungitur, solutio trium problematum.* Oxford: Impensis Edvardi Whistler Bibliopolae Oxoniensis.

Tóth, A. R., Orbán, Z., & Bagi, K. (2009). Discrete element analysis of a stone masonry arch. *Mechanics Research Communications, 36(4)*, 469-480.

Truesdell, C. A., & Noll, W. (1965). The non-linear field theories of mechanics. In S. Flugge (Ed.), *Handbuch der Physik* (Vol. III/3, pp. 1-579). Berlin-Heidelberg-New York: Springer Verlag.

Vanderbei, R. J. (2015). *Linear programming*. Springer.

Varignon. (1725). *Nouvelle mécanique ou statique dont le projet fut donné en MDCLXXXVII. Ouvrage posthume (2 vols).* Paris: chez Claude Jombert.

Viollet-le-Duc, E.E. (1858–1868). *Dictionnaire raisonné de l'architecture franĆcaise du XI e au XVI e Siècle, 10 vols.* Paris: Bance-Morel.

Ware, S. (1809). *A treatise of the properties of arches, and their abutment piers.*

Wolfram, S. (2003). *The Mathematica Book* (5th ed.). Wolfram Media.

Yim, S. C., & Lin, H. (1991). Nonlinear impact and chaotic response of slender rocking objects. *Journal of Engineering Mechanics, 117(9)*, 2079-2100.

Yvon Villarceau, A. (1854). L'établissement des arches de pont. Institut de France, Académie des Sciences, Mémoires présentés par divers savants, 12, 503.